

REPORT DOCUMENTATION PAGE

Form Approved
OMB No. 0704-0188

Public reporting burden for this collection of information is estimated to average 1 hour per response, including the time for reviewing instructions, searching data sources, gathering and maintaining the data needed, and completing and reviewing the collection of information. Send comments regarding this burden estimate or any other aspect of this collection of information, including suggestions for reducing this burden to Washington Headquarters Service, Directorate for Information Operations and Reports, 1215 Jefferson Davis Highway, Suite 1204, Arlington, VA 22202-4302, and to the Office of Management and Budget, Paperwork Reduction Project (0704-0188) Washington, DC 20503.

PLEASE DO NOT RETURN YOUR FORM TO THE ABOVE ADDRESS.

1. REPORT DATE (DD-MM-YYYY) 05-08-2013		2. REPORT TYPE FINAL		3. DATES COVERED (From - To) 01-01-2011 -- 31-07-2013	
4. TITLE AND SUBTITLE Experimental Characterization of Supercavitating Fins Piercing a Ventilated Supercavity				5a. CONTRACT NUMBER	
				5b. GRANT NUMBER N00014-11-1-0156	
				5c. PROGRAM ELEMENT NUMBER	
6. AUTHOR(S) Matthew Gordon				5d. PROJECT NUMBER	
				5e. TASK NUMBER	
				5f. WORK UNIT NUMBER	
7. PERFORMING ORGANIZATION NAME(S) AND ADDRESS(ES) Stevens Institute of Technology One Castle Point on Hudson Hoboken, NJ 07030				8. PERFORMING ORGANIZATION REPORT NUMBER	
9. SPONSORING/MONITORING AGENCY NAME(S) AND ADDRESS(ES) Office of Naval Research REG BOSTON N62879 495 SUMMER STREET ROOM 627 BOSTON, MA 02210-2109				10. SPONSOR/MONITOR'S ACRONYM(S) ONR	
				11. SPONSORING/MONITORING AGENCY REPORT NUMBER	
12. DISTRIBUTION AVAILABILITY STATEMENT Distribution Statement A: Approved for public release, distribution is unlimited.					
13. SUPPLEMENTARY NOTES					
14. ABSTRACT This report presents the results from water tunnel experiments on supercavitating fins performed at the Garfield Thomas Water Tunnel of the Pennsylvania State University's Applied Research Laboratory. Finite span fins with wedge cross sections piercing the boundary of a ventilated supercavity were tested over a range of conditions. Lift, drag, and shaft torque were measured using a six degree-of-freedom force and moment transducer. Tunnel velocity, cavity size, fin chord, angle of attack, and sweepback angle were varied systematically. For all conditions, gas was entrained in the low pressure base wake produced by the fin, forming a ventilated trailing cavity. At low angles of attack, the cavity formed from the trailing edges of the fin's pressure and suction sides. At higher angles of attack, the suction side of the fin ventilated, which resulted in cavity formation from the leading and trailing edges of the fin's pressure side. A decrease in lift and shaft torque was observed when the fin ventilated, along with a rearward shift in the center of pressure. Unsteady state tests were performed where the fins were oscillated about their spanwise axis over a range of rates and angles.					
15. SUBJECT TERMS supercavitation, fins, cavity-piercing					
16. SECURITY CLASSIFICATION OF:			17. LIMITATION OF ABSTRACT U	18. NUMBER OF PAGES 196	19a. NAME OF RESPONSIBLE PERSON Dr. John Dzielski
a. REPORT U	b. ABSTRACT U	c. THIS PAGE U			19b. TELEPHONE NUMBER (Include area code) 201-216-8782

EXPERIMENTAL CHARACTERIZATION OF SUPERCAVITATING FINS PIERCING
A VENTILATED CAVITY BOUNDARY

ABSTRACT

This thesis presents the results from recent water tunnel experiments on supercavitating fins performed at the Garfield Thomas Water Tunnel facility of the Pennsylvania State University's Applied Research Laboratory. Finite span fins with wedge cross sections piercing the boundary of a ventilated supercavity were tested over a range of conditions to explore the effects of varying fin geometry and flow parameters. Lift, drag, and shaft torque were measured using a six degree-of-freedom force and moment transducer. Tunnel velocity, cavity size, fin chord, angle of attack, and sweepback angle were varied systematically. For all conditions examined, gas was entrained in the low pressure base wake produced by the fin, forming a ventilated trailing cavity. At low angles of attack, the trailing cavity formed from the trailing edges of the fin's pressure and suction sides. At higher angles of attack, the suction side of the fin ventilated, which resulted in cavity formation from the leading and trailing edges of the fin's pressure side. A decrease in lift and shaft torque was observed when the fin ventilated, along with a rearward shift in the center of pressure. Unsteady state tests were performed where the fins were oscillated about their spanwise axis over a range of rates and angles of attack to study the mechanism of transition. A noticeable hysteresis was found between the angle of attack at which suction-side ventilation occurred and the angle at which the fin transitioned back to base ventilation. A corresponding hysteresis was also present in the measured lift, shaft torque, and center of pressure.

Author: Matthew A. Gordon

Advisor: Dr. John Dzielski

Date: December 17, 2012

Department: Civil, Environmental, and Ocean Engineering

Degree: Master of Engineering - Ocean Engineering

Acknowledgments

The author would like to recognize and thank all parties that contributed to the content of this thesis. First, the author would like to thank Dr. Maria Medieros, Dr. Ron Joslin, and the Department of the Navy, Office of Naval Research for providing funding under the University/Laboratory Initiative (ULI Program) through Award Nos. N00014-11-1-0159 and N00014-11-1-0156, making this thesis possible. The author would also like to thank his advisor, Dr. John Dzielski, his Navy Laboratory mentor, Mr. Michael Moeny, and his thesis committee member, Dr. Raju Datla for their guidance and support throughout the project. Finally, the author would like to thank Marshall Reid at Stevens and Ronald Ayers Jr. at ARL for fabricating test hardware.

Table of Contents

Abstract	iii
Acknowledgments	iv
List of Tables	ix
List of Figures	xi
1 Introduction	1
1.1 Cavitation	1
1.2 Supercavitation	3
1.3 Supercavitating Hydrofoils	8
1.4 Surface Piercing Hydrofoils	13
1.5 Hydrodynamic Forces	14
1.6 Project Description	16
2 Description of Experimental Work	18
2.1 Overview	18
2.2 Experimental Facility	18

2.3	Unswept Fin Testing	20
2.3.1	Preliminary Estimates	20
2.3.2	Test Hardware	24
2.3.3	Instrumentation and Data Acquisition	27
2.3.4	Unswept Fin Test Methodology	29
2.4	Swept Fin Testing	31
2.4.1	Test Hardware	31
2.4.2	Instrumentation and Data Acquisition	35
2.4.3	Swept Fin Test Methodology	37
3	Test Data Reduction	39
3.1	Steady State Test Data	39
3.1.1	Post-Processing	39
3.1.2	Uncertainty Analysis	44
3.1.3	Tunnel Wall Corrections	47
3.2	Unsteady Test Data	49
4	Experimental Results and Discussion	52
4.1	Wake Forms and Cavity Structures	52
4.1.1	Trailing Cavities from Unswept Fins	52
4.1.2	Trailing Cavities from the Swept Fins	60
4.1.3	Thickness of the Ventilated Supercavity	66
4.1.4	Gas Entrainment and the Reentrant Jet	69
4.2	Steady State Testing	71
4.2.1	Fin Force and Moment Measurements	71
4.2.2	Comparison with Theory	93
4.2.3	Cavity Instability	97

4.3	Transition and Hysteresis	100
4.3.1	Modes of Transition	101
4.3.2	Transition Angle of Attack	103
4.4	Effects of Varying Ventilation Rate	110
5	Conclusions and Future Work	114
5.1	Summary and Conclusions	114
5.2	Future Recommendations	117
A	Cavitator Dimensions and Locations	120
B	Damage to the Two-Inch Fin	126
C	Additional Setup Photos	129
D	Plots of Steady State Data	135
D.1	Measured Lift	135
D.2	Measured Drag	138
D.3	Measured Normal Force	141
D.4	Measured Tangent Force	144
D.5	Measured Shaft Torque M_z	147
D.6	Measured Lift Coefficient	150
D.7	Measured Drag Coefficient	153
D.8	Measured Moment Coefficient	156
E	Transition Angles of Attack	160
E.1	Transition to Fully Ventilated	161
E.2	Transition to Base Ventilated	164

Bibliography

List of Tables

2.1	Limits and Sensitivity of the AMTI Transducer	28
3.1	Estimated Systematic Errors for Different Measurement Systems	46
4.1	Effective wedge half-angles and chord lengths for the swept fins	62
4.2	Measured cavitation number from the swept fin tests, based on cavity pressure. Most of the cavity pressure measurements from the unswept fin tests were no good, which is why they were omitted from the table	75
4.3	Measured cavity thickness, in inches at the fin's leading edge at zero angle of attack for all combinations of chord, cavitator, sweepback angle, and tunnel velocity tested. Cavitators c1 and c2 are the small and large curved cavitators used during the unswept testing, and f1 and f2 are the small and large flat cavitators used during the swept fin testing, respectively	76

- 4.4 Reference area used to calculate force and moment coefficients, in square inches. Reference area is the area of the fin above a line drawn tangent to the flow from where the fin intersects the cavity boundary at the leading edge. Cavitators c1 and c2 are the small and large curved cavitators used during the unswept testing, and f1 and f2 are the small and large flat cavitators used during the swept fin testing, respectively. 76
- 4.5 Aspect ratios for each chord, sweep, cavitator combination tested 79
- 4.6 Reynolds Numbers for Various Test Conditions 87
- 4.7 Froude Numbers for Various Test Conditions 87

List of Figures

1.1	Schematic of Various Cavitating Flow Regimes, adapted Stinebring et al. (2002)	3
1.2	Artificially Ventilated Supercavity, adapted from Dzielski et al. (2012)	4
1.3	Reentrant Jet Cavity Closure Showing Ventilation Gas Expulsion through Toroidal Vorticies	6
1.4	Various types of Cavitation on Traditional and Supercavitating Hydrofoil Sections, Adapted from (Auslaender, 1962)	9
1.5	Leading Edge Vibration on a Supercavitating Fin with a Wedge Cross Section, $\alpha = 8^\circ$, $V = 148$ ft/s, adapted from (Auslaender, 1962)	12
1.6	Sign conventions for Lift, Drag, Shaft Torque (Mz), Normal Force and Tangent Force. All vectors illustrate positive direction.	15
1.7	Object operating in an artificially ventilated supercavity fitted with a cavity piercing fin.	17
2.1	Schematic of the Twelve-Inch Water Tunnel at ARL/PSU, adapted from (Stinebring et al., 2002)	19

2.2	Lift and Drag Coefficients for a Flat Plate Hydrofoil vs. Angle of Attack and Cavitation Number using Wu's Free Streamline Theory (Wu, 1955).	21
2.3	Estimated Lift and Drag for a Fin with $\psi = 7.5^\circ$, $S = 6in$, operating at $V = 45ft/s$ and $\sigma = 0.1$, piercing a 2 inch cavity.	23
2.4	Schematic of the unswept fin test platform used to make measurements on a cavity piercing fin. The surface of a cavity running object was simulated as the top of the water tunnel. Fins mounted flush to the wall and hung down into the free stream. Cavities were created along the top of the tunnel with a wall cavitator.	24
2.5	Unswept Fin Test Apparatus Installed in the 12 Inch Water Tunnel at ARL	25
2.6	Wedge Cavitator used for Unswept Fin Testing	26
2.7	Family of Wedge Fins	27
2.8	Video Cameras on Custom Mount	29
2.9	Aluminum Base Plate for the Swept Fin Apparatus	32
2.10	Aluminum Base Plate for the Swept Fin Apparatus Fitted with a Wall Cavitator	33
2.11	Models of the Swept Fin Apparatus set up with a fin swept to 30 degrees	34
2.12	Swept Fin Apparatus Installed in the Twelve-Inch Water Tunnel at ARL set up with a fin swept to 45 degrees.	34
2.13	Timing Belt Fin Actuation Mechanism and Optical Encoder	36
3.1	Typical Time History from Steady State Unswept Fin Testing	41
3.2	Tares for 2in Fin Swept to 45 Degrees	44
3.3	Errors in the Measurement of a Variable X, Large Number of Measurements	45

- 3.4 Identification of the location of the transition from base to full ventilation using time history of M_y . Left shows gradual transition, and right shows the more dramatic “flash” ventilation. 50
- 4.1 Base ventilated fin from the side, $\alpha = 0^\circ$, no sweep, 1 inch chord 53
- 4.2 Base ventilated fin looking down the span from the fin tip, $\alpha = 0^\circ$, no sweep, 1 inch chord 53
- 4.3 Asymmetric vortex cavities forming from the tip of a base ventilated fin at a non-zero angle of attack, looking down the span from the fin tip. 3 inch chord, $\alpha = 3^\circ$, no sweep 54
- 4.4 Photo of a base ventilated fin, taken from the suction side, 1 inch chord at an angle of attack of 5 degrees, no sweep 55
- 4.5 Vaporous cavitation on a yawed fin at a low cavitation number showing the three low pressure regions that encourage the formation of a fully ventilated trailing cavity when the fin pierces a ventilated cavity boundary. $\alpha = 15^\circ$, no sweep, 1 inch chord, photographed with 1/40 second exposure time. 56
- 4.6 Fully ventilated supercavitating fin piercing a ventilated cavity boundary, photo taken from suction side of the fin, $\alpha = 15^\circ$, 1 inch chord, no sweep, photographed with 1/60 second exposure. 57
- 4.7 Fully ventilated supercavitating fin piercing a ventilated cavity boundary, looking down span from fin tip, $\alpha = 20^\circ$, 1 inch chord, no sweep. 58
- 4.8 The angle at which the cavity boundary over the suction side forms at, with respect to the incoming flow, varies with the fin’s angle of attack. This is shown here for the unswept 3 inch chord fin for $\alpha = 10^\circ, 15^\circ, 20^\circ$ 58

- 4.9 Vaporous partial cavity formed near the leading edge of an unswept base ventilated fin during steady state testing. 2 inch chord, $\alpha = 5^\circ$, photo taken with 1/160 second exposure time 59
- 4.10 Progression of ventilated partial cavities during transition between fully and base ventilated operation. The figure on the left shows a large partial cavity present at the beginning of transition, the figure in the middle shows a smaller ventilated partial cavity at a slightly lower angle of attack, and the figure on the right shows horizontal streak cavities present immediately before transition is complete. Approximate shapes of the rear of the partial cavities are outlined in blue. 60
- 4.11 Trapezoidal planform of the 2 inch chord fin swept back 45 degrees. Region above the dashed line has a constant triangular cross section with respect to the incoming flow. Region below the dashed line tapers to a point. 61
- 4.12 Base ventilated swept supercavitating fin, viewed from suction side, 2 inch chord, $\alpha = 5^\circ$, $\gamma = 45^\circ$, $V = 25 ft/s$, photo taken with 1/200 second exposure time. Dark spots on the fin surface are droplets of water stuck to the suction side of the fin inside the cavity 63
- 4.13 Base ventilated swept supercavitating fin, view from the bottom of the tunnel, 2 inch chord, $\alpha = 0^\circ$, $\gamma = 30^\circ$ 64
- 4.14 Base ventilated swept supercavitating fin, view from the bottom of the tunnel, 2 inch chord, $\alpha = 3^\circ$, $\gamma = 30^\circ$ 64
- 4.15 Fully ventilated swept supercavitating fin, view from the suction side, 2 inch chord, $\alpha = 15^\circ$, $\gamma = 45^\circ$, $V = 25 ft/s$, photo taken with 1/200 second exposure time 65

- 4.16 Ventilated partial cavities on the 2 inch fin swept to 45° , $V = 25\text{ft/s}$, at angles of attack, from left to right for the top and bottom rows, of 5.5, 5, 4.5, 4, 3.5, and 3 degrees, respectively. Photo taken with an exposure time of 1/200 second. 66
- 4.17 Deformation of the ventilated cavity boundary on the suction side (left), pressure side (right) for a swept fin at $\pm 12.5^\circ$, compared to the fin at zero degrees (center), 2 inch fin, $V = 25\text{ft/s}$, $\gamma = 30^\circ$ 67
- 4.18 Fin planform area, measured from the suction side of the fin, as a function of angle of attack and tunnel velocity, 2 inch chord, $\gamma = 30^\circ$, large cavitator 68
- 4.19 Deformation of the cavity along the top of the tunnel downstream of the fin. The cavity appears to be collapsing on the pressure side. 2 inch fin, small cavitator, $\alpha = 7.5^\circ$, $V = 35\text{ft/s}$, $\gamma = 30^\circ$ 69
- 4.20 Reentrant jet striking cavity walls downstream of an unswept cavity piercing fin. 1 inch chord, $V=35\text{ft/s}$, $\alpha = 5^\circ$ 70
- 4.21 Sequence showing the reentrant jet striking the rear of a swept fin and inducing a partial cavity collapse. Images taken from high-speed video shot at 600 fps. Cavity collapse and reformation took a little less than one second. 2 inch fin, $V=35\text{ft/s}$, fin being rotated about its axis. 72
- 4.22 Typical steady state experimental data showing lift as a function of angle of attack and tunnel velocity. 73
- 4.23 Typical steady state experimental data showing drag as a function of angle of attack and tunnel velocity. 73
- 4.24 Typical pressure distribution along the pressure and suction sides of a thin, traditional airfoil at non-zero incidence. Pressure distribution approximated using XFOil 74

4.25	Pressure distribution along pressure side of the fin for a fully ventilated flat plate inclined to 10 degrees. Experimental data replotted from (Meijer, 1965).	74
4.26	Diagram showing reference area used for force and moment coefficients, outlined in red	75
4.27	Lift coefficient vs. Angle of Attack and Froude Number, 2 inch chord, $\gamma = 0^\circ$, large cavitator	77
4.28	Lift coefficient vs. Angle of Attack and Froude Number, 1 inch chord, $\gamma = 0^\circ$, large cavitator	77
4.29	Lift coefficient vs. Angle of Attack and Froude Number, 2 inch chord, $\gamma = 30^\circ$, large cavitator	78
4.30	Lift coefficient vs. Angle of Attack and Froude Number, 2 inch chord, $\gamma = 45^\circ$, small cavitator	78
4.31	Lift coefficient plotted against angle of attack and aspect ratio for the unswept fins.	79
4.32	Lift coefficient plotted against angle of attack and aspect ratio for fins swept to 30° .	80
4.33	Lift coefficient plotted against angle of attack and aspect ratio for fins swept to 45° .	80
4.34	Lift coefficient plotted against angle of attack and sweep, comparing $\gamma = 30^\circ$ and 45° for $\Lambda \approx 1$.	81
4.35	Lift coefficient plotted against angle of attack and sweep, $\gamma = 30^\circ$ and 45° for $\Lambda \approx 0.75$.	82

- 4.36 Lift coefficient plotted against angle of attack and sweep $\gamma = 0^\circ$ and 30° for $\Lambda \approx 2$. The six points at angles of attack of 5 and 6 degrees for the unswept fin are significantly higher than the measured values for the swept fin because the transition occurred later for the unswept fin than it did for the swept fin. 82
- 4.37 Drag coefficient as a function of angle of attack and tunnel velocity, 1 inch chord, $\gamma = 0^\circ$, large cavitator 85
- 4.38 Drag coefficient as a function of angle of attack and tunnel velocity, 2 inch chord, $\gamma = 0^\circ$, small cavitator 85
- 4.39 Drag coefficient as a function of angle of attack and tunnel velocity, 1 inch chord, $\gamma = 30^\circ$, large cavitator 87
- 4.40 Drag coefficient as a function of angle of attack and tunnel velocity, 2 inch chord, $\gamma = 30^\circ$, small cavitator 87
- 4.41 Drag coefficient from the unswept fin testing plotted against angle of attack and aspect ratio for $R_n = 3.1 * 10^5$, $F_r = 21.4$, 1 inch chord, 35ft/s 88
- 4.42 Drag coefficient from the unswept fin testing plotted against angle of attack and aspect ratio for $R_n = 4.0 * 10^5$, $F_r = 27.5$, 1 inch chord, 45ft/s 88
- 4.43 Drag coefficient plotted against angle of attack and sweep $\gamma = 30^\circ$ and 45° for $\Lambda \approx .75$. The effects of differences in Reynolds and Froude numbers are assumed to be negligible, though that may not be the case. 89
- 4.44 Lift/Drag Ratio from the unswept fin testing plotted against angle of attack and tunnel velocity, 2 inch chord, large cavitator 90
- 4.45 Lift/Drag Ratio from the unswept fin testing plotted against angle of attack and tunnel velocity, 1 inch chord, small cavitator 90
- 4.46 Lift/Drag Ratio from the unswept fin testing plotted against angle of attack and aspect ratio, 2 inch chord, $R_n = 8.1 * 10^5$, $F_r = 19.4$ 91

4.47	Lift/Drag Ratio from the unswept fin testing plotted against angle of attack and aspect ratio, 1 inch chord, $R_n = 4.0 * 10^5$, $F_r = 27.5$	91
4.48	Non-dimensionalized shaft torque plotted as a function of angle of attack and tunnel velocity, 2 inch chord, $\gamma = 30^\circ$, small cavitator	91
4.49	Non-dimensionalized shaft torque plotted as a function of angle of attack and tunnel velocity, 2 inch chord, $\gamma = 45^\circ$, small cavitator	91
4.50	Center of pressure, measured from the leading edge as a function of angle of attack and tunnel velocity, 2 inch chord, $\gamma = 30^\circ$, small cavitator, percent of chord	92
4.51	Center of pressure, measured from the leading edge as a function of angle of attack and sweepback angle, 2 inch chord, small cavitator, percent of chord. Data presented for fins swept to 30 and 45 degrees.	94
4.52	Comparison of theory and measured lift coefficients, 2 inch chord, $\gamma = 0^\circ$, large cavitator.	95
4.53	Comparison of theory and measured lift coefficients, 2 inch chord, $\gamma = 45^\circ$, small cavitator	95
4.54	Comparison of theory and measured drag coefficients, 2 inch chord, $\gamma = 0^\circ$, large cavitator.	96
4.55	Comparison of theory and measured drag coefficients, 2 inch chord, $\gamma = 30^\circ$, small cavitator	96
4.56	Time history of measured normal force from steady state run showing instability in the trailing cavity, 1 inch chord, $\alpha = 6^\circ$, $V=45\text{ft/s}$, Small Cavitator	97

- 4.57 Photos showing the progression of the sporadic transition instability found during the steady state fin experiments, 2 inch chord, $\alpha = 6^\circ$, no sweep, $V=45\text{ft/s}$, large cavitator. A) The fin is base ventilated at the beginning of the run; B) A partial cavity forms near the leading edge; C) gas is pulled into the low pressure region over the suction side, forming a large ventilated partial cavity; D) The reentrant jet begins to lap on the back of the fin near the fin tip, (this makes the cavity near the tip a milky white color); E) The reentrant jet chokes off the partial cavity over the suction side, resulting in cavity collapse; F) The tip vortex appears to ventilate, pulling gas toward the leading edge to re-inflate the ventilated cavity over the suction side; G) Cavity re-forms and is clear for a moment; H) Process repeats itself 99
- 4.58 Time history of measured normal force from steady state run showing instability in the trailing cavity, 1 inch chord, $\alpha = 5^\circ$, $V=45\text{ft/s}$, Small Cavitator 100
- 4.59 Sequence showing flash ventilation of the two-inch chord fin swept to 30 degrees, while the angle of attack was increasing. Frames taken from a high-speed video shot at 600 fps. Current sequence spanned about 15 frames, which is equal to about 0.025 seconds. 102
- 4.60 Time history of measured normal force and angle of attack from unsteady state test with the one-inch chord fin swept to 30 degrees, showing gradual transition where ventilated partial cavities forms and grew during transition. 104
- 4.61 Plot showing the angle of attack at which transition from base to fully ventilated operation occurred as a function of the angular velocity of the fin at transition. No noticeable trend could be detected for any conditions tested. This plot is for data from the unswept 1 inch chord fin at 35 ft/s. 104

- 4.62 Ventilation angle of attack plotted against nominal tunnel velocity, 1 inch chord, $\gamma = 0^\circ$, small cavitator 105
- 4.63 Ventilation angle of attack plotted against nominal tunnel velocity, 2 inch chord, $\gamma = 30^\circ$, small cavitator 105
- 4.64 Ventilation angle plotted against sweep angle, 1 inch chord, $V=35\text{ft/s}$, small cavitator 106
- 4.65 Ventilation angle plotted against sweep angle, 2 inch chord, $V=25\text{ft/s}$, small cavitator 106
- 4.66 Ventilation angle plotted against chord length, $\gamma = 0^\circ$, $V=25\text{ft/s}$, small cavitator 106
- 4.67 Ventilation angle plotted against chord length, $\gamma = 30^\circ$, $V=35\text{ft/s}$, small cavitator 106
- 4.68 Data from an unsteady test where the fin was oscillated about its spanwise axis, showing the normal force F_N as a function of angle of attack. A fairly large hysteresis is present between where the fin transitions to and from fully ventilated operation. The data plotted here is for an unswept fin oscillated at 18 cycles per minute, 2 inch chord, 45ft/s . 107
- 4.69 Data from an unsteady test where a swept fin was oscillated about its spanwise axis, showing the normal force F_N as a function of angle of attack. The hysteresis is smaller for the swept fin than it was for the unswept fin. $\gamma = 30^\circ$, $V=45\text{ft/s}$, 2 inch chord 108

- 4.70 Data from an unsteady test where a swept fin was oscillated about its spanwise axis, showing the normal force F_N as a function of angle of attack. Here, the fin gradually transitioned from base to fully ventilated, and no hysteresis was observed. $\gamma = 30^\circ$, $V=45\text{ft/s}$, 1 inch chord. The spikes at higher angles of attack are a result of the reentrant jet lapping on the rear of the fin. 109
- 4.71 Measured cavity thickness at the leading edge of the fin at zero degrees vs. entrainment coefficient. 110
- 4.72 Trailing cavities for different flow rates. Trailing cavity is murky due to reentrant jet effects at low flow rates and is clear at high flow rates. At the lowest flow rate, the trailing cavity was also found to be significantly shorter than what was found at the other conditions. One-inch chord, $\gamma = 45^\circ$, $\alpha = 0^\circ$ 112
- 4.73 Lift plotted against angle of attack and flow rate, 1 inch chord fin, $\gamma = 45^\circ$, $V=45\text{ft/s}$ 113
- 4.74 Shaft torque plotted against angle of attack and flow rate, 1 inch chord fin, $\gamma = 45^\circ$, $V=45\text{ft/s}$ 113
- 4.75 Measured cavitation number vs. Flow Coefficient for the 1 inch chord fin piercing a cavity off the small cavitator, $V=45\text{ft/s}$, $\gamma = 45^\circ$, averaged over $\alpha = \pm 12.5^\circ$ 113

List of Symbols

- A Planform Area
- A_s Wetted Surface Area
- B/B_o Ratio of Foil Area to Tunnel Cross-Sectional Area
- B_x Systematic/Bias Error in a Particular Measurement X
- C_D Drag Coefficient $C_D = D/(1/2\rho V^2 A)$
- C_{DT} Drag Coefficient Corrected for Tunnel Wall Effects
- C_{D2d} Estimated Drag Coefficient of a Two-Dimensional Section
- C_{D3d} Estimated Drag Coefficient of a Three-Dimensional Section
- C_{Di} Induced Drag Coefficient
- C_f Friction Coefficient
- C_L Lift Coefficient $C_L = L/(1/2\rho V^2 A)$
- C_{L2d} Estimated Lift Coefficient of a Two-Dimensional Section
- C_{L3d} Estimated Lift Coefficient of a Three-Dimensional Section

- C_P Pressure Coefficient defined as $C_P = \frac{P - P_\infty}{1/2\rho V_\infty^2}$
- C_M Moment Coefficient $C_M = M/(1/2\rho V^2 A c)$
- C_q Flow Coefficient
- D Measured Drag
- D_f Friction Drag
- D_i Induced Drag
- F_N Force Normal to the Centerline of the Fin
- F_r Froude Number
- F_τ Force Tangent to the Centerline of the Fin
- L Measured Lift
- L_p Center of Pressure Measured from Leading Edge, Non-Dimensionalized by Fin Chord
- M Measured Moment
- P_∞ Static/Ambient Pressure
- P_1 Reference Pressure for Gas Flowmeter, taken as 14.7 psia
- P_2 Pressure used to Calculate Actual Gas Flow Rate, in psia
- P_c Cavity Pressure
- P_g Partial Pressure of Non-condensable Gas in Supercavity
- P_t Total Pressure, Measured in the Settling Chamber Upstream of the Test Section

- P_v Partial Pressure of Vapor in the Supercavity
- P_{vap} Vapor Pressure of Water
- P_x Random/Precision Error in a Particular Measurement X
- Q Gas Injection Rate
- Q_1 Measured Ventilation Gas Flow Rate in Standard Cubic Feet per Minute (SCFM)
- Q_2 Actual Ventilation Gas Flow Rate at Tunnel Conditions
- R_n Reynolds Number, $R_e = VL/\nu$
- S Span of the Fin
- T_1 Reference Temperature, taken as 530° Rankine
- T_2 Reference Temperature for Calculating Actual Gas Flow Rate, taken as Tunnel Temperature in Rankine
- U_r Total Uncertainty Propagated Through a Reduction Equation into a Final Measurement r
- U_x Total Uncertainty in a Particular Measurement X
- V_∞ Free Stream Velocity
- a_{3d} Lift Curve Slope, Corrected for Finite Aspect Ratio Effects
- a_o Section Lift Curve Slope
- a_{so} Lift Curve Slope of Swept Fin
- c Chord Length

- c_e Effective Chord Length, Calculated as $c_e = c/\cos(\gamma)$
- e_o Oswald Efficiency Factor
- e_1 correction factor for planform geometry
- g Acceleration due to Gravity
- n Number of samples of a particular measurement, used to calculate mean and standard deviation
- s Standard Deviation
- t_c Cavity Thickness at the Leading Edge of the Fin
- t/c Thickness to chord ratio
- w_c Approximate Width of Cavity Along the Top of the Tunnel
- \bar{x} Mean of n number of measurements
- Λ Aspect Ratio
- ψ Fin Wedge Half-Angle
- ψ_e Wedge Half-Angle of the Swept Fins with respect to the Incoming Flow
- α Angle of Attack of the fin, in Radians
- α_T Angle of Attack, Corrected for Tunnel Wall Effects
- α_d Angle of Attack, in Degrees
- γ Fin Sweepback Angle, From Vertical
- δ Wall Correction Factor

- η Lift/Drag Ratio
- θ_i Absolute Sensitivity Coefficients for Calculating Propagation of Error through a Reduction Equation
- ν Kinematic Viscosity
- ρ Density of Water
- σ_c Cavitation Number Based on Cavity Pressure, also known as the Cavity Underpressure
- σ_i Incipient Cavitation Number
- σ_v Vapor Cavitation Number

Chapter 1

Introduction

1.1 Cavitation

Cavitation is a phenomenon that occurs when vaporous cavities form in regions of low pressure in a homogeneous liquid. The likelihood that cavitation is to exist for a particular flow geometry is described by a non-dimensional parameter called the cavitation number. Cavitation number describes the relationship between the static and dynamic pressures in a fluid, and is commonly defined as:

$$\sigma_v = \frac{P_\infty - P_{vap}}{\frac{1}{2}\rho V_\infty^2} \quad (1.1)$$

where P_∞ is the ambient pressure, P_{vap} is the liquid's vapor pressure, ρ is the density, and V_∞ is a reference velocity. Physically, the numerator can be thought of as the pressure in a fluid tending to collapse a cavity, while the denominator is the pressure tending to form one (Knapp et al., 1970).

The term incipient cavitation is used to describe the condition when cavitation initially appears. Incipient cavitation occurs when the cavitation number drops below a critical value, σ_i . The critical cavitation number is dependent on a variety of factors, including flow geometry, viscosity, turbidity, and the quantity of non-condensable gas dissolved in

the liquid (Franc and Michel, 2004, Ch. 1).

Cavitation inception will generally occur in a flow over a body at the location of the minimum pressure coefficient, $C_{P_{min}}$, which is defined as:

$$C_{P_{min}} = \frac{P_{min} - P_{\infty}}{\frac{1}{2}\rho V_{\infty}^2} \quad (1.2)$$

where P_{min} is the minimum pressure in the fluid.

It is commonly assumed that cavitation first occurs when the minimum pressure in a fluid drops below the vapor pressure, P_{vap} (Franc and Michel, 2004, Ch. 1). With this assumption, the incipient cavitation number can be defined as:

$$\sigma_i = -C_{P_{min}} \approx -\frac{P_{vap} - P_{\infty}}{\frac{1}{2}\rho V_{\infty}^2} \quad (1.3)$$

Decreasing cavitation number results in an increase in the severity of cavitation, which can be accomplished by either increasing the reference velocity, V_{∞} or decreasing the ambient pressure, P_{∞} . As cavitation number is decreased beyond the incipient cavitation number, sheet and attached cavitation develop. Dropping the cavitation number even further results in the formation of larger cavities that stretch beyond the cavitating body. This phenomenon is known as supercavitation. These various forms of cavitation are shown in fig. 1.1, for the case where ambient pressure is decreased from non-cavitating to supercavitating flow. More information on the various types of cavitation can be found in (Franc and Michel, 2004; Knapp et al., 1970).

Cavitation is generally an undesirable phenomenon. The presence of cavitation has been found to result in a decrease in performance of hydraulic machinery such as pumps, turbines and propellers. The rapid formation and collapse of cavities has been found to produce excessive noise and vibration. The rapid collapse of cavities in a fluid near surfaces

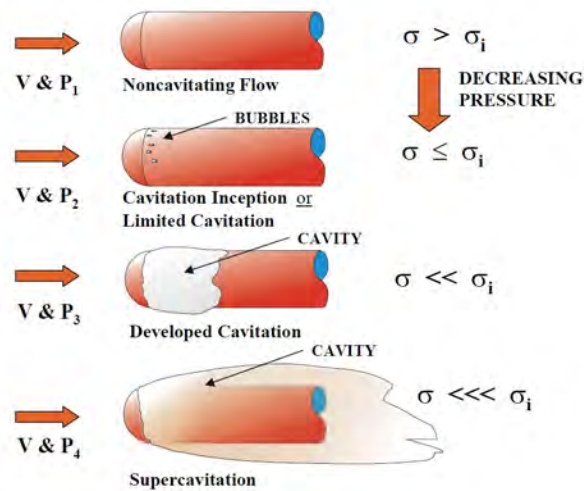


Figure 1.1: Schematic of Various Cavitating Flow Regimes, adapted Stinebring et al. (2002)

has also been found to result in erosion. Examples of cavitation damage can be found in (Knapp et al., 1970, Ch. 1).

1.2 Supercavitation

As the cavitation number for a particular flow is decreased, small cavities attached to a cavitating body, also known as a cavitator, will expand and ultimately form a supercavity. This cavity will remain attached to the cavitating body and close somewhere downstream. The shape of the supercavity will generally remain constant for a given set of conditions, though significant oscillations may be present where the cavity closes (Stinebring et al., 2002). A typical supercavity is shown in fig. 1.2.

In real flows, supercavities are typically filled with a mixture of vapor and non-condensable gas (Franc and Michel, 2004, Ch. 1, 8). Thus, the actual pressure in the cavity can be defined as:

$$P_c = P_v + P_g \quad (1.4)$$

where P_v and P_g are the partial pressures of the vapor and gas in the cavity, respectively.

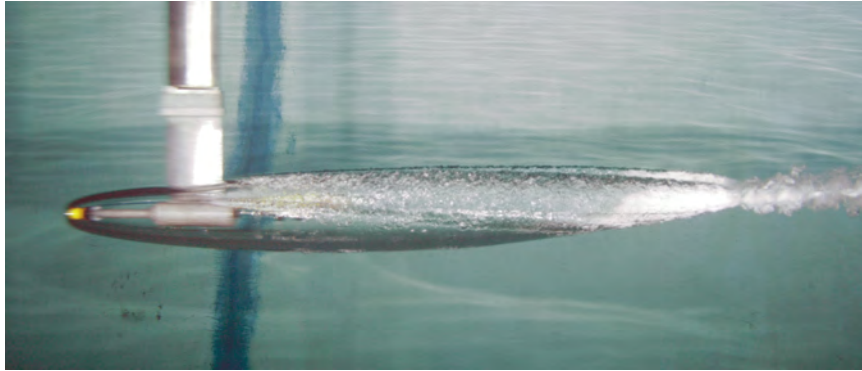


Figure 1.2: Artificially Ventilated Supercavity, adapted from Dzielski et al. (2012)

Equation 1.1 assumes that P_g is negligible, which is not always the case. For developed cavitation and supercavitation, it is common to use a variation of eq. (1.1), sometimes referred to the cavity underpressure (Franc and Michel, 2004). This is defined as:

$$\sigma_c = \frac{P_\infty - P_c}{\frac{1}{2}\rho V_\infty^2} \quad (1.5)$$

Franc and Michel (Franc and Michel, 2004, Ch. 1) argue that the cavity underpressure is “...a true scaling parameter, as the numerator expresses an actual pressure difference inside the flow domain.”

Semenenko (2002b) suggests that supercavitation generally occurs at cavitation numbers less than about 0.1. To attain a cavitation number of this magnitude in water at standard temperature and pressure, a cavitating body would need to travel at nearly 150 ft/s. Increasing the depth will increase the ambient pressure and ultimately increase the required velocity.

Under some conditions, supercavitation can be artificially induced at lower velocities and higher pressures by injecting a non-condensable gas into the low-pressure wake generated behind a cavitator. This gas will displace the liquid in the wake and form what is called an artificially ventilated supercavity. Injecting gas into the wake increases P_g which

decreases the cavity underpressure, σ_c . As discussed in (Schauer, 2003; Knapp et al., 1970; Stinebring et al., 2002), natural and artificially ventilated supercavities have nearly the same profile for a given cavity underpressure and flow geometry.

In many cases, supercavities are so long that they will begin to curve upwards due to buoyancy. This is especially true for artificially ventilated supercavities, which can occur at moderate velocities, compared to natural supercavities. A non-dimensional number, called Froude number is commonly used to characterize the effects of gravity. Froude number describes the relationship between inertial and gravitational forces in a free surface flow, and is commonly defined as:

$$F_r = \frac{V_\infty}{\sqrt{gl}} \quad (1.6)$$

where g is the acceleration due to gravity and l is a reference length, commonly taken to be cavity length or a characteristic length on the cavitator. Semenenko (2002a) mentions that gravity effects are considerable only when $\sigma_c F_r < 2$, for a circular cavitator, where the characteristic length is taken as cavitator diameter. Experiments have shown that gravity affects cavity length and the force coefficients generated by a supercavitating body (Franc and Michel, 2004, Ch. 9).

The rate of gas injected into a cavity is commonly represented by the flow coefficient, defined as:

$$C_q = \frac{Q}{V_\infty A} \quad (1.7)$$

where Q is the volumetric flow rate into the cavity and A is a reference surface area, commonly taken to be the frontal area of the cavitator or as cavitator diameter squared.

At finite cavitation numbers, the pressure inside the cavity is always less than the surrounding pressure. For pressure and inertia forces to be in balance, the cavity boundary must be concave inwards (Franc and Michel, 2004, Ch. 6). Somewhere downstream, the upper and lower surfaces will come together and close the cavity. Commonly, cavity

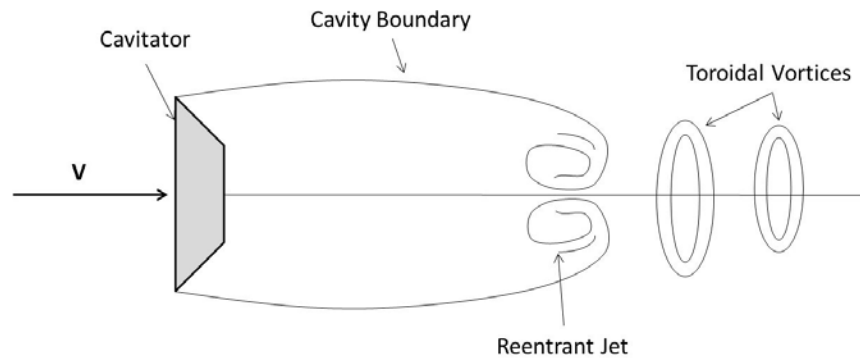


Figure 1.3: Reentrant Jet Cavity Closure Showing Ventilation Gas Expulsion through Toroidal Vorticities

closure is accomplished through the formation of a reentrant jet.

When non-condensable gas is used to ventilate the cavity, mass conservation requires that the flow rate into the cavity must equal the flow rate out at the end. Three typical modes of air evacuation have been observed for ventilated supercavities, as discussed in (Semenenko, 2002b; Franc and Michel, 2004). The first mode typically occurs at high Froude numbers and relatively high values of cavity underpressure, where gravity effects are negligible and the cavities are nearly axisymmetric. Here, the tail of the cavity rolls forward forming a reentrant jet. The closure region of the cavity generally appears frothy, and gas will periodically be expelled in the form of toroidal vorticities (Semenenko, 2002b), as illustrated in fig. 1.3.

At lower Froude numbers and moderate values of σ_c , buoyancy tends curve the cavity upwards and deforms the cavity's cross-section (Franc and Michel, 2004, Ch. 9). The tail of the cavity will tend to roll up into two hollow vortex tubes that pull gas out of the cavity. This mode of operation is commonly referred to as the twin vortex regime.

Franc and Michel (2004, Ch. 9) explain that the upward curvature of the cavity centerline results in a variation in velocity along the cavity wall. Using the Bernoulli equation, they were able to approximate the velocity along the top (V_+) or the bottom (V_-) of the

cavity as:

$$V_{\pm} \approx V_{\infty} - \frac{gz_{\pm}}{V_{\infty}} \quad (1.8)$$

where z_{\pm} is the distance from the center of the cavitating body to the top or bottom cavity boundary. This velocity difference results in a circulation, Γ which is discharged through the twin counter-rotating vortices in the wake. A great diagram of this can be found on page 211 of (Franc and Michel, 2004).

Campbell and Hilborne (1958) carried out an experimental investigation on the air entrainment behind artificially ventilated cavities behind disc cavitators. Through this, they were able to determine that reentrant jet closure occurs when $F_r \sigma_c > 1$ and twin vortex closure occurs when $F_r \sigma_c < 1$. Here, the reference length, l , in Froude number is the diameter of the disc cavitator.

The third mode of closure that is commonly found is unsteady cavity pulsation, which typically occurs when gas injection rates are extremely high. A theoretical analysis by Paryshev found that the dynamic properties of ventilated supercavities are dependent on a non-dimensional parameter β , which is defined as (Franc and Michel, 2004, Ch. 9):

$$\beta = \frac{\sigma_v}{\sigma_c} \quad (1.9)$$

Paryshev found that ventilated cavities are stable when $1 \geq \beta < 2.625$ and unstable when $\beta > 2.645$.

There is a large amount of published work on the subject of supercavitating flows, most of which has not covered in this brief overview. For more information on supercavitation, see Franc and Michel's book *Fundamentals of Cavitation* (Franc and Michel, 2004).

1.3 Supercavitating Hydrofoils

Hydrofoils are commonly used on marine vehicles for maneuvering, ride control, dynamic lift, and drag reduction. For relatively low speed applications, typically below about 45 knots (Conolly, 1975), foils typically have curved sections similar to subsonic airfoils. At higher speeds, hydrofoils with curved sections operating at an angle of incidence are susceptible to cavitation, which will typically result in a fluctuation in forces and moments, vibration, noise, and erosion of the hydrofoil surface (Auslaender, 1962).

Figure 1.4 shows the development of cavitation over a two-dimensional section as cavitation number is decreased. When the cavitation number is decreased beyond the inception value, small vaporous cavities form in regions of low pressure on the fin's suction side. A further decrease in cavitation number results in the formation of developed sheet cavitation. This partial cavity will continue to grow as the cavitation number is reduced even further. Eventually, the cavity closure point will move downstream of the fin, forming a supercavity. Buffeting can occur when the cavity closure point is close to the trailing edge of the fin, where the reentrant jet slaps on the back of the fin. Stable supercavitation will occur when the closure point moves far enough downstream that the reentrant jet is dissipated before it reaches the trailing edge of the foil (Auslaender, 1962).

For high speed applications, it can be difficult to avoid cavitation on the surfaces of hydrofoils with curved airfoil sections. The issues associated with the onset of cavitation can be avoided by choosing sections designed to induce the formation of a supercavity (Auslaender, 1962). These sections typically employ sharp leading edges and blunt trailing edges, similar to the ones shown in the lower part of fig. 1.4. At low angles of attack, cavities will tend to form from the blunt trailing edge in a configuration that will be referred to in this paper as base ventilated. At high angles of attack, cavities tend form from the sharp leading edge and the trailing edge of the pressure side in a configuration that

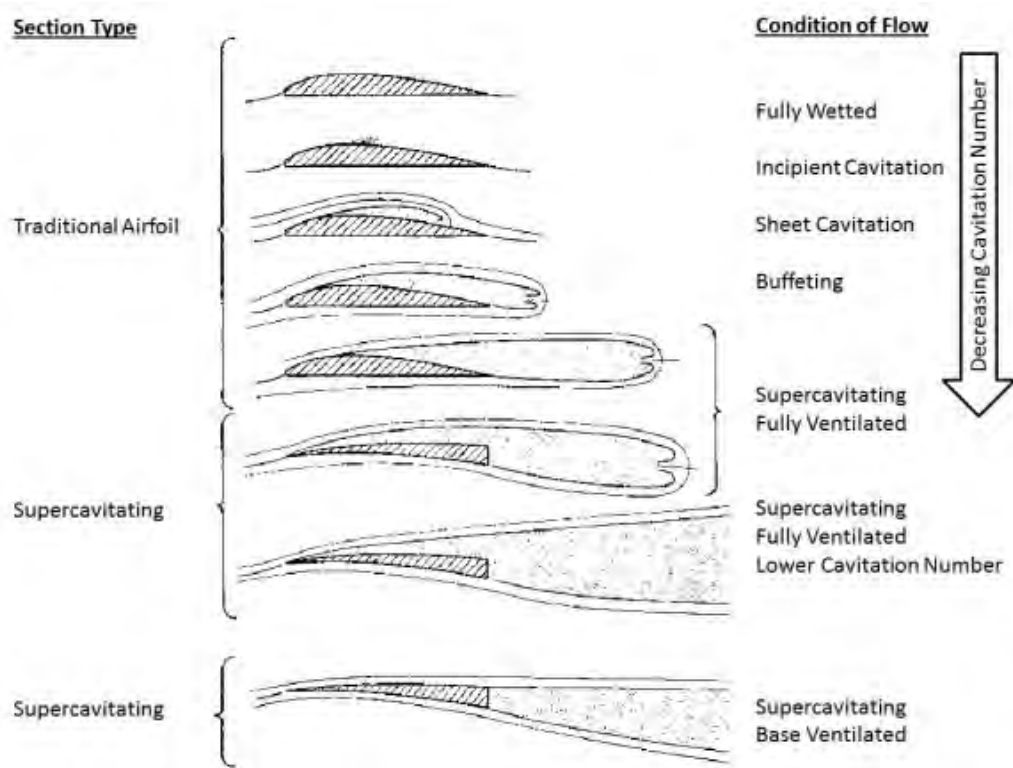


Figure 1.4: Various types of Cavitation on Traditional and Supercavitating Hydrofoil Sections, Adapted from (Auslaender, 1962)

will be referred to as fully ventilated. Auslaender (1962) explained that fully ventilated hydrofoils are typically favorable for high speed operation because once ventilated, no further cavitation or ventilation can occur, resulting in a stable lifting surface free from force discontinuities, erosion, and buffeting.

There has been a great deal of research focused on predicting the performance of supercavitating hydrofoil sections both experimentally and analytically. Many of the theoretical investigations employ a version of the classical Helmholtz free boundary theory (Milne-Thomson, 1949), where the surfaces of trailing cavities are modeled as free streamlines of constant pressure. Early investigations typically considered the flow about objects at zero cavitation number and infinite depth. Later, a variety of models were developed to account for the effects of operating at finite cavitation number (Kinnas, 2002a) and operating close to a free surface (Auslaender, 1962).

One of the more successful free-streamline theories was the non-linear method presented by Wu (1955). He adapted the free boundary theories developed by Helmholtz (1868) and others to estimate the force and moment characteristics of flat-plate and concave circular arc hydrofoils. A dissipative cavity closure model by Roshko (1954) was employed to account for the effects of finite cavitation number. Experimental investigations by Parkin (1956) and Waid and Lindberg (1957) show good agreement over a range of conditions for two-dimensional supercavitating hydrofoil sections.

Tulin and Burkart (1955) were able to show that an arbitrary supercavitating hydrofoil section could be reduced to an equivalent airfoil problem, which greatly simplified analysis. Through linearization of the equivalent airfoil problem, they determined that the lift, drag and moment coefficients for a two-dimensional flat-plate hydrofoil at an infinite depth and zero cavitation number could be approximated as:

$$C_L \approx \frac{\pi\alpha}{2} \tag{1.10}$$

$$C_D \approx \frac{\pi\alpha^2}{2} \quad (1.11)$$

$$C_M \approx \frac{5\pi\alpha}{32} \quad (1.12)$$

where α is the angle of incidence, in radians. Here, moment is taken about the fin's leading edge.

Tulin and Burkart (1955) were also interested in designing low-drag hydrofoil sections. They approached the problem by assigning an optimal pressure distribution to the equivalent linearized airfoil problem, and then back calculated the corresponding hydrofoil section. According to their linearized theory, their new sections could provide the same lift as a flat plate, with as little as one-sixth of the drag. Their linearized theory did not, however, consider the effects of finite cavitation number nor did it take into account foil strength.

Johnson (1958) presented corrections for finite depth of submersion, aspect ratio, and thickness, based on the linearized theory of Tulin and Burkart (1955). When the fins were fully ventilated, fairly good agreement was found between experimental results and those predicted by the corrected linearized theory over a range of conditions at low cavitation numbers (Johnson, 1958; Christopher and Johnson, 1960). Lift was generally in good agreement. The predicted drag tended to be low, but was generally within 10 percent. Results did, however, deviate as cavitation number was increased from nearly zero.

Christopher and Johnson (1960) performed towing tank experiments on sharp supercavitating fins at speeds up to 200ft/s. During testing, they found that the leading edge of the foil would vibrate at angles of attack less than 12 degrees when towed at speeds greater than about 128-139 ft/s. Inception of this leading edge vibration was found to be a function of angle of attack, velocity, and submersion depth. Figure 1.5 shows a hydrofoil experiencing leading edge vibration, which can be observed as a ripple in the trailing cav-

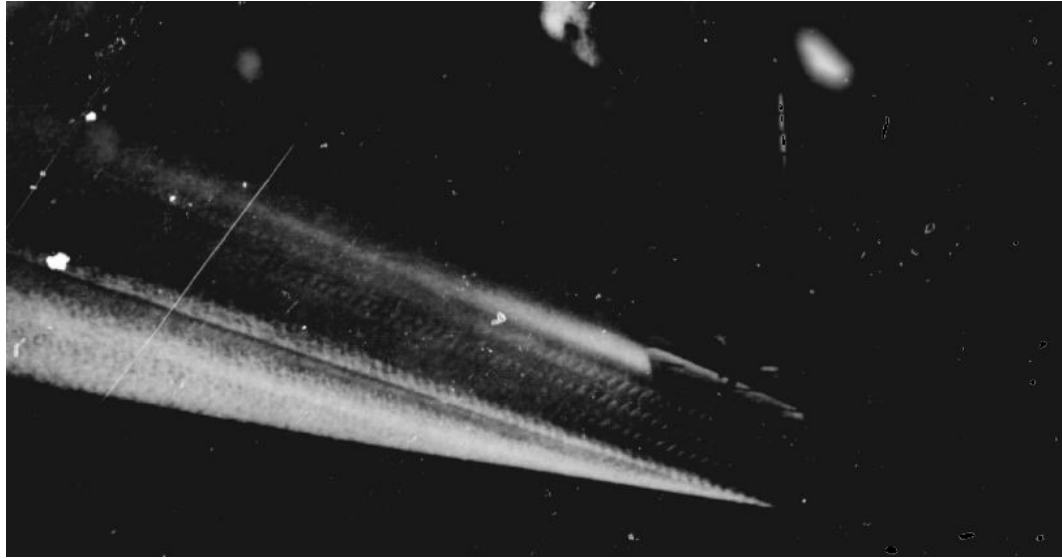


Figure 1.5: Leading Edge Vibration on a Supercavitating Fin with a Wedge Cross Section, $\alpha = 8^\circ$, $V = 148$ ft/s, adapted from (Auslaender, 1962)

ity. Auslaender (1962) mentioned that this can typically be remedied by rounding out part of the otherwise extremely sharp leading edge.

Song (1969) investigated the vibration of supercavitating hydrofoils through a series of exploratory water tunnel experiments on symmetric and asymmetric wedge sections. The study found that cavitating flow is generally unstable, and that there exists a characteristic frequency at which the forces and moments will oscillate. These frequencies were found to be a function of flow velocity and cavity length (i.e. cavitation number). Song (1969) also discussed the presence of flutter-like hydro-elastic instabilities that occurred when the fins were partially ventilated.

Many more recent efforts have been focused on predicting performance numerically through boundary element methods and RANSE models (Kinnas, 2002a). The primary focus of these works has been to account for three-dimensional effects and accurately predict the effects of finite section thickness on cavity shape at finite cavitation numbers.

A very large body of work exists on the subject of supercavitating hydrofoils, much

of which is not covered here. Long lists of references on the subject can be found in (Auslaender, 1962), (Tulin and Hsu, 1980) and (Kinnas, 2002b).

1.4 Surface Piercing Hydrofoils

When surface piercing struts and hydrofoils operate at sufficiently high velocity, air is pulled down and entrained in the low pressure wake, forming a trailing cavity. This phenomenon, typically known as strut ventilation or air leakage, results in drastic changes in strut forces and moments on the hydrofoil (Morgan, 1969; Breslin and Skalak, 1959).

Breslin and Skalak (1959) observed several mechanisms of air leakage on yawed surface-piercing hydrofoils with airfoil sections. The first mode occurred on lifting foils yawed to high angles of attack. Here, air was pulled down into the low pressure wake region, forming a trailing cavity from the leading and trailing edges of the foil. This mode of cavity formation was found to be the result of boundary layer separation. The velocity at which this occurred was found to be dependent on the foil section, aspect ratio, and angle of attack.

For some conditions, air leakage was found to occur through the tip vortex. Here, the tip vortex would pull air down from the free surface, forming an aerated tube, which began downstream of the foil and propagated forward. When the aerated vortex reached the tip of the hydrofoil, a full trailing cavity typically formed, along with a loud, sharp sound (Breslin and Skalak, 1959).

Wetzel (1958) studied the formation of trailing cavities behind surface piercing cylinders of varying diameter. The larger diameter cylinders were found to form trailing cavities gradually, where the cavity slowly grew in depth with increasing velocity. The smaller diameter cylinders were found to “flash ventilate,” where cavities formed suddenly at a particular velocity. This mode of air entrainment was also found with yawed low aspect

ratio fins.

The trailing cavities behind the flash ventilated cylinders were found to collapse at velocities lower than the velocity at which they formed. Wetzel (1958) found that this hysteresis was a function of several factors, including Weber number (ratio of forces due to inertia and surface tension) and Reynolds number (ratio of forces due to inertia and viscosity). For applications operating at very high Reynolds numbers, this hysteresis was commonly found to disappear, as discussed by Baker (1975). However, this hysteresis is still significant for lower Reynolds number applications.

Breslin and Delleur (1956) studied free surface effects on drag of surface piercing struts. Their study showed that piercing a strut through a free surface resulted in the formation of surface waves, spray, and trailing cavities attached to the atmosphere. Each of these were found to have an impact on the total drag of a particular strut, in addition to the profile and induced drag (Morgan, 1969).

Savitsky and Breslin (1966) found that the drag due to the formation of surface waves was only significant at Froude numbers less than about 4.3. They also found that the additional drag due to spray formation was typically only important at higher Froude numbers, where significant spray was typically generated. Morgan (1969) added that the cavity drag was primarily a function of cavitation number.

1.5 Hydrodynamic Forces

The hydrodynamic force on a body traveling through a fluid can typically be thought of as the sum of the effects due to the pressure and shear stress distributions on the body. The net hydrodynamic force, $\bar{\mathbf{R}}$, on the object can be found by integrating the pressure and shear

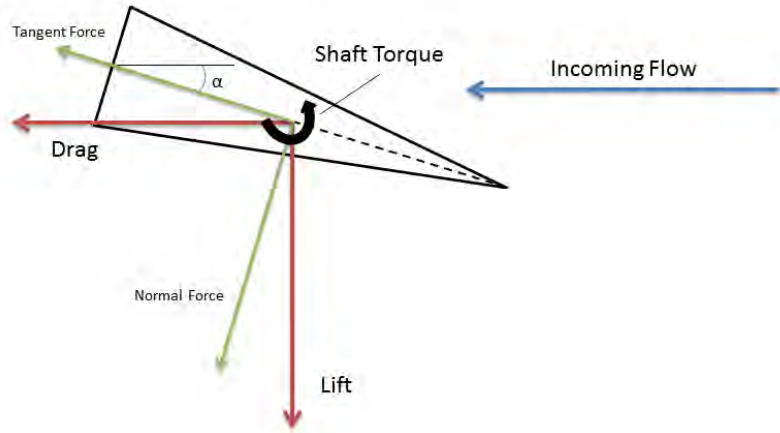


Figure 1.6: Sign conventions for Lift, Drag, Shaft Torque (M_z), Normal Force and Tangent Force. All vectors illustrate positive direction.

stress distributions over the body's surface area S . This can be written as:

$$\bar{\mathbf{R}} = - \iint_S P \bar{\mathbf{n}} dS + \iint_S \tau \bar{\mathbf{t}} dS \quad (1.13)$$

where P is pressure, τ is the shear stress, $\bar{\mathbf{n}}$ and $\bar{\mathbf{t}}$ are normal and tangent unit vectors, respectively (Anderson, 1999).

The resultant force, $\bar{\mathbf{R}}$, can be redefined a couple of ways. The most common is to deconstruct it into components normal and tangent to the incoming flow. The normal component is commonly referred to as lift, L , and the tangential component is commonly referred to as drag, D . When forces act at a distance from a reference axis, moments are generated. In this report, moment about the fin's spanwise axis is studied. Figure 1.6 shows the sign conventions of lift, drag, and moment used in this report.

Forces and moments are typically presented in non-dimensional form. The lift, drag

and moment coefficients typically take on the form:

$$C_L = \frac{L}{0.5\rho V^2 A} \quad (1.14)$$

$$C_D = \frac{D}{0.5\rho V^2 A} \quad (1.15)$$

$$C_M = \frac{M}{0.5\rho V^2 A c} \quad (1.16)$$

where ρ is the density of the fluid, A is the planform area, and c is the chord length.

The hydrodynamic efficiency of a body is typically studied as the lift to drag ratio, which can be defined as:

$$\eta = \frac{L}{D} = \frac{C_L}{C_D} \quad (1.17)$$

1.6 Project Description

Under some conditions, an object traveling underwater can inject a non-condensable gas into a low pressure region created near its leading edge, forming an artificially ventilated supercavity. This ventilated cavity will surround part or all of the object. One means of affecting control to such an object could be through a use of supercavitating fins. Depending on the shape of the cavity, the fins may operate in a configuration where they pierce through the wall of the ventilated supercavity, as shown in fig. 1.7. Limited previous work by Wosnik and Arndt (2009) found that fins piercing a ventilated cavity boundary behave differently than traditional supercavitating fins. Specifically, they found that the formation of attached trailing cavities behind the fins resulted in non-linearities in the measured force and moment characteristics. These non-linearities needed to be characterized and researched further before fins could be designed for applications.

The focus of this project was to identify some of the unique characteristics of cavity

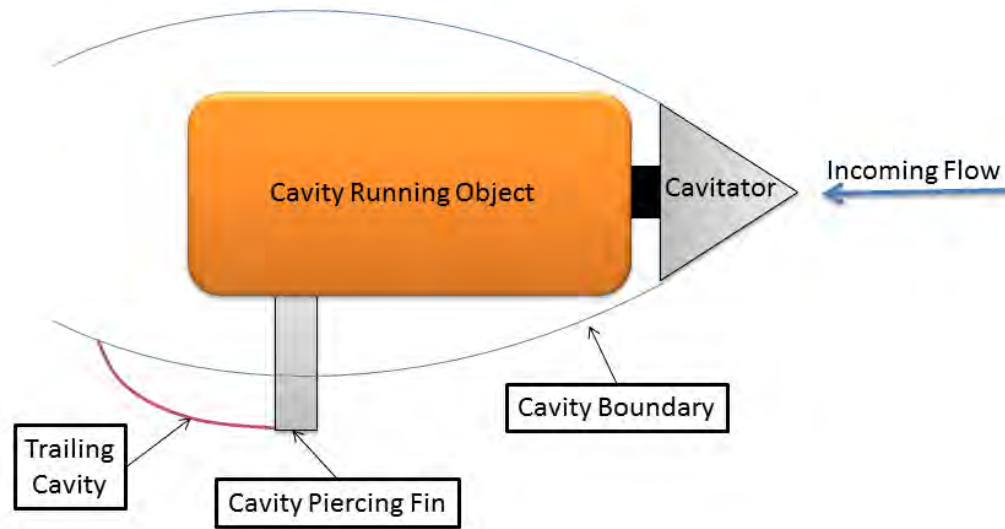


Figure 1.7: Object operating in an artificially ventilated supercavity fitted with a cavity piercing fin.

piercing fins to help develop the basic scientific understanding necessary to properly design fins for applications. This was accomplished through a series of water tunnel experiments at ARL that simulated the bottom half of fig. 1.7. Measurements were made on cavity piercing fins with finite aspect ratios and wedge cross sections over a range of conditions to explore the effects of varying fin geometry and flow parameters. Lift, drag, and shaft torque were measured with a six degree-of-freedom force and moment transducer. Tunnel velocity, cavity size, fin chord length, and angle of attack were varied systematically.

This project spanned a two year period. During the first year, measurements were made on vertical fins with rectangular planforms. During the second year, measurements were made on swept fins rotated about their spanwise axis.

Chapter 2

Description of Experimental Work

2.1 Overview

A series of exploratory water tunnel experiments were designed and executed at the Applied Research Laboratory at the Pennsylvania State University (ARL/PSU). Steady and unsteady state tests were performed to study the force and moment characteristics of supercavitating fins piercing a ventilated cavity boundary. Steady state measurements were made with the fin held at a fixed angle of attack during a run. Unsteady measurements were made on fins oscillated about their spanwise axes in a sinusoidal motion during a run.

The experimental work spanned a two year period. The first experiments were carried out during the summer of 2011 on unswept fins. The unswept fin data was post-processed and analyzed during the following months. A second experiment was designed and carried out during the summer of 2012 on fins swept to 30 and 45 degrees from vertical.

2.2 Experimental Facility

Experiments were performed in the twelve-inch water tunnel at ARL's Garfield Thomas Water Tunnel facility. The twelve-inch tunnel was a closed jet, closed circuit tunnel, with two interchangeable working sections for different test purposes. A rectangular test section

12-Inch Water Tunnel

1951

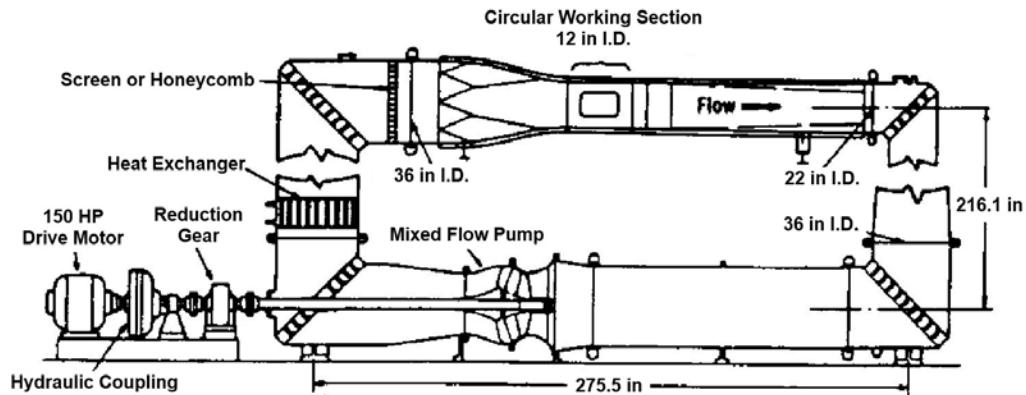


Figure 2.1: Schematic of the Twelve-Inch Water Tunnel at ARL/PSU, adapted from (Stinebring et al., 2002)

could be installed to carry out two-dimensional flow studies. A circular test section, with a twelve-inch diameter could be installed for three-dimensional flow studies. A schematic of the twelve-inch tunnel is shown in fig. 2.1.

The circular test section of the twelve-inch water tunnel featured observation windows on the bottom, left, and right, and has a removable top plate. The tunnel was driven by a 150hp electric induction motor, which could move the water in the tunnel at velocities up to nearly 80ft/s. The tunnel was fitted with a pressure regulation system capable of varying the pressure in the test section from 3 psia to about 60 psia over the full velocity range. The tunnel was also attached to a degassing system, which could be used to remove excess air and bubbles from the water.

Static pressure, P_{∞} , in the test section was measured through pressure taps fitted with absolute pressure transducers. Total pressure, P_t , in the tunnel was measured through a kiel probe fitted upstream of the test section in the settling chamber. Tunnel velocity in

the round test section was determined using the following relation:

$$V_{\infty} = 12 \sqrt{\frac{P_t - P_{\infty}}{0.5\rho}} \quad (2.1)$$

where pressure is in psi, and density is in slugs/ft³. The temperature of the water in the tunnel was monitored during the run, and was later used to calculate the density, using the following empirical formula:

$$\rho = 1.932346 + 4.24809T_w \times 10^{-4} - 6.389964T_w^2 \times 10^{-6} + 1.591633T_w^3 \times 10^{-8} \quad (2.2)$$

based on data from (Saunders, 1957, Appendix 3). Here, temperature is in Fahrenheit.

2.3 Unswept Fin Testing

Experiments on unswept fins were carried out at ARL during the summer of 2011. The main objective was to document and characterize the lift, drag, and moment characteristics of unswept fins piercing a ventilated cavity boundary. A systematic series of tests were performed on three hydrofoils with wedge cross sections at three tunnel velocities, piercing two different sized cavities.

2.3.1 Preliminary Estimates

Before test hardware could be designed, estimates of the forces and moments expected during the experiment were required. Wu's free streamline theory (Wu, 1955) was used to calculate the lift, drag, and moment coefficients of two-dimensional supercavitating hydrofoil sections at angles of attack between 0-20 degrees.

Wu's model predicted that the lift and drag coefficients of a two-dimensional fully cavitating hydrofoil section decreased with cavitation number, as shown in fig. 2.2 for the

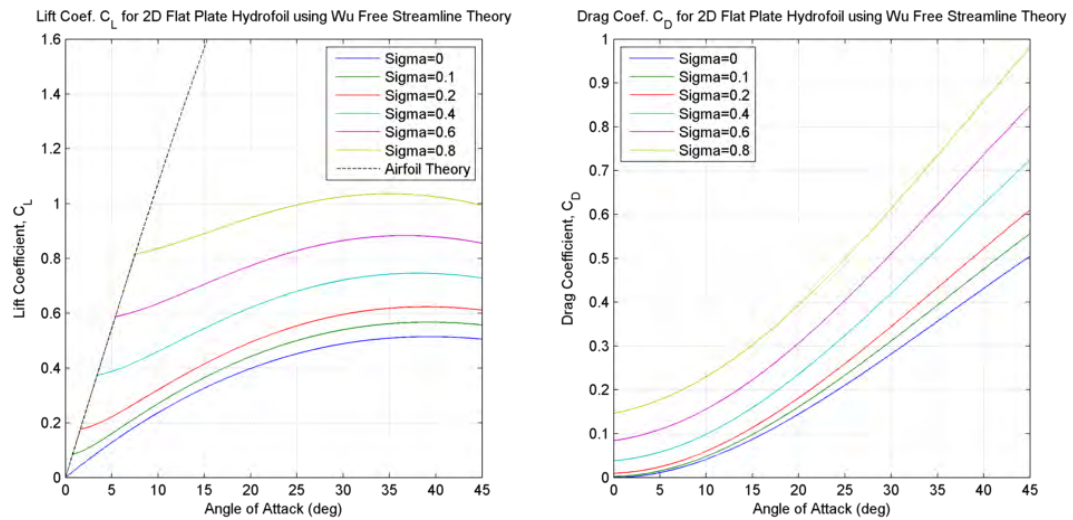


Figure 2.2: Lift and Drag Coefficients for a Flat Plate Hydrofoil vs. Angle of Attack and Cavitation Number using Wu's Free Streamline Theory (Wu, 1955).

case of a flat plate hydrofoil. Wu's model assumed that the trailing cavity formed from the leading and trailing edges of the hydrofoil. At lower angles of attack, this assumption was no longer valid, and the model broke down. Wu (1955) suggested that, at these low angles of attack, lift coefficients could be approximated using thin airfoil theory.

It was of interest to model a supercavitating fin with a wedge cross section. At low angles of attack, the pressure and suction sides of the fin were typically wetted, forming a base ventilated trailing cavity. At higher angles of attack, the suction side typically ventilated, forming a fully ventilated trailing cavity, as illustrated in fig. 1.4.

When the wedge section was fully ventilated, the suction side was no longer in contact with the fluid. Here, the fin operated as if it were a supercavitating flat plate hydrofoil. As a result, the angle of attack of the inclined surface became the sum of the fin's angle of attack and the wedge half-angle, ψ .

For the preliminary estimates, it was assumed that the fin would be base vented at angles of attack less than the wedge half-angle. This was thought to be a good approximation because the suction side remained inclined to the flow at angles of attack less than the

half-angle. When the fin was rotated beyond the half-angle, an adverse pressure gradient was thought to form on the suction side, resulting in a transition to fully ventilated operation. Though transition was likely to occur at lower angles of attack, this approximation was used because it provided a reasonable upper limit.

Wu's free streamline theory was used to estimate the lift and drag coefficients of the ventilated fins. For the base ventilated fins, lift coefficients were estimated using thin airfoil theory (Anderson, 1999). The drag coefficients were estimated using an empirical method for a yawed wedge developed by Cox and Clayden (1958).

The fully ventilated two-dimensional lift and drag coefficients were estimated as:

$$C_{L2d} \approx \frac{2\pi}{J} \left(1 + \sigma_c + \frac{\epsilon^2}{4}\right) \cos \beta \left(\sin \beta + A_1 + \frac{\epsilon^2 \sin \beta (\sin \beta + A_1)^2 + A_1^2 (A_1 - \sin \beta)}{4(\sin \beta + \frac{A_1}{2})^4} \right) \quad (2.3)$$

$$C_{D2d} \approx \frac{2\pi}{J} \left(1 + \sigma_c + \frac{\epsilon^2}{6}\right) \left(\sin \beta + \frac{A_1}{2}\right)^2 \quad (2.4)$$

where α is angle of attack and:

$$\beta = (\alpha + \psi) + \frac{1}{2} \left(\sqrt{(\alpha + \psi)^2 + \epsilon^2} - (\alpha + \psi) \right) - \frac{\epsilon^2}{4(\pi - (\alpha + \psi))} \quad (2.5)$$

$$A_1 = \frac{9}{16} \left(\sqrt{(\alpha + \psi)^2 + \epsilon^2} - (\alpha + \psi) \right) + \frac{9\epsilon^2}{32(\pi - (\alpha + \psi))} \quad (2.6)$$

$$J = 4 + \pi \sin \beta + A_1(\pi + 2.72 \sin \beta) \quad (2.7)$$

$$\epsilon = \frac{1}{2} \ln(1 + \sigma_c) \quad (2.8)$$

The base ventilated two-dimensional lift and drag coefficients were estimated as:

$$C_{L2d} = \pi \sin 2\alpha \quad (2.9)$$

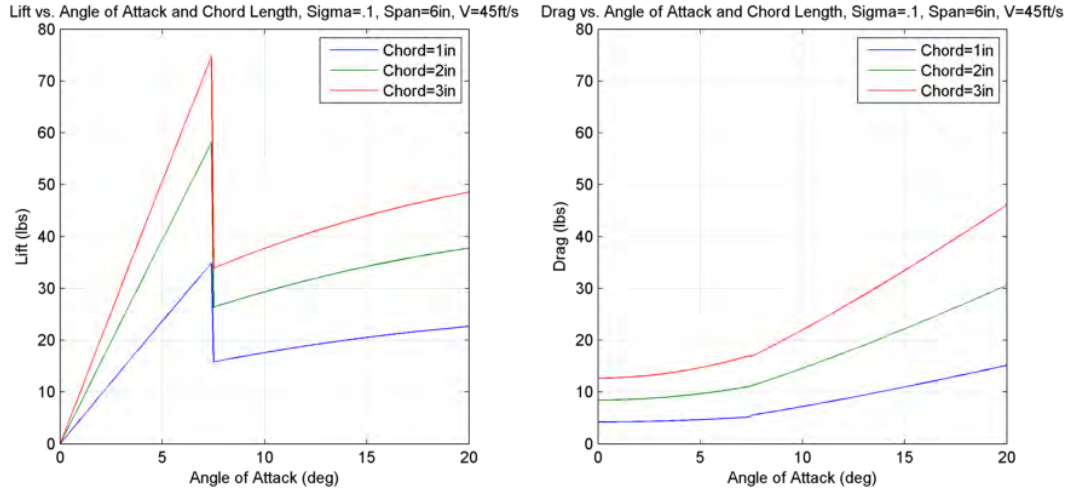


Figure 2.3: Estimated Lift and Drag for a Fin with $\psi = 7.5^\circ$, $S = 6in$, operating at $V = 45ft/s$ and $\sigma = 0.1$, piercing a 2 inch cavity.

$$C_{D2d} = 0.3(1 + 0.00742\alpha_d^2)(t/c) \quad (2.10)$$

where t/c is the thickness to chord ratio, and α_d is angle of attack, in degrees.

Lifting line theory was used to account for three-dimensional effects due to finite aspect ratio (Anderson, 1999). The three-dimensional lift coefficient was approximated as:

$$C_{L3d} = C_{L2d} \left(\frac{\Lambda}{\Lambda + 2} \right) \quad (2.11)$$

Here Λ is the aspect ratio, defined as S^2/A , where S is fin span. No corrections were worked in for planform shape. The two dimensional drag coefficient was corrected for finite aspect ratio effects as:

$$C_{D3d} = C_{D2d} + \frac{C_{L3d}^2}{\pi\Lambda} \quad (2.12)$$

A brief parametric study was performed to investigate the effects of varying fin planform area and tunnel velocity on fin lift and drag. Typical results are shown in fig. 2.3 for the case of a fin with a 7.5 degree half-angle, a 6 inch span, S , operating at a cavitation number of 0.1 and a tunnel velocity of 45 ft/s.

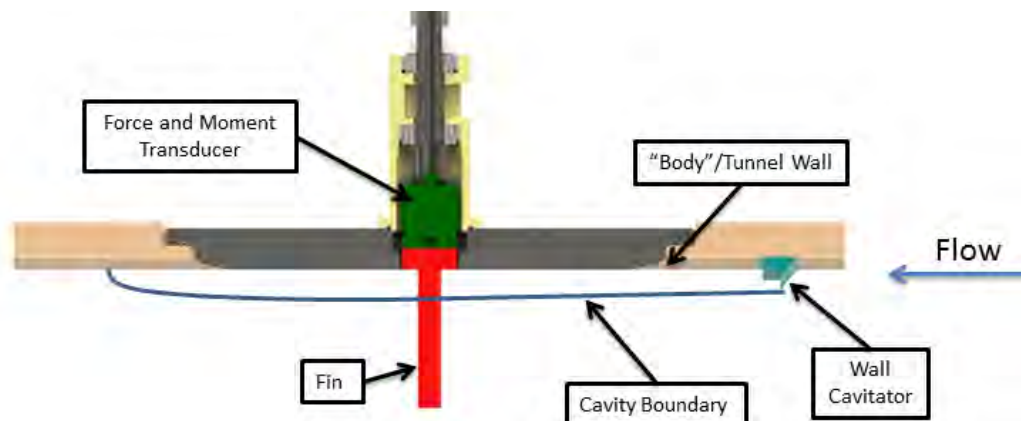


Figure 2.4: Schematic of the unswept fin test platform used to make measurements on a cavity piercing fin. The surface of a cavity running object was simulated as the top of the water tunnel. Fins mounted flush to the wall and hung down into the free stream. Cavities were created along the top of the tunnel with a wall cavitator.

2.3.2 Test Hardware

Test hardware was designed to simulate the bottom half of fig. 1.7. A schematic of this is shown in fig. 2.4. To keep costs down, an apparatus from a previous experimental program was adapted for this work. The hardware, shown in fig. 2.5 mounted in place of the removable top plate in the twelve-inch water tunnel's round test section. With this hardware, fins could either be held in place at a fixed angle of attack, or rotated about their spanwise axes in a sinusoidal fashion during a run.

Fins were mounted to a force and moment transducer which could be bolted to a bearing supported shaft. The shaft was fitted to a cam/follower mechanism, driven by a variable speed AC motor. This mechanism was used to adjust the fin's angle of attack between steady state runs, and oscillate the fin over a range of angles during unsteady runs. The amplitude of oscillation could be varied by swapping the cam.

A 3600 line rotary encoder was used to measure the fin's angle of attack during testing. The encoder was actuated with a timing belt, as shown in fig. 2.5.

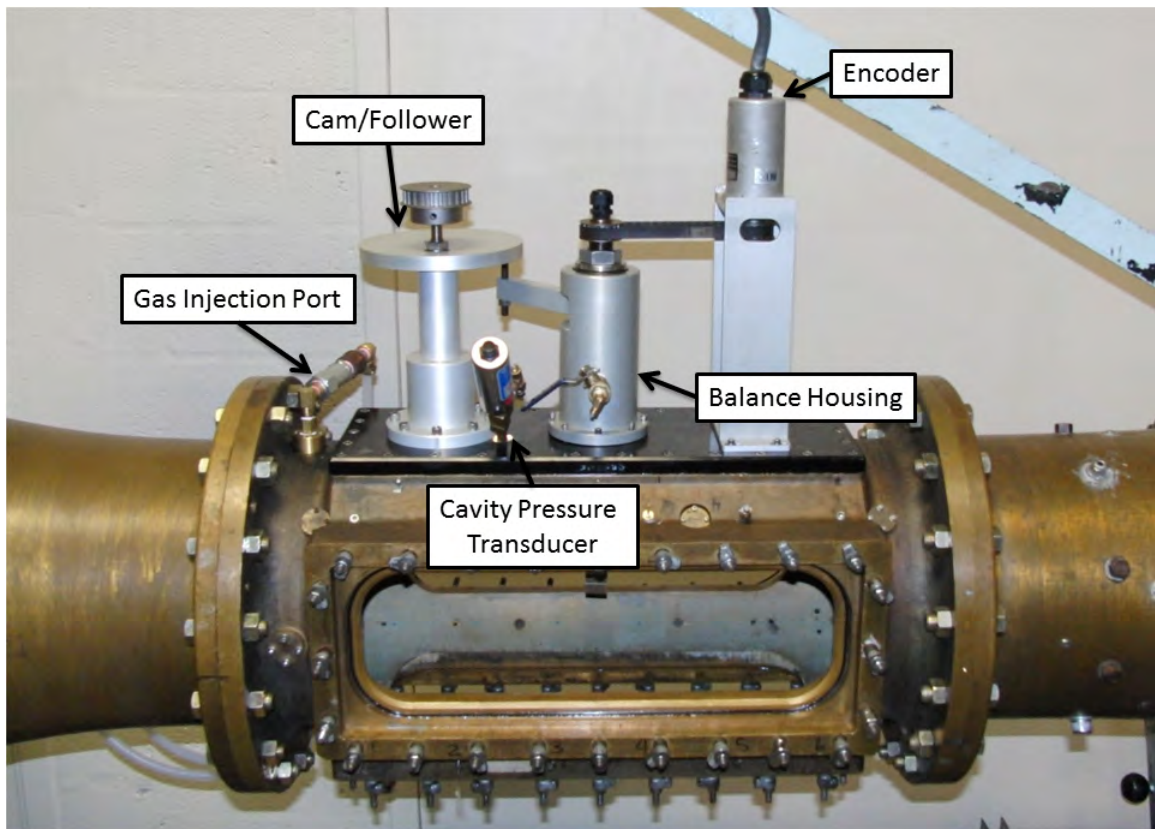


Figure 2.5: Unswept Fin Test Apparatus Installed in the 12 Inch Water Tunnel at ARL



Figure 2.6: Wedge Cavitator used for Unswept Fin Testing

An artificially ventilated supercavity was created along the top of the tunnel for the fin to pierce through. This was accomplished by mounting a wedge shaped step to the tunnel wall upstream of the fin apparatus. Two of these wedge cavitators were fabricated to generate cavities of different thicknesses. The cavitators were made from 6061 aluminum, and were curved to match the inner surface of the test section. One of the cavitators is shown in fig. 2.6. The cavitator in the photo has a sharp step to encourage flow separation. Additional information on the cavitators used can be found in Appendix A.

These artificial supercavities were ventilated with compressed dry air through an injection port fitted downstream of the cavitator. A gas deflector was mounted over the injection port to direct the gas away from the cavity boundary. The ventilation gas was supplied from six high pressure gas cylinders. The six cylinders were attached in parallel to a dome valve, which reduced the pressure to about 120 psi. The gas was then directed through a flow regulator and a flowmeter, and finally injected into the tunnel. The injection port was fitted with a check valve to keep water out of the gas lines. A ball valve was used to turn the gas on and off between tests.

A static pressure tap was cut into the base of the unswept fin apparatus to measure the pressure in the cavity. A pressure transducer was mounted as close to vertical as possible to keep water out of the transducer. A bleed valve was fitted onto the transducer to

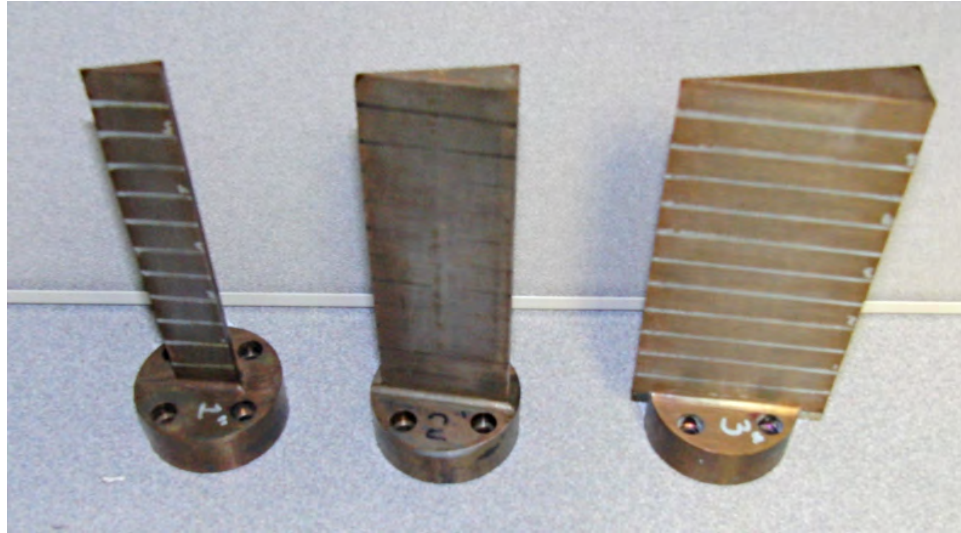


Figure 2.7: Family of Wedge Fins

purge the line of water before each test.

A family of three supercavitating fins were designed and built. The fins had wedge cross sections with 7.5 degree half-angles. The three fins were made with six-inch spans, chord lengths of 1, 2, and 3 inches, and had rectangular planforms. Each fin was fabricated with a large base designed to mount directly to the chosen force and moment transducer. The fins were fabricated from 17-4PH stainless steel. This grade was chosen for its strength, hardness, and resistance to corrosion. A process called electrical discharge machining (EDM) was used to cut the fin surfaces. After fabrication, the fins were heat treated to harden the material. A photo of the three fins is shown in fig. 2.7. The horizontal lines on the fins mark 1/2 inch increments, which were used to measure cavity thickness.

2.3.3 Instrumentation and Data Acquisition

Data was recorded using a National Instruments data acquisition system. Sensor voltage signal outputs were collected using an NI BNC-2090A BNC breakout box and then sampled through an NI PXI-6225 16-bit analog multifunction data acquisition card in an NI

PXI-1033 PXI chassis. A LabView program was used to acquire the sampled voltage signals, convert the signals to appropriate engineering units, and save the data for later use.

The forces and moments on the fins were measured using a six degree-of-freedom force and moment transducer. An AMTI SP2.5d-1k-6010 transducer was chosen based on the predicted loads. The limits and sensitivities of the transducer channels are listed in table 2.1. An AMTI MSA-6 MiniAmp strain gage amplifier and signal conditioner was used to supply an excitation voltage and amplify the signals from the transducer.

Table 2.1: Limits and Sensitivity of the AMTI Transducer

Force/Moment	Maximum Load	Sensitivity
Fx	500 lbs	$3.046 \mu V/V_{exc}-lb$
Fy	500 lbs	$3.061 \mu V/V_{exc}-lb$
Fz	1000 lbs	$0.781 \mu V/V_{exc}-lb$
Mx	1000 in-lbs	$4.435 \mu V/V_{exc}-in-lb$
My	1000 in-lbs	$4.368 \mu V/V_{exc}-in-lb$
Mz	500 in-lbs	$2.834 \mu V/V_{exc}-in-lb$

Fin motions were recorded using a 3600 line optical encoder by BEI Motion Control Systems attached to the fin shaft via a one-to-one timing belt mechanism. A second BEI optical encoder was fitted to the motor to record angular velocity during unsteady testing.

Cavity pressure, static pressure, and total pressure were measured with Heise DXD 0-100 psi absolute pressure transducers. Cavity and static pressures were measured through flush mounted static pressure ports in the tunnel test section. The total pressure was measured with a pitot tube mounted in the settling chamber upstream of the test section contraction nozzle.

The static and total pressure transducers were connected to the tunnel via thin plastic tubing. Between each run, the pressure in the water tunnel was brought above atmospheric so the tubing could be bled to remove any trapped air.

The ventilation gas flow rate was measured using a Sierra Instruments 830 series

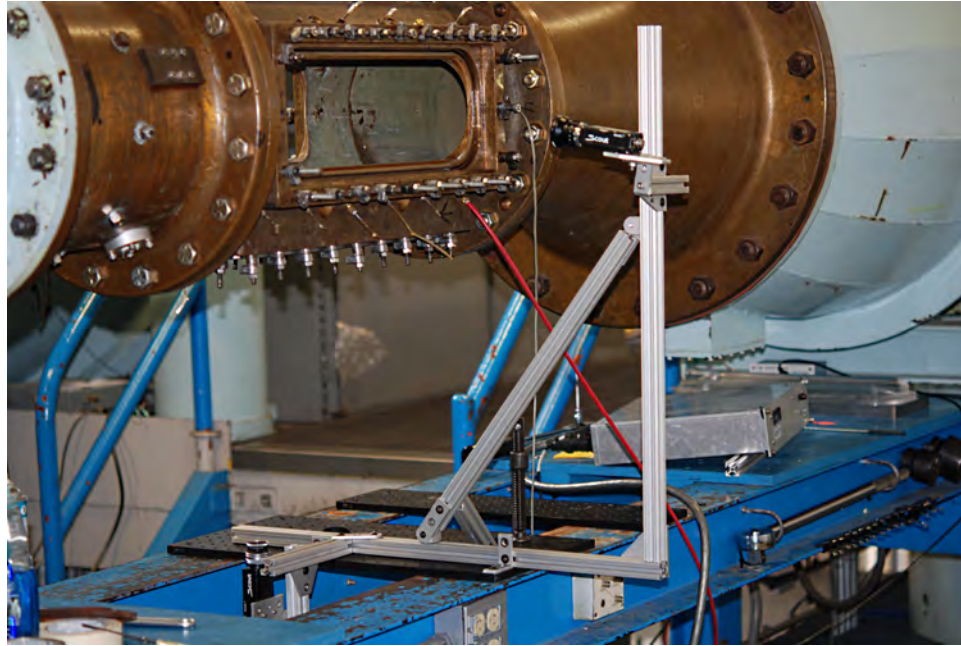


Figure 2.8: Video Cameras on Custom Mount

0-50 SCFM flow meter. Gas pressure and temperature were also recorded.

Water temperature was measured using a Stolabs type PL temperature sensor. These measurements were later used to calculate water density and viscosity.

Two Basler Scout color CCD video cameras were used to document the experiments. One camera observed the fin from the side of the water tunnel, and the other looked down the fin's span from the tip. The videos were acquired at 25 frames per second using the same LabView program that acquired the data. Figure 2.8 shows the two cameras mounted onto the water tunnel.

2.3.4 Unswept Fin Test Methodology

Steady and unsteady state tests were performed on all three fins over a range of conditions. During each run, tunnel velocity, gas injection rate, and tunnel pressure were held constant. Steady state tests were performed with the fins at fixed angles of attack. Unsteady state tests were performed where the fins were oscillated over a range of angles in a sinusoidal

fashion.

Steady state tests were performed with the fin at angles of attack above and below the wedge half-angle. The fins were rotated to the required angle of attack before each run. Once the fin's angle of attack was set, the tunnel drive system was engaged, and the tunnel was brought to the appropriate velocity. As the tunnel came up to speed, the pressure in the tunnel was decreased to 10 psia. When the tunnel velocity and pressure settled out, the data acquisition system was started. Ventilation gas was injected for about 15 seconds, after which the data acquisition system and tunnel drive were stopped. The tunnel was then degassed and prepared for the next experiment. Steady state tests were performed at the following conditions:

- *Angle of Attack:* 0, 5, 10, 15, and 20 deg
- *Tunnel Velocity:* 25, 35, and 45 ft/s
- *Chord Length:* 1, 2, and 3 in.
- *Wall Cavitator Thickness:* 0.5 and 1.0 in.

Unsteady state tests were performed to investigate the mechanism of ventilation and identify any other unsteady characteristics of cavity piercing fins. For these tests, the fin was oscillated about its spanwise axis in a sinusoidal fashion with the motor driven cam/follower mechanism. As before, the tunnel was brought to the required speed and pressure before the run. The data acquisition system was started, along with the fin actuator and ventilation gas. Gas was injected for about 20 seconds, after which the tunnel drive, gas, and actuator were all stopped. Longer runs could not be made because gas would recirculate back into the test section after about 20 seconds. Unsteady tests were performed at the following conditions:

- *Amplitude of Oscillation:* ± 20 deg
- *Frequency of Oscillation:* 18 and 30 oscillations/min
- *Tunnel Velocity:* 25, 35, and 45 ft/s

- *Chord Length:* 1, 2, and 3 in.
- *Wall Cavitator Thickness:* 0.5 and 1.0 in.

Degassing was required between tests to remove the ventilation gas injected into the tunnel to create the supercavities along the top of the tunnel. After each run, most of the gas collected at the top of the tunnel. This gas was removed by bringing the tunnel pressure above atmospheric and opening two vents fitted to the top of the tunnel.

During each run, a portion of the ventilation gas dissolved into the water, and needed to be removed. This was accomplished using the tunnel's pressure and purge systems. The tunnel's internal pressure was brought below atmospheric for a few minutes to pull the gas out of the water, which typically formed small bubbles along the tunnel walls. Periodically, the tunnel drive was engaged to remove the bubbles from the walls and push them toward the top of the tunnel. The gas was then removed using a vacuum pump fitted to the vents at the top of the tunnel. Occasionally, the water was also passed through a bypass system designed to remove dissolved gas and particulates.

2.4 Swept Fin Testing

Experiments on swept fins were performed at ARL during the summer of 2012. The main objective of these tests was to study the lift, drag and moment characteristics of swept fins piercing a ventilated cavity boundary. A systematic series of tests were performed with the same fins as before, using new test fixtures. In these tests, the fins were rotated about their spanwise axis, while swept back to 30 and 45 degrees from vertical.

2.4.1 Test Hardware

In early 2012, the water tunnel test hardware was redesigned. Several improvements were made based on lessons learned during the previous summer's testing. A method to vary fin

sweepback angle was also worked in.

During the 2011 testing, several problems arose from the large amount of gas needed to adequately ventilate the supercavity generated along the top of the tunnel. To reduce the gas requirements, the entire experiment was scaled down. The fin's length was reduced from 6 inches to 4 inches, and new, smaller cavitators were designed.

A large aluminum plate was designed to fit onto the top of ARL's twelve-inch water tunnel, and acted as a foundation for the new test hardware. A large gas injection port was cut into the new plate upstream of where the fin was supposed to be. A static pressure tap and a mount for a vertical pressure transducer was cut downstream to measure cavity pressure. A model of the new base plate is shown in fig. 2.9.

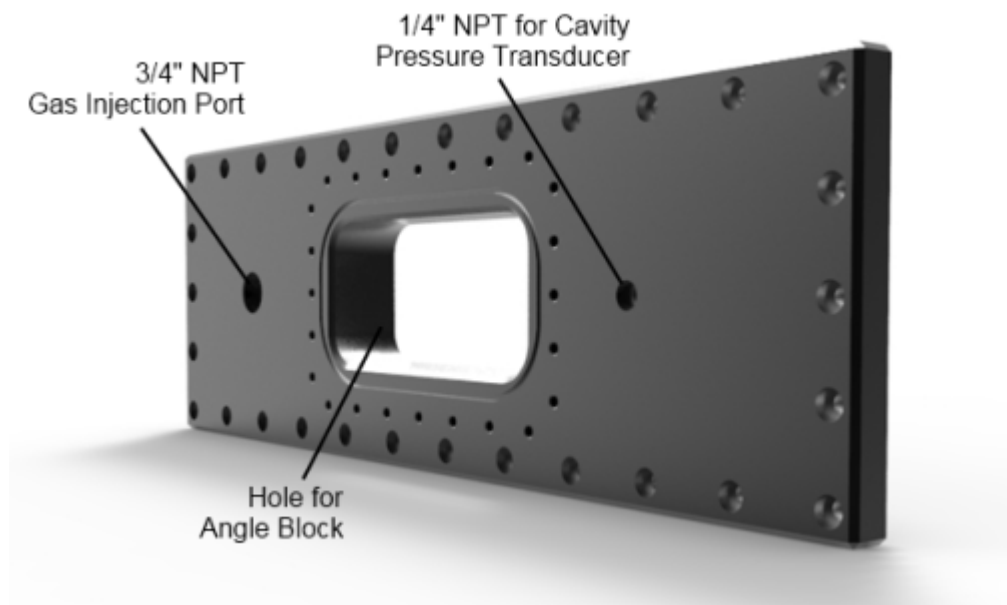


Figure 2.9: Aluminum Base Plate for the Swept Fin Apparatus

Flat wall cavitators were designed to mount directly to the aluminum plate over the gas injection port. The new cavitators were slotted to double as gas deflectors. A model of one of the new cavitators can be found in fig. 2.10, mounted to the aluminum base plate.

To make testing more efficient, the cam/follower mechanism was replaced with a

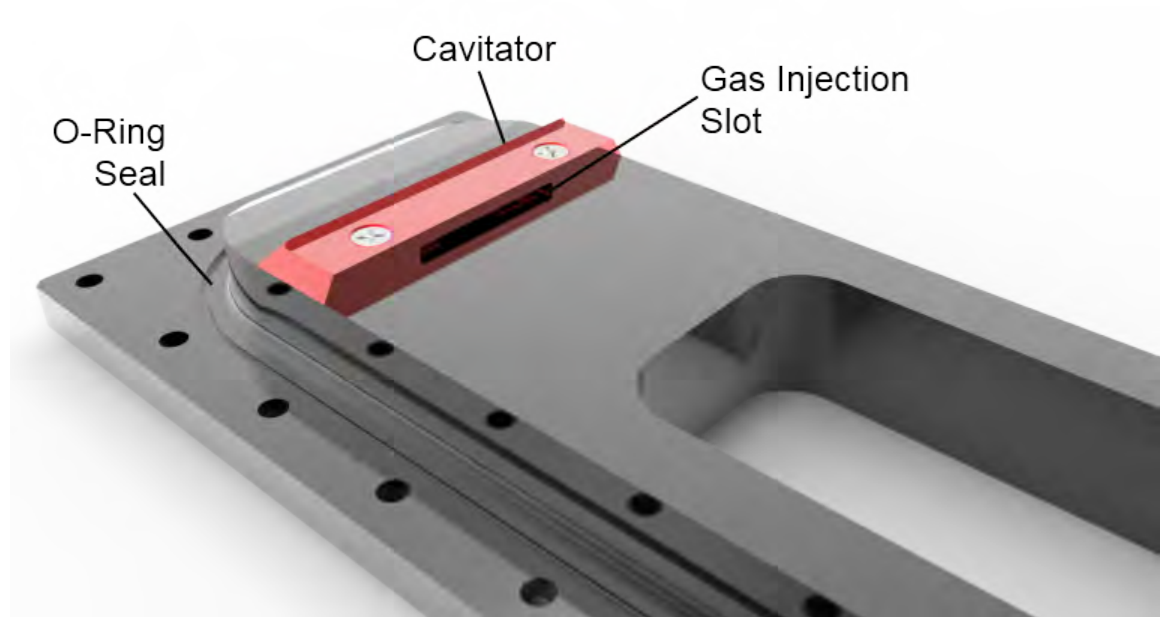


Figure 2.10: Aluminum Base Plate for the Swept Fin Apparatus Fitted with a Wall Cavitator

servomotor, which allowed for multiple data points to be gathered per run. The servomotor also provided finer control over the fin's position. The motor was attached to the fin with a 2:1 timing belt drive system.

As before, the fin was mounted to a force and moment transducer fitted to a bearing supported shaft. The balance housing and fin were mounted to the angled surface of a large aluminum block designed to fit onto the aluminum plate. The large aluminum block was used to induce sweep and support the new actuation system. Two blocks were fabricated to sweep the fins to 30 and 45 degrees from vertical. The new system reused two of the fins from the previous year's testing.

A model of new test apparatus is shown in fig. 2.11. The model shows the apparatus set up with a fin swept to 30 degree from vertical. The actual apparatus installed in the water tunnel is shown in fig. 2.12, set up for fin swept to 45 degrees.

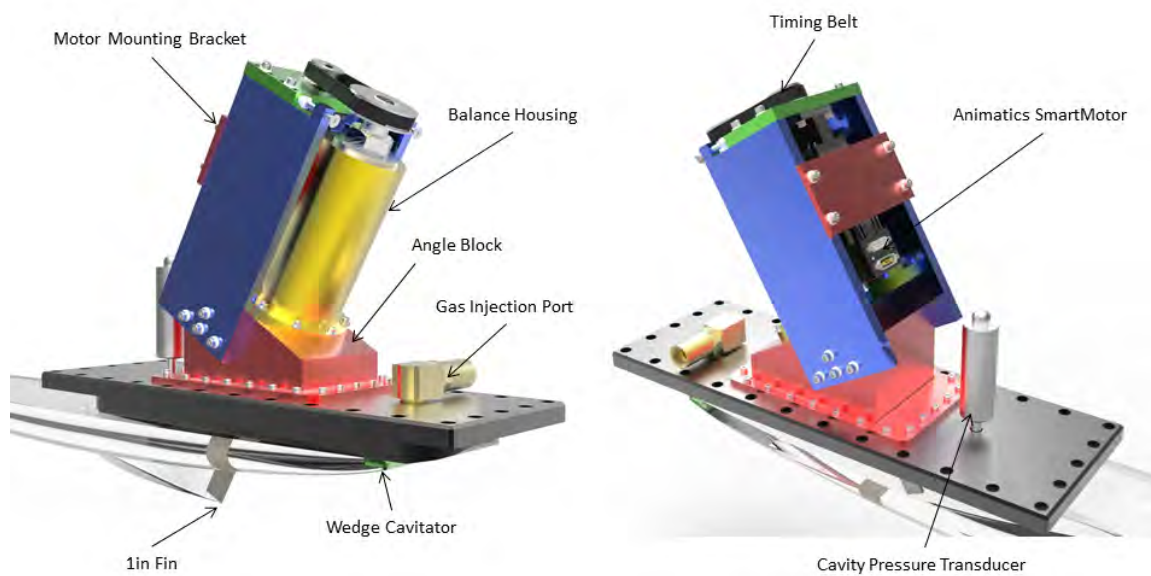


Figure 2.11: Models of the Swept Fin Apparatus set up with a fin swept to 30 degrees

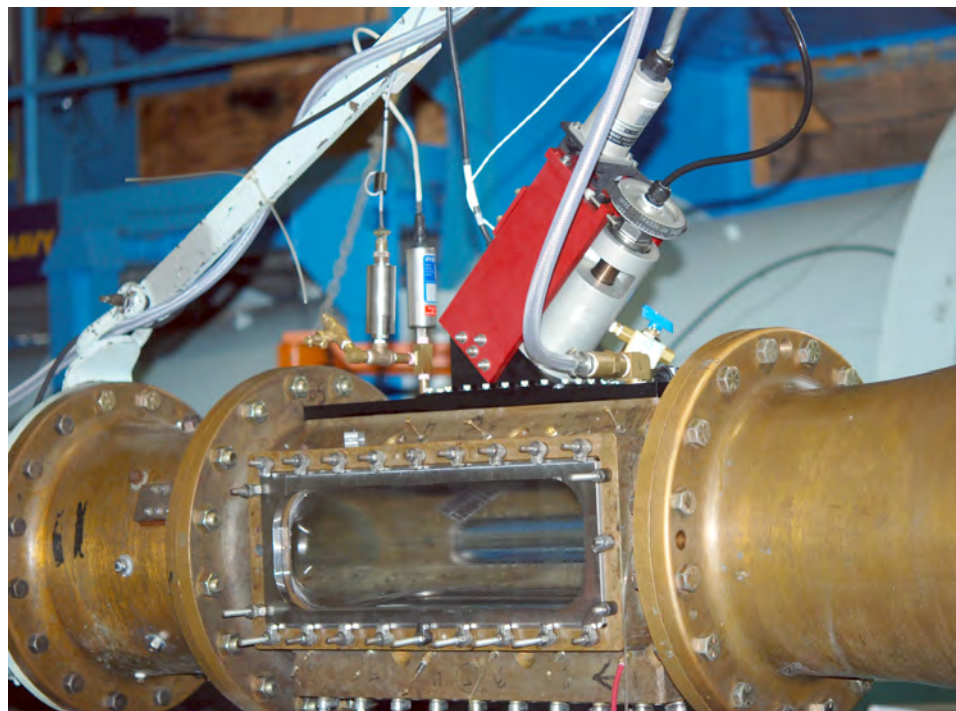


Figure 2.12: Swept Fin Apparatus Installed in the Twelve-Inch Water Tunnel at ARL set up with a fin swept to 45 degrees.

2.4.2 Instrumentation and Data Acquisition

Data and videos were collected with a National Instruments acquisition system, similar to the one used during the previous summer. As was the case before, a LabView program, was used to sample test data and videos. Test data was sampled at 500 *Hz* and videos were acquired at 30 frames per second.

Another AMTI SP2.5d-1k-6010 force and moment transducer was used for the swept fin testing. This cell was chosen because it was the smallest sensor available that could handle the expected fully wetted loads. For the swept fin tests, the AMTI MSA-6 MiniAmp was replaced with an AMTI Gen5 amplifier, which provided more precise control over excitation voltages and a wider range of amplifier gains.

Fin motion was recorded using the same BEI Motion Control Systems encoder, driven by the timing belt fin actuation mechanism. A bracket was used to hold the encoder against the outer side of the timing belt. For most runs, a double-sided belt was used to ensure proper tracking between the encoder and the actuator. The timing belt fin actuator and encoder can be seen in fig. 2.13.

For the early tests, the encoder was fitted with a drive roller and read fin motions from the back of a single sided timing belt. The lack of a mechanical joint between the encoder and belt was found to result in zero drift over time. To fix this, the timing belt was swapped for a double sided HTD toothed timing belt and the drive roller was replaced with a timing belt pulley, as shown in fig. C.6.

An Animatics SmartMotor SM2310D servo drive motor was used to actuate the fin. The motor was controlled using an integrated micro-controller and a 2000 line optical encoder attached to the motor output shaft. The motor output was reduced using a 100:1 Stober ServoFit Precision Gearhead to increase the motor's precision and torque. With the addition of the gearhead, each line on the motor's optical encoder corresponded to a 1/1111

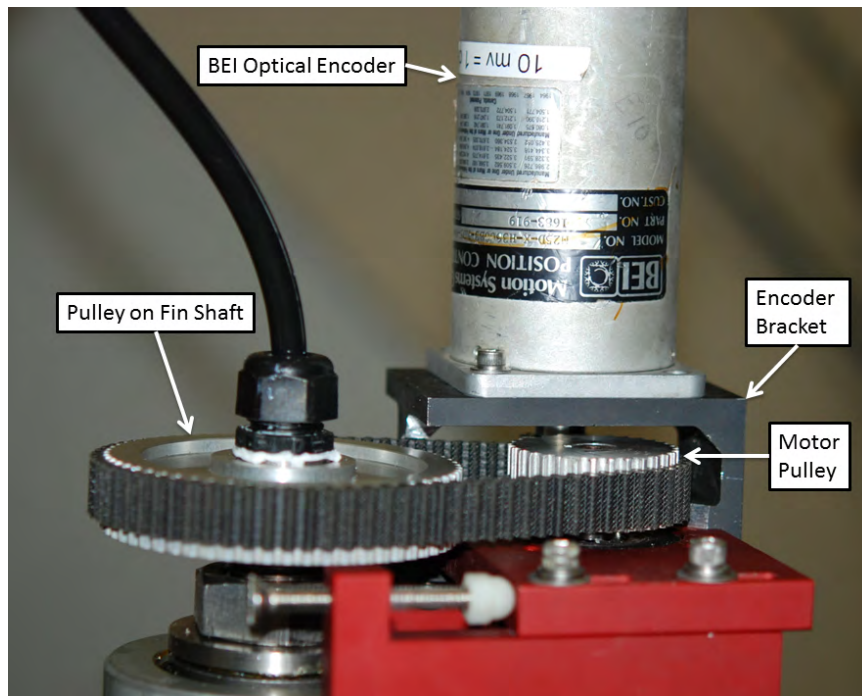


Figure 2.13: Timing Belt Fin Actuation Mechanism and Optical Encoder

degree rotation of the gearhead's output shaft.

The Heise DXD transducers were used once again to measure the cavity, static, and total pressures. The transducers were re-configured so they could be sampled at a faster rate. Unfortunately, the maximum sampling rate of the Heise transducers was still very low, on the order of 10 *Hz*. Because of this, an Omegadyne 0-50 psig transducer was used in parallel with the Heise transducer for higher resolution cavity pressure measurements.

The gas flow rate was measured using the same Sierra Instruments 830 series flowmeter. The meter was sent back to the factory and re-calibrated before testing.

The same two Basler Scout color CCD cameras were used for documentation purposes. As before, one camera observed the fin from the side, and the other observed from the fin tip. The LabView program synced the videos with the acquired data, and overlaid data and timestamps onto the videos.

A Nikon D80 DSLR camera was used to take photos during testing. The camera

was placed on a tripod beside the tunnel, and was focused on the suction side of the fins. A digital I/O port from the Animatics SmartMotor and a relay were used to trigger the camera each time the fin was actuated.

For some of the later runs, high speed color videos were taken using a Casio EX-F1 camera at 600 frames per second.

Additional setup photos are shown in Appendix C.

2.4.3 Swept Fin Test Methodology

As before, steady and unsteady state tests were performed on the swept fins over a range of conditions. For all cases, tunnel velocity, gas injection rate, and tunnel pressure were held constant during each run.

The servomotor allowed for several steady state conditions to be tested per run. As before, tests were performed with the fin at angles of attack above and below the wedge half-angle. The fins were rotated to the zero position before each run. Once the fin was set, the tunnel drive was engaged and the tunnel was brought to the appropriate velocity. As the tunnel came up to speed, the pressure in the tunnel was decreased. The data acquisition system was started when the tunnel pressure and velocity reached stable conditions. The ventilation gas was started, and the servomotor was engaged. The servomotor was pre-programmed to move the fin from the zero position to 3-4 different angles of attack over a 15 second period. The motor would stop the fin at the desired angles of attack for 3-4 seconds. Half way through the dwell period, the motor controller would trigger the Nikon D80 camera. At the end of the control program, the motor returned the fin back to zero. The ventilation gas and tunnel drive system were stopped when the fin returned back to the zero position. After each run, the tunnel was degassed and prepared for the next condition.

Each steady state condition was approached from higher and lower angles of attack to investigate non-linear behavior associated with the formation and collapse of the

fully ventilated trailing cavity. During these experiments, the test parameters took on the following values:

- *Angle of Attack*: 0, 1, 2, 3, 4, 4.5, 5, 7.5, 10, 12.5, and 15 deg
- *Tunnel Velocity*: 25, 35, and 45 ft/s
- *Chord Length*: 1 and 2 in.
- *Wall Cavitator Thickness*: 1/4 and 3/8 in.
- *Sweep Angle*: 30 and 45 deg from vertical

Unsteady state tests were performed to investigate the mechanism of ventilation and explore the effects of varying the angular velocity of the fin's actuation. The new actuator allowed for finer control of the fin's angular velocity and acceleration.

As was done with the steady state tests, the fin was centered before each run. When the tunnel was brought to stable conditions, the data acquisition and ventilation systems were started. After a moment, a cavity formed along the top of the tunnel, and the fin actuator was initiated. Tests typically lasted about 20 seconds, after which the ventilation gas was turned off and the tunnel drive was disengaged.

Chapter 3

Test Data Reduction

3.1 Steady State Test Data

Steady state measurements were made with the fin at fixed angles of attack above and below the wedge half-angle. The steady state test data needed to be post-processed and reduced for analysis.

3.1.1 Post-Processing

MATLAB[®] was used to post-process the recorded time history files, and organize the reduced data to a file. The data from the unswept fin testing was considered first. Typical raw data from the unswept fin testing is shown below in fig. 3.1.

The post-processing program allowed the user to plot the time history files and select regions to post-process. The post-processing bounds were chosen to start after the reached steady conditions after gas injection, and stop sometime before the gas was turned off. The mean, \bar{x} and standard deviation, s , were calculated for each data channel over the selected region using the following relations:

$$\bar{x} = \frac{1}{n} \sum_{i=1}^n x_i \quad (3.1)$$

$$s = \left(\frac{1}{n-1} \sum_{i=1}^n (x_i - \bar{x})^2 \right)^{\frac{1}{2}} \quad (3.2)$$

where n is the number of individual readings x_i .

The program loaded the side video for the specific run to measure the cavity thickness. The user was shown a frame of the video, and was prompted to select the ruled lines on the fin and the outline of the cavity. With this, the fin program calculated the cavity thickness at the leading and trailing edges of the fin.

Several corrections were made to the raw data. First, the actual volumetric flow rate, Q_2 into the tunnel was calculated from the measured value, Q_1 , in SCFM. This was necessary because the pressure and temperature in the tunnel differed from the standard values the flowmeter was referenced to. This conversion was applied using the following relation:

$$Q_2 = \frac{P_1 T_2}{P_2 T_1} Q_1 \quad (3.3)$$

where P_1 and P_2 are the reference and actual pressures, and T_1 and T_2 are the reference and actual temperatures, respectively. In this case, pressure was in psi and temperature was in Rankine, as suggested by the manufacturer (Sierra, 1994).

The velocity needed to be corrected two ways. First, the static pressure used to calculate the velocity was taken at a different height than the total pressure. The static head, $\rho\Delta z$, of the height difference was subtracted to align the two pressure measurements on the same plane.

The second correction applied to the measured velocity was to correct for the blockage effects due to the presence of the supercavity along the top of the tunnel. The cavity constricted the flow of water, which resulted in an increase in velocity. Assuming incom-

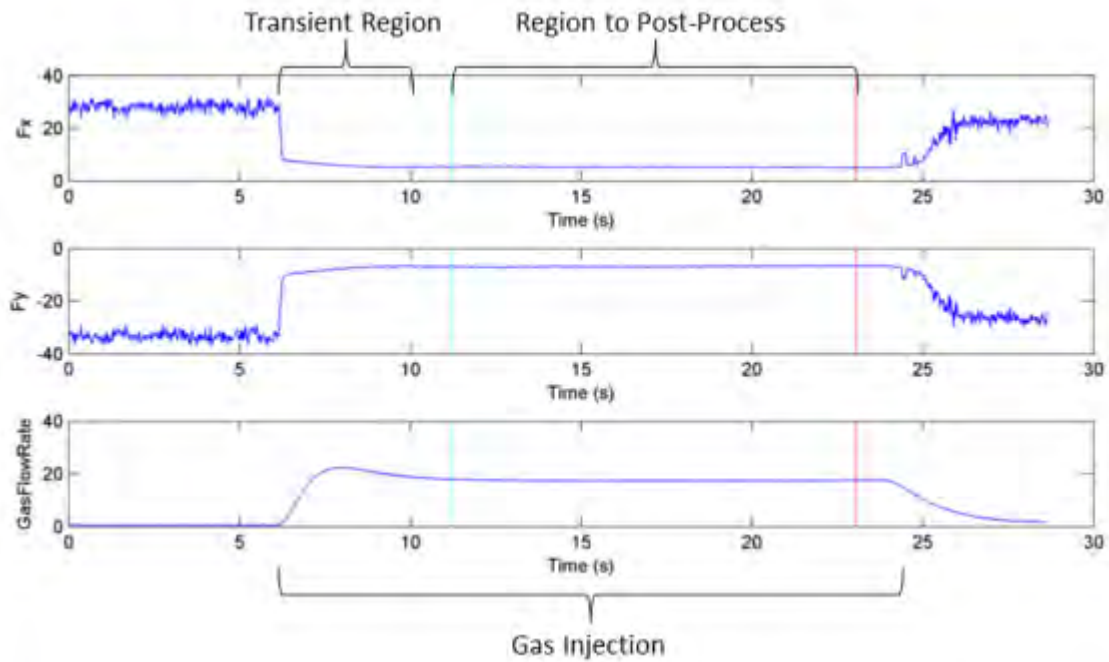


Figure 3.1: Typical Time History from Steady State Unswept Fin Testing

pressible flow, continuity requires that the following relation hold:

$$V_1 A_1 = V_2 A_2 \quad (3.4)$$

where A_1 and V_1 are the cross sectional area of the test section and velocity without a cavity, and A_2 and V_2 are the area and velocity with the cavity. The continuity equation was rearranged to obtain the following relationship:

$$V_2 = \frac{V_1 A_1}{A_2} \quad (3.5)$$

The tunnel cross sectional area with the cavity present, A_2 was estimated as:

$$A_2 = A_1 - t_c w_c \quad (3.6)$$

where t_{le} and w_{le} are the thickness and width of the cavity at the leading edge of the fin.

A corrected cavity underpressure, σ_c was calculated using the new, corrected values for static pressure and velocity using eq. (1.5). Unfortunately, most of the cavity pressure measurements from the unswept fin tests were found to be no good. Luckily, as discussed in chapter 4, the measured forces and moments were found to be fairly insensitive to variations in cavitation number and flow rates, over the ranges tested.

The corrected data was then used to calculate the normal and tangential forces, lift, drag, center of pressure, and their respective non-dimensional characteristics. Due to the orientation of the force and moment transducer during the unswept fin testing, the forces were found using the following reduction equations:

$$F_N = -(F_x - F_y) \cos(\pi/4) \quad (3.7)$$

$$F_\tau = -(F_x + F_y) \cos(\pi/4) \quad (3.8)$$

$$L = F_N \cos(\alpha) - F_\tau \sin(\alpha) \quad (3.9)$$

$$D = F_N \sin(\alpha) + F_\tau \cos(\alpha) \quad (3.10)$$

These were non-dimensionalized using eqs. (1.14) and (1.15)

A similar approach was taken with the swept fin data. As discussed in chapter 2, the new drive mechanism allowed for several conditions to be tested per run. The post-processing program needed to be modified to process multiple parts of each time history file.

A function was added to the post-processing program to analyze the time history of fin position, and isolate where the fin was moving and where the fin was stationary. This was accomplished by taking the gradient of the encoder signal to get angular velocity. The function then used that signal to determine where the fin started and stopped moving.

The program then plotted the time history file and prompted the user to select the region to be post-processed. Means and standard deviations were found over the selected region. The side and top videos were also cut such that they began when the fin started moving to a trajectory, and stopped when the fin started moving to the next trajectory.

Cavity thickness was measured from the side photos taken with the Nikon D80, instead of from the side video. As before, the program prompted the user to select the ruled lines on the fin and the cavity boundary, and calculated the cavity thickness at the leading and trailing edges.

The velocity, pressure, cavitation number, and gas flow rate were all corrected as they had been for the unswept fin testing. An additional correction was also applied to the forces and moments. This was done to compensate for the fact that sweeping the fin moved the center of gravity away from the fin's axis of rotation. When the swept fins were rotated about their axes, the center of gravity moved around, which resulted in changes in the measured forces and moments.

Tare runs were performed for each fin and sweep combination to quantify effects of moving the center of gravity. For each configuration, the fin was slowly rotated about its axis over a range of angles of attack while suspended in air. MATLAB[®] was then used to fit equations to the tare data as a function of angle of attack. A function was added to the post-processing program to apply the corrections to the forces and moments. Figure 3.2 shows the tares for the 2 inch fin swept to 45 degrees. The tares for F_z and M_z are not shown because their components were found to be negligible.

As before, the corrected data was used to calculate the forces and moments. Due to the orientation of the force and moment transducer during the swept fin testing, the normal and tangential forces were found as:

$$F_N = -(F_x + F_y) \cos(\pi/4) \quad (3.11)$$

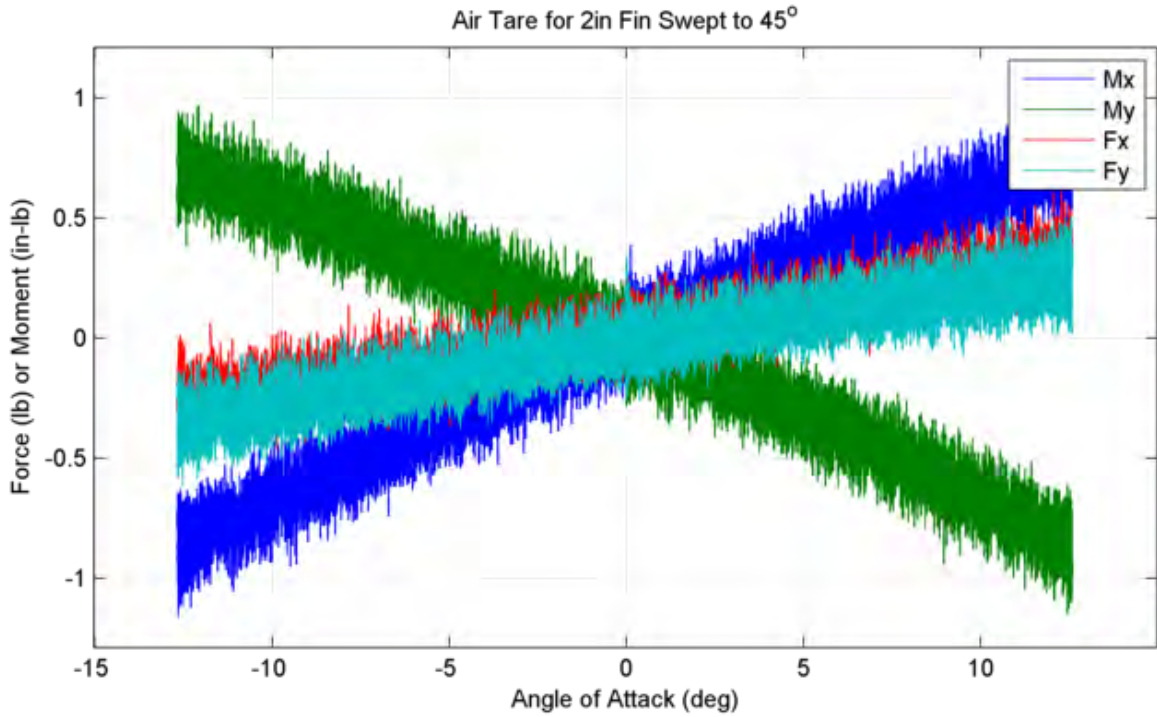


Figure 3.2: Tares for 2in Fin Swept to 45 Degrees

$$F_{\tau} = (F_x \cos(\gamma) \cos(\pi/4) - F_y \cos(\gamma) \cos(\pi/4) - F_z \sin(\gamma)) \quad (3.12)$$

where γ is the sweep angle, from vertical. The lift and drag forces were found using eqs. (3.9) and (3.10).

3.1.2 Uncertainty Analysis

The total uncertainty of any measurement can be estimated as the root-sum-square (RSS) of the systematic and random errors associated with the measurement. Coleman and Steele (1999) define the systematic error as a fixed offset in a measurement. This is sometime referred to as the bias error. They also defined random error as the error resulting from random fluctuations in a measurement system. Figure 3.3 shows the error associated with

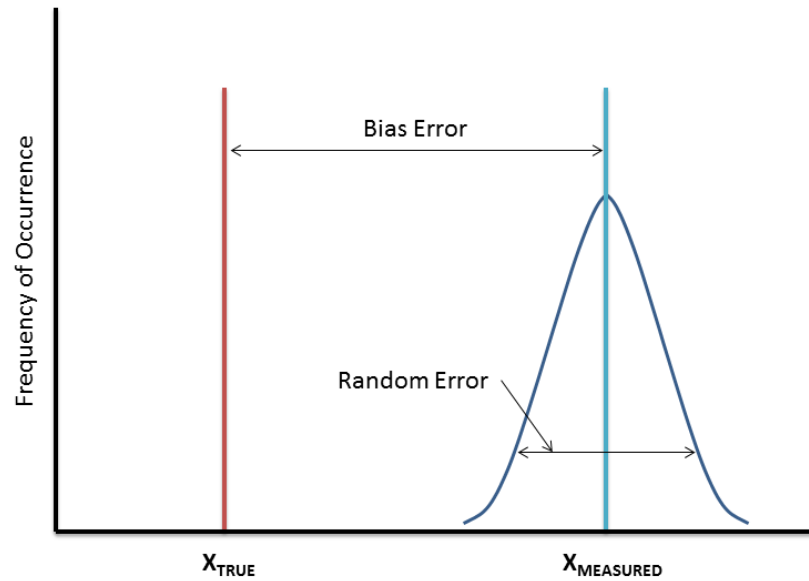


Figure 3.3: Errors in the Measurement of a Variable X, Large Number of Measurements

the particular measurement of a variable X. The total uncertainty can be defined as:

$$U_x^2 = B_x^2 + P_x^2 \quad (3.13)$$

where B_x is the systematic error and P_x is the random error.

The systematic errors needed to be specified for each measured variable. These were typically estimated as the advertised uncertainty of the measurement devices used. The estimated systematic errors for the various instruments used are shown below in table 3.1.

The random error associated with the measured values was taken as the 95% confidence interval of region post processed, which was estimated as

$$P_x = \frac{2s}{\sqrt{n}} \quad (3.14)$$

Most of the test data was passed through reduction equations such as eqs. (3.9) and (3.10) to convert the raw data into a useful form. The propagation of uncertainty

Table 3.1: Estimated Systematic Errors for Different Measurement Systems

Measurement	2011 Testing	2012 Testing	Unit
Angle of Attack	0.333	0.15	<i>deg</i>
Fin Planform	Chord/8	Chord/10	<i>in</i> ²
Velocity	0.75	0.5	<i>ft/s</i>
F _x	0.157	0.216	<i>lb</i>
F _y	0.435	0.382	<i>lb</i>
F _z	0.694	0.520	<i>lb</i>
M _x	2.200	0.205	<i>in - lb</i>
M _y	0.744	0.371	<i>in - lb</i>
M _z	1.679	1.015	<i>in - lb</i>
Water Temp.	0.15	0.15	<i>°F</i>
Pressure	0.02	0.02	<i>psia</i>

through these reduction equations was accounted for using a method described by Coleman and Steele (1999, Chap. 3). The uncertainty of the final value, U_r , was found as the RSS of the uncertainties associated with the various measurements used to calculate the final value. The uncertainty in the result could be defined as:

$$U_r^2 = \left(\frac{\partial r}{\partial X_1} \right)^2 U_{X_1}^2 + \left(\frac{\partial r}{\partial X_2} \right)^2 U_{X_2}^2 + \dots + \left(\frac{\partial r}{\partial X_j} \right)^2 U_{X_j}^2 \quad (3.15)$$

where U_{X_i} are the uncertainties in measurement X_i . If the partial derivatives, called the “absolute sensitivity coefficients” in (Coleman and Steele, 1999), are redefined as θ_i , eq. (3.15) can be rewritten in compact form:

$$U_r^2 = \sum_{i=1}^j \theta_i^2 U_{X_i}^2 \quad (3.16)$$

This method was used to calculate the uncertainty of the measured lift, drag, and the relevant force and moment coefficients.

3.1.3 Tunnel Wall Corrections

The presence of solid walls around the fin result in changes in the flow field, which typically need to be corrected for. The effects of these extraneous forces can be felt in a variety of ways, depending on flow geometry (Rae Jr. and Pope, 1984). The solid tunnel walls tend to increase the dynamic pressure on a lifting body, resulting in an increase in the measured forces and moments at a given angle of attack. This effect is typically referred to as solid blockage. The tunnel walls also tend to constrict expansion in the wake region. This effect, typically know as wake blockage, results in a decrease in the measured drag. For an open jet tunnel, these effects are typically reversed. Finally, boundary layer growth along the solid tunnel walls can reduce the pressure along the length of the test section, creating an additional drag force. Luckily, ARL's twelve-inch water tunnel was designed to have zero longitudinal pressure gradients along the test section to counter the effects of boundary layer growth.

A method described by Maixner (1977) was used to quantify the effects of the tunnel walls. Maixner (1977) completed a water tunnel investigation on three geometrically similar supercavitating fins of finite span. He found that he could correct for the tunnel walls by applying a traditional wind tunnel corrections, similar to those described by Rae Jr. and Pope (1984), though this was only valid for supercavitating fins with spans less than or equal to half of the width of the water tunnel.

Corrections for wall effects appeared as additive corrections to the measured angle of attack and drag coefficient. The correction to measured angle of attack was found as:

$$\alpha_T = \alpha + \delta \frac{B}{B_o} C_L (180/\pi) \quad (3.17)$$

where α is the measured angle of attack in degrees, B/B_o is the ratio of foil area to tunnel

cross-sectional area, and δ is a correction factor for the influence of the images of the trailing vortex system. The value of δ is a function of the dimensions of the tunnel, the ratio of the fin's span to the tunnel width, and tunnel boundary conditions (i.e. closed or open jet). Similarly, the correction to the measured drag coefficient was found as:

$$C_{DT} = C_D + \delta \frac{B}{B_o} C_L^2 \quad (3.18)$$

where C_D and C_{DT} are the measured and “true” drag coefficients, respectively.

The value of δ can either be positive or negative, depending on the tunnel wall boundary condition. For closed jet tunnels, δ is a positive number, and can be found from Rae Jr. and Pope (1984, fig. 6.37). For an open jet tunnel, δ is a negative number, and can be found from (Rae Jr. and Pope, 1984, fig. 6.38).

Unfortunately, the fact that the fin is piercing a free surface created along the top of a closed jet tunnel made neither of the two corrections valid. With the cavity present, the tunnel had solid boundaries along the sides and bottom, and a free surface along the top.

The importance of wall corrections was investigated by calculating them for both types of boundaries. The value of δ was found to be roughly 0.06 for a closed tunnel and varied between -0.11 and -0.13 for the open jet. The magnitude of the corrections to drag coefficient were found to typically be less than about 0.3% of the measured drag coefficient for the closed boundary condition, and less than about -0.6% for the open boundary. The correction for angle of attack was found to be less than 0.5% of the measured angle of attack for the closed boundary condition, and less than about -1% for the open boundary.

It is likely that the wall corrections necessary for this specific flow configuration will fall somewhere in between what was estimated for the open and closed jet cases. Since the order of magnitude of the wall corrections were found to be within the error of measurement, it seemed reasonable to omit them. Wall corrections will become especially

important in future experiments utilizing more sensitive instrumentation. Further studies are recommended to quantify the effects of the tunnel walls for cavity piercing fins. These effects can also be minimized in future experiments by reducing the ratio B/B_o , by either using smaller fins or a larger water tunnel.

3.2 Unsteady Test Data

Unsteady state tests were performed where measurements were made on a fin oscillating over a range of angles of attack. The main purpose of the unsteady state testing was to investigate the transition between base and fully ventilated operation. The goal was to characterize how tunnel velocity, fin shape, and angular velocity affect the angle of attack at which transition occurs.

During the unswept fin tests, the fin was oscillated about its spanwise axis using a motor driven cam/follower mechanism. This mechanism rotated the fin in a semi-sinusoidal fashion to angles of attack of +/- 20 degrees, at frequencies of 18 and 30 oscillations per minute.

This mechanism was replaced with a servomotor for the swept fin tests. The new system allowed the user to adjust the angular velocity, angular acceleration, and amplitude of oscillation independently.

A post-processing program was written in MATLAB[®] to allow a user to select where the fin transitioned between base and fully ventilated operation. The program also calculated the angular velocity from the encoder signal, and applied necessary corrections to the measurements.

Transition could typically be identified from the measured forces and moments as either a discontinuity or as a dramatic shift in the slope of the plotted time histories, as shown in fig. 3.4. The transition from base to full ventilation could take on either form,

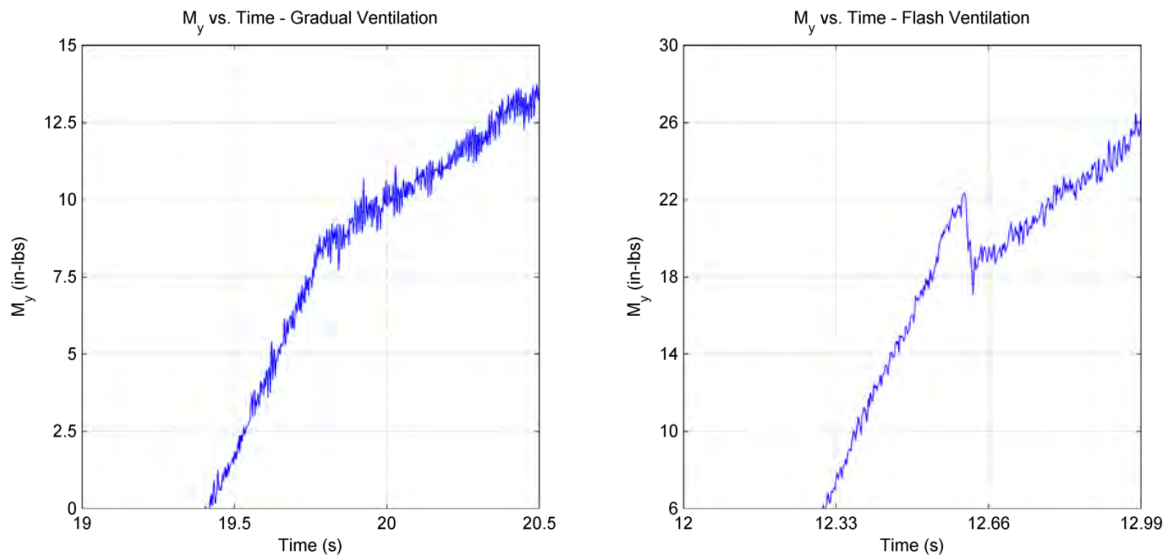


Figure 3.4: Identification of the location of the transition from base to full ventilation using time history of M_y . Left shows gradual transition, and right shows the more dramatic “flash” ventilation.

while the transition back was almost exclusively found to be a gradual shift in the slope of the curve.

The post-processing program plotted time histories of the moment signals, and prompted the user to select where the fin transitioned. The program then found the corresponding angles of attack and angular velocities, and saved them to a file.

The program also applied corrections to the data, similar to the ones applied to the steady state data. As before, this included converting the measured flow rate in SCFM to CFM at tunnel conditions, correcting the tunnel velocity for blockage due to the presence of the cavity, and applying tares for the weight of the fin.

Tares were made where the fins were oscillated at the various angular accelerations performed during unsteady testing. The goal was to correct shaft torque for the additional torque present during acceleration. Upon further investigation of the data, it was found that the angular accelerations used during testing were typically too low to make a noticeable difference in the measurements.

Time histories of lift and drag were calculated using the equations listed earlier. Non-dimensional force and moment coefficients were also calculated for lift, drag, and moment about the spanwise axis of the fin. Planform area for all angles of attack was taken as the wetted area of the cavity piercing fin at an angle of attack of zero degrees, which were measured during the steady state experiments.

Chapter 4

Experimental Results and Discussion

4.1 Wake Forms and Cavity Structures

When a fin with a wedge cross section and rectangular planform pierces a ventilated cavity boundary, gas is entrained in the low pressure wake created by the fin. This entrained gas forms a trailing cavity that remains attached to the fin and closes downstream. During testing, the trailing cavity was found to take on a few unique shapes, based on the fin's angle of attack and sweepback angle. These trailing cavities were connected to the cavities along the top of the tunnel, which provided a source of ventilation gas.

4.1.1 Trailing Cavities from Unswept Fins

Figures 4.1 and 4.2 show the trailing cavity attached to an unswept fin with its centerline aligned with the incoming flow. In this condition, flow stagnated at the leading edge, and was diverted equally along both side of the fin. A positive pressure gradient was maintained along both sides of the fin, which deterred cavitation. The blunt trailing edge created a region of low pressure behind the fin, which encouraged the formation of a base ventilated trailing cavity.

For the conditions tested, the trailing cavity was found to form down the fin's entire span from the tip to the boundary of the supercavity along the top of the tunnel. From the



Figure 4.1: Base ventilated fin from the side, $\alpha = 0^\circ$, no sweep, 1 inch chord



Figure 4.2: Base ventilated fin looking down the span from the fin tip, $\alpha = 0^\circ$, no sweep, 1 inch chord

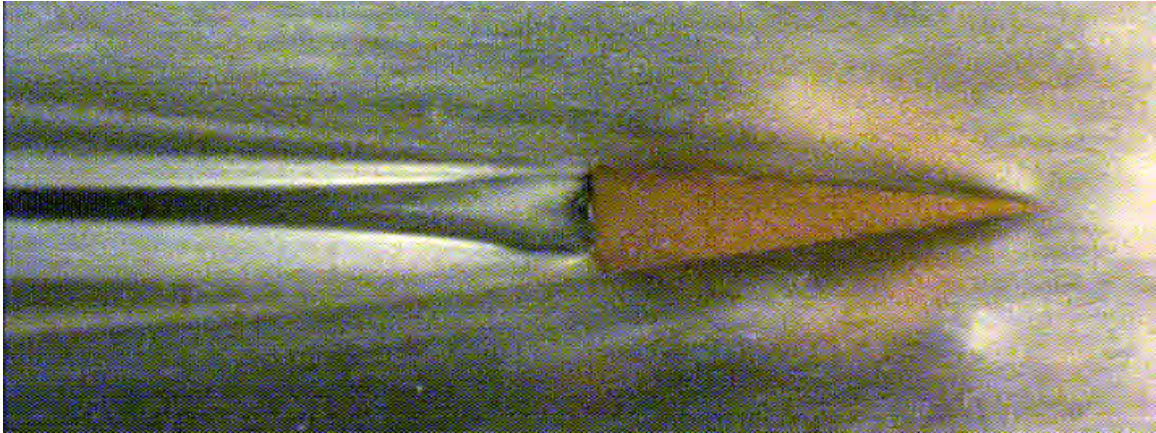


Figure 4.3: Asymmetric vortex cavities forming from the tip of a base ventilated fin at a non-zero angle of attack, looking down the span from the fin tip. 3 inch chord, $\alpha = 3^\circ$, no sweep

side, the boundary of the trailing cavity appeared to form tangent to the incoming flow at the fin tip, and slowly curved upwards downstream, as shown in fig. 4.1. When the fin was base ventilated, the fin tip remained wetted. Looking down the span from the fin tip, shown in fig. 4.2, the trailing cavity boundary appeared to form from the trailing edge, tangent to the surface of the fin.

When the fin was base ventilated, two counter-rotating vortex cavities formed from the fin tip and extended downstream along the cavity boundary. In the spanwise view, the two vortices appeared to rotate into the cavity. When the fin's centerline was aligned with the incoming flow, the two vortices were mirror images of each other, as shown in fig. 4.2.

As the fin's angle of attack was increased, the vortex cavity on the pressure side was found to grow, while the one on the suction side shrunk, as shown in fig. 4.3. This change was a result of asymmetry in the pressure distribution around the fin at non-zero angles of attack. In the side view, the core of the vortex appeared to be aligned with the fin tip. As a result, the large vortex cavity formed from the pressure side created a noticeable bump in the trailing cavity near the fin tip, as shown in fig. 4.4.

As the fin's angle of attack was increased from zero, the stagnation point moved

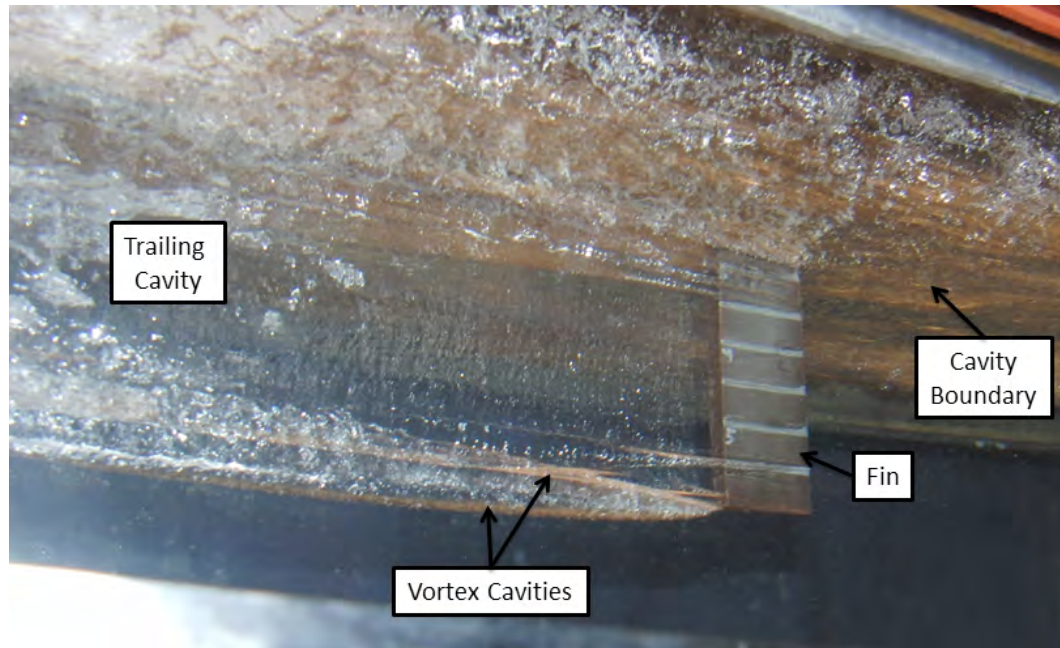


Figure 4.4: Photo of a base ventilated fin, taken from the suction side, 1 inch chord at an angle of attack of 5 degrees, no sweep

away from the leading edge, down the pressure side, as discussed by Cox and Clayden (1958). This movement resulted in the formation of a low pressure region on the suction side near the leading edge. When the fin was rotated to an appropriately high angle of attack, the suction side ventilated, resulting in the formation of a trailing cavity from the sharp leading edge and the trailing edge of the pressure side. In this configuration, called fully ventilated, the fin acted as a flat plate hydrofoil.

At these higher angles of attack, there were typically three regions of low pressure that encouraged the formation of a fully ventilated trailing cavity. As was the case with the base ventilated fin, a region of low pressure was created by the wedge section's blunt trailing edge. An additional low pressure region was created along the suction side of the fin as a result of the movement of the stagnation point down the pressure side. The final region of low pressure was found to occur at the center of the tip vortex, created as a result of three-dimensional lift generation.



Figure 4.5: Vaporous cavitation on a yawed fin at a low cavitation number showing the three low pressure regions that encourage the formation of a fully ventilated trailing cavity when the fin pierces a ventilated cavity boundary. $\alpha = 15^\circ$, no sweep, 1 inch chord, photographed with 1/40 second exposure time.

The existence of these three regions of low pressure were verified by observing the formation of cavitation on a yawed fin at very low cavitation numbers. The existence of large amounts of cavitation in a particular region implied that local pressures were less than the pressures in regions with no cavitation. Figure 4.5 shows large amounts of vaporous cavitation in these three regions for the one inch chord fin at a high angle of attack and low cavitation number.

Figure 4.6 shows the same fin under similar conditions piercing a ventilated cavity boundary. Here, gas was entrained in the low pressure regions shown in fig. 4.5, which resulted in the formation of a fully ventilated trailing cavity. As shown in the figure, the suction side of the fin was completely enclosed in the trailing cavity, along with the fin's tip.

Figure 4.6 also shows that a large vortex cavity formed from the fin tip and merged

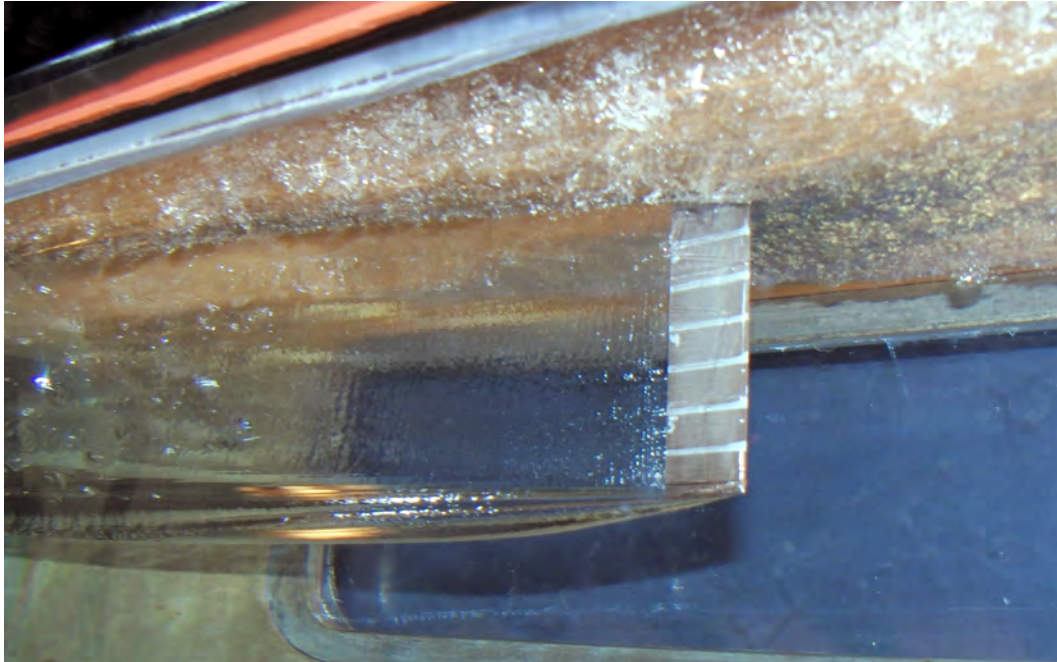


Figure 4.6: Fully ventilated supercavitating fin piercing a ventilated cavity boundary, photo taken from suction side of the fin, $\alpha = 15^\circ$, 1 inch chord, no sweep, photographed with 1/60 second exposure.

with the rest of the trailing cavity. Rotation of the tip vortex cavity was observed to be from the pressure to the suction side. Increasing the fin's angle of attack resulted in an increase of the size of the tip vortex cavity.

Figure 4.7 shows a fully ventilated fin, looking down its span from the tip. On the pressure side, the trailing cavity appeared to form tangent to the fin surface. The boundary on the suction side began at the sharp leading edge of the fin. The angle at which the cavity boundary formed, with respect to the incoming flow, appeared to increase with angle of attack, as shown in fig. 4.8. Additionally, the maximum cavity width appeared to increase with increasing angle of attack. The shape of the trailing cavity was a result of the turning of the flow by the fin.

At some intermediate conditions, partial cavities formed from the leading edge and collapsed somewhere along the suction side of the fin. Two types of partial cavities were

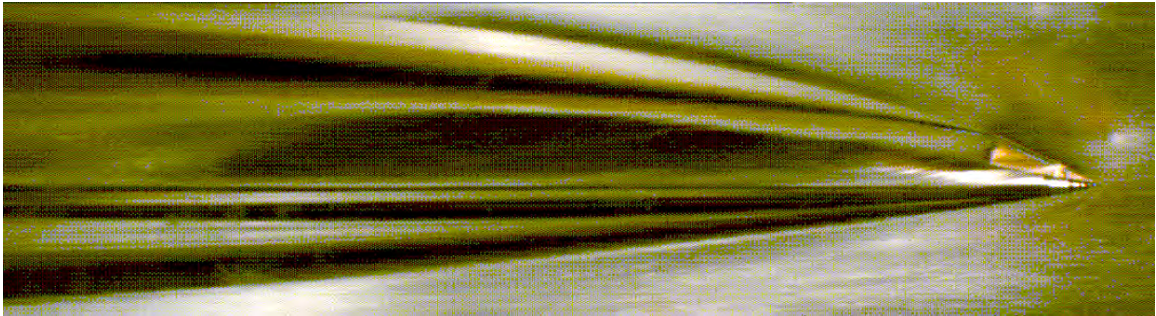


Figure 4.7: Fully ventilated supercavitating fin piercing a ventilated cavity boundary, looking down span from fin tip, $\alpha = 20^\circ$, 1 inch chord, no sweep.

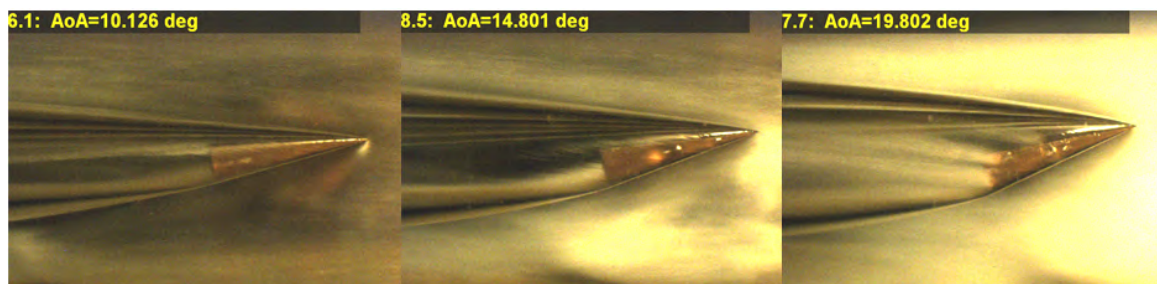


Figure 4.8: The angle at which the cavity boundary over the suction side forms at, with respect to the incoming flow, varies with the fin's angle of attack. This is shown here for the unswept 3 inch chord fin for $\alpha = 10^\circ, 15^\circ, 20^\circ$

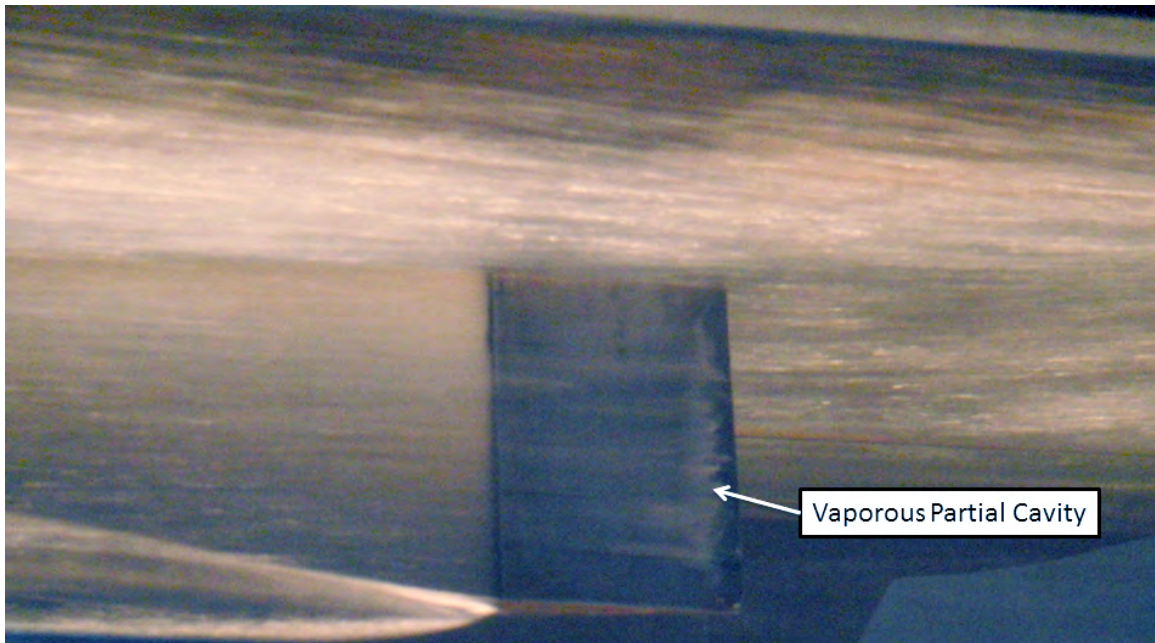


Figure 4.9: Vaporous partial cavity formed near the leading edge of an unswept base ventilated fin during steady state testing. 2 inch chord, $\alpha = 5^\circ$, photo taken with 1/160 second exposure time

found during the unswept fin testing. The first type typically occurred as the fin was operating as base ventilated. Here, vaporous partial cavities would form near the leading edge. The cavities would either collapse almost immediately, or would trigger transition from base to fully ventilated operation. It is interesting to note that these were found during both the steady and unsteady state testing. An example of this type of partial cavity is shown in fig. 4.9.

Ventilated partial cavities were also found. These typically formed during the unsteady state testing, during the transition from fully ventilated back to base ventilated. At the beginning of the transition, the ventilated partial cavity covered the majority of the suction side. As the angle of attack was decreased, the cavity shrunk, moving the closure point toward the leading edge. Just before transition was complete, small, horizontal streak cavities form near the leading edge. These cavities were typically found to extend along the

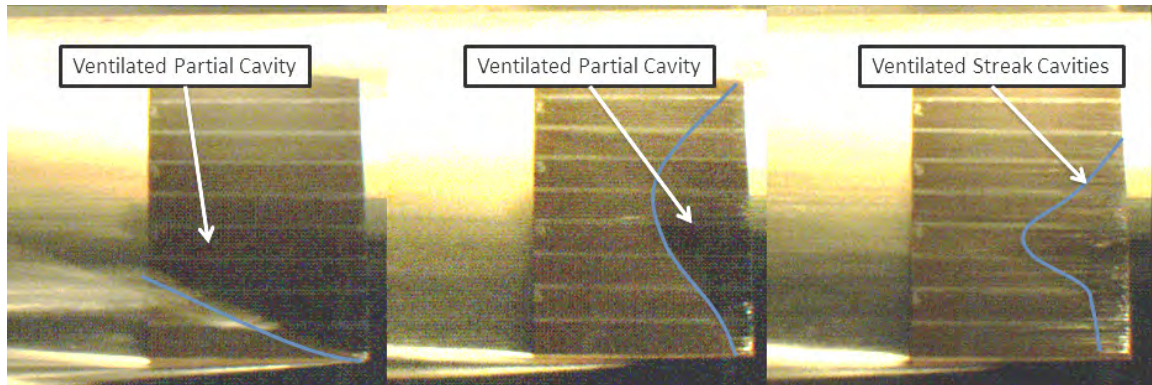


Figure 4.10: Progression of ventilated partial cavities during transition between fully and base ventilated operation. The figure on the left shows a large partial cavity present at the beginning of transition, the figure in the middle shows a smaller ventilated partial cavity at a slightly lower angle of attack, and the figure on the right shows horizontal streak cavities present immediately before transition is complete. Approximate shapes of the rear of the partial cavities are outlined in blue.

majority of the fin's span. Figure 4.10 shows a variety of ventilated partial cavities found during testing.

4.1.2 Trailing Cavities from the Swept Fins

The fins used during the swept fin experiments were the same ones used during the unswept fin testing. The fins were swept back to 30 and 45 degrees from vertical and were rotated about their spanwise axes. Since the same fins were used, the swept fins had trapezoidal planforms which varied with sweep, as shown in fig. 4.11.

In the figure, the region above the black dashed line maintained a constant chord length, with respect to the incoming flow. In the region below the black dashed line, the fin tapered to a point. Though the fin's chord decreased down the span in the tapered region, the fin's thickness to chord ratio (t/c) was maintained. In the non-tapered region, the chord length of the fin measured parallel to the incoming flow changed with sweep angle, γ . The

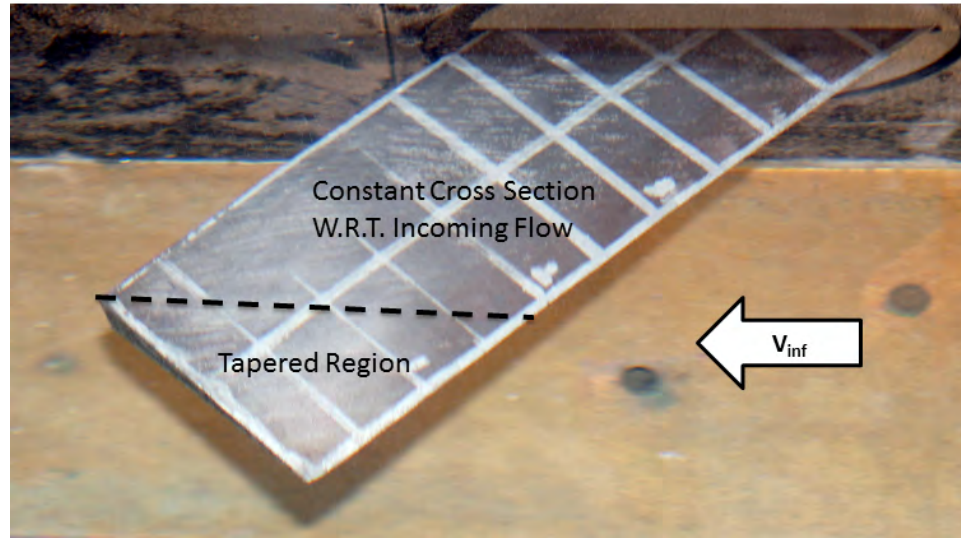


Figure 4.11: Trapezoidal planform of the 2 inch chord fin swept back 45 degrees. Region above the dashed line has a constant triangular cross section with respect to the incoming flow. Region below the dashed line tapers to a point.

resulting effective chord length, c_e , was found as:

$$c_e = c / \cos(\gamma) \quad (4.1)$$

where c is the chord length of the unswept fin. The effective chord length was used for calculating Reynolds and Froude numbers.

Sweeping the fins also changed the fin's cross section with respect to the incoming flow. In fig. 4.11, the region above the black dashed line maintained a constant wedge cross section. In the region below the dashed line, the fin tapered to a point. The cross section in the upper region has a wedge cross section, with chord length c_e . Since the maximum thickness of the wedge was fixed, sweeping the fin resulted in a decrease in the half-angle of the section. The effective half-angle of the swept fin could be found as:

$$\psi_e = \arctan\left(\frac{t}{2c_e}\right) \quad (4.2)$$

Table 4.1: Effective wedge half-angles and chord lengths for the swept fins

c for $\gamma = 0^\circ$	c_e for $\gamma = 30^\circ$	c_e for $\gamma = 45^\circ$	ψ_e for $\gamma = 0^\circ$	ψ_e for $\gamma = 30^\circ$	ψ_e for $\gamma = 45^\circ$
1	1.155 in	1.414 in	7.5°	6.504°	6.135°
2	2.309 in	2.828 in	7.5°	6.504°	6.135°

where t is the thickness of the wedge at the trailing edge and ψ_e is the effective half-angle of the swept fin. The effective half-angles and chord lengths for the fins tested are tabulated in table 4.1.

At low angles of attack, the incoming flow remained attached to the pressure and suction sides of the fin, and formed a trailing cavity downstream in the low pressure wake region. As was the case for the unswept fins, the trailing cavities were found to form down the entire span from the fin tip to the boundary of the supercavity formed along the top of the tunnel. A photo of a typical base ventilated trailing cavity behind a swept fin is shown in fig. 4.12.

The trailing cavities behind the base ventilated swept fins were found to form from the trailing edges of the pressure and suction sides of the fin, as was the case with the unswept fins. Due to the shape of the tapered region, there was no wetting on the tip, as was found during the unswept fin tests.

From the side, the trailing cavity appeared to start from the leading edge, tangent to the incoming flow, and slowly curved upwards, similar to what was found for the unswept fins. Looking down the span, the trailing cavity from the swept fins appeared to have a different structure than what was found during the unswept fin testing. The two vortex cavities found at low angles of attack during the unswept fin testing were not present for any condition. Instead, the trailing cavity near the fin tip had a smooth appearance. This is likely a result of the tapered tip.

When observed from the bottom of the tunnel, the cavity appeared to form tangent to surfaces of the fins, and then expanded and contracted to form a stretched ellipse. The

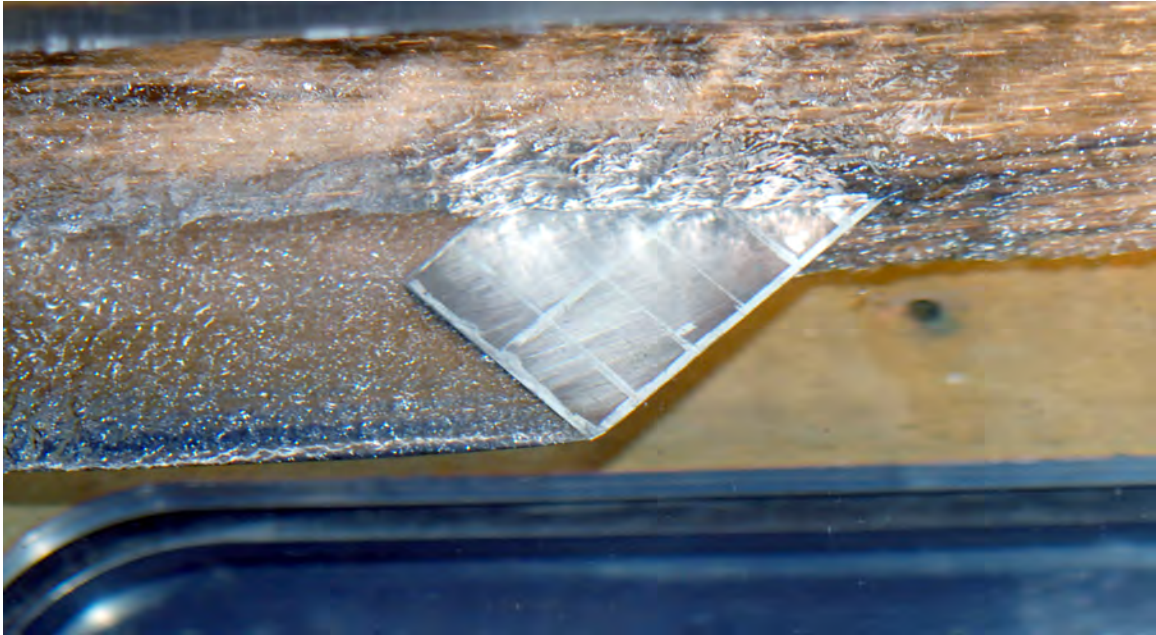


Figure 4.12: Base ventilated swept supercavitating fin, viewed from suction side, 2 inch chord, $\alpha = 5^\circ$, $\gamma = 45^\circ$, $V = 25 ft/s$, photo taken with 1/200 second exposure time. Dark spots on the fin surface are droplets of water stuck to the suction side of the fin inside the cavity

outer shape of the trailing cavity looked similar to the cavities formed from the unswept fins. Figures 4.13 and 4.14 show this for the two-inch fin swept to 30 degrees at angles of attack of zero and three degrees, respectively.

At higher angles of attack, the swept fins transitioned to fully ventilated operation, where the suction side of the fin was engulfed in the trailing cavity. Figure 4.15 shows a fully ventilated trailing cavity from a fin swept to 45 degrees. In the constant planform region, the trailing cavity formed from the leading edge and the trailing edge of the pressure side, and in the tapered region, the cavity formed from the leading edge and the end of the fin.

A variety of ventilated partial cavities were found to form along the suction side of the fin at middling angles of attack. These cavities were found to extend along the leading edge of the fin from the tip. The cavities were typically connected to the trailing cavity

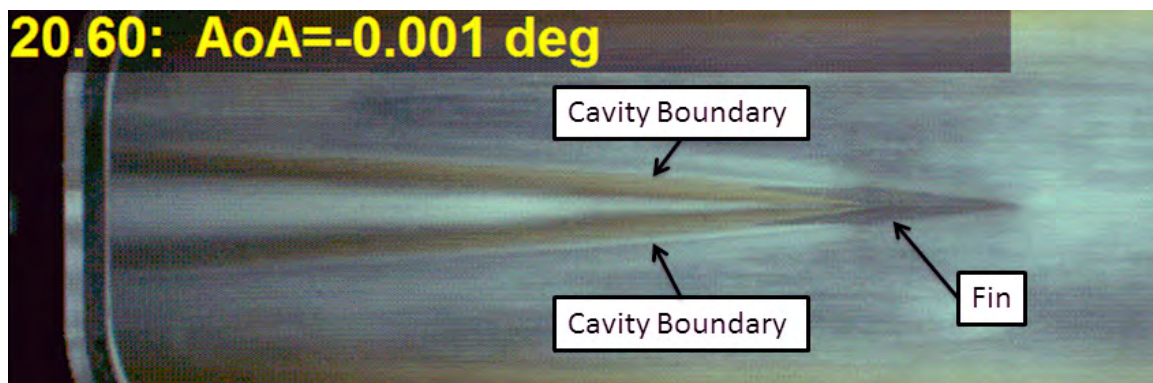


Figure 4.13: Base ventilated swept supercavitating fin, view from the bottom of the tunnel, 2 inch chord, $\alpha = 0^\circ$, $\gamma = 30^\circ$

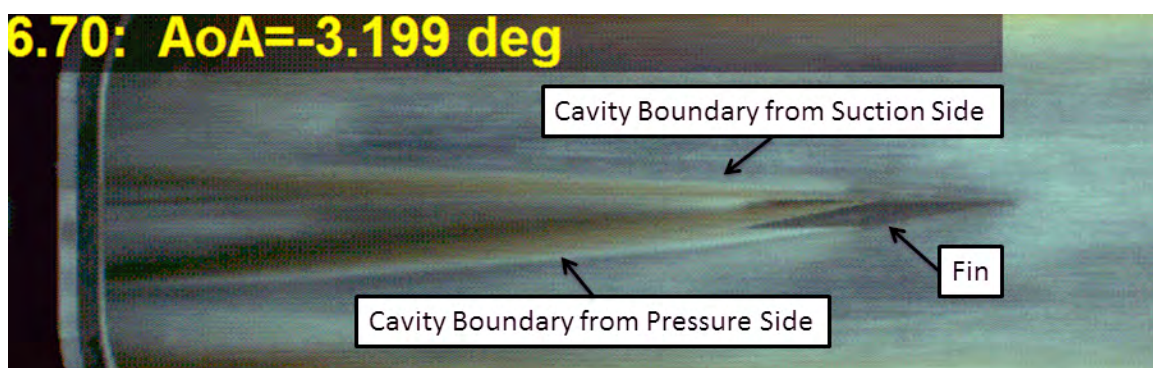


Figure 4.14: Base ventilated swept supercavitating fin, view from the bottom of the tunnel, 2 inch chord, $\alpha = 3^\circ$, $\gamma = 30^\circ$

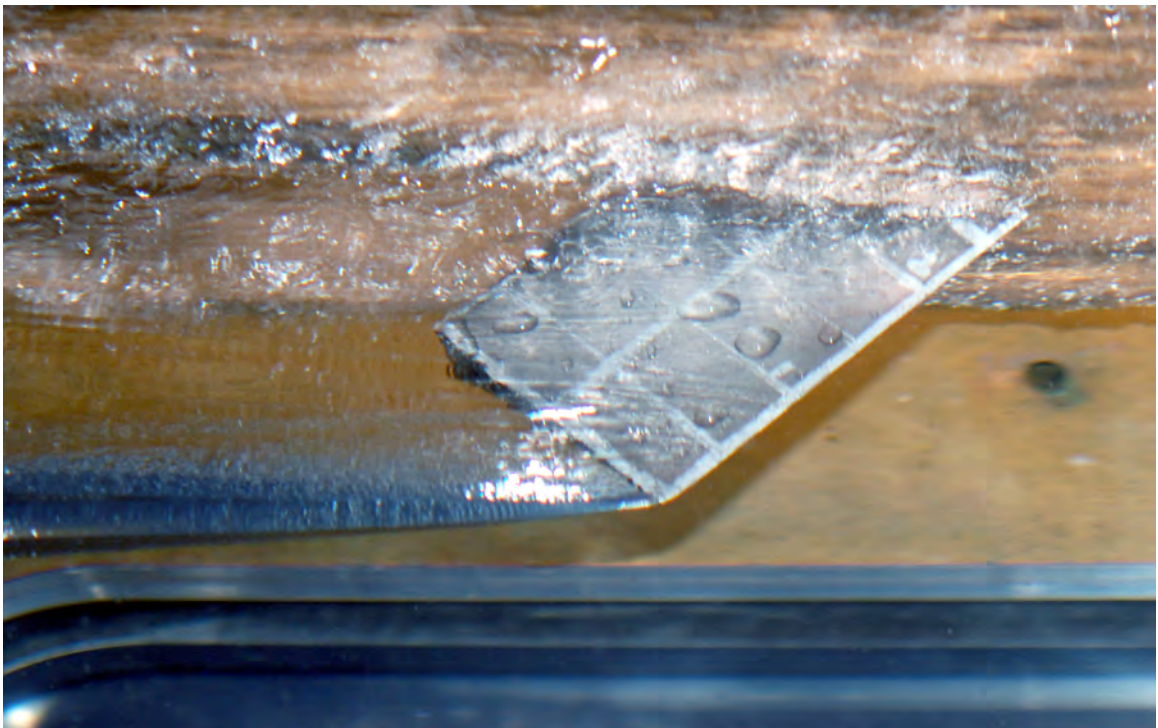


Figure 4.15: Fully ventilated swept supercavitating fin, view from the suction side, 2 inch chord, $\alpha = 15^\circ$, $\gamma = 45^\circ$, $V = 25 ft/s$, photo taken with 1/200 second exposure time

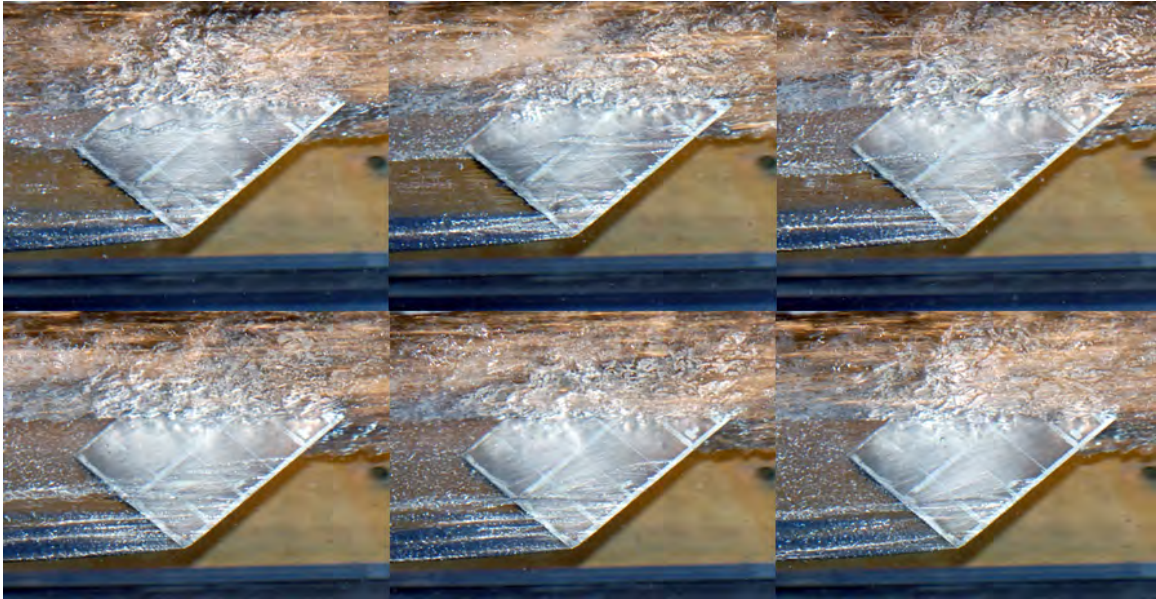


Figure 4.16: Ventilating partial cavities on the 2 inch fin swept to 45° , $V = 25 \text{ ft/s}$, at angles of attack, from left to right for the top and bottom rows, of 5.5, 5, 4.5, 4, 3.5, and 3 degrees, respectively. Photo taken with an exposure time of $1/200$ second.

behind the fin's tapered region, which provided the partial cavity with ventilation gas. The cavities were always present during the transition from fully to base ventilated operation. In some cases, they were also formed during the transition from base to fully ventilated operation. A variety of ventilated partial cavities are shown in fig. 4.16.

Vaporous partial cavities were also found during testing. These were typically present for an instant before the fin transitioned from base to fully ventilated. These vaporous cavities were only present near the leading edge of the fin. These cavities were typically not visible in the 30 fps videos taken using the Basler cameras, but could be clearly observed with the 600 fps images.

4.1.3 Thickness of the Ventilating Supercavity

Artificially ventilated supercavities of various sizes were created along the top of the tunnel to vary fin immersion. Four different cavitators were used throughout testing. As discussed

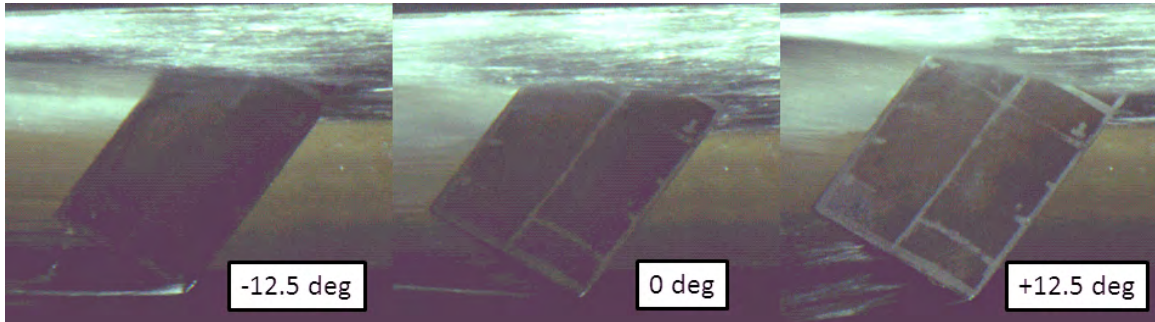


Figure 4.17: Deformation of the ventilated cavity boundary on the suction side (left), pressure side (right) for a swept fin at $\pm 12.5^\circ$, compared to the fin at zero degrees (center), 2 inch fin, $V = 25 \text{ ft/s}$, $\gamma = 30^\circ$

in chapter 2, two curved cavitators were fitted to the tunnel wall upstream of the fin to create cavities for the unswept fin tests. Two smaller flat cavitators were fitted to the base of the swept fin apparatus to create smaller cavities during the swept fin tests.

Cavity thickness was measured at the leading and trailing edges of the fins for each run to estimate the fin's planform area. This thickness was measured from the fin base, vertically down to the cavity boundary. For a particular cavitator, the planform area was found to vary as a function of the angle of attack. Increasing angle of attack resulted in a small decrease in cavity thickness near the leading edge, and a larger decrease at the trailing edge. This deformation occurred on both the pressure and suction sides of the fin, though the changes on the pressure side was typically more dramatic. Typical cavity deformations are shown in fig. 4.17.

The variation of planform area with angle of attack was found to be relatively insensitive to tunnel velocity. These are tabulated in table 4.3. Typically, cavity thickness for a particular cavitator will increase with velocity. The fact that this is not seen here is likely an effect of the solid tunnel walls. The variation of planform with angle of attack and velocity is plotted in fig. 4.18. The planform was measured from the suction side. This was done because the videos and photos acquired during steady state testing were all taken from the suction side to observe if the fin was base or fully ventilated.

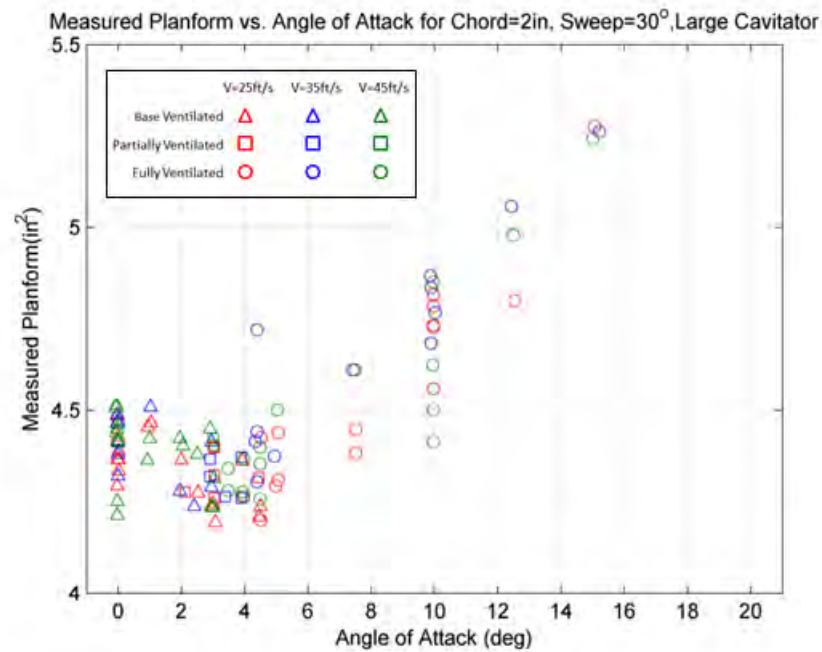


Figure 4.18: Fin planform area, measured from the suction side of the fin, as a function of angle of attack and tunnel velocity, 2 inch chord, $\gamma = 30^\circ$, large cavitator

Downstream of the fin, the cavity along the top of the tunnel was also found to change fairly dramatically as the fin's angle of attack was varied. When the fin's centerline was aligned with the incoming flow, the cavity was symmetric about the fin and closed a long ways downstream, as was shown in fig. 4.13. At higher angles of attack, the ventilated cavity along the top of the tunnel became asymmetric downstream of the fin. The cavity closure point behind the pressure side of the fin was found to move forward with increasing angle of attack. In some extreme cases, the cavity actually closed upstream of the fin. The severity of this asymmetry was found to increase with chord length for a given non-zero angle of attack. These deformations are a result of the influence of the fin on the local pressure distribution. Typical deformations are shown in fig. 4.19.

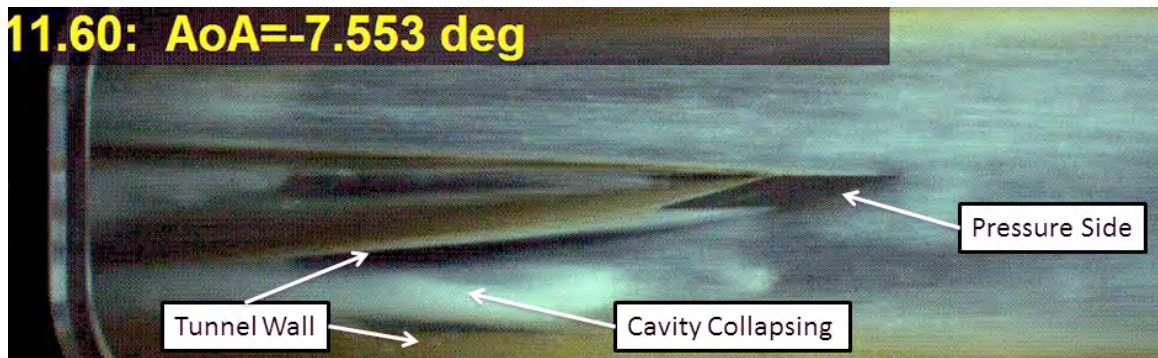


Figure 4.19: Deformation of the cavity along the top of the tunnel downstream of the fin. The cavity appears to be collapsing on the pressure side. 2 inch fin, small cavitator, $\alpha = 7.5^\circ$, $V = 35\text{ft/s}$, $\gamma = 30^\circ$

4.1.4 Gas Entrainment and the Reentrant Jet

The trailing cavity typically closed far downstream of the fin. At the cavity closure point, the gas in the ventilated trailing cavity was expelled into the free stream. Cavity closure could not be observed for all test conditions, as it was found to occur downstream of the test section at higher velocities. Where observations could be made, the primary mode of cavity closure and air evacuation was found to be a result of the formation of a reentrant jet at the end of the cavity. This reentrant jet typically shot forward and slapped against the walls of the trailing cavity, turning them a milky white color. In most cases, the reentrant jet was blown far enough downstream that it dissipated before reaching the fin. At relatively high angles of attack, the reentrant jet was occasionally found to shoot forward and lap against the rear of the fin. Auslaender (1962) referred to this condition as buffeting.

Typically, increasing the flow rate into the cavity generated along the top of the tunnel resulted in a reduction in cavitation number. This caused the trailing cavity to grow in length, which moved the reentrant jet further downstream. This reduced the likelihood of it striking the fin.

When the reentrant jet struck the rear of the fin, small spikes could typically be

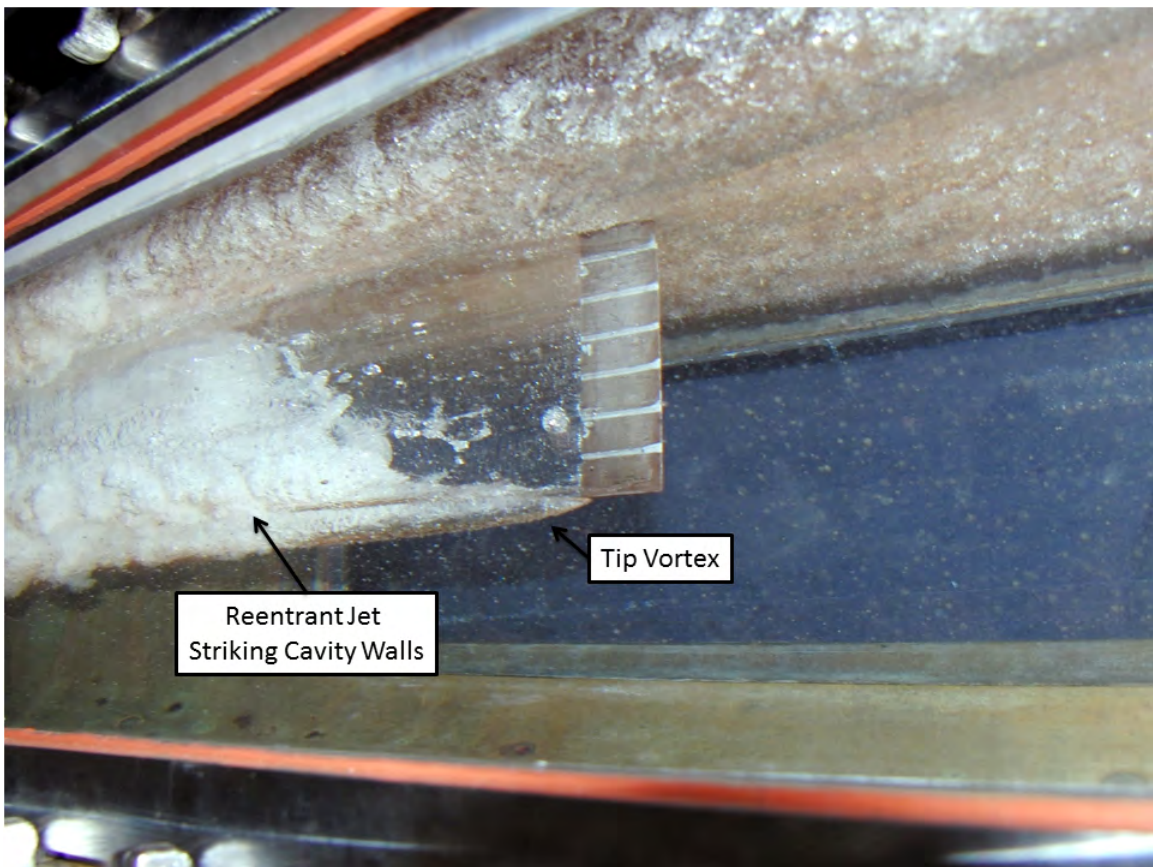


Figure 4.20: Reentrant jet striking cavity walls downstream of an unswept cavity piercing fin. 1 inch chord, $V=35\text{ft/s}$, $\alpha = 5^\circ$

detected in the measured forces and moments. The frequency and magnitude of these effects were found to be directly related to the severity of the reentrant jet activity.

Reentrant jet effects were found to be most severe for the swept fins during base ventilated operation. Here, the reentrant jet was commonly found to strike the rear of the tapered section near the fin tip. In many cases, this choked the cavity near the tip, which caused a partial collapse of the trailing cavity. A typical reentrant jet strike on a swept fin is shown in fig. 4.21.

4.2 Steady State Testing

Measurements were made with the fins held at fixed angles of attack at stable tunnel conditions. The purpose of these experiments was to investigate the sensitivity of the forces and moments on the fin to variations in tunnel velocity, fin chord, cavity immersion, angle of attack, and sweep. The experimental data was reduced, as described in chapter 3. Plots of the data as functions of angle of attack and tunnel velocity are presented in Appendix D.

4.2.1 Fin Force and Moment Measurements

Figures 4.22 and 4.23 show typical experimental data from the steady state unswept fin testing, performed during the summer of 2011. These plots show lift and drag as a function of angle of attack and tunnel velocity for the 2 inch chord fin piercing a 1.75 inch cavity. Here, the lift is plotted as a piecewise function, showing a significant difference in the forces produced when the fin is base and fully ventilated.

When the fin is base ventilated, both the pressure and suction sides remain wetted, and lift is generated in a manner similar to a traditional hydrofoil section (Pearce, 2011). If this is the case, the pressure distribution along the pressure and suction sides should take on a form similar to what is shown in fig. 4.24. The main difference between the pressure

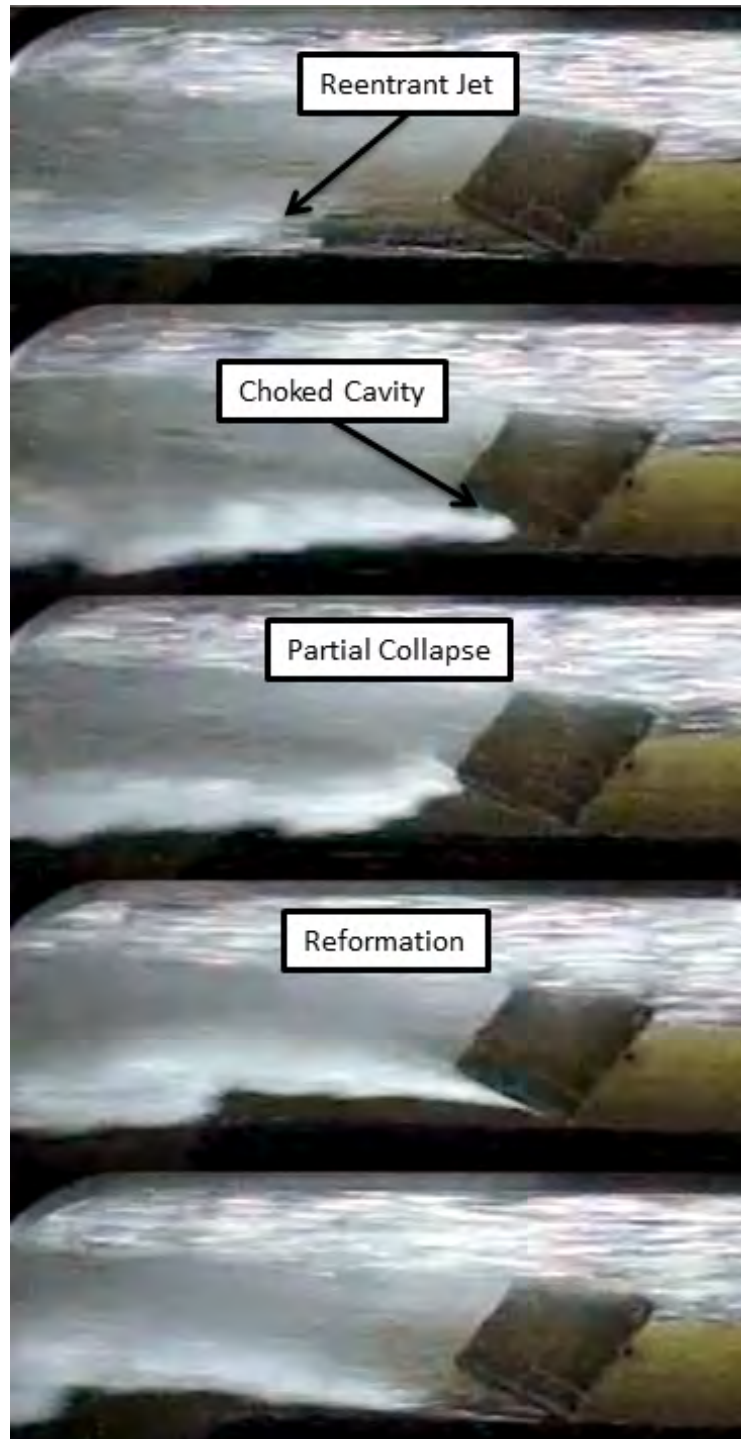


Figure 4.21: Sequence showing the reentrant jet striking the rear of a swept fin and inducing a partial cavity collapse. Images taken from high-speed video shot at 600 fps. Cavity collapse and reformation took a little less than one second. 2 inch fin, $V=35\text{ft/s}$, fin being rotated about its axis.

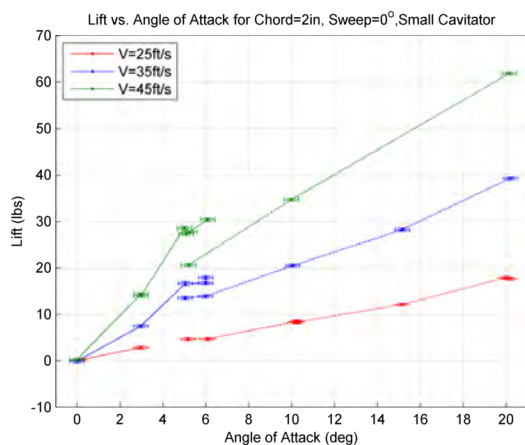


Figure 4.22: Typical steady state experimental data showing lift as a function of angle of attack and tunnel velocity.

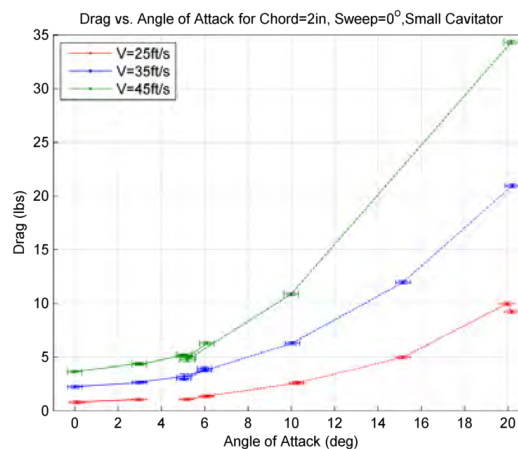


Figure 4.23: Typical steady state experimental data showing drag as a function of angle of attack and tunnel velocity.

distributions of a fully wetted airfoil and a base ventilated fin is the condition at the trailing edge. Here, the pressure along the rear of the fin will be equal to the cavity pressure.

At higher angles of attack, the suction side will typically ventilate, and the fin will act as a fully cavitating flat plate angled to the incoming flow. In this configuration, the pressure distribution along the pressure side will be similar to fig. 4.25. Since the suction side is engulfed in the trailing cavity, the pressure along the fin's surface will be equal to the pressure in the cavity. As a result, the pressure coefficient, eq. (1.2) along the entire suction side will be equal to $-\sigma_c$, which was found to range between 0.1-0.2 during testing, as shown in table 4.2. Recalling the relationship between the pressure distribution along the fin and the resultant force, eq. (1.13), it follows that the resultant force produced by a fully ventilated supercavitating fin will be less than the base ventilated condition at a given angle of attack.

Lift Force

For all conditions tested, lift appeared as a piecewise function with respect to angle of attack. The slope of the lift curve for the base ventilated condition was found to be steeper

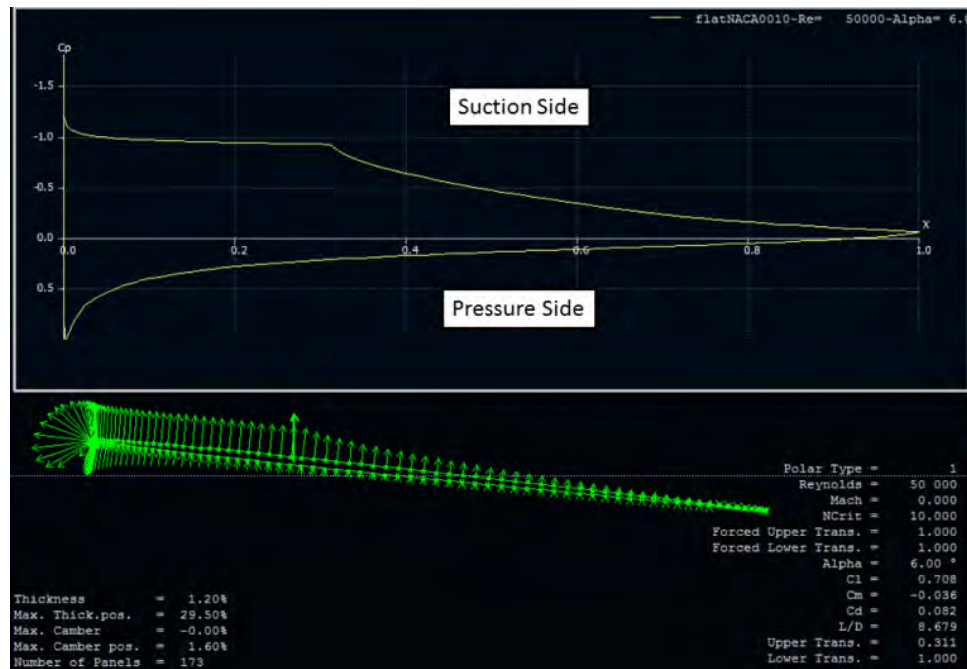


Figure 4.24: Typical pressure distribution along the pressure and suction sides of a thin, traditional airfoil at non-zero incidence. Pressure distribution approximated using XFOil

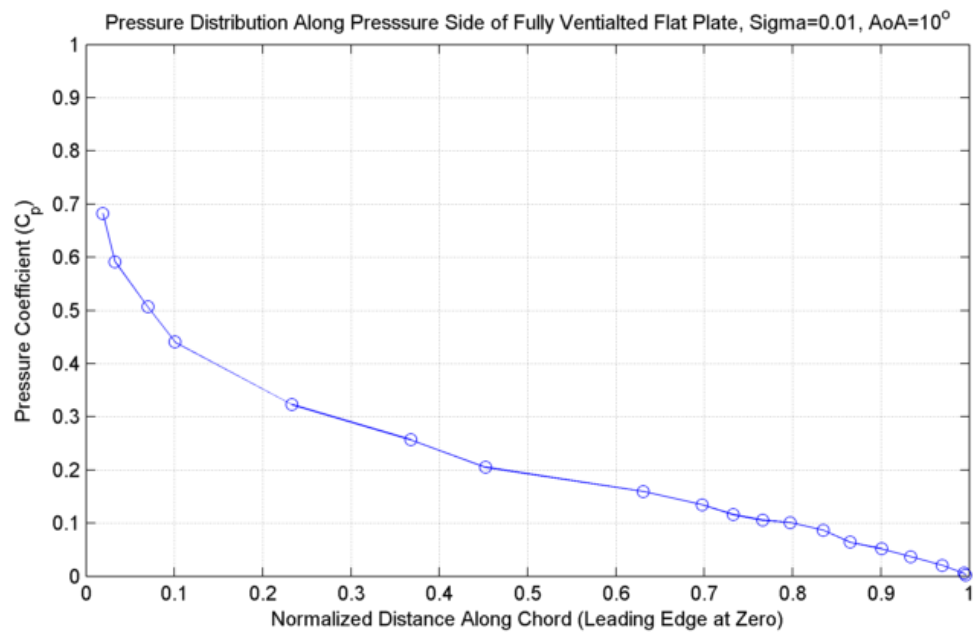


Figure 4.25: Pressure distribution along pressure side of the fin for a fully ventilated flat plate inclined to 10 degrees. Experimental data replotted from (Meijer, 1965).

Table 4.2: Measured cavitation number from the swept fin tests, based on cavity pressure. Most of the cavity pressure measurements from the unswept fin tests were no good, which is why they were omitted from the table

Chord (in)	Cavitator	Sweep (deg)	$V = 25\text{ft/s}$	$V = 35\text{ft/s}$	$V = 45\text{ft/s}$
Chord	Cavitator	Sweepback	25	35	45
1	f1	30	0.18	0.15	0.14
2	f1	30	0.2	0.15	0.13
2	f2	30	0.21	0.19	0.17
1	f1	45	no data	no data	0.15
2	f1	45	0.18	0.17	0.16
2	f2	45	0.19	0.19	0.18

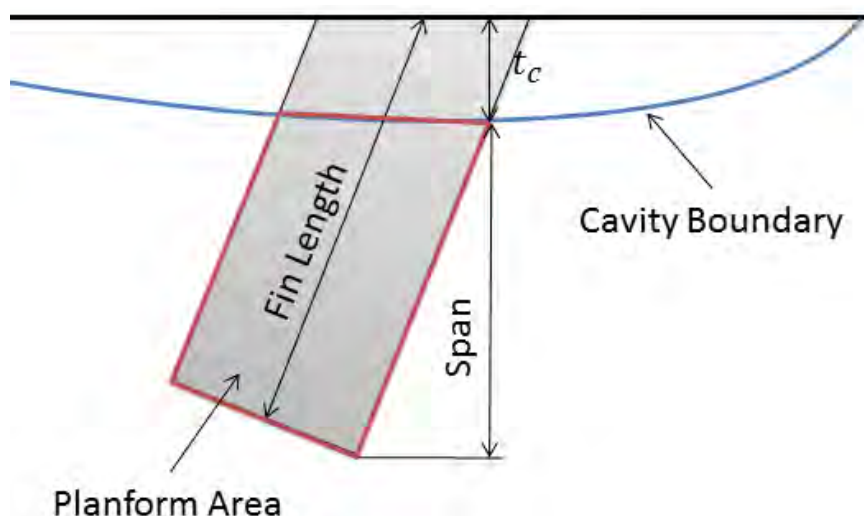


Figure 4.26: Diagram showing reference area used for force and moment coefficients, outlined in red

than the slope for the fully ventilated condition.

Lift coefficients were calculated for all conditions using eq. (1.14). The reference area was taken as the area of the fin above a line drawn tangent to the flow from where the fin intersected the cavity boundary at the leading edge, as shown in fig. 4.26. These are tabulated in table 4.4 for all conditions tested. Typical plots of lift coefficient as a function of angle of attack and Froude number are shown in figs. 4.27 and 4.28 for two unswept fin/cavitator combinations. Additional plots can be found in Appendix D.

Table 4.3: Measured cavity thickness, in inches at the fin's leading edge at zero angle of attack for all combinations of chord, cavitator, sweepback angle, and tunnel velocity tested. Cavitators c1 and c2 are the small and large curved cavitators used during the unswept testing, and f1 and f2 are the small and large flat cavitators used during the swept fin testing, respectively

Chord (in)	Cavitator	Sweep (deg)	$V = 25 ft/s$	$V = 35 ft/s$	$V = 45 ft/s$
1	c1	0	1.75	1.74	1.76
2	c1	0	1.85	1.73	1.79
3	c1	0	1.85	no data	no data
1	c2	0	2.84	2.72	2.67
2	c1	0	2.96	3.15	2.78
3	c2	0	2.61	no data	no data
1	f1	30	1.47	1.42	1.46
2	f1	30	1.45	1.39	1.38
2	f2	30	1.75	1.74	1.7
1	f1	45	no data	no data	1.41
2	f1	45	1.32	1.4	1.36
2	f2	45	1.77	1.65	1.72

Table 4.4: Reference area used to calculate force and moment coefficients, in square inches. Reference area is the area of the fin above a line drawn tangent to the flow from where the fin intersects the cavity boundary at the leading edge. Cavitators c1 and c2 are the small and large curved cavitators used during the unswept testing, and f1 and f2 are the small and large flat cavitators used during the swept fin testing, respectively.

Chord (in)	Cavitator	Sweep (deg)	$V = 25 ft/s$	$V = 35 ft/s$	$V = 45 ft/s$
1	c1	0	4.25	4.26	4.24
2	c1	0	8.30	8.54	8.42
3	c1	0	12.45	no data	no data
1	c2	0	3.16	3.28	3.34
2	c1	0	6.38	6.07	6.38
3	c2	0	10.17	no data	no data
1	f1	30	2.30	2.36	2.31
2	f1	30	4.65	4.79	4.81
2	f2	30	3.93	3.98	4.09
1	f1	45	no data	no data	2.01
2	f1	45	4.26	4.03	4.16
2	f2	45	3.00	3.34	3.14

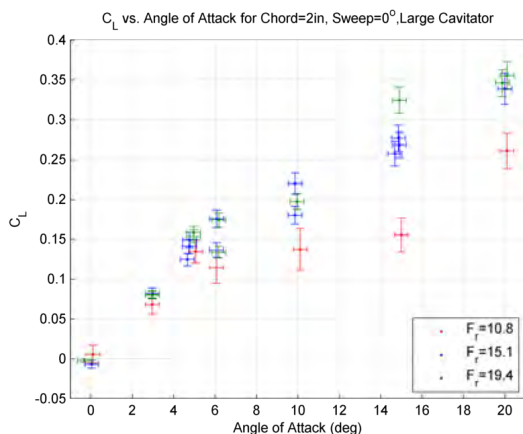


Figure 4.27: Lift coefficient vs. Angle of Attack and Froude Number, 2 inch chord, $\gamma = 0^\circ$, large cavitator

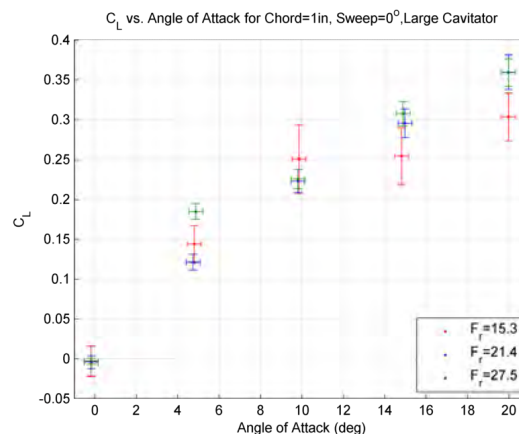


Figure 4.28: Lift coefficient vs. Angle of Attack and Froude Number, 1 inch chord, $\gamma = 0^\circ$, large cavitator

These figures show the sensitivity of lift coefficient to Froude number for the unswept fins. Figure 4.27 shows there is a relationship between Froude number and lift coefficient, which appears to decrease with increasing Froude number. At Froude numbers above about 15, the lift coefficients were typically found to collapse, within the experimental error. This behavior is in agreement with the works of Breslin and Skalak (1959) and Ransleben Jr. (1969), where Froude number effects were reported for surface piercing struts. For surface piercing struts, the Froude number effects were typically reported for $F_r \lesssim 8$, though this critical Froude number was found to vary with aspect ratio and cross section.

No Froude dependence was found in the measured lift coefficients from the swept fin tests. Instead, the measured lift coefficients all appeared to collapse for each combination of fin chord, sweep angle, and cavitator. Examples of this are presented in figs. 4.29 and 4.30. At first glance this seems surprising, as these fins were all tested at Froude numbers less than those of the unswept fin testing. This observation seems to imply that Froude number effects are also related to planform shape. This conclusion is supported by the findings of Ransleben Jr. (1969), who measured the variation in loading along a surface piercing strut, and found that variations in Froude number mostly affected the forces measured near the

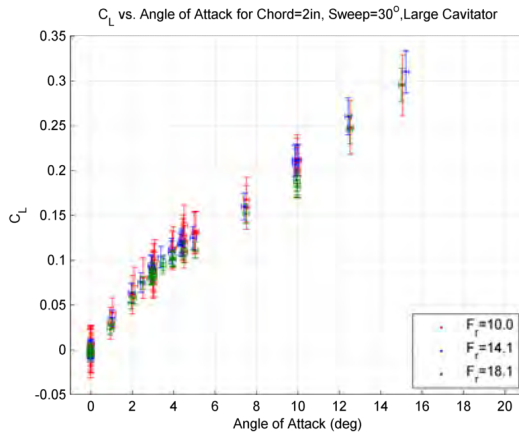


Figure 4.29: Lift coefficient vs. Angle of Attack and Froude Number, 2 inch chord, $\gamma = 30^\circ$, large cavitator

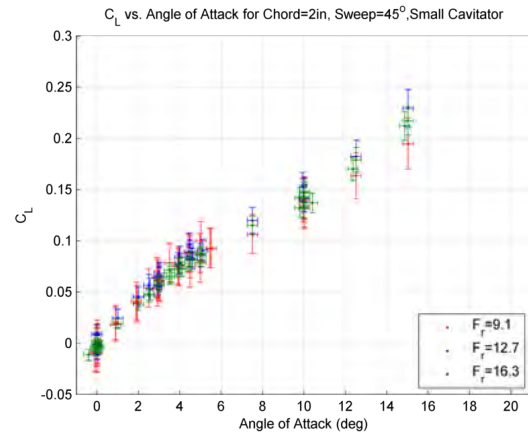


Figure 4.30: Lift coefficient vs. Angle of Attack and Froude Number, 2 inch chord, $\gamma = 45^\circ$, small cavitator

fin tip. The swept fins tested here had planforms that tapered to a point at the fin tip. This taper resulted in an unloading of the lift generated near the tip. Since variations in Froude number were found to predominantly affect the section lift near the tip, it seems reasonable to conclude that Froude number effects were not found for the swept fins because their pointed tips generated a very small portion of the total lift.

The sensitivity of lift coefficient to aspect ratio was studied by plotting lift coefficients as functions of angle of attack and aspect ratio for each sweep angle. The test data used for this analysis was from the 35 and 45 ft/s runs, where the force coefficients were consistently found to collapse. These results are shown in figs. 4.31, 4.32 and 4.33. Here, the aspect ratio was calculated as:

$$\Lambda = \frac{S^2}{A_o} \quad (4.3)$$

where S and A_o are the span and planform area at zero angle of attack, respectively. Span was calculated as the vertical distance between the cavity boundary and the fin tip, as shown in fig. 4.26. Aspect ratios for the conditions tested are listed in table 4.5.

Decreasing aspect ratio typically makes fins less efficient, resulting in a decrease in

Table 4.5: Aspect ratios for each chord, sweep, cavitator combination tested

Chord (in)	Cavitator	Λ for $\gamma = 0^\circ$	Λ for $\gamma = 30^\circ$	Λ for $\gamma = 45^\circ$
1	Small	4.24	1.84	1.15
1	Large	3.34	no data	no data
2	Small	2.11	0.93	0.68
2	Large	1.60	0.80	0.57
3	Small	1.38	no data	no data
3	Large	1.13	no data	no data

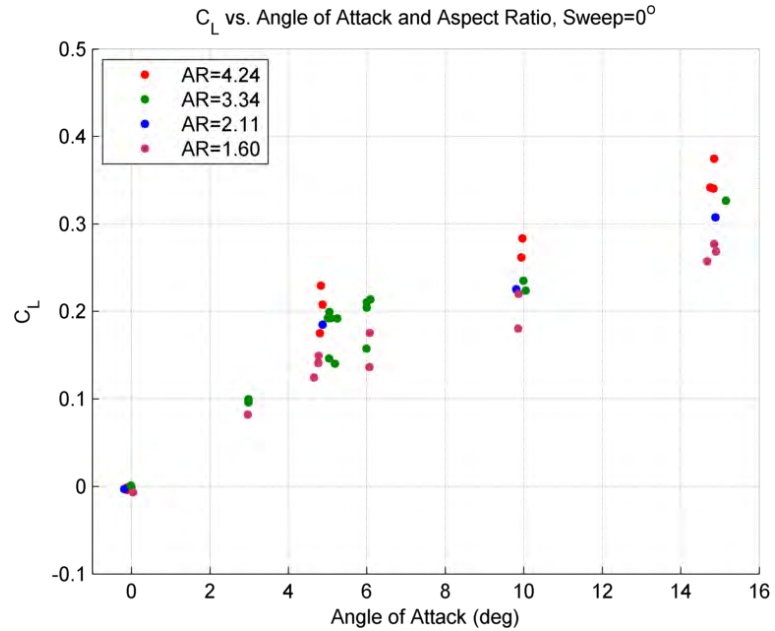


Figure 4.31: Lift coefficient plotted against angle of attack and aspect ratio for the unswept fins.

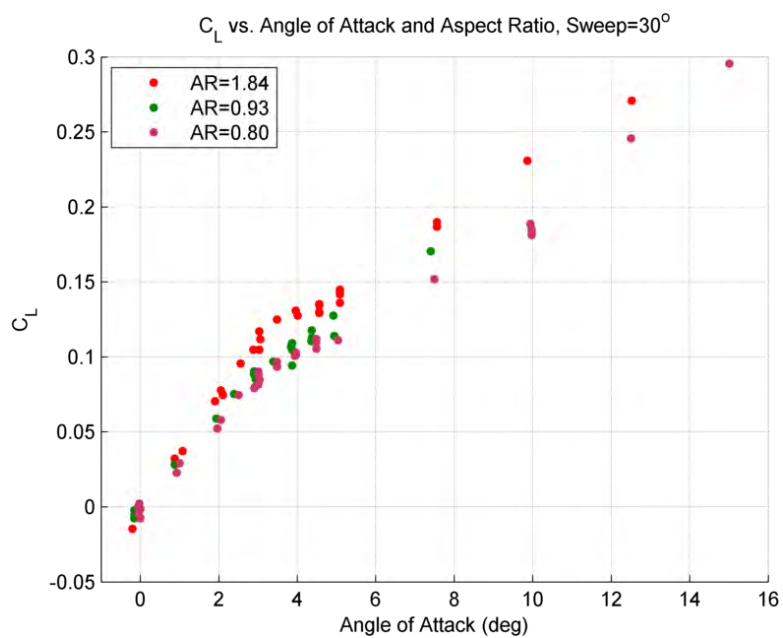


Figure 4.32: Lift coefficient plotted against angle of attack and aspect ratio for fins swept to 30°.

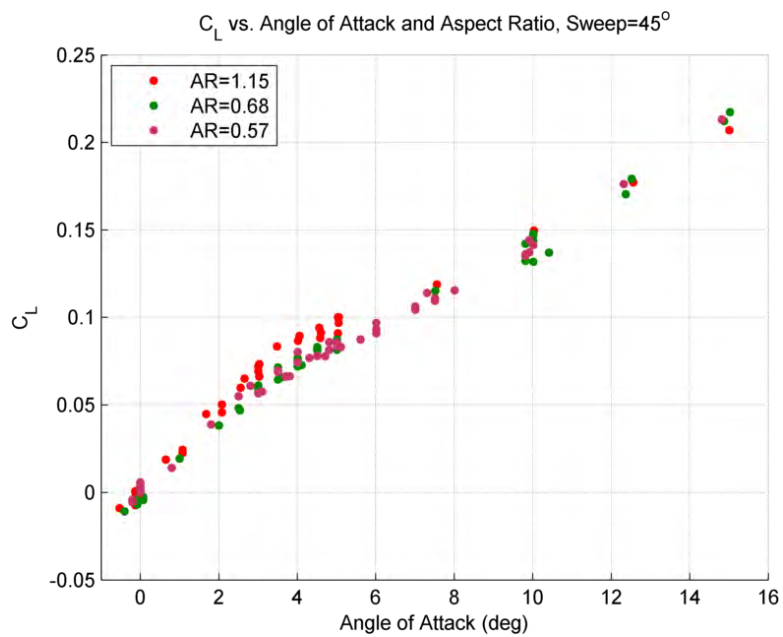


Figure 4.33: Lift coefficient plotted against angle of attack and aspect ratio for fins swept to 45°.

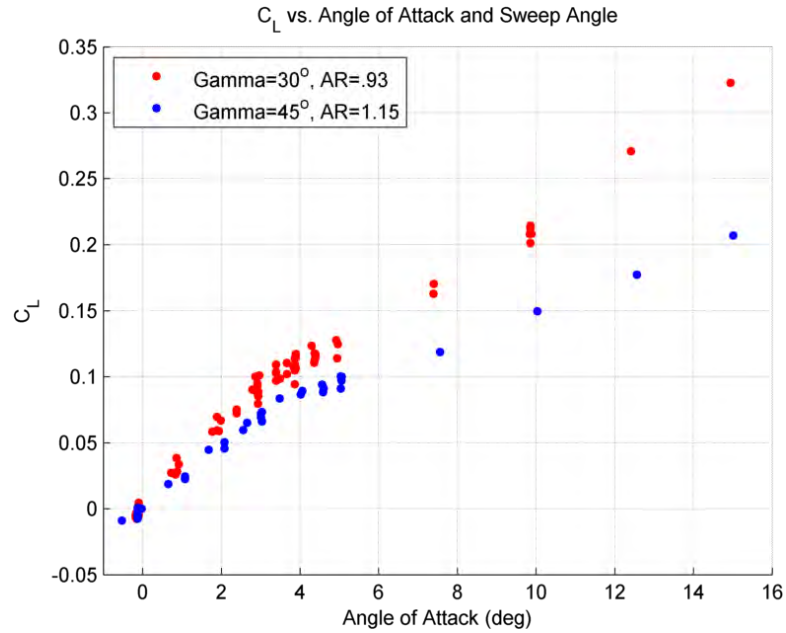


Figure 4.34: Lift coefficient plotted against angle of attack and sweep, comparing $\gamma = 30^\circ$ and 45° for $\Lambda \approx 1$.

the lift curve slope, $a_{3d} = \partial C_L / \partial \alpha$. For moderate and large aspect ratios, these effects can be approximated using Prandtl's lifting line theory (Anderson, 1999). For a particular two-dimensional section, producing a two-dimensional lift curve slope, a_o , the lift coefficient produced by a finite aspect ratio fin at an angle of attack α can be estimated as:

$$C_L = a_{3d} * \alpha = \frac{a_o * \alpha}{1 + a_o / (\pi e_1 \Lambda)} \quad (4.4)$$

where e_1 is a correction for planform geometry, which is typically on the order of 0.9 – 1.0.

As expected from eq. (4.4), decreasing aspect ratio results in a reduction of the measured lift coefficients. The effects of varying aspect ratio are most noticeable in figs. 4.31 and 4.32 because they show data for a wider range of aspect ratios than fig. 4.33.

Sensitivity to the variation of sweep was also considered. To investigate this, the test data was replotted against angle of attack and sweepback angle for similar aspect ratios. The results are shown in figs. 4.34, 4.35 and 4.36.

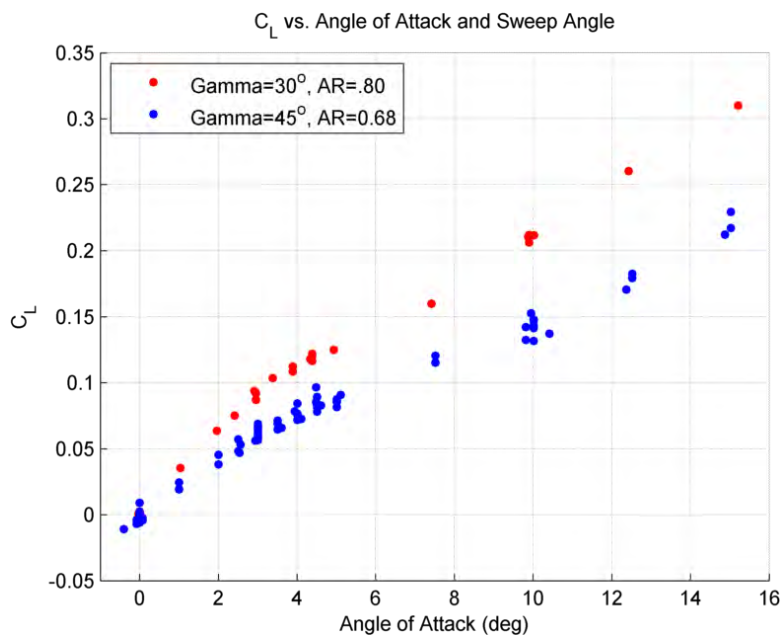


Figure 4.35: Lift coefficient plotted against angle of attack and sweep, $\gamma = 30^\circ$ and 45° for $\Lambda \approx 0.75$.

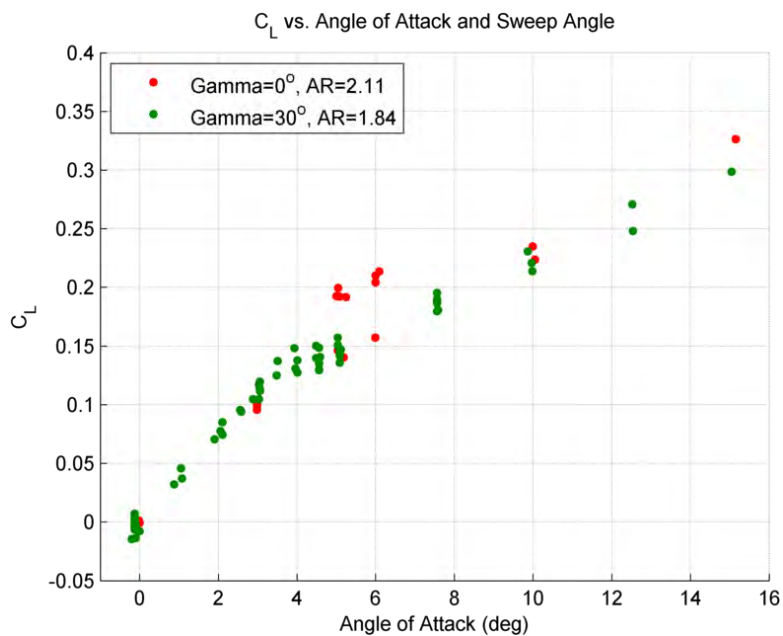


Figure 4.36: Lift coefficient plotted against angle of attack and sweep $\gamma = 0^\circ$ and 30° for $\Lambda \approx 2$. The six points at angles of attack of 5 and 6 degrees for the unswept fin are significantly higher than the measured values for the swept fin because the transition occurred later for the unswept fin than it did for the swept fin.

As described by Anderson (1999), swept fins typically have lower lift coefficients than unswept fins, if everything else remains the same. As previously discussed, lift is primarily a function of the pressure distribution along the section of the fin, which is related to the velocity over the section. Sweeping a fin results in a decrease in the velocity along the section's chord for a given flow velocity. This decrease in chordwise velocity results in a decrease in section lift. For an infinite span fin with a lift curve slope a_o , the effects of sweep can be accounted for using the following approximation from (Anderson, 1999):

$$a_{so} = a_o \cos(\gamma) \quad (4.5)$$

Sweeping a fin also results in the appearance of flow along the span of the fin. This spanwise flow has little effect on the pressure distribution along the fin, and typically only results in an increase in drag (Anderson, 1999).

Figures 4.34 and 4.35 show the sensitivity of the measured lift coefficient to changes in sweep from 30 to 45 degrees from vertical for aspect ratios of 1 and 0.75, respectively. As shown here, the effect of sweeping back a rectangular cavity piercing fin results in a decrease in lift coefficient.

As discussed in a previous section, sweeping the fin also results in changes in planform shape. Changing fin geometry changes the lift distribution along the fin, affecting the fin's efficiency. Rectangular fins are typically less efficient than tapered fins, which means the fins tested here may actually become more efficient as the fin is swept back from vertical. This observation may help explain the results shown in fig. 4.36, where no variation in lift coefficient was found between the vertical fins and fins swept to 30 degrees. Here, it is thought that the rectangular planform may be so inefficient that the losses encountered through sweeping the fin were canceled out by the gains produced by changing the planform shape. Further analysis is recommended to verify this claim.

Drag

The drag of a fin piercing a free surface can be thought of as the linear combination of a number of components. When the fin is not generating lift, the total drag is the sum of the drag of the two-dimensional profile and the residual drag. For a surface piercing fin, the residual drag accounts for the additional drag encountered due to tip effects, the component due to the formation of waves at the free surface, and the drag resulting from the generation of spray. The presence of a trailing cavity may also have an effect (Morgan, 1969).

The profile drag accounts for the effects of pressure drag and skin friction. Pressure drag is the component of drag resulting from an imbalance in the pressure distribution over the fin. Skin friction is a result of shear stress acting on the surface of the fin, and is primarily a function of Reynolds number, as discussed by Lewis (1988, ch. 5). For turbulent flow, the relation between friction drag and Reynolds number can be approximated as:

$$C_f = \frac{D_f}{1/2\rho V^2 A_s} \approx \frac{0.075}{(\log_{10}(R_n) - 2)^2} \quad (4.6)$$

where C_f is the friction coefficient, D_f is friction drag, and A_s is the wetted area. Additional relations are also presented by Lewis (1988) for estimating friction drag in laminar flow.

The free surface contributions to drag typically vary with Froude number. At Froude numbers less than about 4.3, the formation of waves along the free surface results in a significant increase in drag (Savitsky and Breslin, 1966). At higher Froude numbers, spray is created at the surface, resulting in an additional drag component.

Lift generation also contributes to the total drag. This component, typically referred to as the induced drag, is primarily a result of pressure variation along the span caused by the tip vortex. For moderate to high aspect ratios, the induced drag coefficient can be

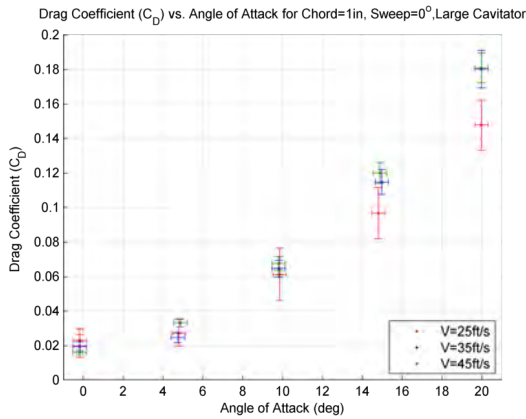


Figure 4.37: Drag coefficient as a function of angle of attack and tunnel velocity, 1 inch chord, $\gamma = 0^\circ$, large cavitator

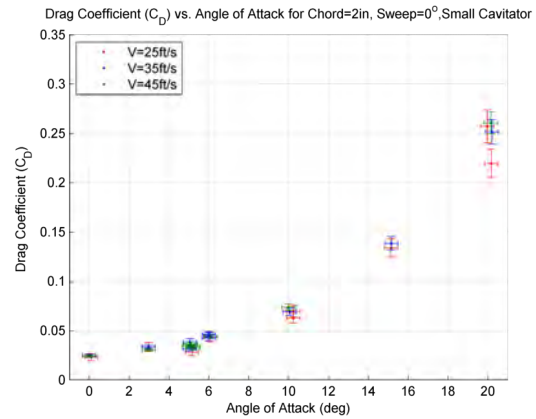


Figure 4.38: Drag coefficient as a function of angle of attack and tunnel velocity, 2 inch chord, $\gamma = 0^\circ$, small cavitator

estimated using Prandtl's lifting line theory as:

$$C_{D_i} = \frac{D_i}{1/2\rho V^2 A} = \frac{C_L^2}{\pi \Lambda e_o} \quad (4.7)$$

where D_i is the induced drag and e_o is the Oswald efficiency factor, which is a function of fin shape. (The Oswald efficiency factor is different from the span correction used in eq. (4.4).)

The measured drag was non-dimensionalized using eq. (1.15). As was the case in calculating lift coefficient, the reference area was taken from table 4.4. Typical plots of drag coefficient as a function of angle of attack and tunnel velocity are shown in figs. 4.37 and 4.38.

The figures show that drag may vary slightly with varying tunnel velocity. Unfortunately, the variation is typically on the order of the measurement error, making it difficult to draw any firm conclusions. The variation with tunnel velocity is likely a result of both Froude and Reynolds number effects.

All tests were performed at Froude numbers much greater than 4, so these variations

with tunnel velocity are most likely not an effect of wave generation along the surface (i.e. the cavity boundary). The variation is also not likely a result of spray generation, as Savitsky and Breslin (1966) found that spray drag was typically independent of Froude and Reynolds number. Thus, this dependence is most likely a result of changes in friction and pressure drag due to variations in Reynolds number, and changes in the induced drag due to the lift coefficient's dependence on Froude number. Additional studies are required to verify the validity of these claims and quantify these effects.

The level of uncertainty in the drag measurements from the swept fin testing made it difficult to draw any significant conclusions from the data. The additional uncertainty in the swept fin measurements was primarily a result of two factors. First, the swept fins had smaller planform areas, which decreased the magnitude of the measured drag, reducing the signal to noise ratio. Second, due to the orientation of the force and moment transducer, the drag became a function of the measured force in the axis along the fin span (F_z). This was not the case for the unswept fin testing, as described in eqs. (3.10) and (3.12). The transducer sensitivity in F_z was almost a quarter of the sensitivity of the other channels, which passed a great deal of noise into the measured drag signal. In future testing, a more sensitive balance should be used. (This was not an option for these experiments, as this was the smallest transducer available that could handle the fully wetted loads experienced before and after gas injection.)

Typical drag measurements are shown in figs. 4.39 and 4.40 in coefficient form as a function of angle of attack and tunnel velocity from the swept fin testing. As was the case with the unswept data, the measured drag coefficients appear to vary with tunnel velocity, though the variations are within the measurement error. Additional studies are required to quantify these effects.

The drag coefficients from the unswept fin tests were replotted as functions of angle of attack and aspect ratio for various combinations of Reynolds and Froude numbers. The

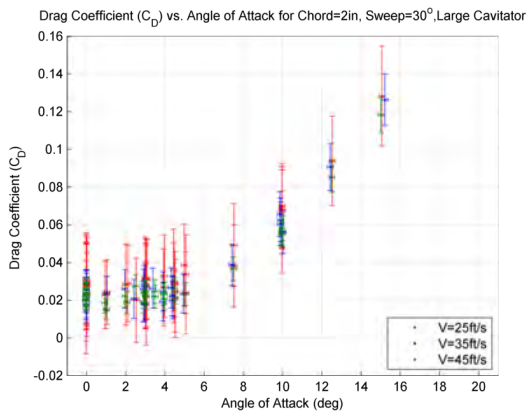


Figure 4.39: Drag coefficient as a function of angle of attack and tunnel velocity, 1 inch chord, $\gamma = 30^\circ$, large cavitator

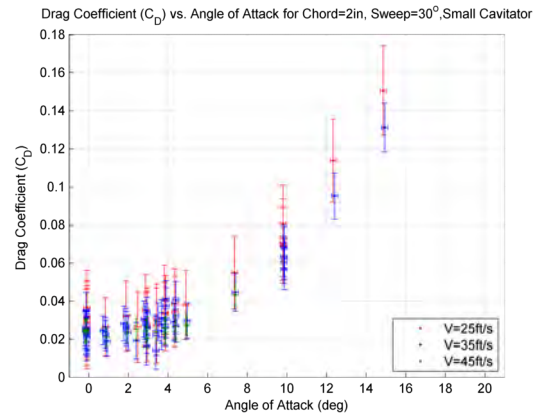


Figure 4.40: Drag coefficient as a function of angle of attack and tunnel velocity, 2 inch chord, $\gamma = 30^\circ$, small cavitator

Table 4.6: Reynolds Numbers for Various Test Conditions

Chord (in)	Sweep (deg)	R_n for V=25ft/s	R_n for V=35ft/s	R_n for V=45ft/s
1	0	2.2E+05	3.1E+05	4.0E+05
2	0	4.5E+05	6.3E+05	8.1E+05
3	0	6.7E+05	no data	no data
1	30	2.6E+05	3.6E+05	4.7E+05
2	30	5.2E+05	7.3E+05	9.4E+05
1	45	no data	no data	5.7E+05
2	45	6.4E+05	8.9E+05	1.1E+06

Table 4.7: Froude Numbers for Various Test Conditions

Chord (in)	Sweep (deg)	F_r for V=25ft/s	F_r for V=35ft/s	F_r for V=45ft/s
1	0	15.3	21.4	27.5
2	0	10.8	15.1	19.4
3	0	8.8	no data	no data
1	30	14.2	19.9	25.6
2	30	10.0	14.1	18.1
1	45	no data	no data	23.1
2	45	9.1	12.7	16.3

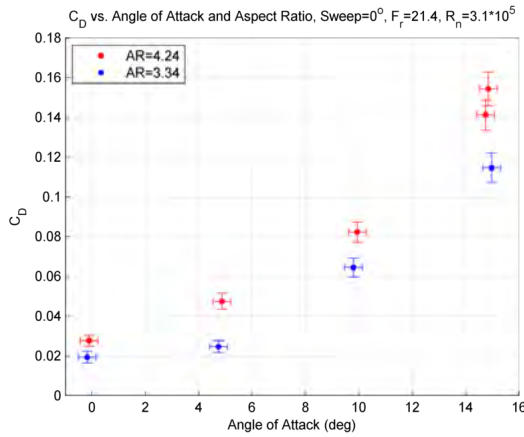


Figure 4.41: Drag coefficient from the unswept fin testing plotted against angle of attack and aspect ratio for $R_n = 3.1 \times 10^5$, $F_r = 21.4$, 1 inch chord, 35ft/s

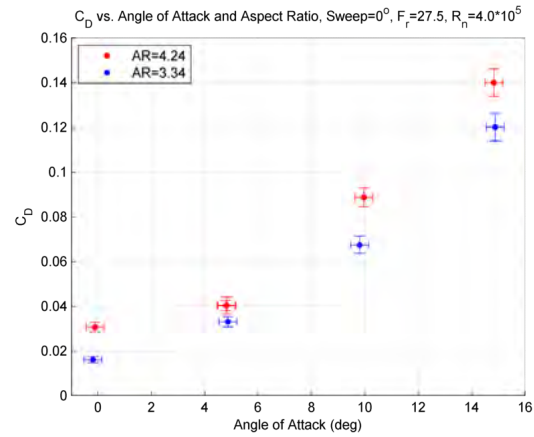


Figure 4.42: Drag coefficient from the unswept fin testing plotted against angle of attack and aspect ratio for $R_n = 4.0 \times 10^5$, $F_r = 27.5$, 1 inch chord, 45ft/s

resulting plots, figs. 4.41 and 4.42, show that reducing aspect ratio decreases the total drag. This trend is in agreement with the findings of Kermeen (1960), who found that decreasing the aspect ratio of a supercavitating fin resulted in a decrease in the measured drag coefficients. Similar trends could not be detected in the swept fin data, though this is likely a result of excessive measurement error.

This decrease in drag with decreasing aspect ratio is partially a result of decreases in the induced drag. At first inspection of eq. (4.7), it seems counterintuitive that reducing the aspect ratio results in a decrease in drag because Λ is in the denominator. However, decreasing aspect ratio also decreases lift for a particular fin, as described in eq. (4.4). It was found here that the changes in lift dominate over the changes in aspect ratio, which results in an overall decrease in measured drag. A portion of this reduction may also be a result of changes in size and shape of the trailing cavity.

The effects of varying sweep are shown in fig. 4.43 for similar conditions. Increasing sweep from 30 to 45 degrees appeared to result in a decrease in the measured drag coefficient. It was assumed that the Froude and Reynolds numbers were close enough not to

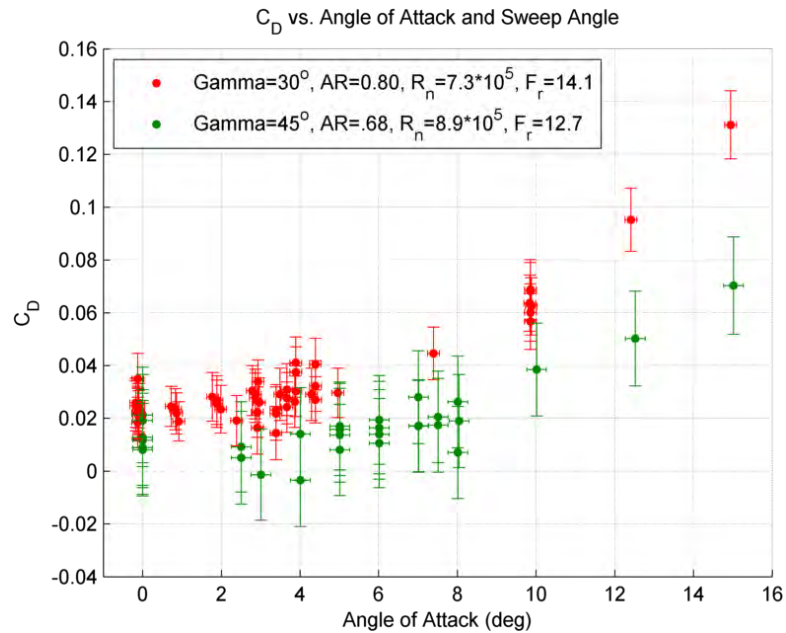


Figure 4.43: Drag coefficient plotted against angle of attack and sweep $\gamma = 30^\circ$ and 45° for $\Lambda \approx .75$. The effects of differences in Reynolds and Froude numbers are assumed to be negligible, though that may not be the case.

have an effect. Further analysis is necessary to verify this assumption. Other comparisons were not practical due to excessive measurement error.

The efficiency of a fin can be quantified using the lift to drag ratio, η . This parameter was calculated for a variety of conditions to study the effects of varying tunnel velocity, aspect ratio, and fin sweep. Unfortunately, the error in the drag measurements propagated through the reduction equation and led to significant variations in η for the swept fin data, especially at low angles of attack.

The lift to drag ratios of some of the measured unswept fin data is shown in figs. 4.44 and 4.45. The most consistent trend in the data is that the fin's efficiency increases with angle of attack during base ventilated operation, and decreases with angle of attack in fully ventilated operation. Figure 4.44 also shows that the lift/drag ratio has some dependence on Froude and/or Reynolds number.

Figures 4.46 and 4.47 show the variation in the lift to drag ratio as a function of

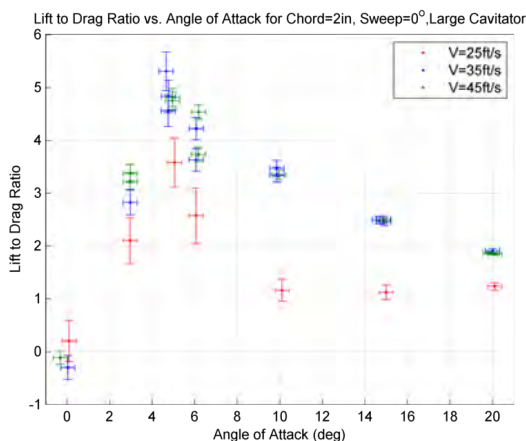


Figure 4.44: Lift/ Drag Ratio from the unswept fin testing plotted against angle of attack and tunnel velocity, 2 inch chord, large cavitator

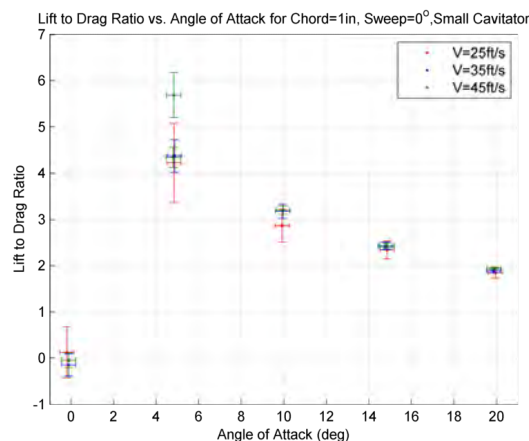


Figure 4.45: Lift/ Drag Ratio from the unswept fin testing plotted against angle of attack and tunnel velocity, 1 inch chord, small cavitator

aspect ratio, using data from the unswept fin tests. As seen in the figures, varying aspect ratios over the ranges tested appear to have very little effect on the lift to drag ratio. Similar trends were seen for the swept fin data, though variability in the data made it difficult to draw firm conclusions. The outlier in fig. 4.47 at 5 degrees for the $\Lambda = 4.24$ condition shows the fin as fully ventilated, while the other points show the fins as base ventilated.

No firm conclusions on the effects of varying sweep could be made, as the differences were found to be within the measurement error.

Shaft Torque and Center of Pressure

The moment about the fin's spanwise axis, which will be referred to as shaft torque, was measured during testing. Typical measurements, non-dimensionalized using eq. (1.16) are shown in figs. 4.48 and 4.49, plotted against angle of attack and tunnel velocity. Over the range tested, the data showed very little dependence on tunnel velocity.

As was the case for the forces, shaft torque was found to change dramatically when the fin transitioned from base to fully ventilated operation. This shift was partially a result

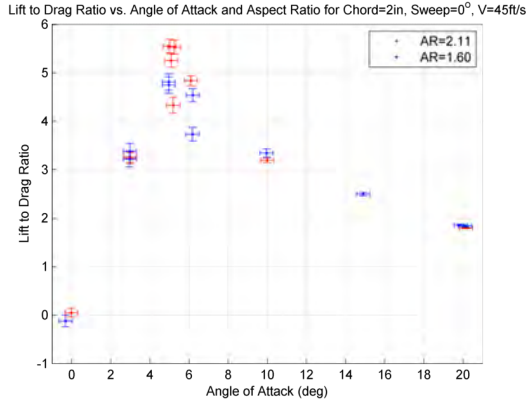


Figure 4.46: Lift/ Drag Ratio from the unswept fin testing plotted against angle of attack and aspect ratio, 2 inch chord, $R_n = 8.1 * 10^5$, $F_r = 19.4$

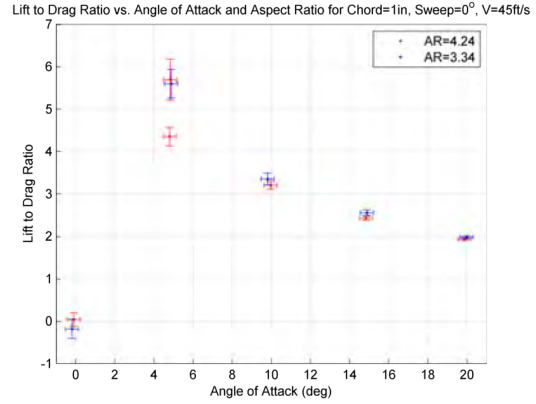


Figure 4.47: Lift/ Drag Ratio from the unswept fin testing plotted against angle of attack and aspect ratio, 1 inch chord, $R_n = 4.0 * 10^5$, $F_r = 27.5$

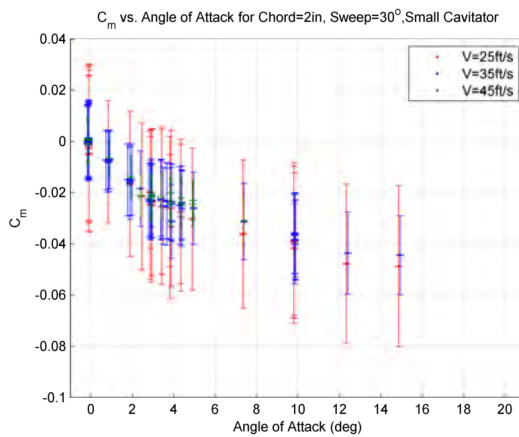


Figure 4.48: Non-dimensionalized shaft torque plotted as a function of angle of attack and tunnel velocity, 2 inch chord, $\gamma = 30^\circ$, small cavitor

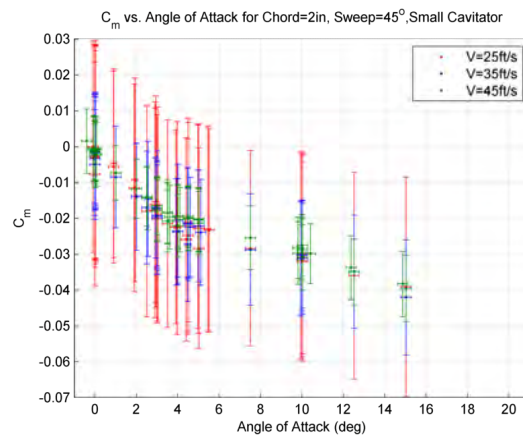


Figure 4.49: Non-dimensionalized shaft torque plotted as a function of angle of attack and tunnel velocity, 2 inch chord, $\gamma = 45^\circ$, small cavitor

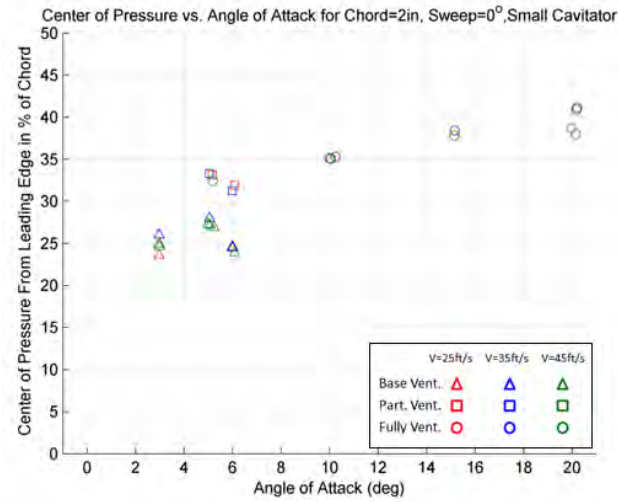


Figure 4.50: Center of pressure, measured from the leading edge as a function of angle of attack and tunnel velocity, 2 inch chord, $\gamma = 30^\circ$, small cavitator, percent of chord

in a drop in the lift generated by the fin, as previously discussed. It was also a result of movement of the center of pressure due to variations in the pressure distribution along the fin section when transition occurred.

To quantify these effects, the center of pressure with respect to the leading edge, was found using the following relation:

$$L_p = \left(c/2 - \frac{M_z}{F_n} \right) / c \quad (4.8)$$

where M_z and F_n are the measured shaft torque and normal force, respectively, and L_p is the center of pressure, non-dimensionalized by chord. Results are shown in fig. 4.50 for the two inch chord unswept fin. This plot shows a general trend, where the center of pressure moves aft when the fin transitions from base to fully ventilated operation. The center of pressure typically appears to be near the quarter chord when the fin is base ventilated, and then shifts aft when the fin ventilated. When the fin operates as fully ventilated, the center of pressure appears to move aft as the angle of attack is increased.

Thin airfoil theory predicts that the center of pressure of a symmetric section will be located one quarter of the way down the chord, which agrees well with the base ventilated measurements. Free streamline theory for a yawed flat plate (Milne-Thomson, 1949) predicts that the center of pressure for a supercavitating flat plate will move aft with increasing angle of attack, from a point roughly one third the way down the chord at 5 degrees, to about a point roughly 38% of the chord at 30 degrees. This trend agrees well with the fully ventilated measurements for the unswept fins. This variation is governed by the following equation:

$$L_p(sc) = \frac{C_m}{C_t} = 1/2 - \frac{3 \cos(\alpha)}{4(4 + \pi \sin(\alpha))} \quad (4.9)$$

The location of the center of pressure for the fully ventilated fin was found to be relatively insensitive to changes in aspect ratio, chord, and tunnel velocity. No significant changes could be found between the unswept fins and the fin swept to 30 degrees. However, sweeping the fin back to 45 degrees was found to result in a noticeable forward shift in the center of pressure, as shown in fig. 4.51. This change is likely a result of the heavily trapezoidal planform.

No firm conclusions could be made for the base ventilated case due to variability in the data. The forces and moments measured in the base ventilated region were typically smaller than the measurements made at higher angles of attack in the fully ventilated region, resulting in unreasonable amounts of variation in the data.

4.2.2 Comparison with Theory

The measured lift and drag coefficients were compared with existing theoretical models. The goal was to check the validity of using simple theoretical models to make engineering approximations of the forces generated by cavity piercing fins. Due to the piecewise nature of the measured forces and moments, the base and fully ventilated regimes were considered

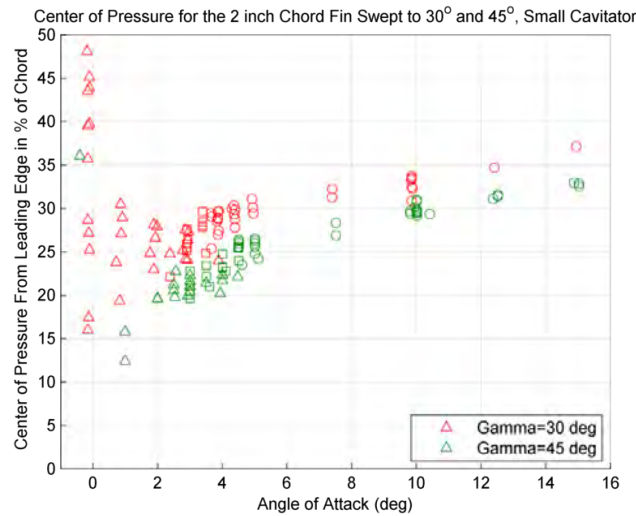


Figure 4.51: Center of pressure, measured from the leading edge as a function of angle of attack and sweepback angle, 2 inch chord, small cavitator, percent of chord. Data presented for fins swept to 30 and 45 degrees.

separately.

The lift coefficients of the base ventilated fin were found by modeling the fin as a traditional airfoil. Verron and Michel (1984) found this to be a valid approximation for base ventilated supercavitating fins of finite span. From thin airfoil theory, the two-dimensional lift curve slope a_o , was approximated as 2π .

The fully ventilated fin was modeled as a fully cavitating flat plate yawed to $\alpha_{fv} = \alpha + \psi$. Here, the linearized theory of Tulin and Burkart (1955) was used to estimate the two-dimensional lift curve slope. For a supercavitating flat plate at zero cavitation number, Tulin and Burkart (1955) suggested that the two-dimensional lift curve slope could be approximated as $\pi/2$.

The aspect ratios of the fins tested ranged from about 0.6 to 4.25, which is outside the range of applicability of Prandtl's lifting line theory, eq. (4.4). Instead, the effects of finite aspect ratio were accounted for using a lifting surface approximation by Helmbold (1942). Anderson (1999) showed that this approximation was valid for aspect ratios from

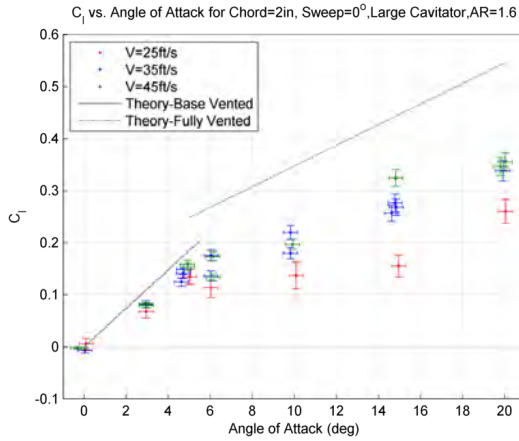


Figure 4.52: Comparison of theory and measured lift coefficients, 2 inch chord, $\gamma = 0^\circ$, large cavitator.

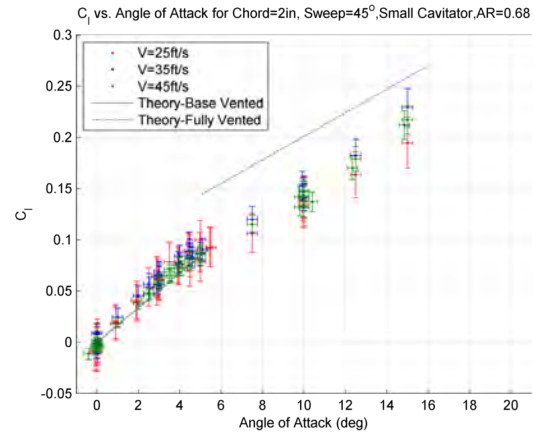


Figure 4.53: Comparison of theory and measured lift coefficients, 2 inch chord, $\gamma = 45^\circ$, small cavitator

0.5 to 6. Thus, the three-dimensional lift curve slope was approximated as:

$$a_{3d} = \frac{a_o}{\sqrt{1 + \left(\frac{a_o}{\pi e_1 \Lambda}\right)^2} + \frac{a_o}{\pi e_1 \Lambda}} \quad (4.10)$$

where e_1 is a correction factor for fin geometry, which is typically on the order of 0.95 for traditional airfoils. The effects of sweep were accounted for by multiplying the two-dimensional lift curve slopes by $\cos(\gamma)$, as recommended by Anderson (1999) for traditional airfoils.

Typical results are shown in figs. 4.52 and 4.53. Additional plots are presented in Appendix D. The figures show reasonable agreement between the approximation and the experimental results for the base ventilated fins. Agreement was typically not as good for the fully ventilated fins. The model was found to overestimate the lift predicted for the fully ventilated fins. This was found to be worst for the unswept fins. It is likely that the simplified model did not accurately capture the flow physics of the fully ventilated fins.

The total drag was assumed to be the sum of the section drag coefficient and the drag induced by lift generation. At low angles of attack, the section drag coefficient was

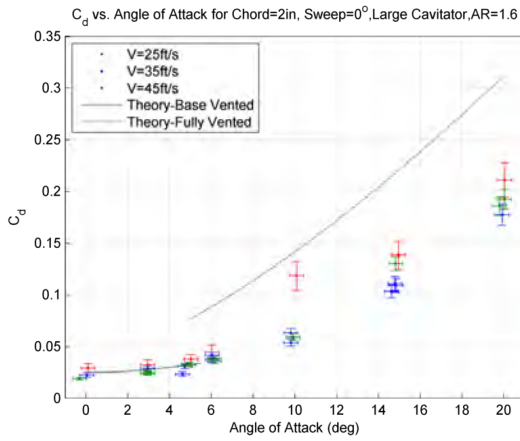


Figure 4.54: Comparison of theory and measured drag coefficients, 2 inch chord, $\gamma = 0^\circ$, large cavitator.

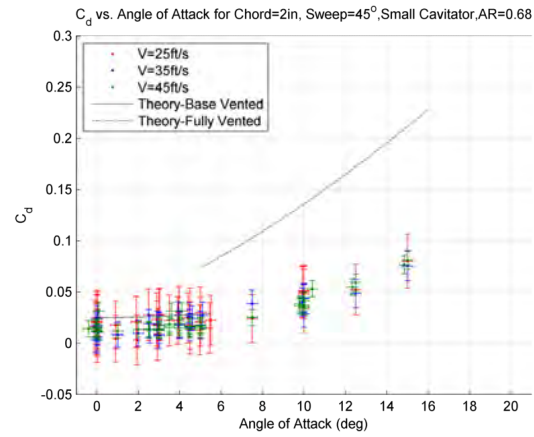


Figure 4.55: Comparison of theory and measured drag coefficients, 2 inch chord, $\gamma = 30^\circ$, small cavitator

assumed to be a constant value taken from Hoerner (1958) for a surface piercing strut. At higher angles of attack, when the fin was fully ventilated, the section drag coefficient was estimated using an approximation presented by Tulin and Burkart (1955), for a fully cavitating flat plate at zero cavitation number. The fully ventilated section drag coefficient was estimated as:

$$C_{D2d} \approx \frac{2\pi \sin^2(\alpha + \Psi)}{4 + \pi \sin(\alpha + \psi)} \quad (4.11)$$

Equation (1.11) presented earlier is actually a linearized approximation of this formulation.

The induced drag was estimated using eq. (4.7). For this model, the Oswald efficiency factor in eq. (4.7) was assumed to be 0.9.

Typical results are shown in figs. 4.54 and 4.55. Fairly good agreement was found between the approximation and the measured results for the base ventilated case. Agreement was found to improve if the section drag coefficient was taken as the measured value at zero angle of attack. The fully ventilated model was found to consistently overestimate drag.

Though traditional airfoil and supercavitating plate theories failed to accurately pre-

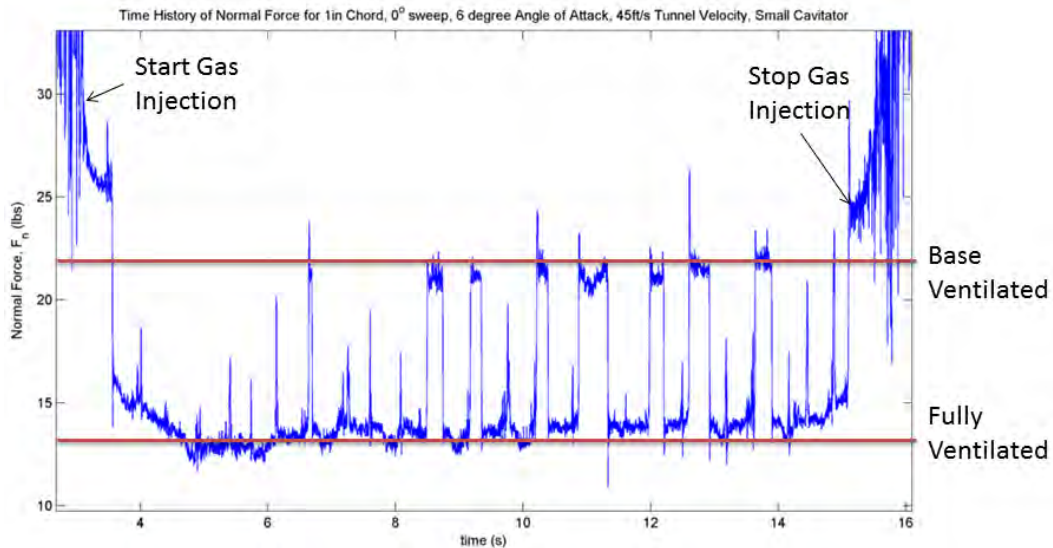


Figure 4.56: Time history of measured normal force from steady state run showing instability in the trailing cavity, 1 inch chord, $\alpha = 6^\circ$, $V=45\text{ft/s}$, Small Cavitator

dict the measured lift and drag coefficients of the fully ventilated fins, they were able to capture the trends in the data fairly well. The estimated lift and drag coefficients were found to differ from the measured values by a fairly consistent amount over the range of conditions tested. Further studies are recommended to develop a more complete prediction method that models the physics more accurately.

4.2.3 Cavity Instability

An interesting instability was found during some of the steady state fin testing, where the fin would transition between base and fully ventilated operation sporadically, while the fin was held at a fixed angle of attack. This was found to occur only for the unswept fins at angles of attack near, but less than the wedge half-angle. Each transition resulted in a dramatic shift in the measured forces and moments.

A typical time history of the measured normal force from the one-inch chord fin experiencing this instability at an angle of attack of six degrees is plotted in fig. 4.56.

As shown in the figure, a trailing cavity formed once gas injection began, resulting in a noticeable drop in the measured normal force. During formation, the fin was initially base ventilated. After a moment, the fin transitioned to fully ventilated. Small spikes began to appear about a second after the initial transition. These spikes were a result of the reentrant jet from the rear of the cavity shooting forward and lapping on the rear of the fin. After a few seconds, part of the reentrant jet moved even further forward and struck the cavity boundary over the suction side of the fin. Some of the strikes appeared to be so powerful, that they choked the cavity over the suction side and forced the fin to transition to base ventilated. While the fin was base ventilated, vaporous partial cavities could typically be observed near the leading edge of the fin on the suction side. After being base ventilated for a brief period of time, gas was pulled down into the low pressure region on the suction side, which forced the fin to transition back to fully ventilated operation. Each time the fin transitioned from fully ventilated to base ventilated, the measured normal force was seen to spike from about 14lbs to 23lbs. A sequences of photos showing this process is presented in fig. 4.57.

This instability was only found for the unswept fins tested at velocities of 35 and 45ft/s. It was seen almost every time the one-inch chord fin was held at an angle of attack of five and six degrees. For the two-inch chord fin, the instability was occasionally observed at five degrees, however it was more common at six degrees. When no instability was present at angles of attack of five degrees, two flow patterns were typically observed. In some cases, vaporous partial cavities were found to form sporadically near the leading edge, similar to what was shown in fig. 4.9. In other cases, stable ventilated partial cavities formed over the majority of the suction side, as shown in fig. 4.58. Here, ventilated partial cavities appear to form in the low pressure region behind the fin, and in the low pressure region along the suction side, as shown in fig. 4.5. The tip vortex from the leading edge did not appear to be strong enough to pull in gas to ventilate the tip. This second condition was also typically

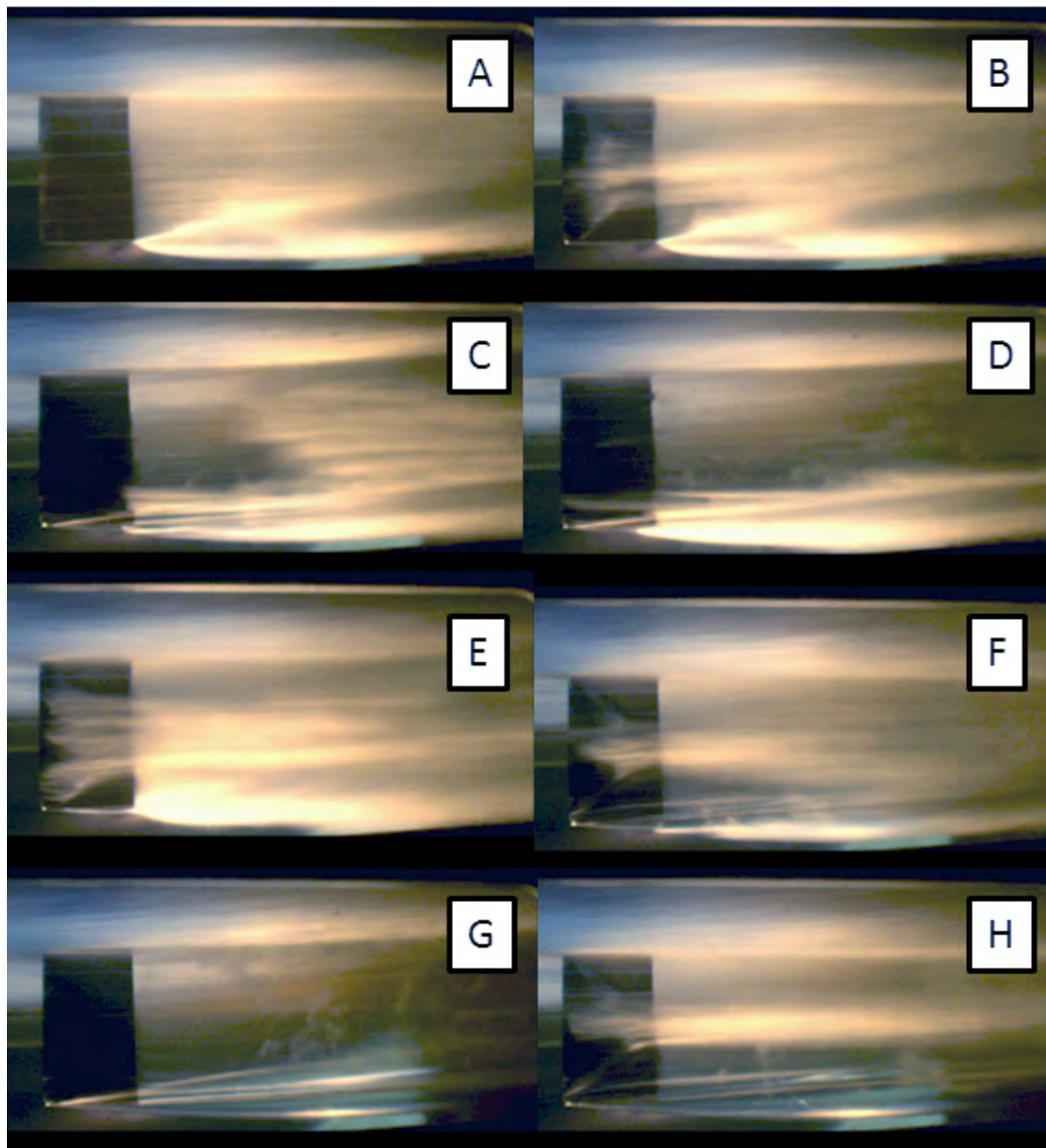


Figure 4.57: Photos showing the progression of the sporadic transition instability found during the steady state fin experiments, 2 inch chord, $\alpha = 6^\circ$, no sweep, $V=45\text{ft/s}$, large cavitator. A) The fin is base ventilated at the beginning of the run; B) A partial cavity forms near the leading edge; C) gas is pulled into the low pressure region over the suction side, forming a large ventilated partial cavity; D) The reentrant jet begins to lap on the back of the fin near the fin tip, (this makes the cavity near the tip a milky white color); E) The reentrant jet chokes off the partial cavity over the suction side, resulting in cavity collapse; F) The tip vortex appears to ventilate, pulling gas toward the leading edge to re-inflate the ventilated cavity over the suction side; G) Cavity re-forms and is clear for a moment; H) Process repeats itself

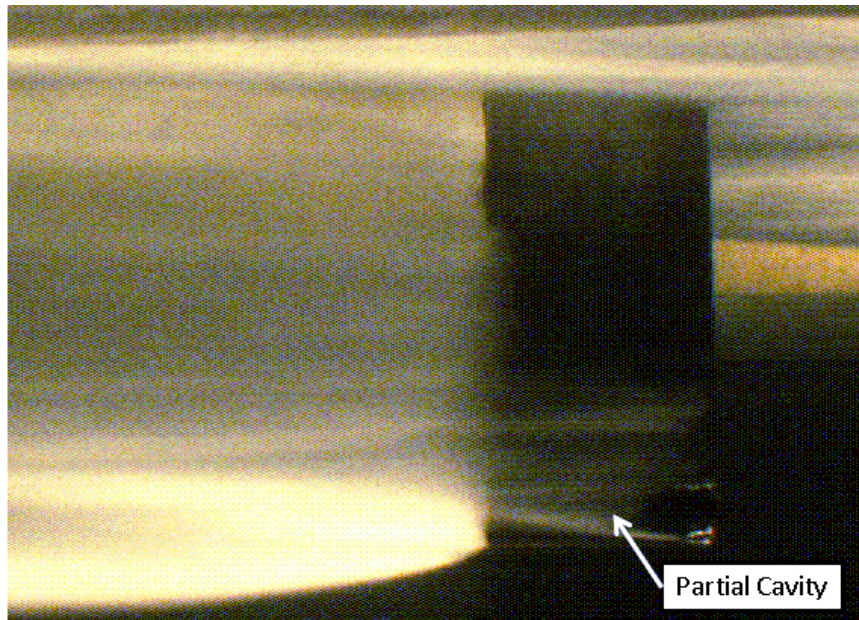


Figure 4.58: Time history of measured normal force from steady state run showing instability in the trailing cavity, 1 inch chord, $\alpha = 5^\circ$, $V=45\text{ft/s}$, Small Cavitator

found for the one and two-inch chord fins at five and six degrees operating at 25ft/s, where the instability was never present.

This instability was not found when the fins were rotating about their spanwise axes, nor was it found during the swept fin tests.

4.3 Transition and Hysteresis

Unsteady state tests were performed for a variety of conditions to study the transition between base and fully ventilated operation. Here, measurements were made while the fin was rotated about its spanwise axis over a range of angles of attack. The purpose of these tests was to study the mechanism of transition, and explore how varying tunnel velocity, aspect ratio, sweep angle, and angular velocity affected the angle at which transition occurred.

4.3.1 Modes of Transition

During testing, two different modes of transition were typically observed. The first mode, called “flash ventilation” was only observed when the fin transitioned from base to fully ventilated. Here, the trailing cavity was found to grow and engulf the entire suction side of the fin nearly instantaneously. As a result, a dramatic shift was found in the measured forces and moments, as is shown on the right side of fig. 3.4. In many cases, small vaporous partial cavities were found to form along the leading edge for an instant before full transition occurred. In some of the high-speed videos taken during the swept fin testing, it was found that these vaporous partial cavities would commonly form and collapse several times before the fin finally transitioned. When transition was finally observed on the swept fins, it was found to occur from the tip, as shown in fig. 4.59. The timescale for flash ventilation was observed to be on the order of a few hundredths of a second. High-speed videos were not available from the unswept fin tests. As a result, no firm observations could be made on the formation of the fully ventilated trailing cavities for the unswept fins.

The second mode of transition was typically found to occur when the fin transitioned back from fully to base ventilated operation. Here, transition was observed as a gradual shift in the slope of the forces and moments, without the dramatic spike found with flash ventilation. For the transition from fully to base ventilated, the process was observed to be as follows. As the angle of attack was decreased from fully ventilated, the suction side of the fin would eventually come in contact with the cavity boundary near the trailing edge. This resulted in the formation of a ventilated partial cavity along the suction side. These cavities would then shrink as the angle of attack was decreased, until they disappeared altogether, completing the transition. For the unswept fins, the ventilated partial cavities were found to shrink towards the leading edge, similar to fig. 4.10. For the swept fins, the ventilated partial cavities were found to shrink towards the tip, similar to what was shown

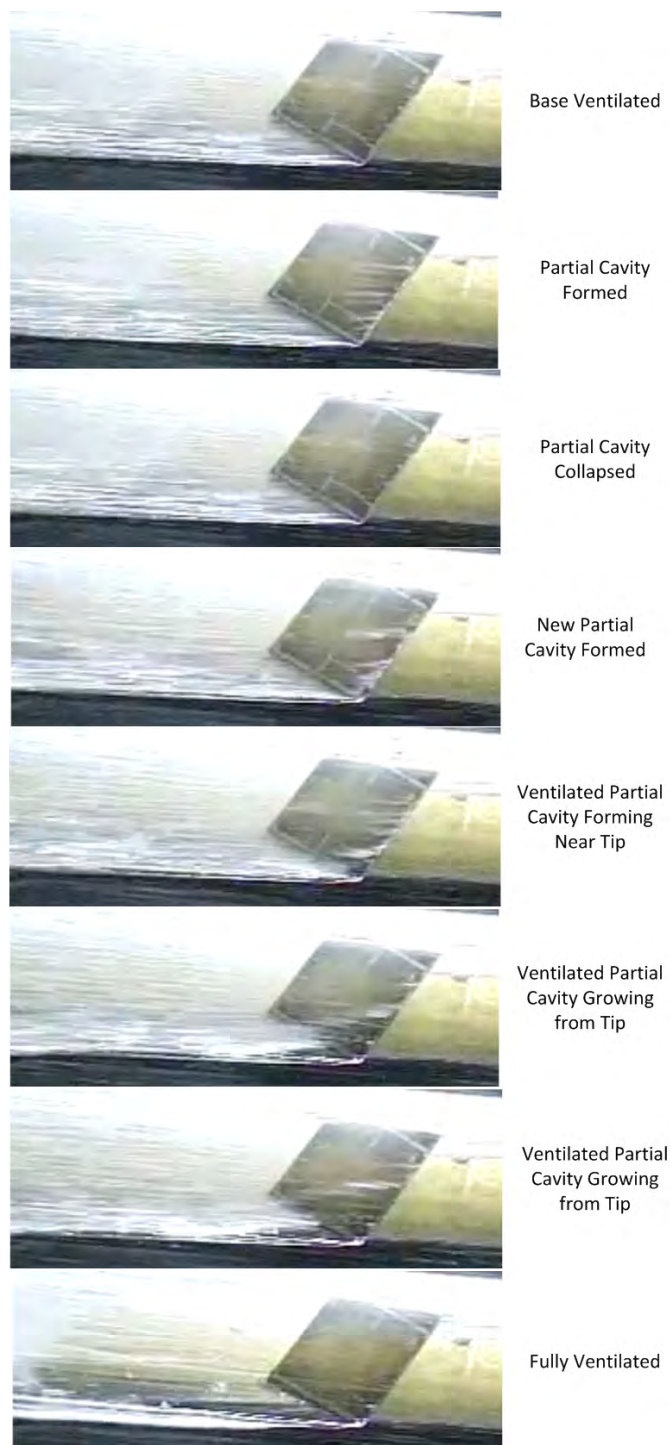


Figure 4.59: Sequence showing flash ventilation of the two-inch chord fin swept to 30 degrees, while the angle of attack was increasing. Frames taken from a high-speed video shot at 600 fps. Current sequence spanned about 15 frames, which is equal to about 0.025 seconds.

in fig. 4.16.

Gradual ventilation was also found from base to fully ventilated operation under some conditions during the swept fin testing. When this occurred, a small ventilated partial cavity formed near the tip. As the fin's angle of attack increased, the partial cavity grew and extended down the span of the fin toward the root. Gradual ventilation was the primary mode of transition for the one-inch chord fin swept to 30 and 45 degrees. Unlike flash ventilation, which was nearly instantaneous, the timescale for gradual ventilation was observed to be anywhere from a few tenths of a second to a few seconds, depending on the angular velocity of rotation. The ventilated partial cavity on the fin was typically found to remain a constant size and shape if the fin was brought to a halt during the transition, though quick decelerations were found to force the fin to fully ventilate.

4.3.2 Transition Angle of Attack

The angle of attack at which transition occurred was measured from the unsteady testing time history files, using the method described in chapter 3. The goal was to characterize how changes in fin planform, sweep, angular velocity, and tunnel velocity influenced the angle of attack where transition occurred.

Transition from Base to Fully Ventilated

No noticeable dependence could be found between the angle of attack at which transition to fully ventilated operation occurred and angular velocity over the range of conditions tested. Typical results showing the sensitivity of the transition angle of attack, henceforth referred to as the "ventilation angle," are plotted in fig. 4.61. It seems plausible that a dependence may exist at significantly higher angular velocities, though further studies are necessary to verify this.

The test data showed a very slight dependence on tunnel velocity. Though the effects

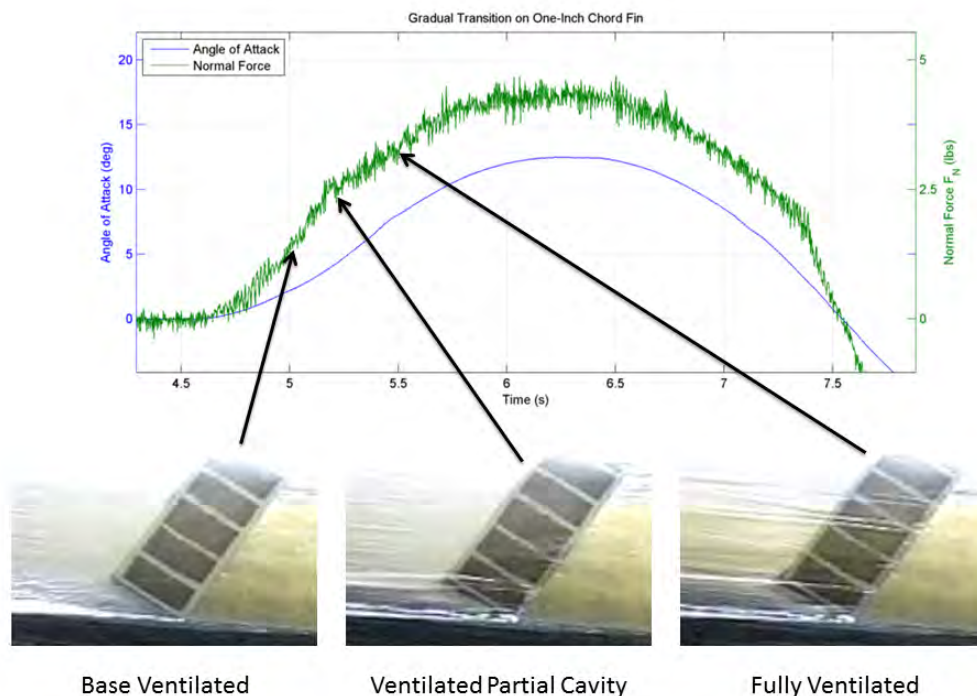


Figure 4.60: Time history of measured normal force and angle of attack from unsteady state test with the one-inch chord fin swept to 30 degrees, showing gradual transition where ventilated partial cavities forms and grew during transition.

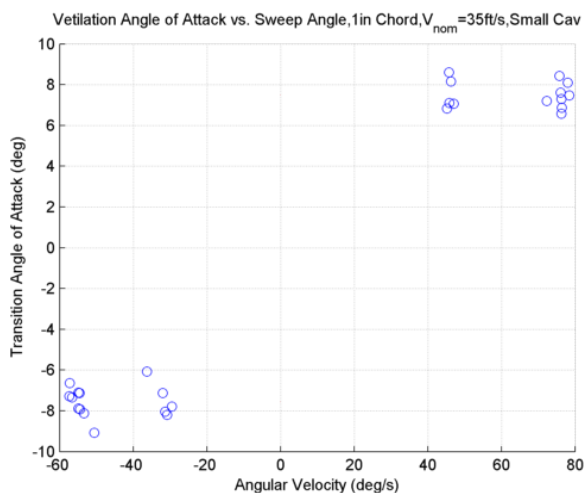


Figure 4.61: Plot showing the angle of attack at which transition from base to fully ventilated operation occurred as a function of the angular velocity of the fin at transition. No noticeable trend could be detected for any conditions tested. This plot is for data from the unswept 1 inch chord fin at 35 ft/s.

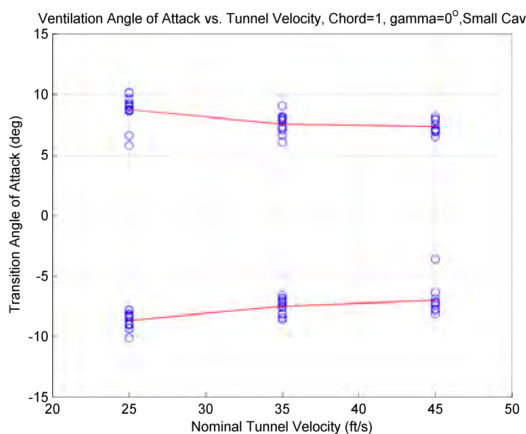


Figure 4.62: Ventilation angle of attack plotted against nominal tunnel velocity, 1 inch chord, $\gamma = 0^\circ$, small cavitator

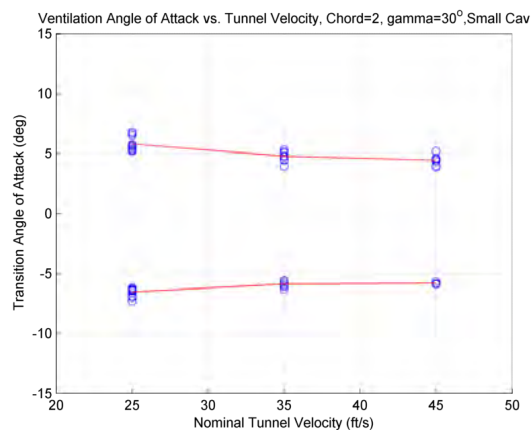


Figure 4.63: Ventilation angle of attack plotted against nominal tunnel velocity, 2 inch chord, $\gamma = 30^\circ$, small cavitator

are likely on the order of the error of measurement, there appears to be a fairly consistent decrease in the ventilation angle with increasing tunnel velocity. Typical test data plotted as a function of ventilation angle and tunnel velocity is shown in figs. 4.62 and 4.63. There is a slight asymmetry in the angle at which the two-inch chord fin transitioned, as shown in fig. 4.63, which is likely a result of damage on the fin tip. This damage is described in Appendix B.

A more pronounced trend was found with varying sweep angle, for a each chord and cavitator combination at a particular tunnel velocity. Typical results showing this consistent trend can be found in figs. 4.64 and 4.65. This trend shows that planform shape has a large influence on the ventilation angle.

Varying chord length was also found to affect the ventilation angle. Figures 4.66 and 4.67 show the measured angle of transition against chord length, for constant tunnel velocity, cavitator size, and sweep angle. Increasing chord length, while keeping all else equal, appeared to result in an increase in the angle at which transition occurs. This is analogous to saying reducing aspect ratio resulted in an increase in the ventilation angle.

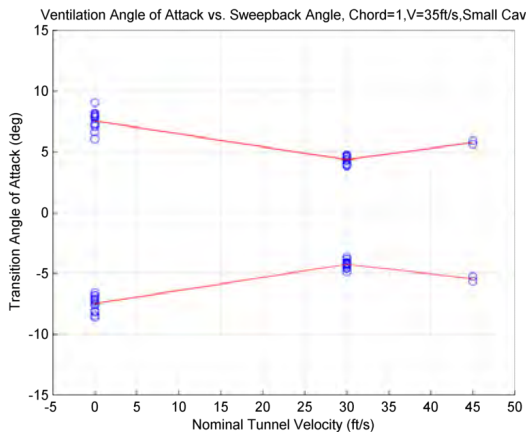


Figure 4.64: Ventilation angle plotted against sweep angle, 1 inch chord, $V=35\text{ft/s}$, small cavitator

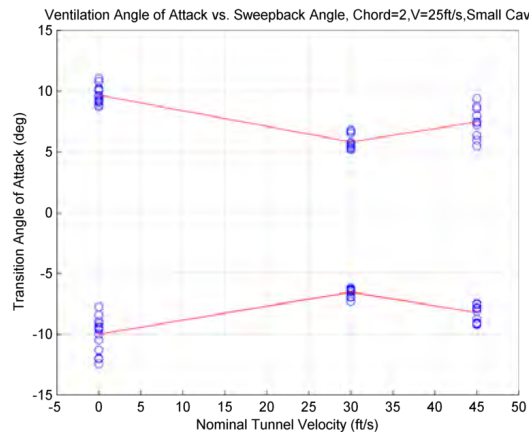


Figure 4.65: Ventilation angle plotted against sweep angle, 2 inch chord, $V=25\text{ft/s}$, small cavitator

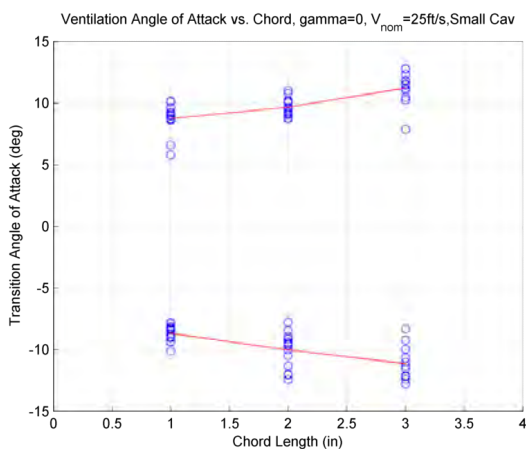


Figure 4.66: Ventilation angle plotted against chord length, $\gamma = 0^\circ$, $V=25\text{ft/s}$, small cavitator

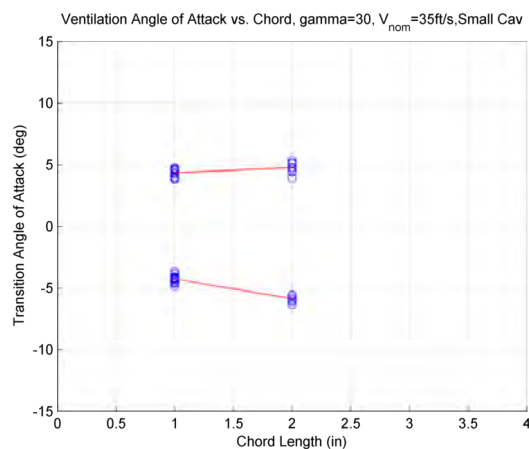


Figure 4.67: Ventilation angle plotted against chord length, $\gamma = 30^\circ$, $V=35\text{ft/s}$, small cavitator

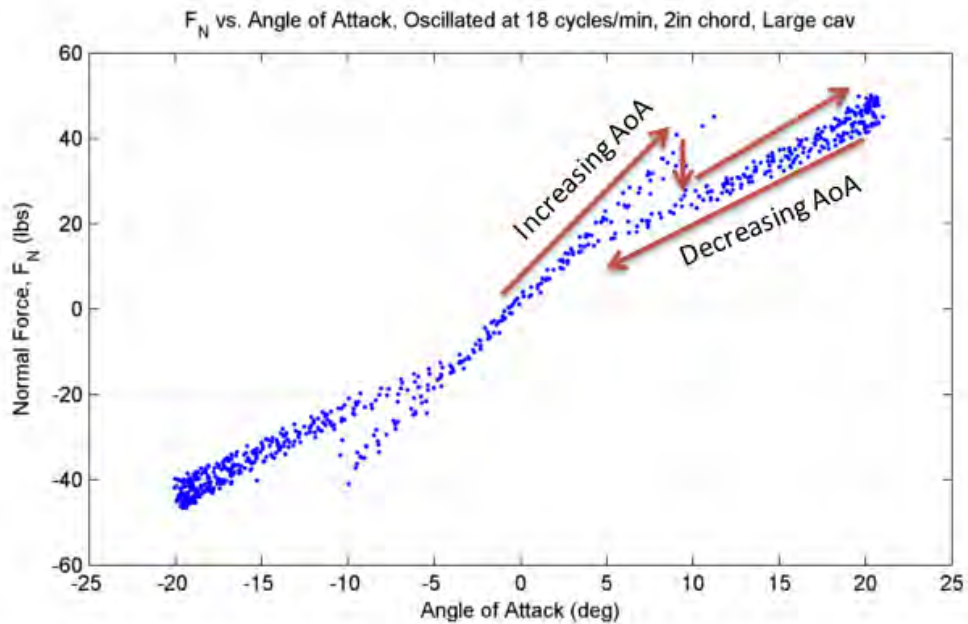


Figure 4.68: Data from an unsteady test where the fin was oscillated about its spanwise axis, showing the normal force F_N as a function of angle of attack. A fairly large hysteresis is present between where the fin transitions to and from fully ventilated operation. The data plotted here is for an unswept fin oscillated at 18 cycles per minute, 2 inch chord, 45ft/s.

Transition from Fully to Base Ventilated and Hysteresis

The fully ventilated fins typically transitioned back to base ventilated gradually, as described previously. The measured forces and moments appeared as faired curves connecting the base and fully ventilated measurements. Transition back to base ventilated operation was typically found to occur at an angle of attack less than the ventilation angle. An illustrative example of this is shown in fig. 4.68, where the measured normal force taken during an unsteady run was plotted against angle of attack. A noticeable hysteresis can be seen between where the fin transitions to fully ventilated and where it transitions back.

No significant trends could be identified in the measured reattachment angle of attack when plotted against tunnel velocity, chord, and sweep angle. If there is a sensitivity, it is likely that it fell within the error of measurement, which was on the order of about 3/4

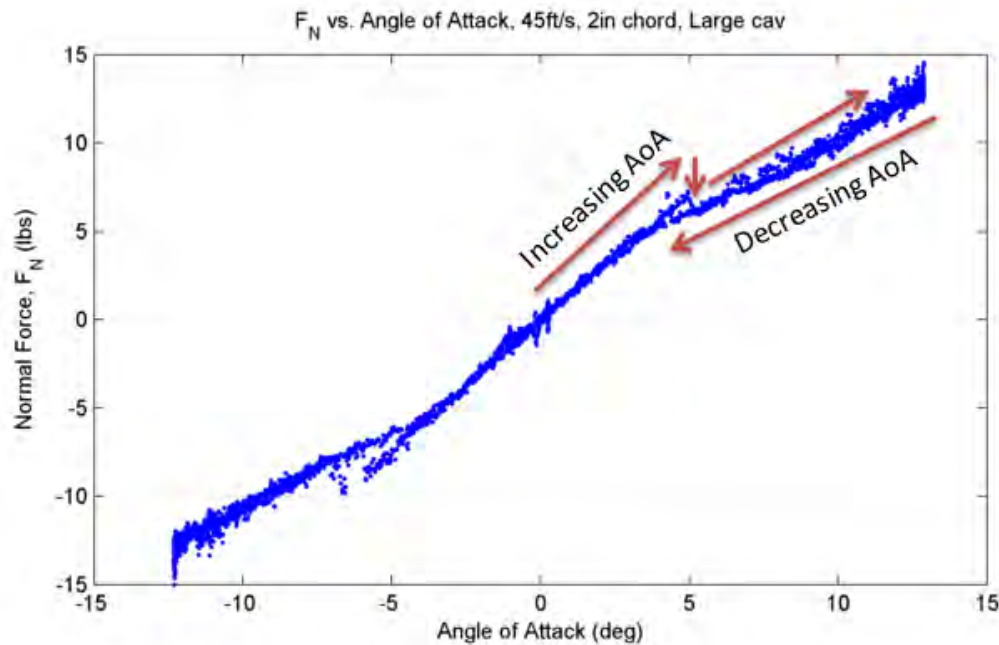


Figure 4.69: Data from an unsteady test where a swept fin was oscillated about its spanwise axis, showing the normal force F_N as a function of angle of attack. The hysteresis is smaller for the swept fin than it was for the unswept fin. $\gamma = 30^\circ$, $V=45\text{ft/s}$, 2 inch chord

degrees. As a result, the magnitude of the measured hysteresis was primarily a function of the ventilation angle of attack. The observed trends for the magnitude of the hysteresis were similar to the ones observed for the ventilation angle.

Figure 4.69 shows the normal force plotted against angle of attack for a fin swept to 30 degrees. Here, it can be seen that the hysteresis region is significantly smaller than what was observed for the unswept fins, which agrees well with the observations made earlier about the ventilation angle.

Chord length was observed to have a dramatic effect on the ventilation angle of attack, where the angle at which ventilation occurred was found to decrease with chord length. Similar trends were seen in the magnitude of the hysteresis.

The hysteresis was not found to be affected by changing the angular velocity of the fin over the range tested. This may not be the case for higher angular velocities.

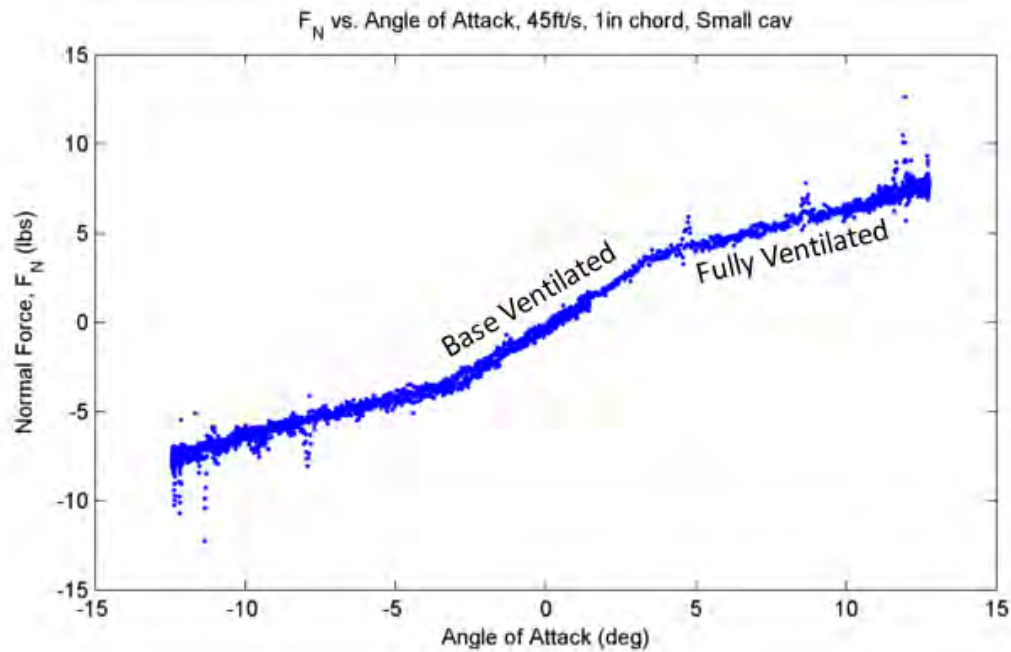


Figure 4.70: Data from an unsteady test where a swept fin was oscillated about its spanwise axis, showing the normal force F_N as a function of angle of attack. Here, the fin gradually transitioned from base to fully ventilated, and no hysteresis was observed. $\gamma = 30^\circ$, $V=45\text{ft/s}$, 1 inch chord. The spikes at higher angles of attack are a result of the reentrant jet lapping on the rear of the fin.

Hysteresis in the measured forces and moments were only found when the fins flash ventilated. Similar observations were made by Breslin and Skalak (1959) for ventilation on yawed surface piercing struts. No hysteresis was found when the fin gradually transitioned to fully ventilated. An example of this is presented in fig. 4.70, for the one-inch chord fin at 45ft/s.

Additional plots showing where the fin transitioned can be found in Appendix E. These plots show the angle of attack where transition occurred, plotted against tunnel velocity for different combinations of chord length, sweepback angle, and cavitator.

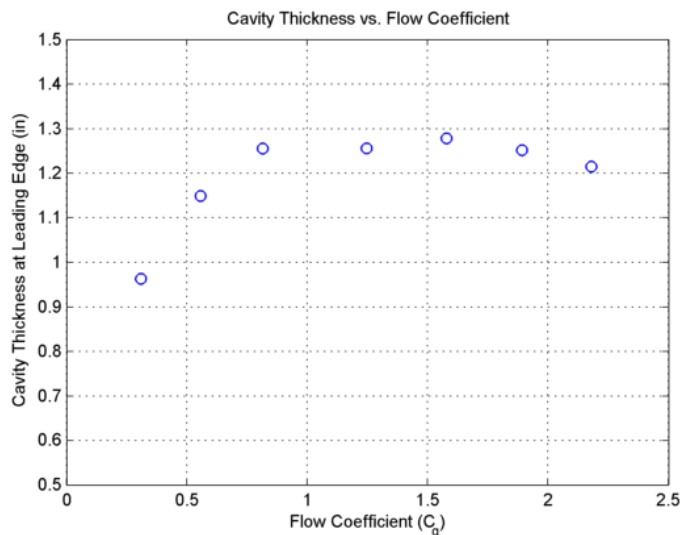


Figure 4.71: Measured cavity thickness at the leading edge of the fin at zero degrees vs. entrainment coefficient.

4.4 Effects of Varying Ventilation Rate

A brief study was performed to investigate the effects of varying the amount of gas injected into the supercavity along the top of the tunnel. Due to time constraints, this was only performed for the one-inch chord fin swept to 45 degrees from vertical piercing a cavity from the small cavitator. Here, the fin was oscillated slowly to $\pm 12.5^\circ$ with the tunnel operating at 45ft/s. Seven separate runs were performed with different flow rates. Injection rates were varied from 7.5-45.5 CFM.

The flow coefficient, C_q was calculated for each condition, using the frontal area of the cavitator as the reference area. The flow coefficient was plotted against the measured cavity thickness at the leading edge of the fin, which is shown in fig. 4.71. The figure shows that cavity thickness is relatively insensitive to changes in entrainment coefficient, except at comparatively low values. This behavior is likely a result of the solid tunnel walls.

Changes in the entrainment coefficient primarily affected the shape and structure of the trailing cavity behind the fin. At very low flow rates, the trailing cavity was observed

to be very short. As a result, the reentrant jet formed at the trailing edge of the cavity was found to shoot forward and impinge onto the rear of the fin. As the flow rate increased, the trailing cavity was found to grow, moving the cavity closure point further downstream. Eventually, the closure point moved far enough away that the reentrant jet dissipated before it could hit the fin. Similar trends were also observed for the cavity along the top of the tunnel. This is shown in fig. 4.72 looking at the fin from the side.

The measured forces and moments were found to vary slightly with flow rate. The forces and moments measured at very low flow rates were typically a bit higher than those measured at higher flow rates. Variation appeared to decay rapidly, in a manner similar to what was found for cavity thickness. Examples of this are shown in figs. 4.73 and 4.74 for lift and shaft torque. This dependence is likely a result of variations in cavity thickness and changes in cavity pressure as a result of increasing flow rate.

The mean cavitation number was calculated for each flow rate, and is shown in fig. 4.75. There appeared to be a steady decrease in cavitation number with increasing flow coefficients. This trend is in agreement with observations by Wosnik and Arndt (2009).

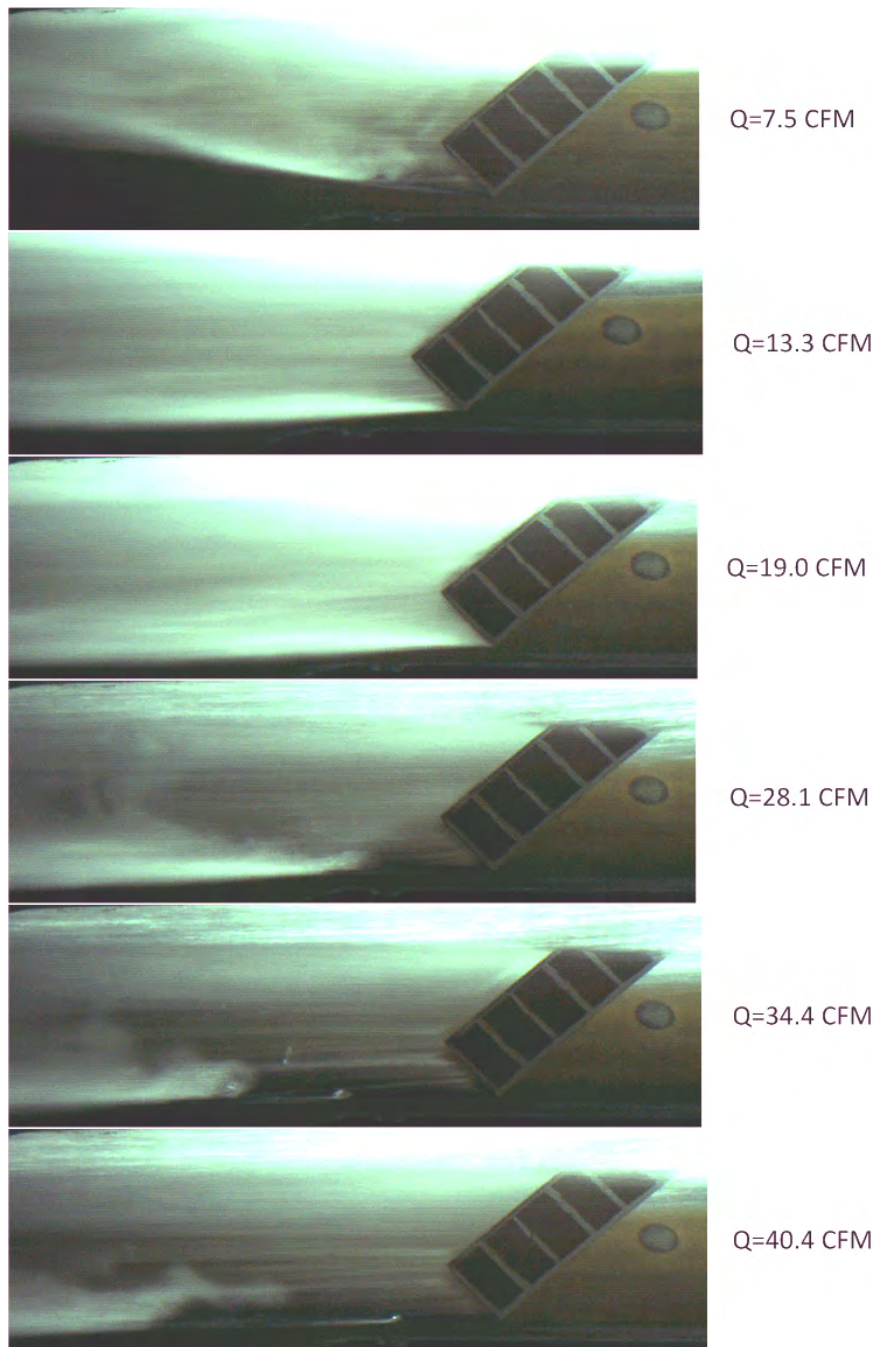


Figure 4.72: Trailing cavities for different flow rates. Trailing cavity is murky due to reentrant jet effects at low flow rates and is clear at high flow rates. At the lowest flow rate, the trailing cavity was also found to be significantly shorter than what was found at the other conditions. One-inch chord, $\gamma = 45^\circ$, $\alpha = 0^\circ$

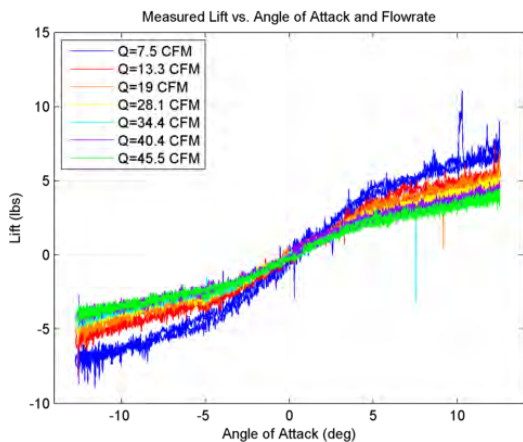


Figure 4.73: Lift plotted against angle of attack and flow rate, 1 inch chord fin, $\gamma = 45^\circ$, $V=45\text{ft/s}$

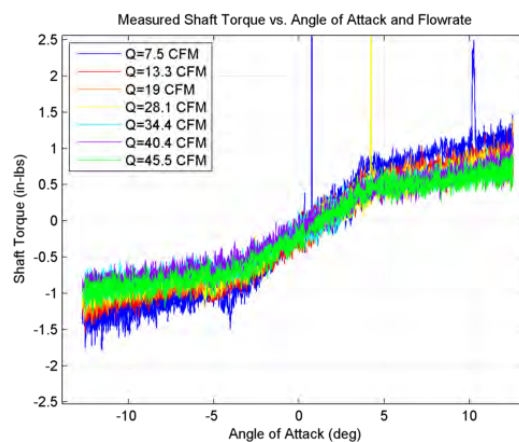


Figure 4.74: Shaft torque plotted against angle of attack and flow rate, 1 inch chord fin, $\gamma = 45^\circ$, $V=45\text{ft/s}$

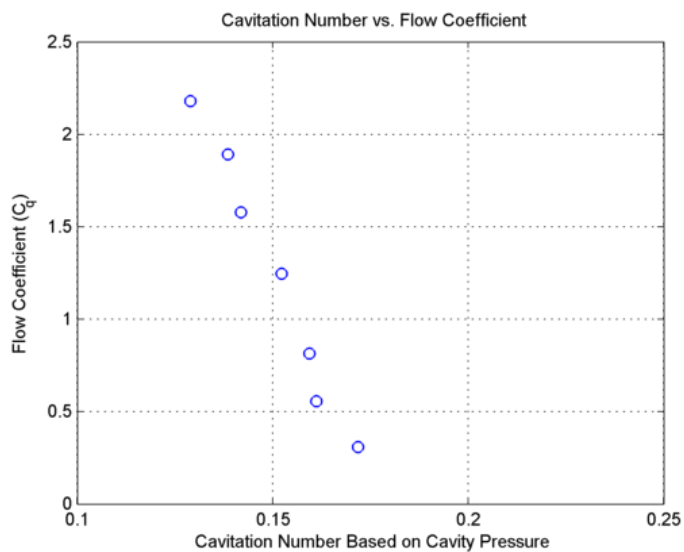


Figure 4.75: Measured cavitation number vs. Flow Coefficient for the 1 inch chord fin piercing a cavity off the small cavitator, $V=45\text{ft/s}$, $\gamma = 45^\circ$, averaged over $\alpha = \pm 12.5^\circ$

Chapter 5

Conclusions and Future Work

5.1 Summary and Conclusions

Exploratory water tunnel experiments on supercavitating fins were performed at the Applied Research Laboratory's Garfield Thomas Water Tunnel facility. Steady and unsteady state measurements were made on finite span fins piercing the boundary of an artificially ventilated supercavity and into the free stream. The effects of varying fin geometry and flow parameters were investigated.

Tests were performed in the round, three-dimensional section of ARL's twelve-inch water tunnel over the course of a two year period. During the first year, tests were performed on fins with rectangular planforms and wedge cross sections. Forces and moments were measured using a six component force and moment transducer. Legacy hardware and test fixtures were adapted where possible. Steady state measurements were made on fins at fixed angles of attack. Unsteady state measurements were made on fins rotating about their spanwise axes.

During the second year, additional experiments were performed on the same fins swept back to 30 and 45 degrees. These fins were swept back and rotated about their spanwise axes. The resulting swept fins had trapezoidal planforms. New test fixtures were designed and fabricated to make steady and unsteady state measurements on the swept fins.

Ventilated supercavities were formed along the top of the water tunnel using sharp, wall mounted cavitators with half wedge cross sections. Compressed dry air was injected directly downstream of the cavitators to ventilate the cavities. Cavitators of different sizes were used during testing to change cavity thickness and vary fin immersion.

For all conditions examined, gas was entrained in the low pressure wake created behind the fin, forming a ventilated trailing cavity. At low angles of attack, the trailing cavity was found to form from the trailing edges of the fin's pressure and suction sides. At higher angles of attack, the suction side of the fin was found to ventilate, resulting in a dramatic change in the structure of the trailing cavity. In this condition, the trailing cavity formed from the sharp leading edge and the trailing edge of the fin's pressure side. The trailing cavity from the leading edge typically covered the fin's suction side. For the unswept fin, the fin tip was found to remain wetted at low angles of attack. At higher angles of attack, the tip vortex was found to ventilate and detach from the top of the fin.

These changes in the trailing cavity were found to have a noticeable effect on the measured forces and moments. Decreases in lift and shaft torque were observed when the suction side ventilated, along with a noticeable rearward shift in the fin's center of pressure. The slopes of the measured lift and moment curves were also found to decrease.

Fins with different chord lengths were tested at three tunnel velocities. The measured lift coefficients from the unswept fin tests were found to vary at low Froude numbers. Above Froude numbers of about 15, the measured lift coefficients were typically found to collapse within the error of measurement. No Froude number dependence was found for the swept fins, which is likely a result of the pointed tip. The measured drag coefficients were also found to vary with tunnel velocity.

Fin aspect ratio was varied during testing. The measured lift coefficients were found to decrease with decreasing aspect ratio, which agrees well with theory. Decreasing aspect ratio was also found to result in a decrease in the measured drag coefficient, which agrees

with observations by Kermeen (1960) who found a similar trend for non-cavity piercing supercavitating fins. This drop in drag with aspect ratio is a result of variations in the induced drag. Reducing aspect ratio reduces the lift coefficients for a particular condition, which results in a decrease in the induced drag. No dependence was observed on the measured lift to drag ratio.

Changing the sweep angle from 30 to 45 degrees was found to result in a decrease in the measured lift coefficients, which agrees well with theory (Anderson, 1999). No change in the lift coefficients could be detected between the runs at 0 and 30 degrees. Similar trends were found in the measured drag coefficients. Changing fin sweepback angle was also found to move the center of pressure. Increasing the sweep angle from 30 to 45 degrees resulted in a noticeable forward shift in the center of pressure. The lack of variation between the measurements on the vertical fins and the fins swept to 30 degrees is likely a result of changes in planform shape.

The measured lift and drag were compared with a simple theoretical model. At low angles of attack, the fins were modeled as traditional airfoils. At higher angles of attack, the fins were modeled as fully cavitating flat plates inclined to the flow. Thin airfoil theory was used to estimate the lift curve slope at low angles of attack. A theory by Tulin and Burkart (1955) for yawed supercavitating plates at zero cavitation number was used to estimate the lift curve slope at higher angles of attack. Three-dimensional effects on the lift curve were accounted for using a lifting surface approximation by Helmbold. At low angles of attack, the two-dimensional section drag was taken from Hoerner (1958). At higher angles of attack, the section drag was estimated using a theory by Tulin and Burkart (1955). The additional drag due to lift was accounted for using lifting line theory, as discussed by Anderson (1999).

Fairly good agreement was found between the predicted and measured values at low angles of attack. Agreement was found to improve when the two-dimensional section drag

coefficient was taken as the measured drag coefficient at zero angle of attack. At higher angles of attack, the supercavitating model was found to consistently overestimate the lift and drag coefficients.

Unsteady state tests were performed to study the mechanism of transition, where the fins were oscillated over a range of angles of attack during each run. Two modes of transition were identified. One mode, called flash ventilation, occurred where the trailing cavity transitioned rapidly. This mode of transition was observed as a discontinuity in the measured forces and moments. The second mode was more gradual, where the fin transitioned gradually. No discontinuities were found in the measurements when the fin transitioned gradually.

The angle at which the suction side ventilated was found to vary with changes in sweep angle, tunnel velocity, and chord length. The angle of attack where the fin transitioned back was found to be relatively constant throughout testing. When fins flash ventilated, a noticeable hysteresis was found between the angle of attack at which suction-side ventilation occurred and the angle at which the fin transitioned back. A corresponding hysteresis was also present in the measured lift, shaft torque, and center of pressure. The magnitude of the observed hysteresis varied as test parameters were changed. No hysteresis was observed when the fins transitioned gradually.

5.2 Future Recommendations

This study provided a good introduction to the general trends and characteristics of finite span wedge fins piercing a ventilated cavity boundary. Several additional studies are recommended to better understand some of the phenomena observed during testing.

Some of these experiments should be repeated using more sensitive instrumentation to get a better understanding of how the forces and moments vary with test parameters.

This is especially important for drag and shaft torque, where high measurement error made it difficult to draw firm conclusions.

During testing, velocity was measured with pressure transducers. One transducer was fitted to the test section, and the other was fitted upstream in the settling chamber. Directly after gas injection, large fluctuations were found in the measured tunnel velocity. It was difficult to tell if these were real. In future tests, tunnel velocity should be measured using a remote sensing technique such as Laser Doppler Velocimetry (LDV), to eliminate this uncertainty.

Additional studies are recommended to characterize the complex fin/cavity interactions observed during testing. It would be interesting to see how these interactions change with varying Froude number and cavity dimensions. A large body of information is available for ventilated supercavities off axisymmetric cavitators. For comparison purposes, it may be more practical to make observations on fins piercing an axisymmetric cavity, in a configuration similar to what was presented by Hjartarson et al. (2009). Part of this work should also quantify how adding fins changes the amount of gas required to adequately ventilate the cavities.

The work of Wetzel (1958) suggests that the hysteresis observed here during the unsteady state tests may vary with Reynolds and Weber numbers. Additional studies are recommended to quantify these effects, and identify how they vary with changing platform shape.

During testing, vaporous partial cavities were found to form and collapse a few times before the fin transitioned to fully ventilated operation. In some cases, it appeared that the partial cavities would form and trigger transition. It would be interesting to investigate how varying the vaporous cavitation number affects when and how the fin transitions.

Finally, tunnel wall effects for cavity piercing fins should be studied, and a correction method should be devised. This will become especially important if more sensitive

instrumentation is used.

Appendix A

Cavitator Dimensions and Locations

Cavitators were mounted flush to the top of the tunnel to generate different sized supercavities. These cavitators had wedge cross sections and sharp trailing edges to encourage flow separation.

During the unswept fin tests, large cavitators were mounted roughly 17 inches upstream of the fin's centerline. Gas was injected about 3 inches downstream of the cavitators. These large cavitators were curved to match the inner surface of the water tunnel. The nominal thicknesses of these two cavitators were 0.5 and 1 inches. The two curved cavitators are shown below in fig. A.1. Dimensions of these two cavitators are listed in figs. A.3 and A.4.

During the swept fin tests, smaller, flat cavitators were mounted to the tunnel about 9 inches upstream of the centerline of the fin, and gas was injected through the cavitator. These cavitators were made flat to mount flush against the top of the bottom of the swept fin apparatus. The cavitators had nominal thicknesses of 0.25 and 0.375 inches, and are shown in fig. A.2. Dimensions of these two cavitators are shown in figs. A.5 and A.6.

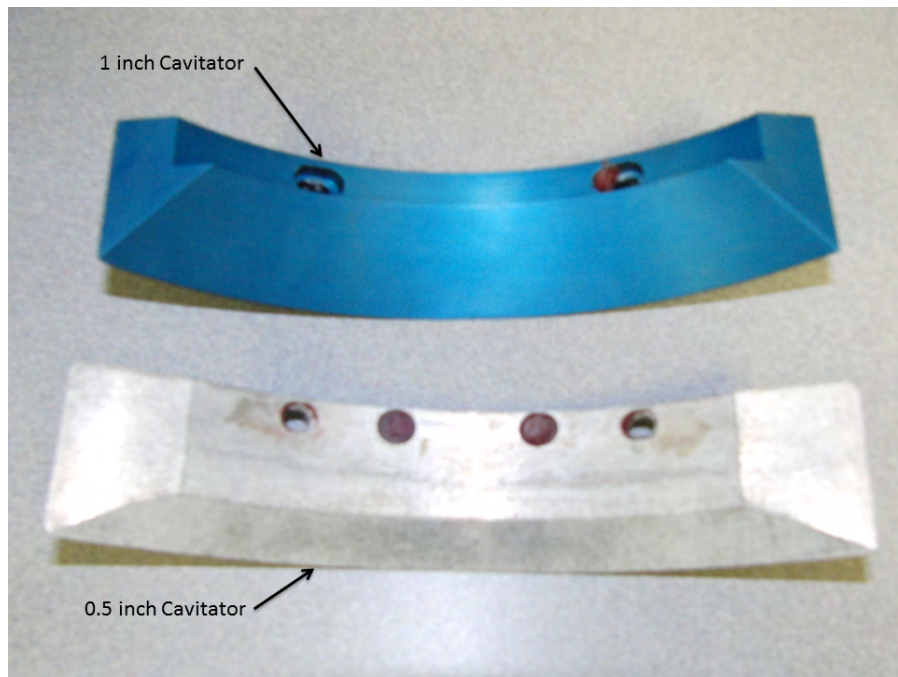


Figure A.1: Curved wall cavitators used during the unswept fin tests



Figure A.2: Flat wall cavitators used during the swept fin tests

Figure A.3: Dimensions of small curved cavitator used during the unswept fin tests (c1)

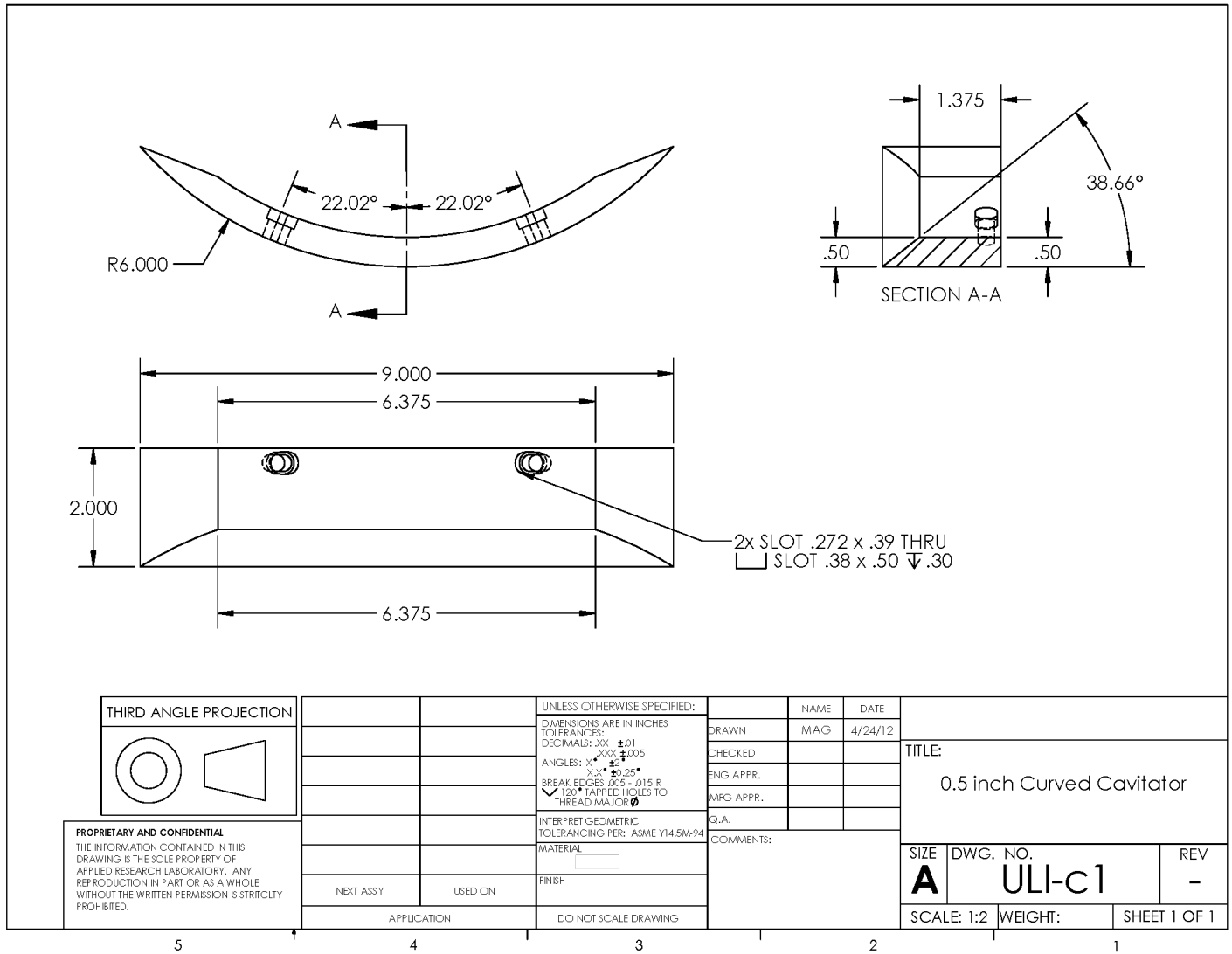


Figure A.4: Dimensions of large curved cavitator used during the unswept fin tests (c2)

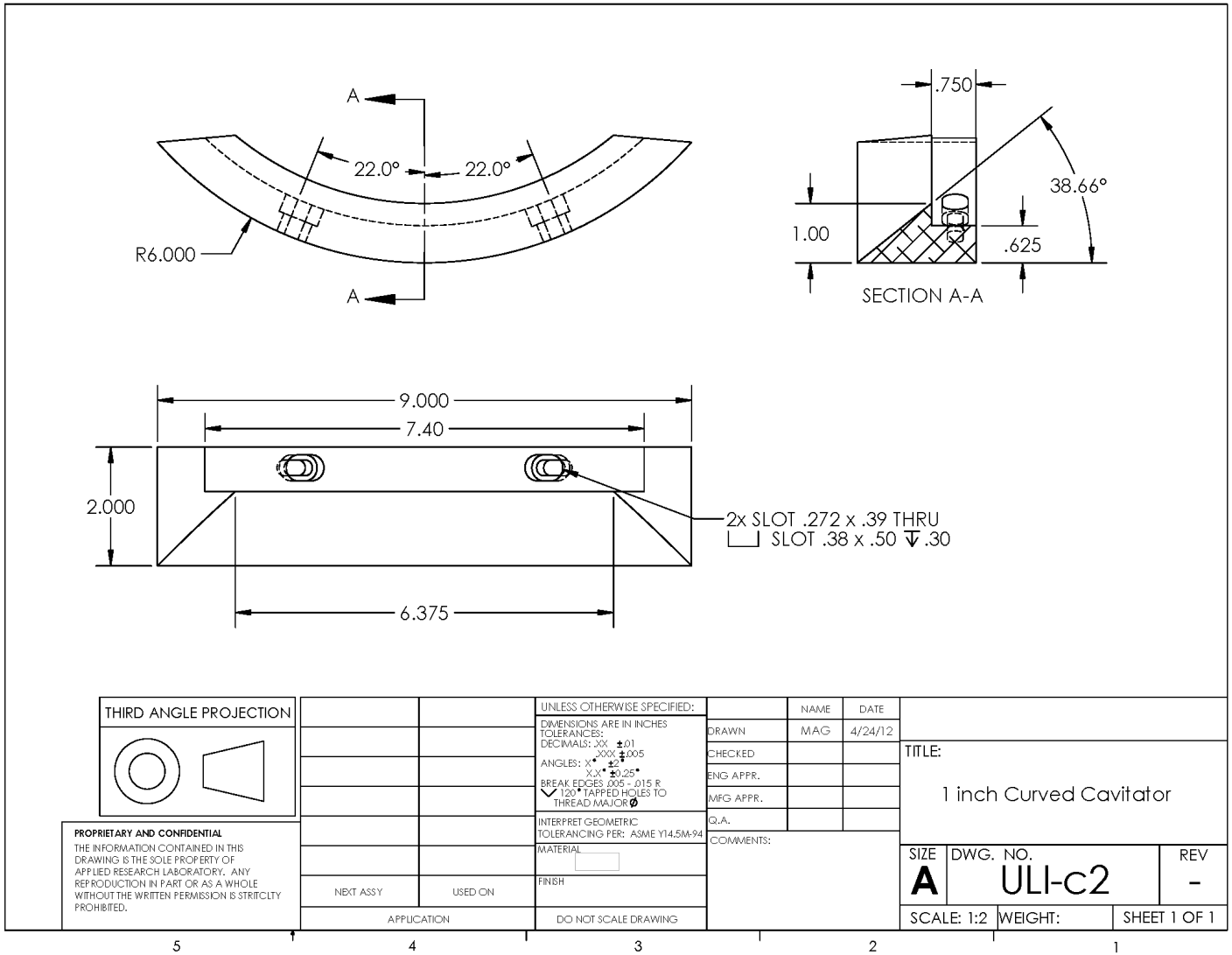


Figure A.5: Dimensions of small flat cavitator used during the swept fin tests (f1)

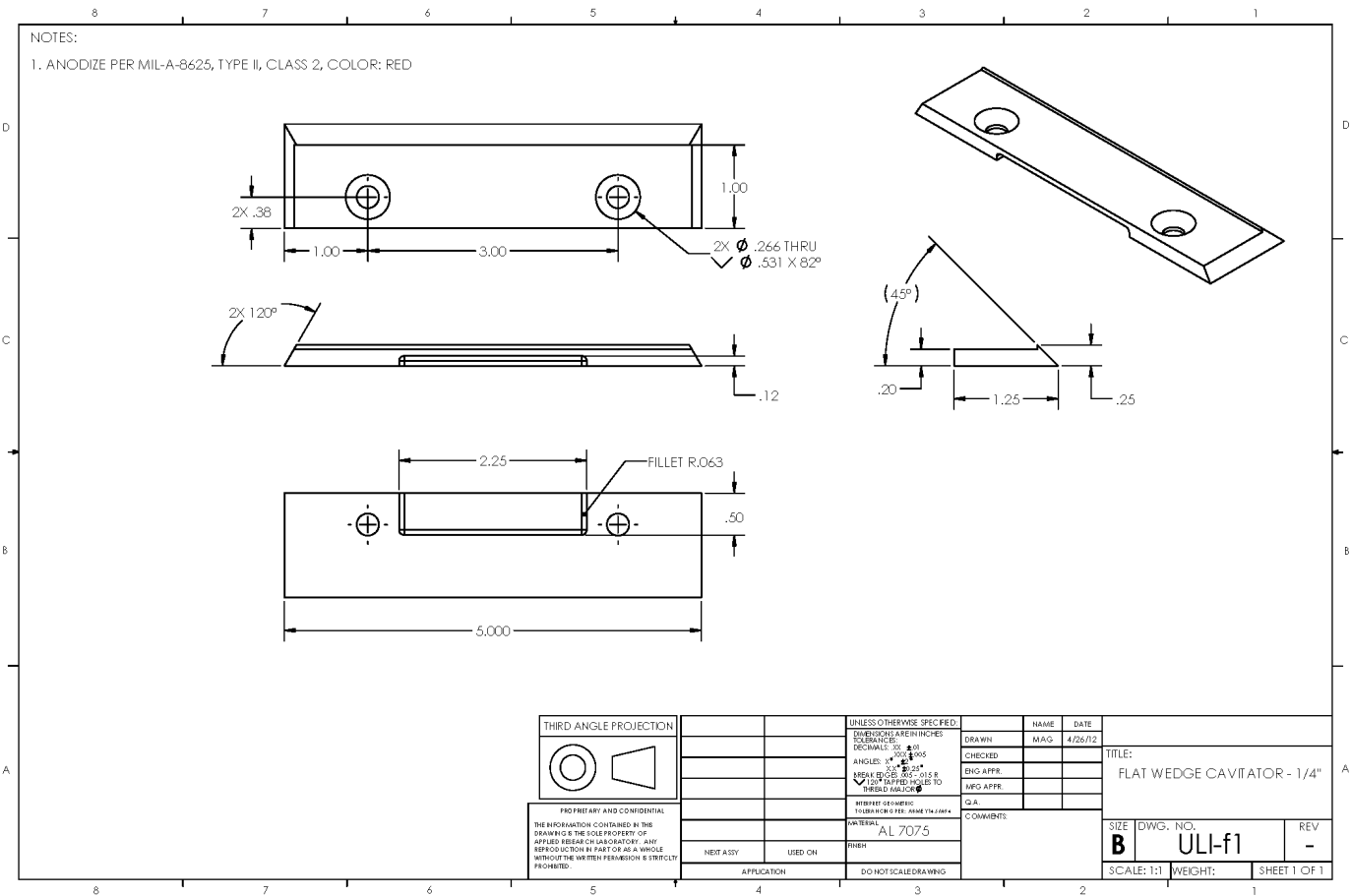
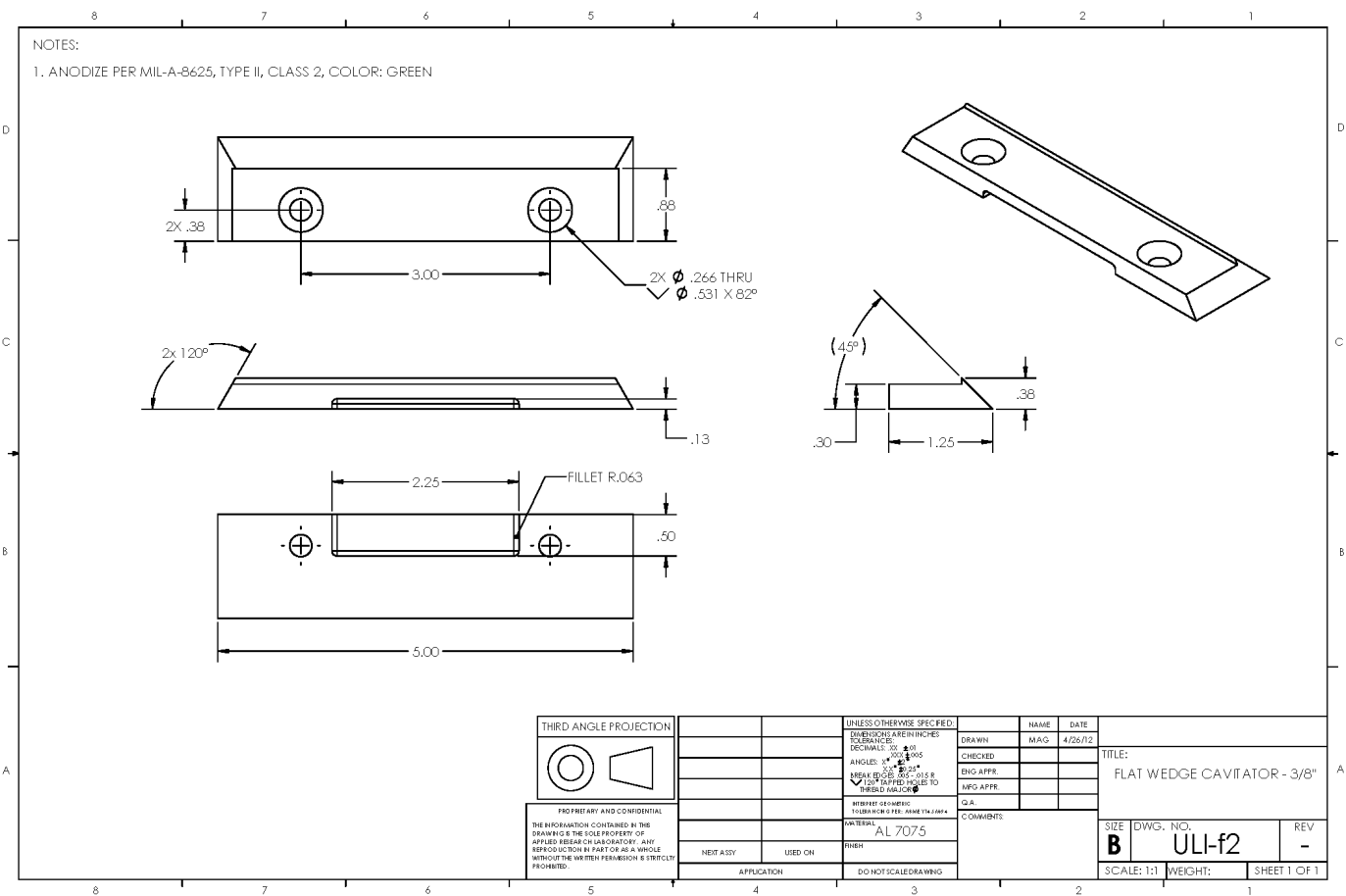


Figure A.6: Dimensions of large flat cavitator used during the swept fin tests (f2)



Appendix **B**

Damage to the Two-Inch Fin

The tip of the two-inch chord fin was damaged during fabrication. A tool broke during a machining operation, which took a notch out of the fin tip at the leading edge. Since it was impractical to fabricate a new fin, the affected region was faired to a knife edge, as shown in figs. B.1 and B.2. The chip spanned a region roughly 0.05in along the chord and 0.16 inches along the span. It is likely that the damaged tip influenced the measured forces, moments, and the angles of attack where transition occurred. The fin was not repaired for the second year's testing for consistency.

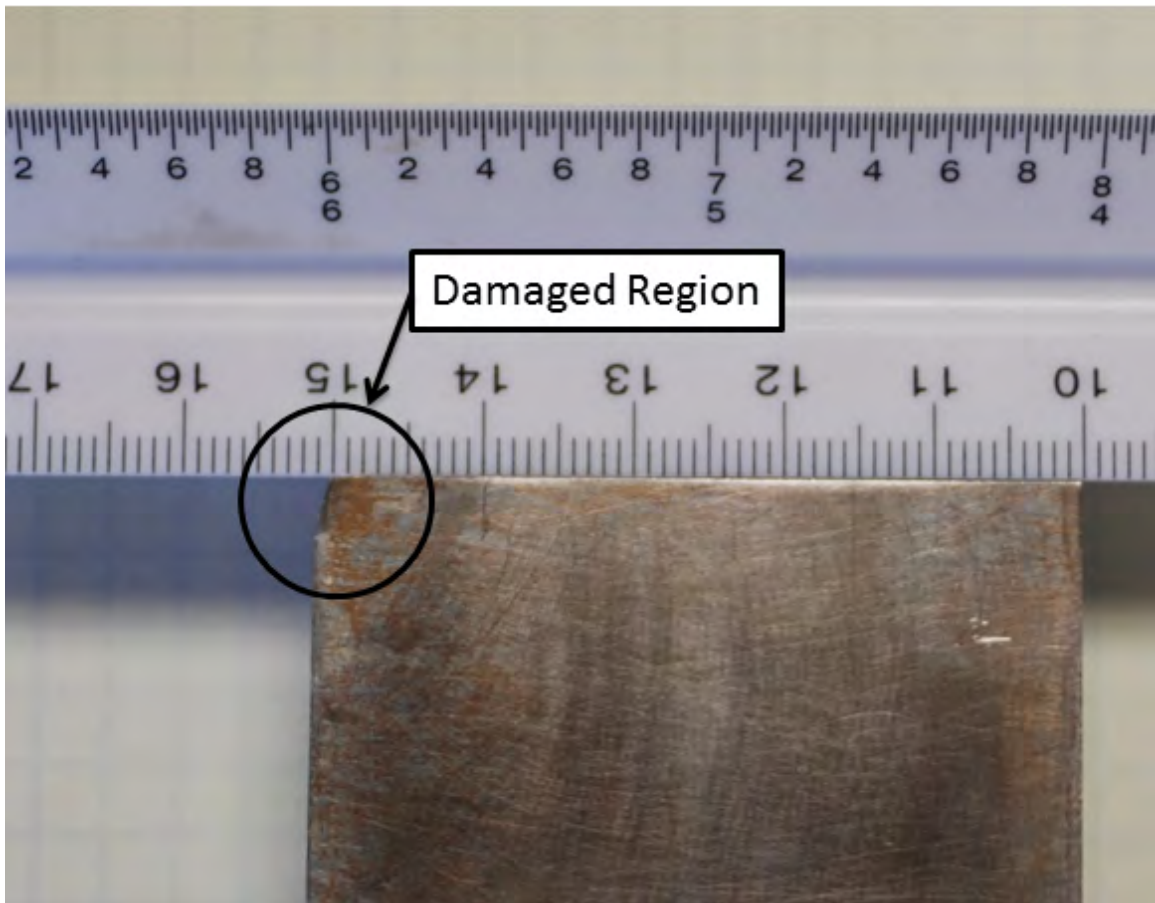


Figure B.1: Damage to the tip of the two-inch chord fin near the tip. The damaged area was faired to a knife edge at the leading edge. Scale here is in cm, (1in = 2.54cm)

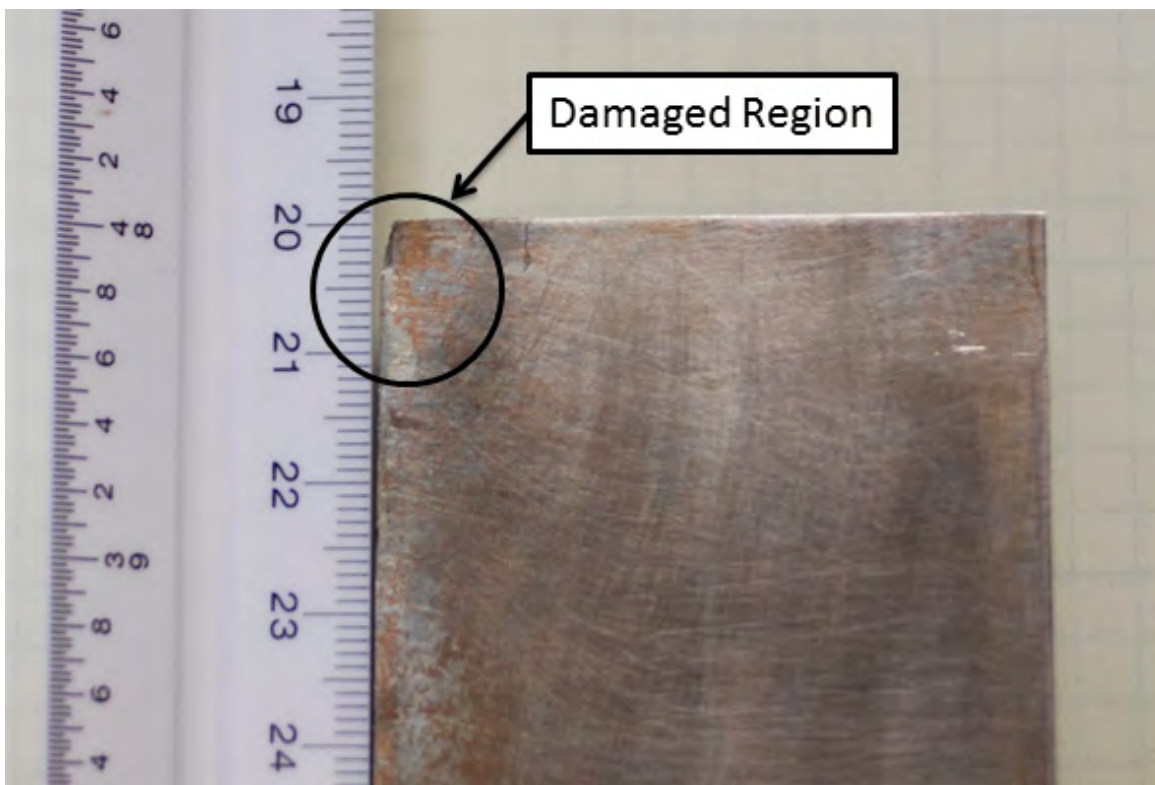


Figure B.2: Damage to the tip of the two-inch chord fin near the tip. Scale is in cm, (1in = 2.54cm)

Appendix **C**

Additional Setup Photos

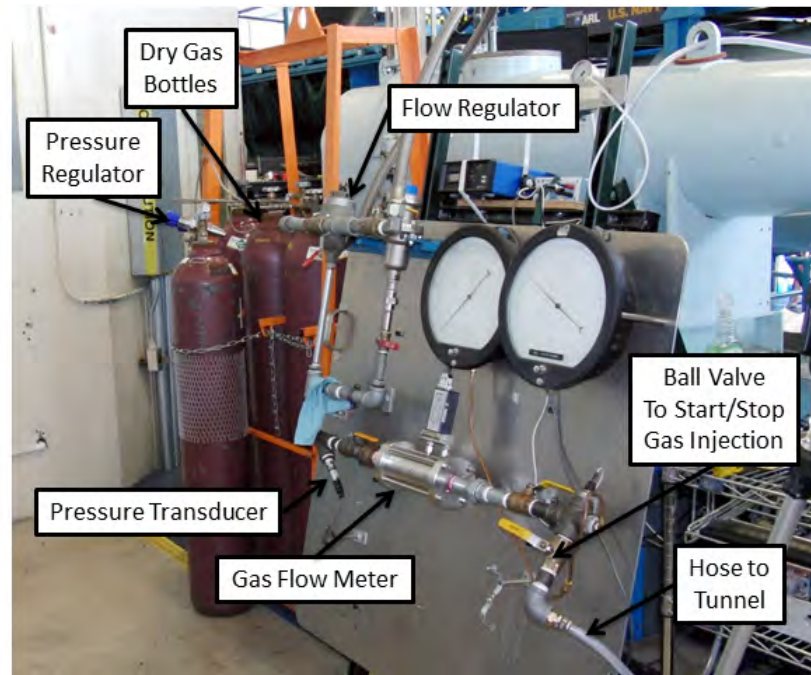


Figure C.1: Gas injection system used to ventilated the supercavities along the top of the tunnel.

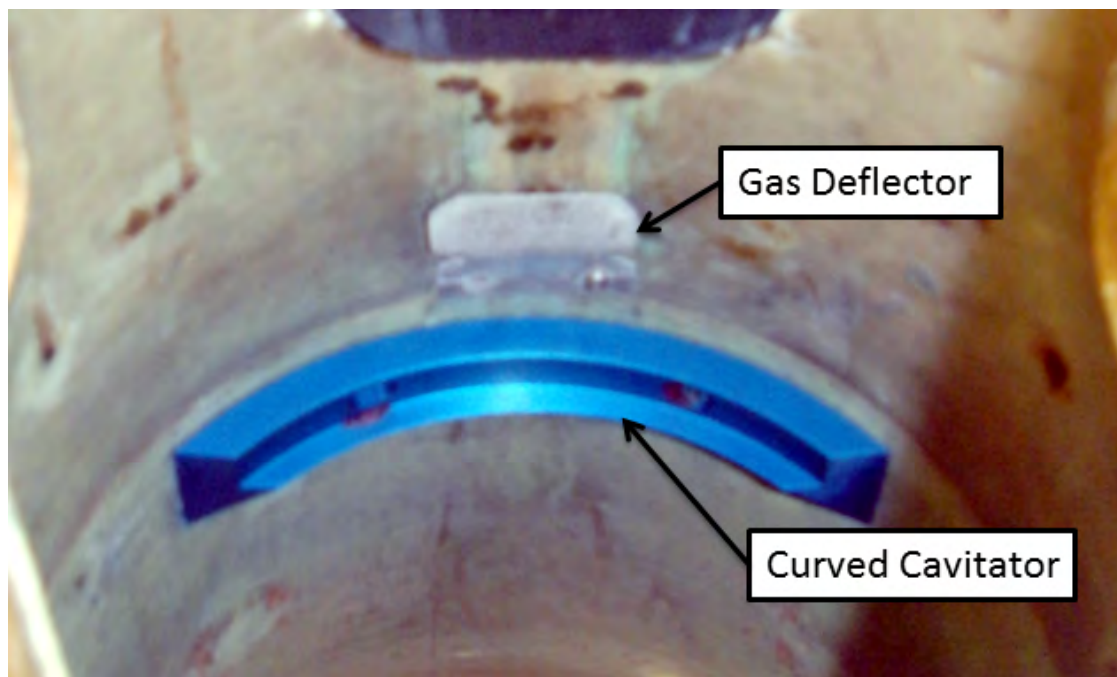


Figure C.2: Curved wall cavitator and gas deflector mounted in the water tunnel, looking upstream in the test section.

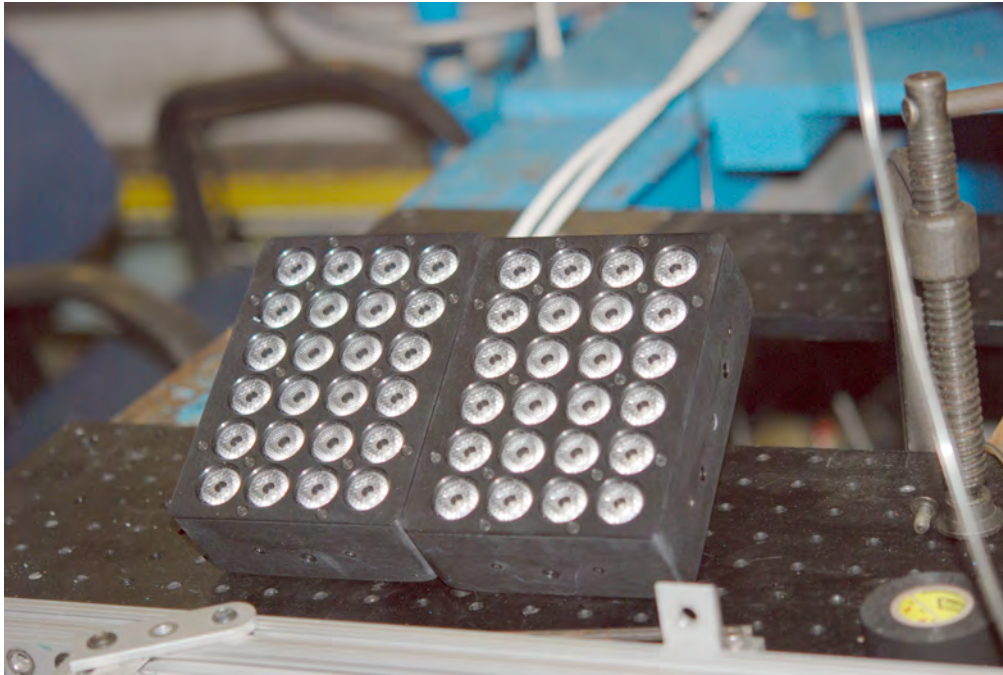


Figure C.3: High-power LED lights used during swept fin testing.



Figure C.4: Basler Scout color video camera used to observe the fin from the bottom of the tunnel, looking down the fin's span.

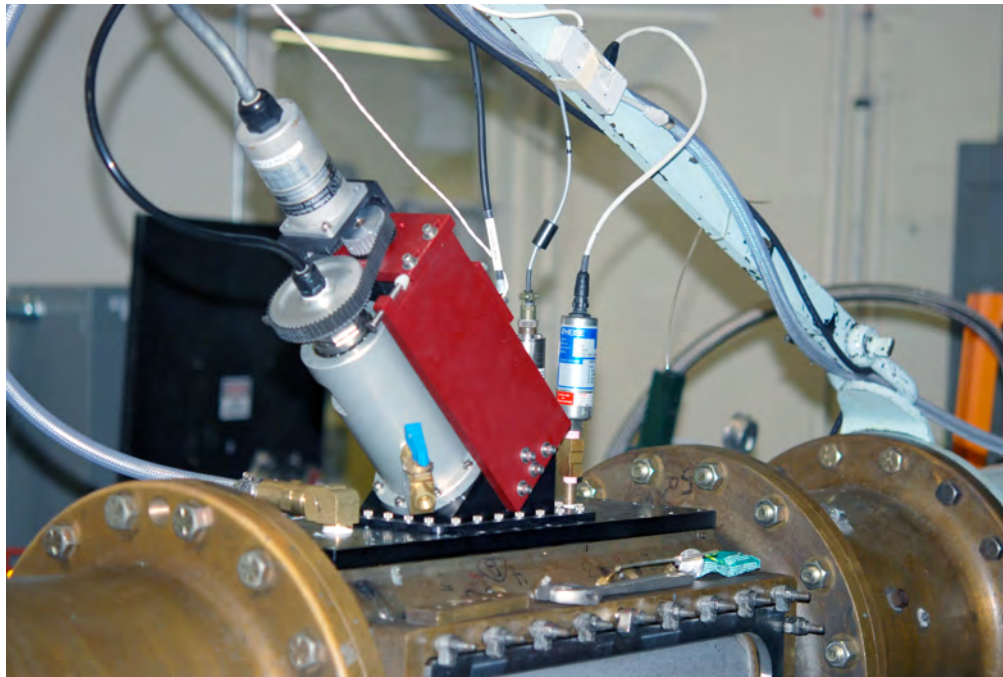


Figure C.5: Swept fin test apparatus, set up with a fin swept to 45 degrees.

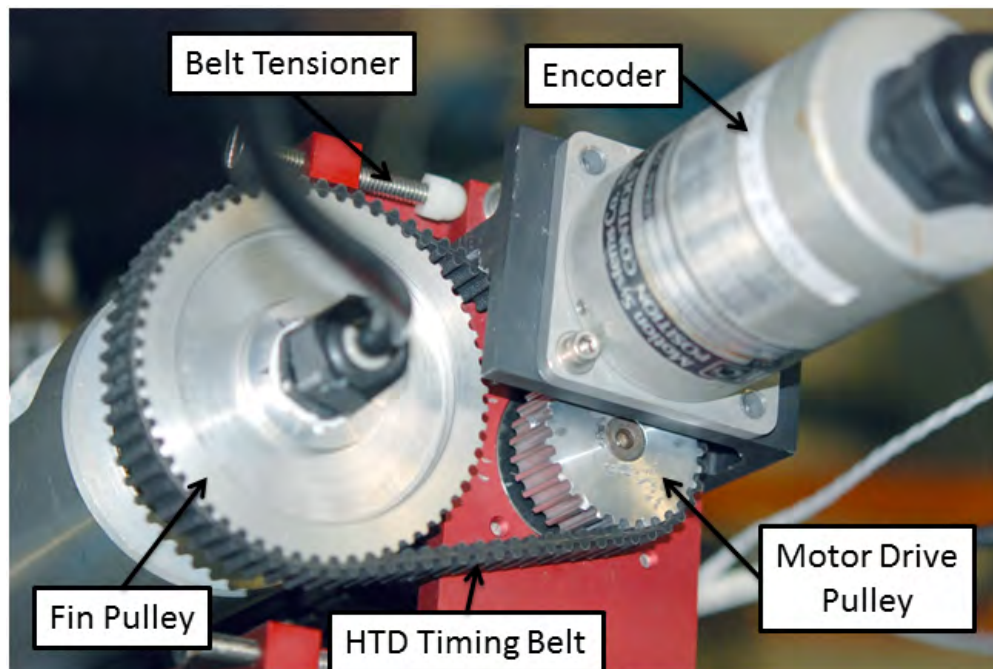


Figure C.6: Timing belt driven fin actuation mechanism used during swept fin testing, showing drive pulley, encoder, and fin pulley.

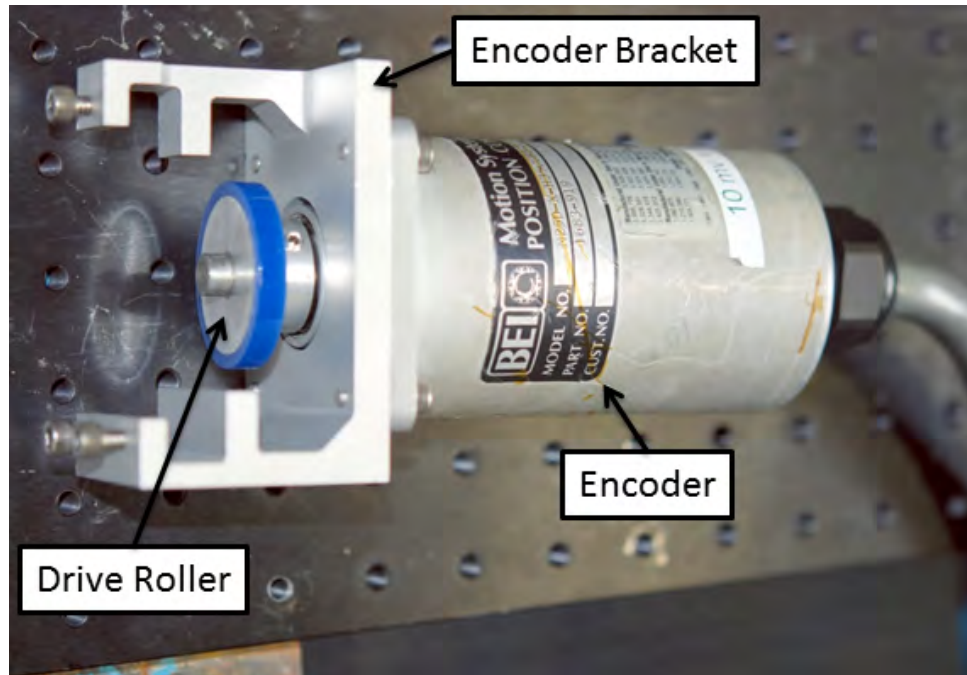


Figure C.7: Encoder on mounting bracket with drive roller used in for the first third of testing. This roller was later replaced with a timing belt pulley

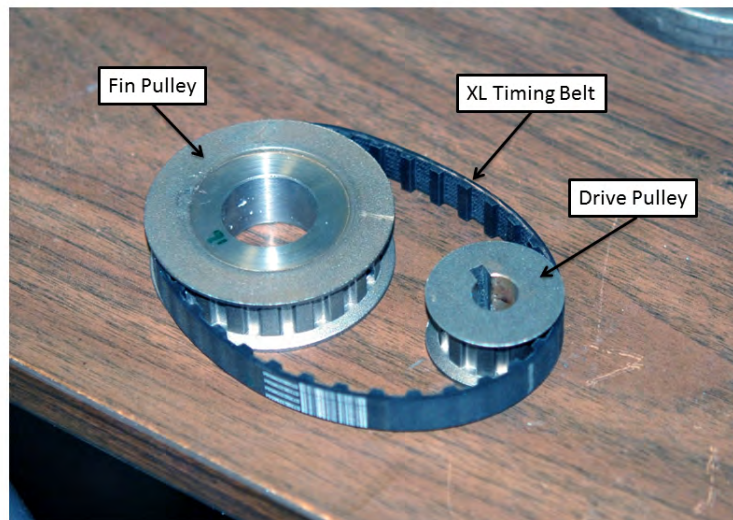


Figure C.8: Single sided XL timing belt drive system used for the first third of testing. Encoder was driven off the flat side of timing belt. This system was later replaced with a double sided HTD timing belt shown in fig. C.6.



Figure C.9: Encoder resolver used to monitor fin's angle of attack.

Appendix D

Plots of Steady State Data

Plots of steady state data are presented in this section. The measured lift, drag, normal force, tangent force, shaft torque (M_z), lift coefficient, drag coefficient and moment coefficient are plotted against angle of attack and tunnel velocity. Sign conventions are shown in fig. 1.6.

D.1 Measured Lift

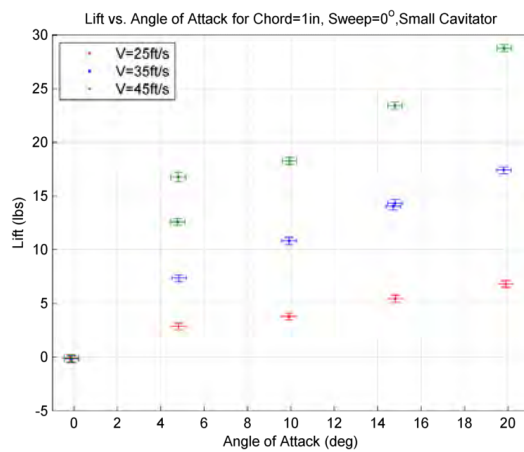


Figure D.1: Lift vs. Angle of Attack and Tunnel Velocity, 1 inch chord, $\gamma = 0^\circ$, small cavitator

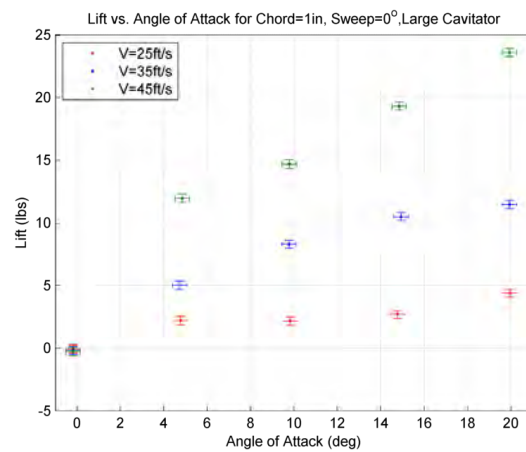


Figure D.2: Lift vs. Angle of Attack and Tunnel Velocity, 1 inch chord, $\gamma = 0^\circ$, large cavitator

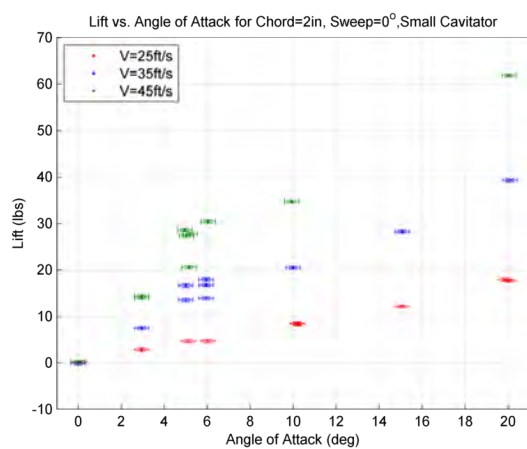


Figure D.3: Lift vs. Angle of Attack and Tunnel Velocity, 2 inch chord, $\gamma = 0^\circ$, small cavitator

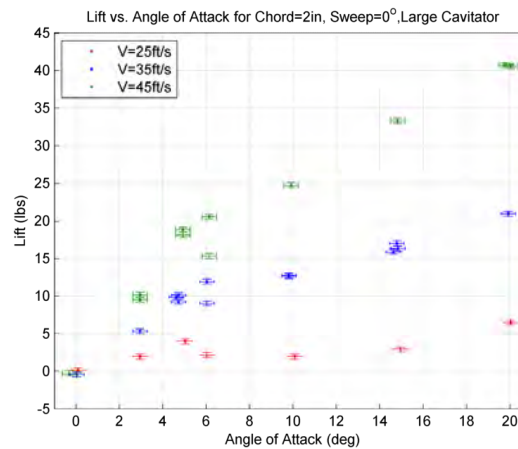


Figure D.4: Lift vs. Angle of Attack and Tunnel Velocity, 2 inch chord, $\gamma = 0^\circ$, large cavitator

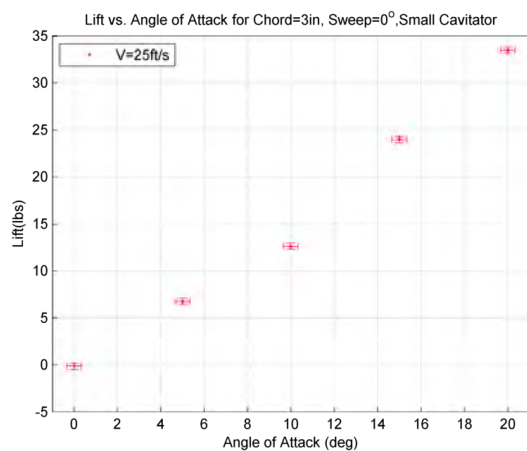


Figure D.5: Lift vs. Angle of Attack and Tunnel Velocity, 3 inch chord, $\gamma = 0^\circ$, small cavitator

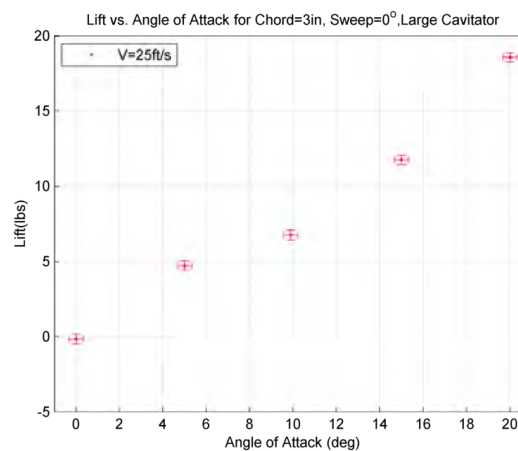


Figure D.6: Lift vs. Angle of Attack and Tunnel Velocity, 3 inch chord, $\gamma = 0^\circ$, large cavitator

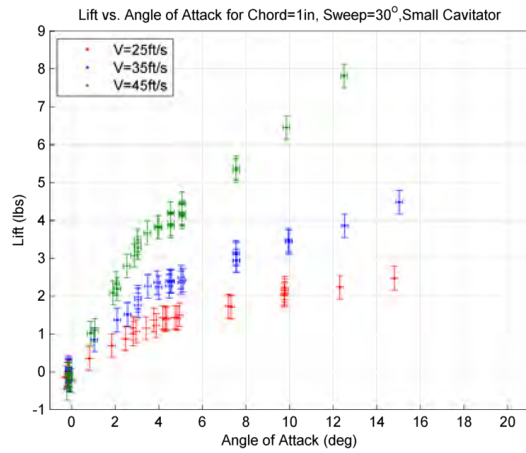


Figure D.7: Lift vs. Angle of Attack and Tunnel Velocity, 1 inch chord, $\gamma = 30^\circ$, small cavitator

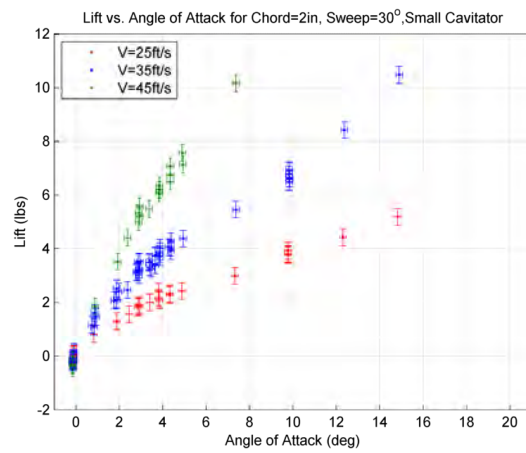


Figure D.8: Lift vs. Angle of Attack and Tunnel Velocity, 2 inch chord, $\gamma = 30^\circ$, small cavitator

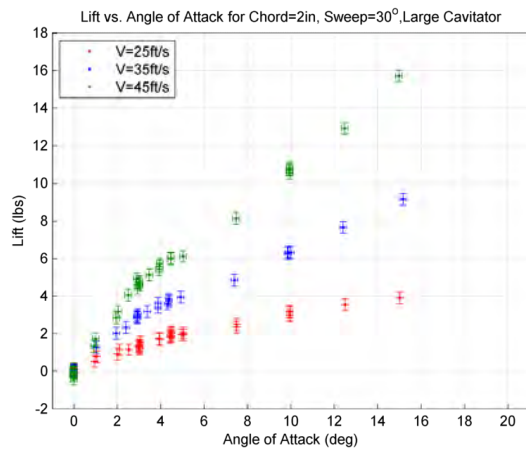


Figure D.9: Lift vs. Angle of Attack and Tunnel Velocity, 2 inch chord, $\gamma = 30^\circ$, large cavitator

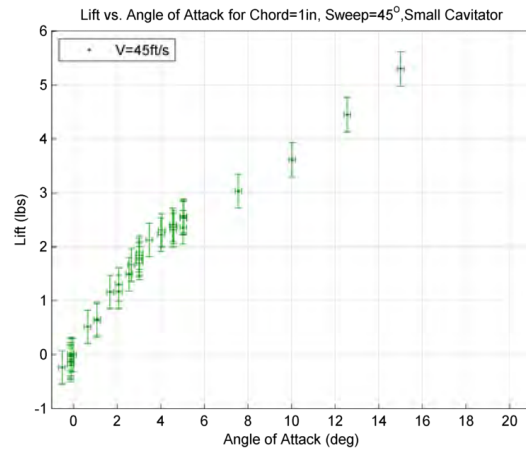


Figure D.10: Lift vs. Angle of Attack and Tunnel Velocity, 1 inch chord, $\gamma = 45^\circ$, small cavitator

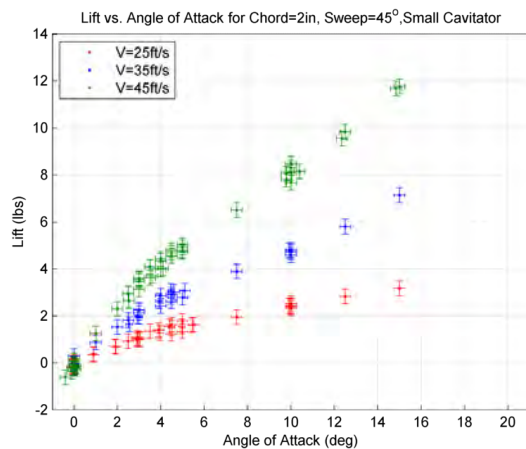


Figure D.11: Lift vs. Angle of Attack and Tunnel Velocity, 2 inch chord, $\gamma = 45^\circ$, small cavitator

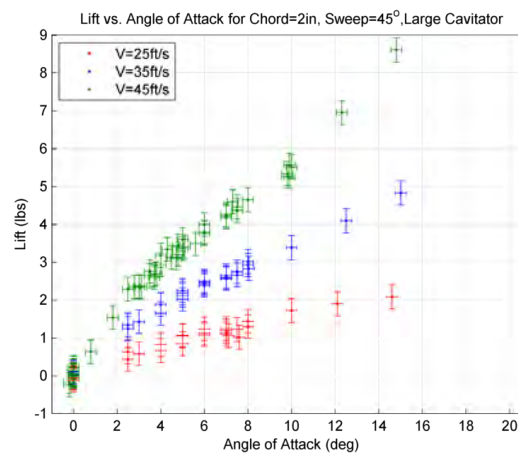


Figure D.12: Lift vs. Angle of Attack and Tunnel Velocity, 2 inch chord, $\gamma = 45^\circ$, large cavitator

D.2 Measured Drag

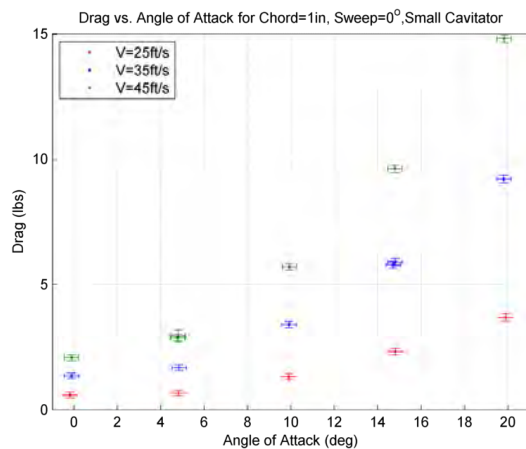


Figure D.13: Drag vs. Angle of Attack and Tunnel Velocity, 1 inch chord, $\gamma = 0^\circ$, small cavitator

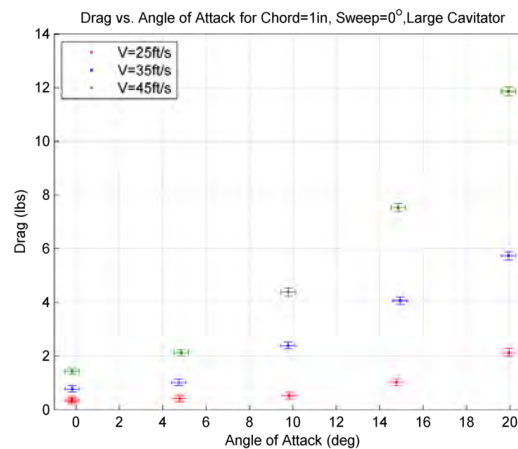


Figure D.14: Drag vs. Angle of Attack and Tunnel Velocity, 1 inch chord, $\gamma = 0^\circ$, large cavitator

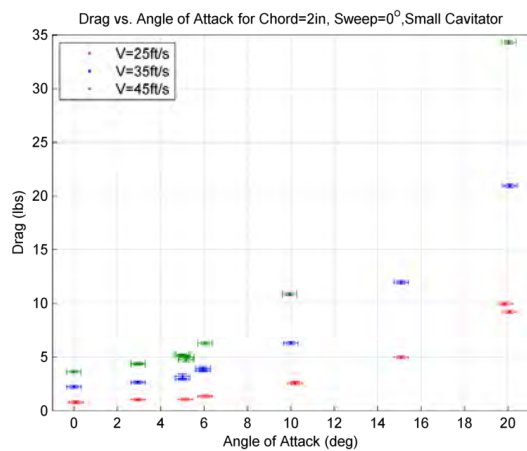


Figure D.15: Drag vs. Angle of Attack and Tunnel Velocity, 2 inch chord, $\gamma = 0^\circ$, small cavitator

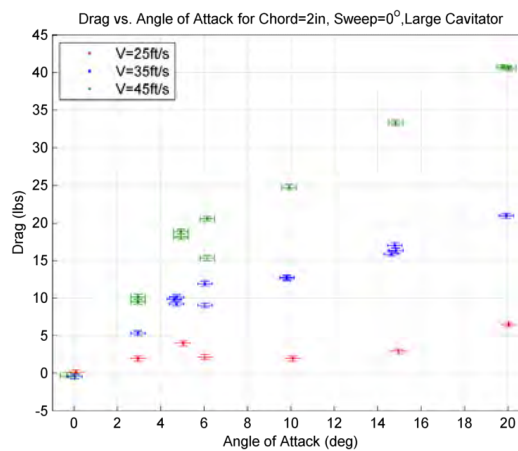


Figure D.16: Drag vs. Angle of Attack and Tunnel Velocity, 2 inch chord, $\gamma = 0^\circ$, large cavitator

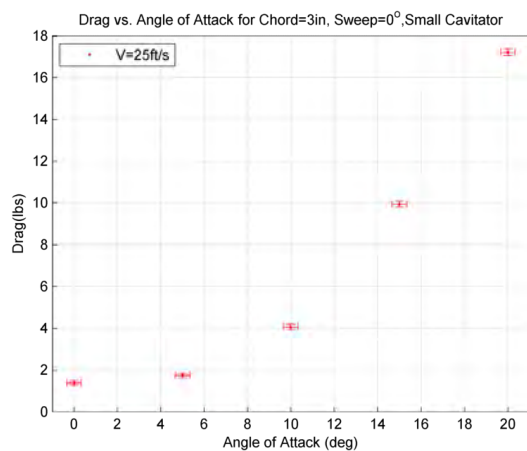


Figure D.17: Drag vs. Angle of Attack and Tunnel Velocity, 3 inch chord, $\gamma = 0^\circ$, small cavitator

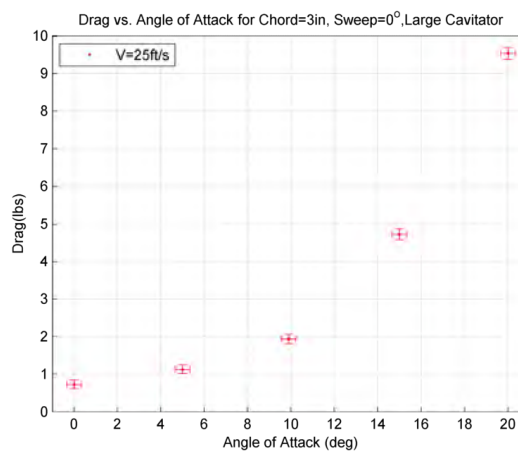


Figure D.18: Drag vs. Angle of Attack and Tunnel Velocity, 3 inch chord, $\gamma = 0^\circ$, large cavitator

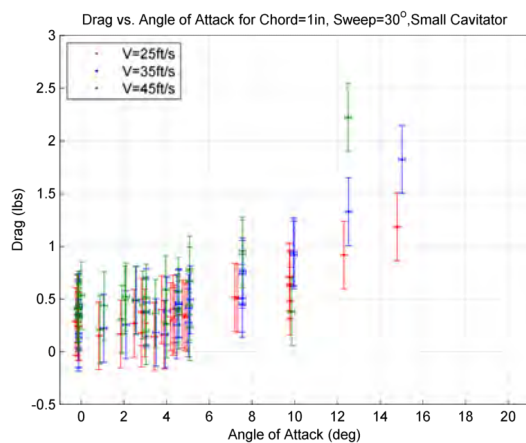


Figure D.19: Drag vs. Angle of Attack and Tunnel Velocity, 1 inch chord, $\gamma = 30^\circ$, small cavitor

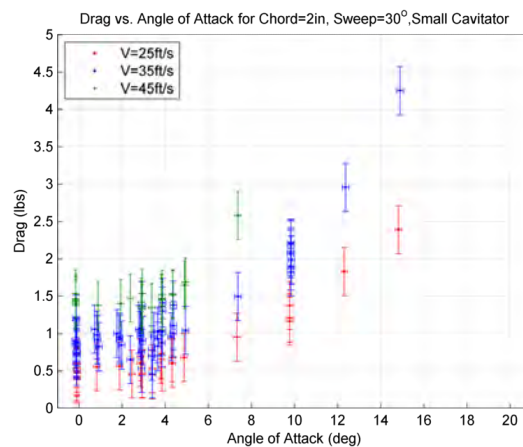


Figure D.20: Drag vs. Angle of Attack and Tunnel Velocity, 2 inch chord, $\gamma = 30^\circ$, small cavitor

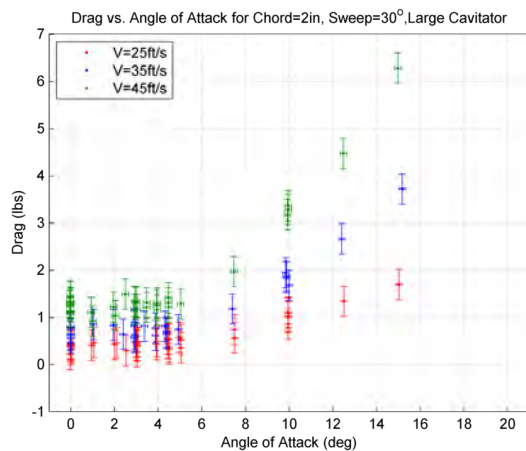


Figure D.21: Drag vs. Angle of Attack and Tunnel Velocity, 2 inch chord, $\gamma = 30^\circ$, large cavitor

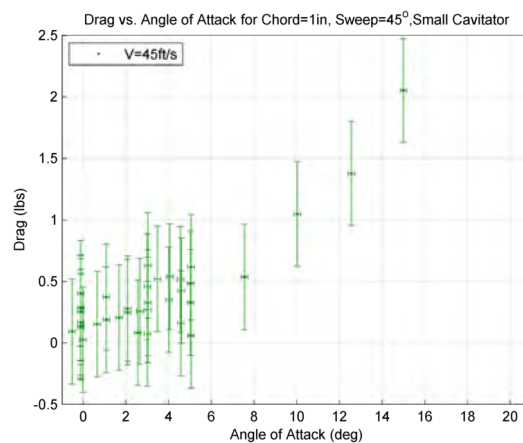


Figure D.22: Drag vs. Angle of Attack and Tunnel Velocity, 1 inch chord, $\gamma = 45^\circ$, small cavitor

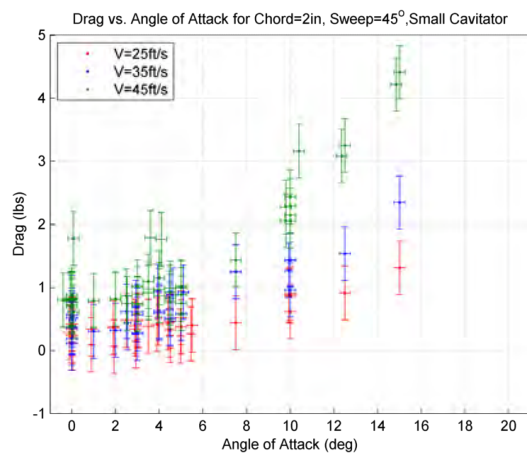


Figure D.23: Drag vs. Angle of Attack and Tunnel Velocity, 2 inch chord, $\gamma = 45^\circ$, small cavitation

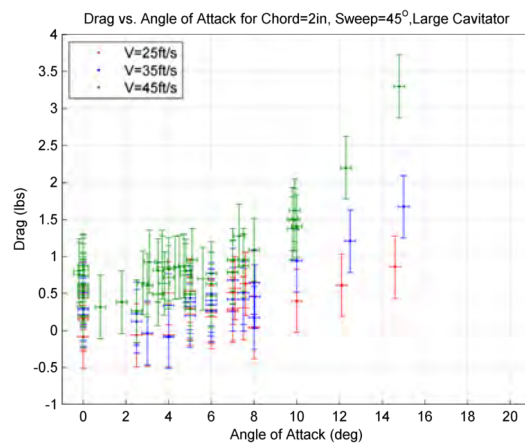


Figure D.24: Drag vs. Angle of Attack and Tunnel Velocity, 2 inch chord, $\gamma = 45^\circ$, large cavitation

D.3 Measured Normal Force

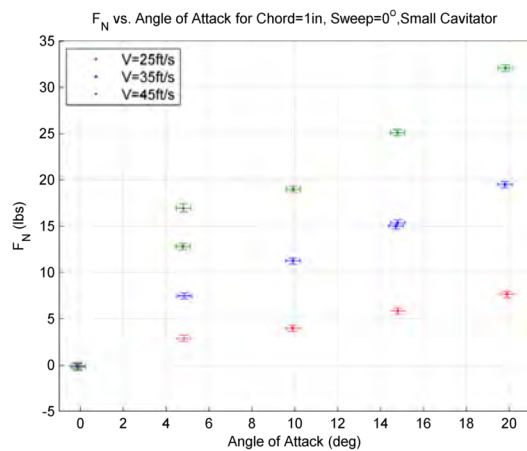


Figure D.25: Normal Force F_N vs. Angle of Attack and Tunnel Velocity, 1 inch chord, $\gamma = 0^\circ$, small cavitation

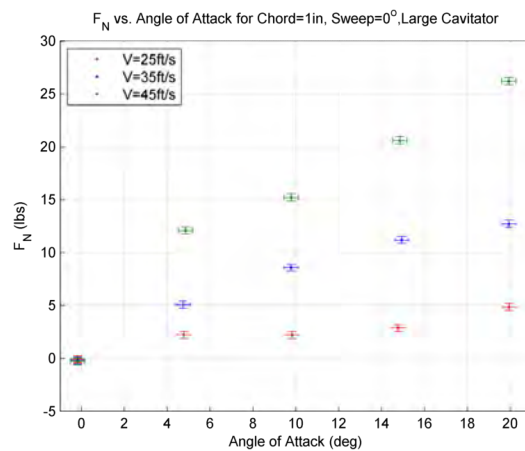


Figure D.26: Normal Force F_N vs. Angle of Attack and Tunnel Velocity, 1 inch chord, $\gamma = 0^\circ$, large cavitation

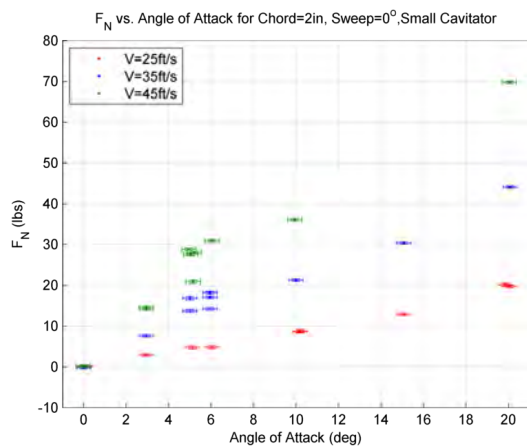


Figure D.27: Normal Force F_N vs. Angle of Attack and Tunnel Velocity, 2 inch chord, $\gamma = 0^\circ$, small cavitator

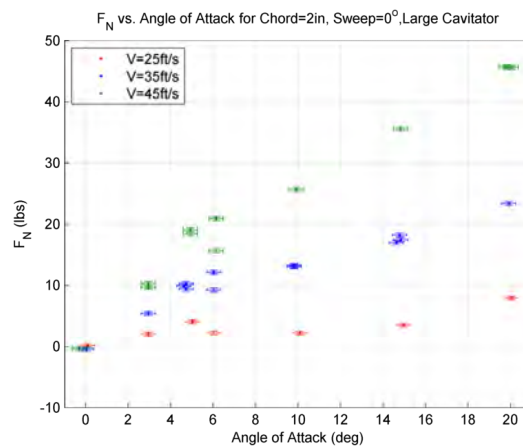


Figure D.28: Normal Force F_N vs. Angle of Attack and Tunnel Velocity, 2 inch chord, $\gamma = 0^\circ$, large cavitator

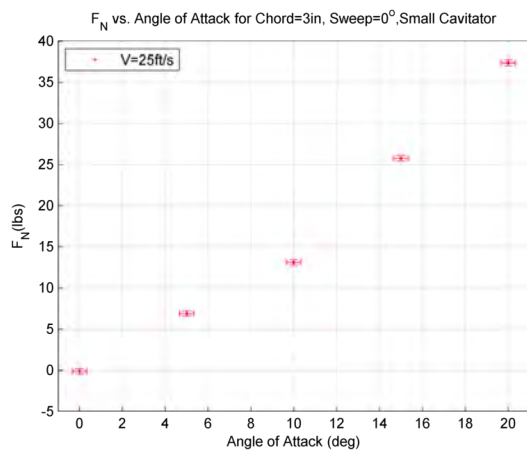


Figure D.29: Normal Force F_N vs. Angle of Attack and Tunnel Velocity, 3 inch chord, $\gamma = 0^\circ$, small cavitator

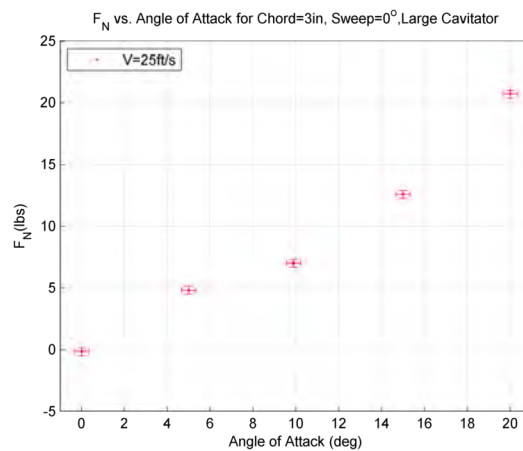


Figure D.30: Normal Force F_N vs. Angle of Attack and Tunnel Velocity, 3 inch chord, $\gamma = 0^\circ$, large cavitator

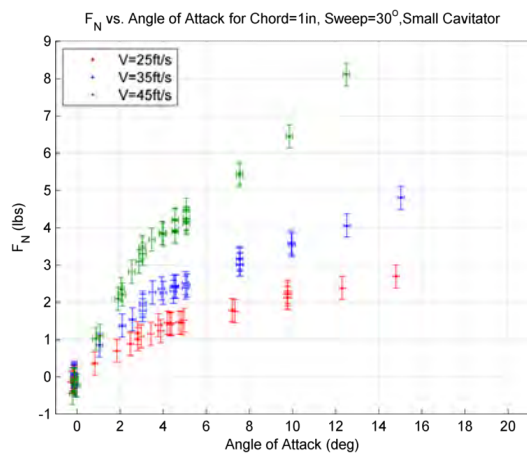


Figure D.31: Normal Force F_N vs. Angle of Attack and Tunnel Velocity, 1 inch chord, $\gamma = 30^\circ$, small cavitator

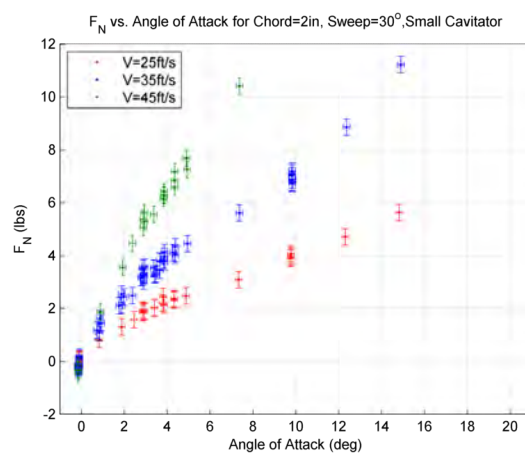


Figure D.32: Normal Force F_N vs. Angle of Attack and Tunnel Velocity, 2 inch chord, $\gamma = 30^\circ$, small cavitator

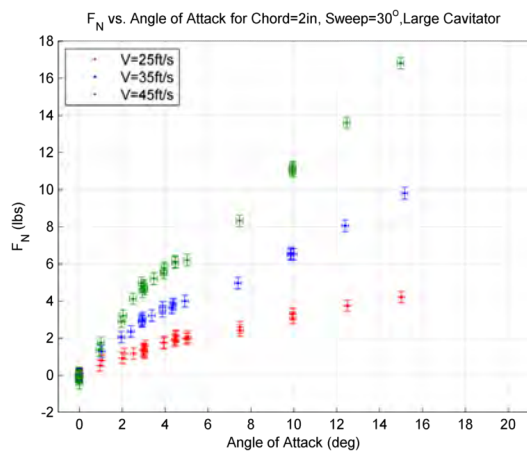


Figure D.33: Normal Force F_N vs. Angle of Attack and Tunnel Velocity, 2 inch chord, $\gamma = 30^\circ$, large cavitator

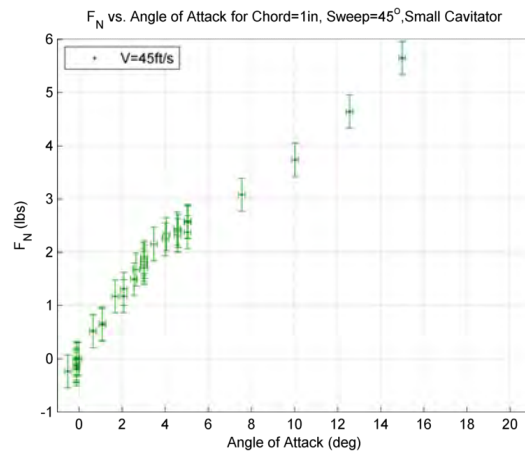


Figure D.34: Normal Force F_N vs. Angle of Attack and Tunnel Velocity, 1 inch chord, $\gamma = 45^\circ$, small cavitator

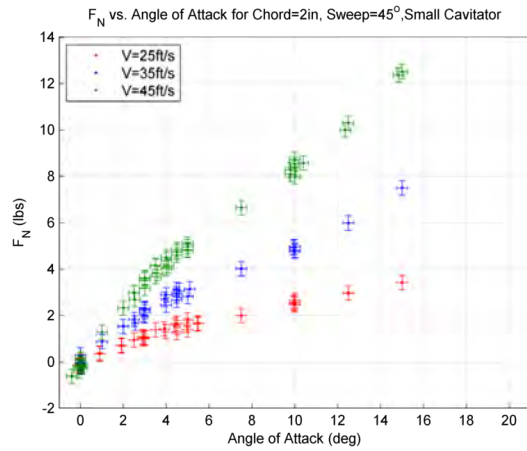


Figure D.35: Normal Force F_N vs. Angle of Attack and Tunnel Velocity, 2 inch chord, $\gamma = 45^\circ$, small cavitator

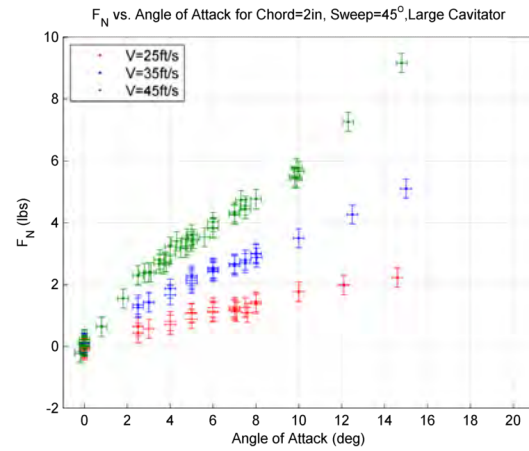


Figure D.36: Normal Force F_N vs. Angle of Attack and Tunnel Velocity, 2 inch chord, $\gamma = 45^\circ$, large cavitator

D.4 Measured Tangent Force

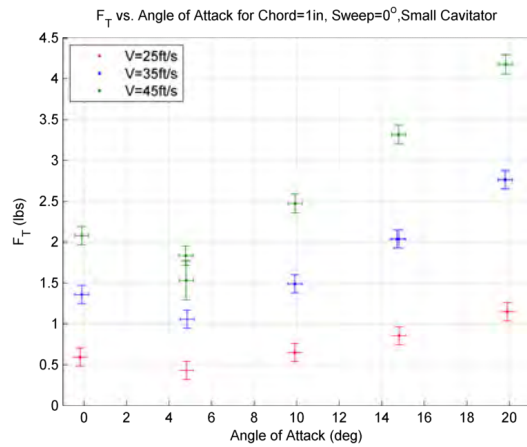


Figure D.37: Tangent Force F_T vs. Angle of Attack and Tunnel Velocity, 1 inch chord, $\gamma = 0^\circ$, small cavitator

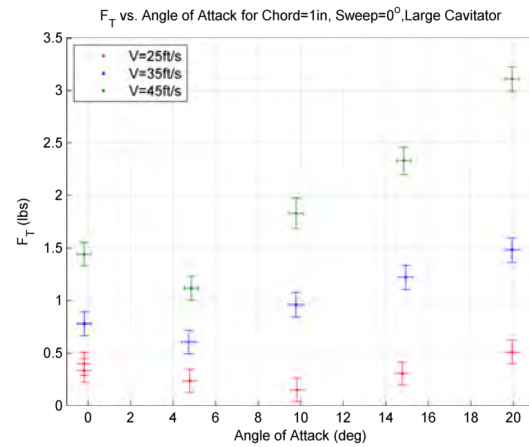


Figure D.38: Tangent Force F_T vs. Angle of Attack and Tunnel Velocity, 1 inch chord, $\gamma = 0^\circ$, large cavitator

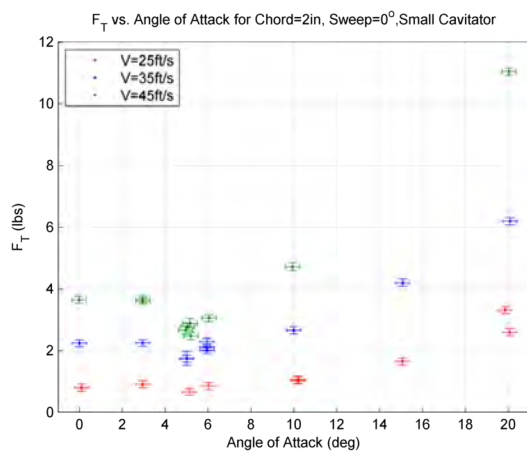


Figure D.39: Tangent Force F_T vs. Angle of Attack and Tunnel Velocity, 2 inch chord, $\gamma = 0^\circ$, small cavitator

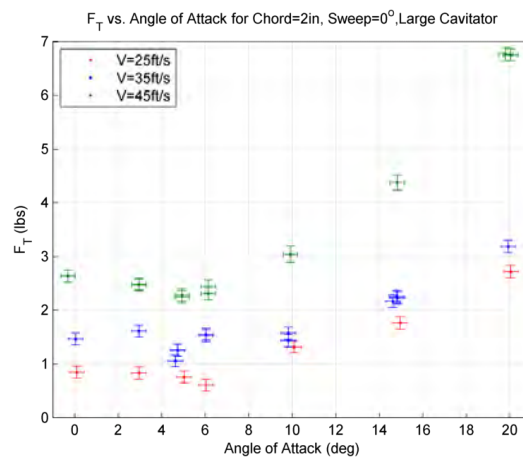


Figure D.40: Tangent Force F_T vs. Angle of Attack and Tunnel Velocity, 2 inch chord, $\gamma = 0^\circ$, large cavitator

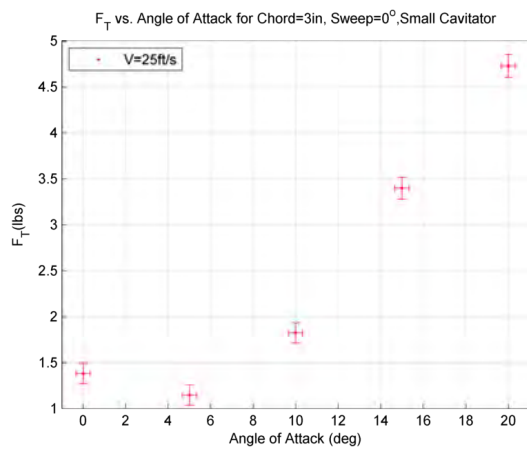


Figure D.41: Tangent Force F_T vs. Angle of Attack and Tunnel Velocity, 3 inch chord, $\gamma = 0^\circ$, small cavitator

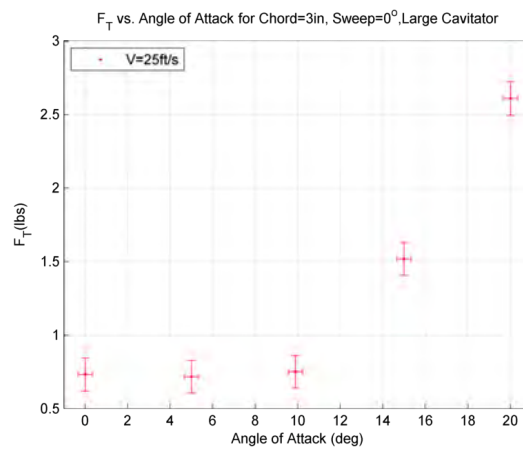


Figure D.42: Tangent Force F_T vs. Angle of Attack and Tunnel Velocity, 3 inch chord, $\gamma = 0^\circ$, large cavitator

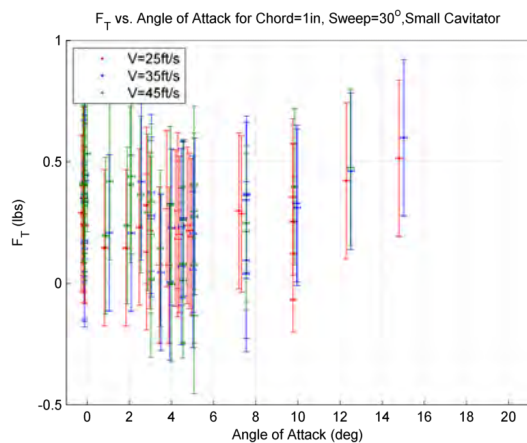


Figure D.43: Tangent Force F_T vs. Angle of Attack and Tunnel Velocity, 1 inch chord, $\gamma = 30^\circ$, small cavitator

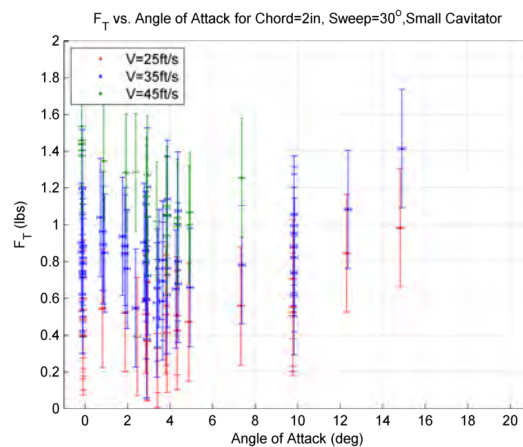


Figure D.44: Tangent Force F_T vs. Angle of Attack and Tunnel Velocity, 2 inch chord, $\gamma = 30^\circ$, small cavitator

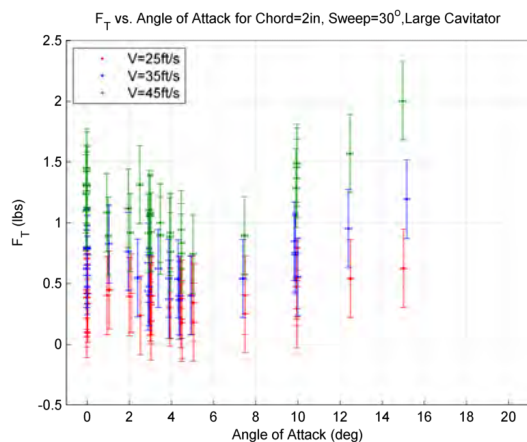


Figure D.45: Tangent Force F_T vs. Angle of Attack and Tunnel Velocity, 2 inch chord, $\gamma = 30^\circ$, large cavitator

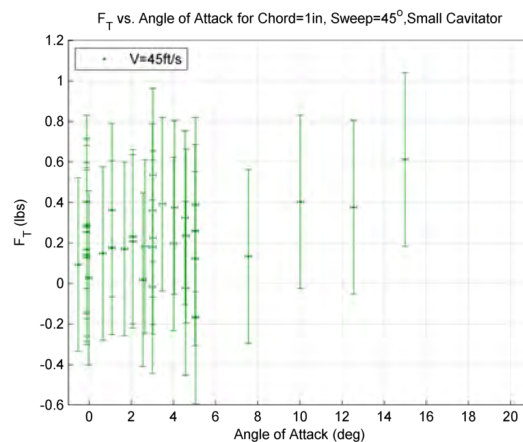


Figure D.46: Tangent Force F_T vs. Angle of Attack and Tunnel Velocity, 1 inch chord, $\gamma = 45^\circ$, small cavitator

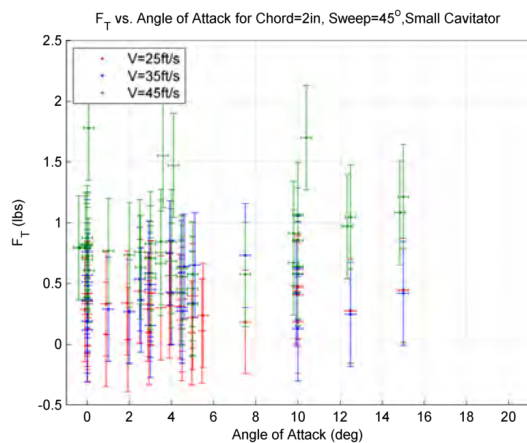


Figure D.47: Tangent Force F_τ vs. Angle of Attack and Tunnel Velocity, 2 inch chord, $\gamma = 45^\circ$, small cavitator

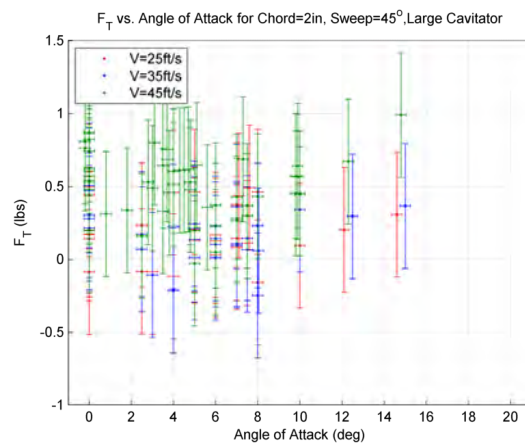


Figure D.48: Tangent Force F_τ vs. Angle of Attack and Tunnel Velocity, 2 inch chord, $\gamma = 45^\circ$, large cavitator

D.5 Measured Shaft Torque M_z

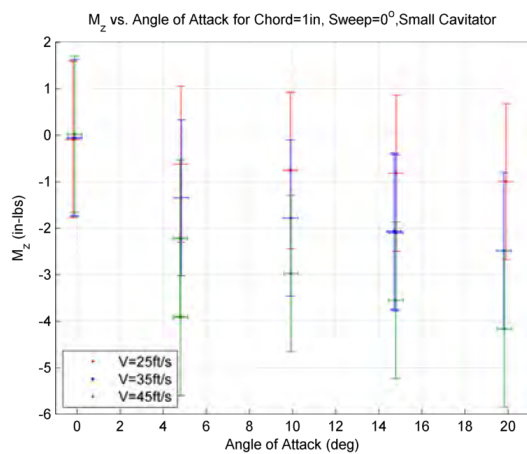


Figure D.49: Shaft Torque M_z vs. Angle of Attack and Tunnel Velocity, 1 inch chord, $\gamma = 0^\circ$, small cavitator

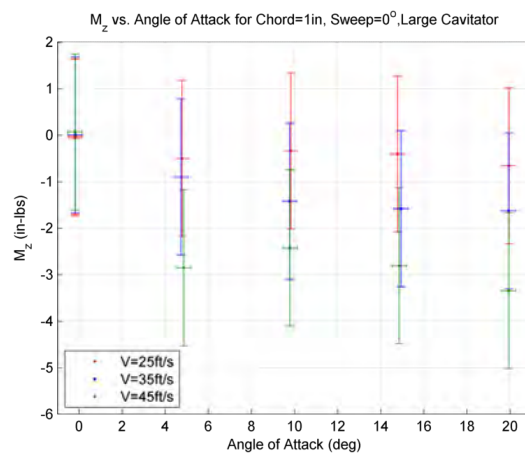


Figure D.50: Shaft Torque M_z vs. Angle of Attack and Tunnel Velocity, 1 inch chord, $\gamma = 0^\circ$, large cavitator

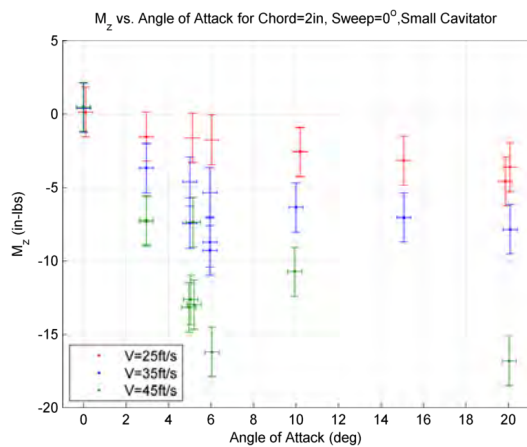


Figure D.51: Shaft Torque M_z vs. Angle of Attack and Tunnel Velocity, 2 inch chord, $\gamma = 0^\circ$, small cavitator

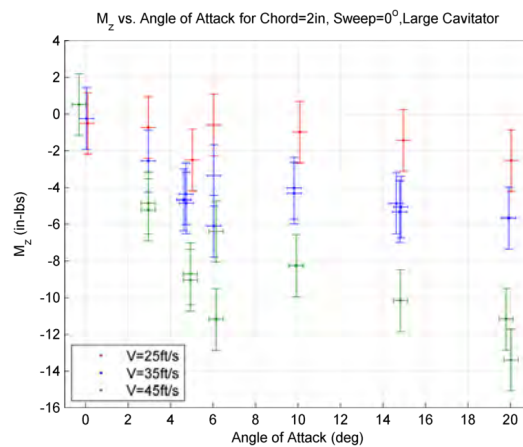


Figure D.52: Shaft Torque M_z vs. Angle of Attack and Tunnel Velocity, 2 inch chord, $\gamma = 0^\circ$, large cavitator

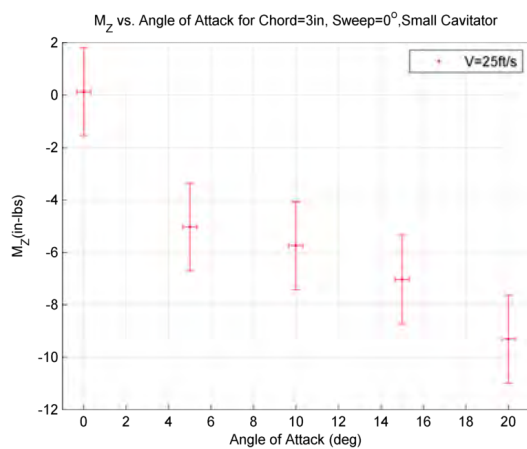


Figure D.53: Shaft Torque M_z vs. Angle of Attack and Tunnel Velocity, 3 inch chord, $\gamma = 0^\circ$, small cavitator

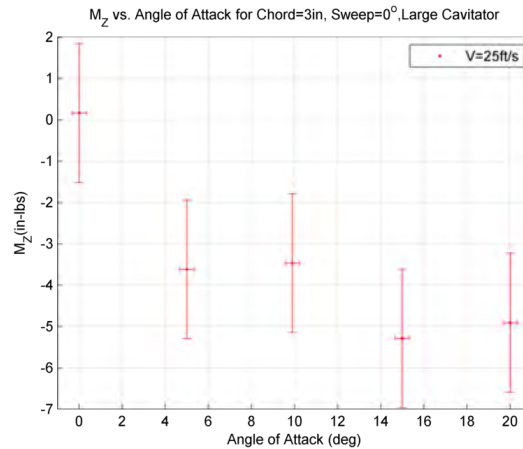


Figure D.54: Shaft Torque M_z vs. Angle of Attack and Tunnel Velocity, 3 inch chord, $\gamma = 0^\circ$, large cavitator

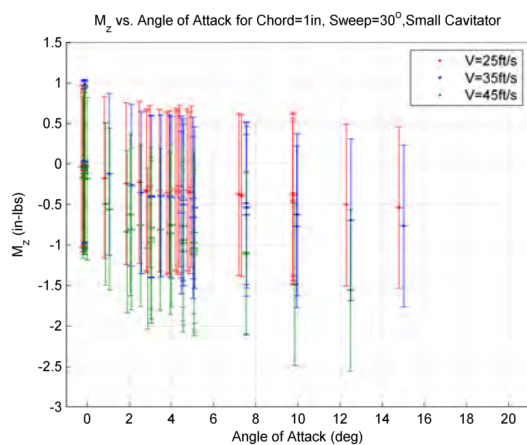


Figure D.55: Shaft Torque M_z vs. Angle of Attack and Tunnel Velocity, 1 inch chord, $\gamma = 30^\circ$, small cavitator

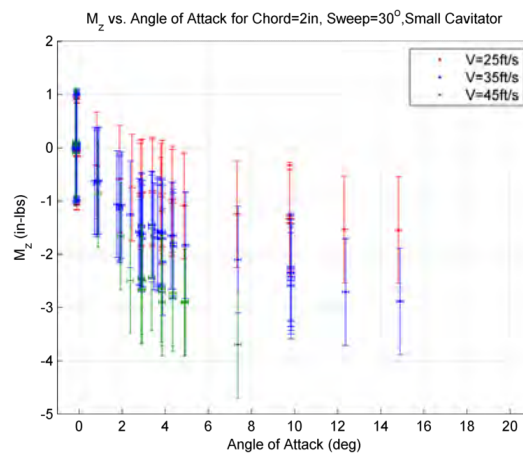


Figure D.56: Shaft Torque M_z vs. Angle of Attack and Tunnel Velocity, 2 inch chord, $\gamma = 30^\circ$, small cavitator

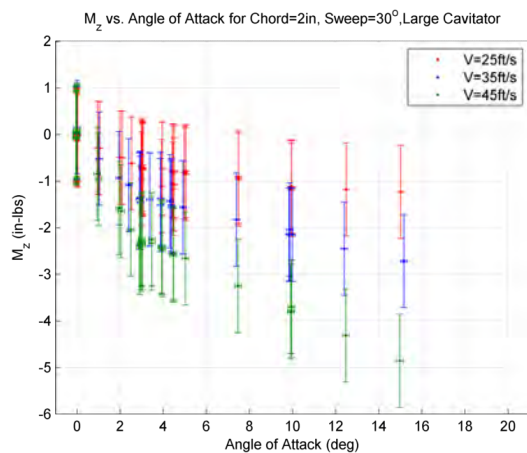


Figure D.57: Shaft Torque M_z vs. Angle of Attack and Tunnel Velocity, 2 inch chord, $\gamma = 30^\circ$, large cavitator

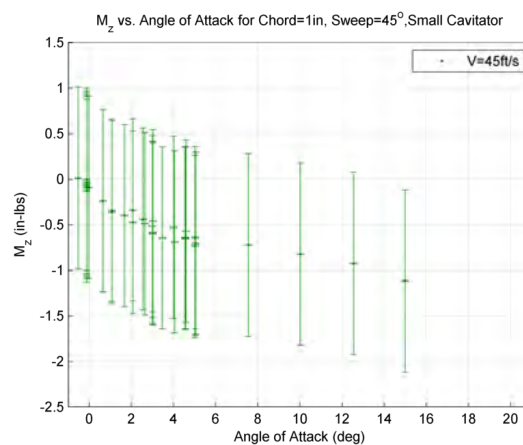


Figure D.58: Shaft Torque M_z vs. Angle of Attack and Tunnel Velocity, 1 inch chord, $\gamma = 45^\circ$, small cavitator

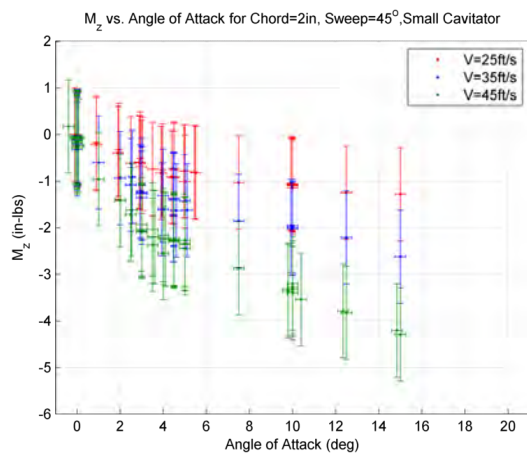


Figure D.59: Shaft Torque M_z vs. Angle of Attack and Tunnel Velocity, 2 inch chord, $\gamma = 45^\circ$, small cavitator

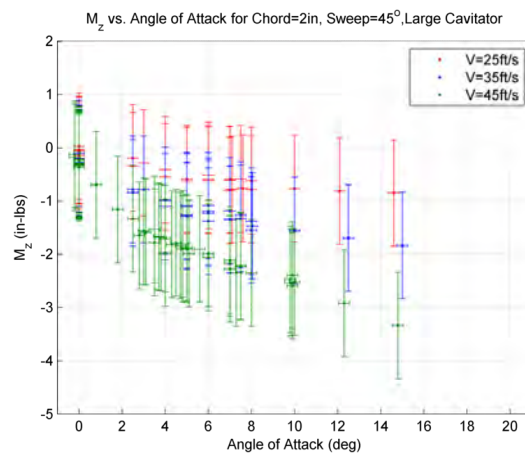


Figure D.60: Shaft Torque M_z vs. Angle of Attack and Tunnel Velocity, 2 inch chord, $\gamma = 45^\circ$, large cavitator

D.6 Measured Lift Coefficient

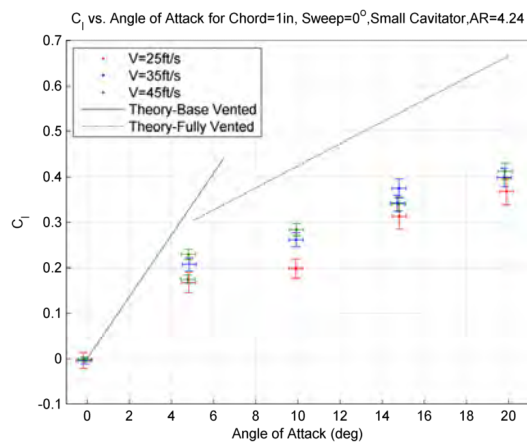


Figure D.61: Lift Coefficient C_L vs. Angle of Attack and Tunnel Velocity, 1 inch chord, $\gamma = 0^\circ$, small cavitator

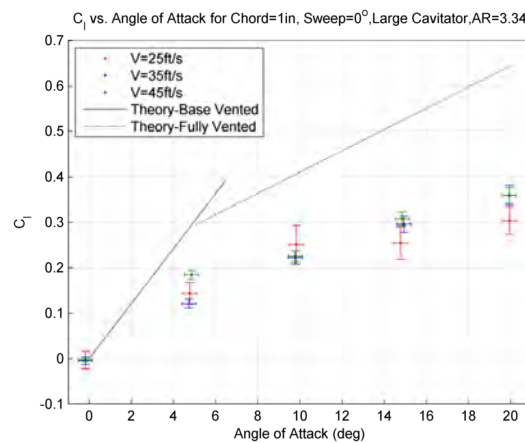


Figure D.62: Lift Coefficient C_L vs. Angle of Attack and Tunnel Velocity, 1 inch chord, $\gamma = 0^\circ$, large cavitator

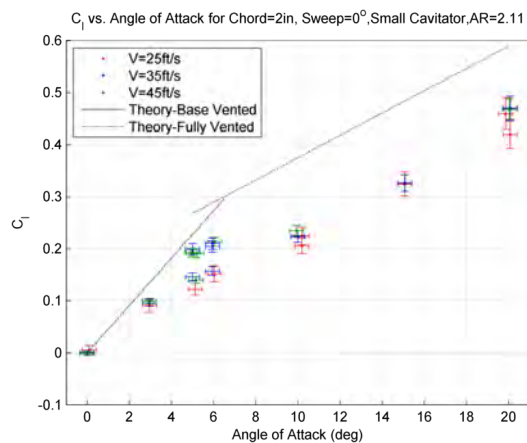


Figure D.63: Lift Coefficient C_L vs. Angle of Attack and Tunnel Velocity, 2 inch chord, $\gamma = 0^\circ$, small cavitator

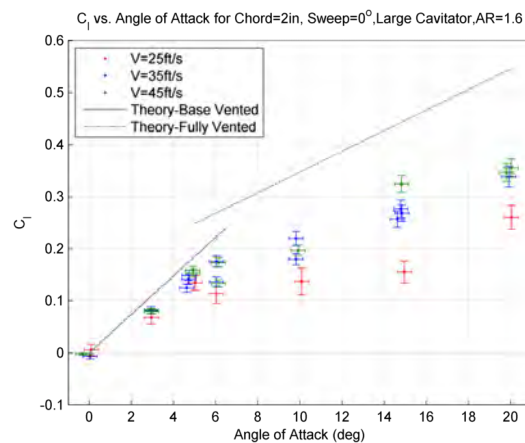


Figure D.64: Lift Coefficient C_L vs. Angle of Attack and Tunnel Velocity, 2 inch chord, $\gamma = 0^\circ$, large cavitator

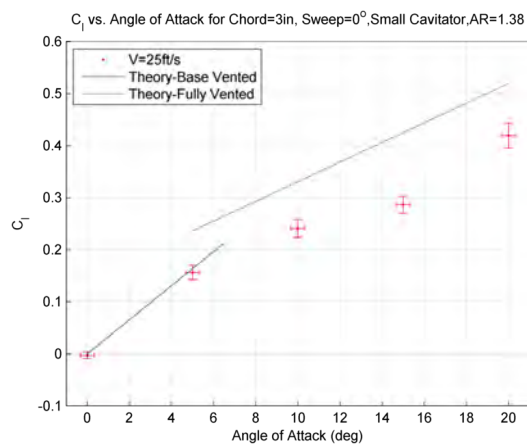


Figure D.65: Lift Coefficient C_L vs. Angle of Attack and Tunnel Velocity, 3 inch chord, $\gamma = 0^\circ$, small cavitator

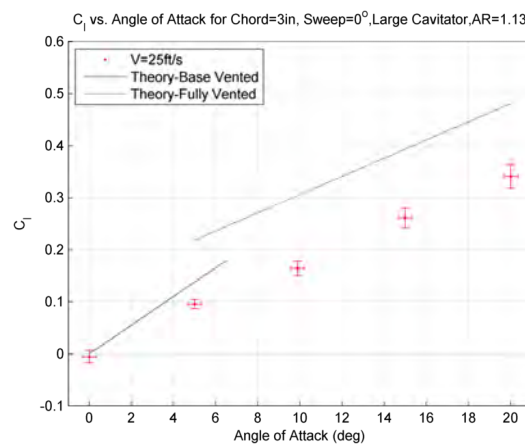


Figure D.66: Lift Coefficient C_L vs. Angle of Attack and Tunnel Velocity, 3 inch chord, $\gamma = 0^\circ$, large cavitator

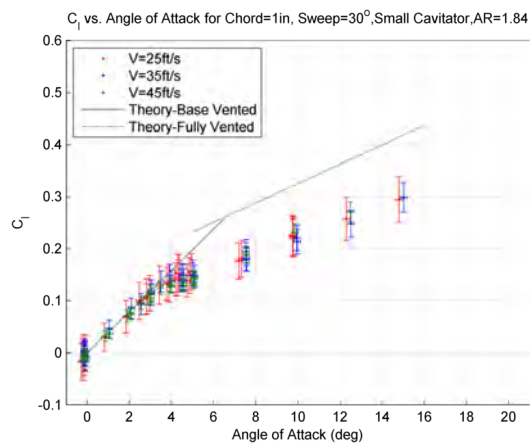


Figure D.67: Lift Coefficient C_L vs. Angle of Attack and Tunnel Velocity, 1 inch chord, $\gamma = 30^\circ$, small cavitator

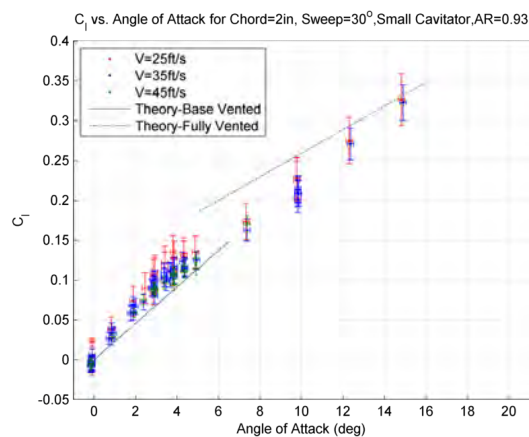


Figure D.68: Lift Coefficient C_L vs. Angle of Attack and Tunnel Velocity, 2 inch chord, $\gamma = 30^\circ$, small cavitator

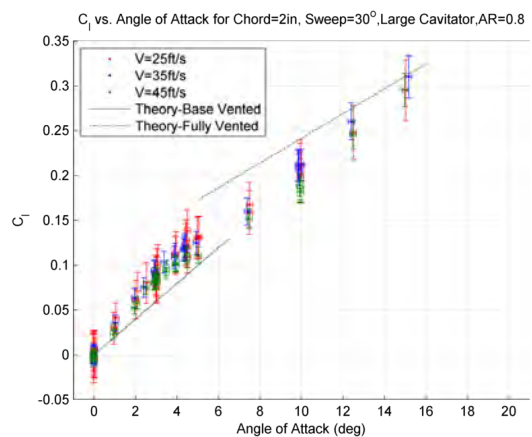


Figure D.69: Lift Coefficient C_L vs. Angle of Attack and Tunnel Velocity, 2 inch chord, $\gamma = 30^\circ$, large cavitator

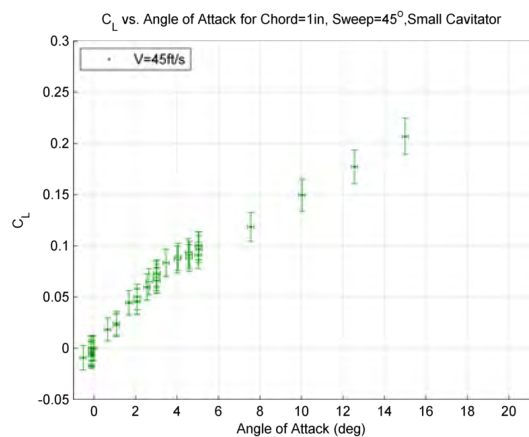


Figure D.70: Lift Coefficient C_L vs. Angle of Attack and Tunnel Velocity, 1 inch chord, $\gamma = 45^\circ$, small cavitator

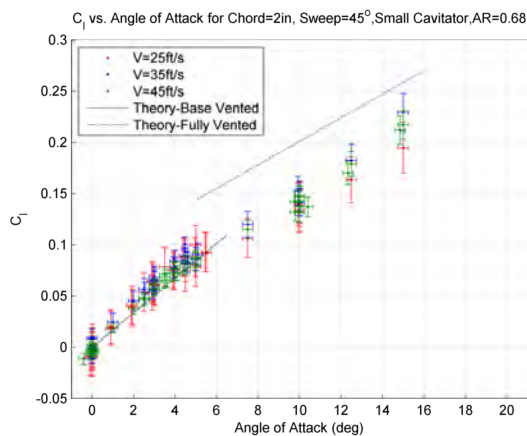


Figure D.71: Lift Coefficient C_L vs. Angle of Attack and Tunnel Velocity, 2 inch chord, $\gamma = 45^\circ$, small cavitator

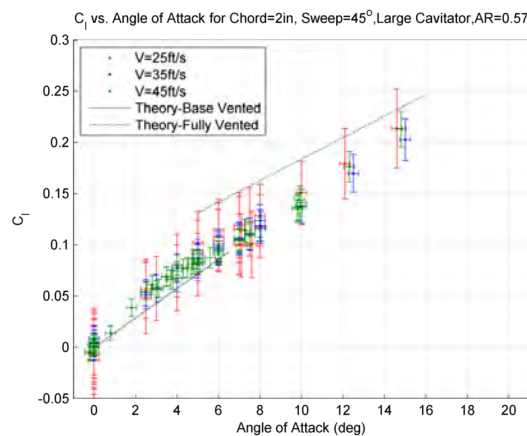


Figure D.72: Lift Coefficient C_L vs. Angle of Attack and Tunnel Velocity, 2 inch chord, $\gamma = 45^\circ$, large cavitator

D.7 Measured Drag Coefficient

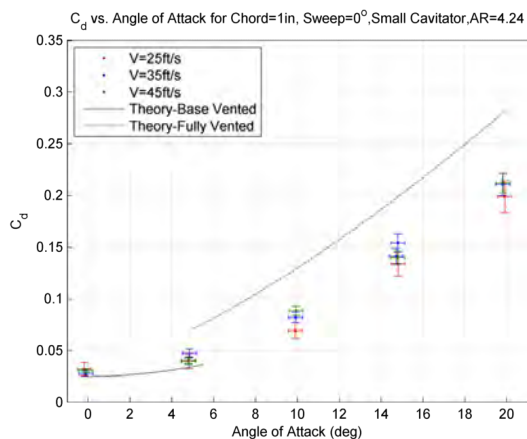


Figure D.73: Drag Coefficient C_D vs. Angle of Attack and Tunnel Velocity, 1 inch chord, $\gamma = 0^\circ$, small cavitator

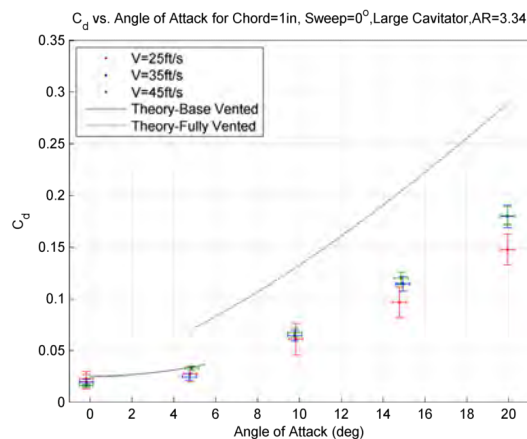


Figure D.74: Drag Coefficient C_D vs. Angle of Attack and Tunnel Velocity, 1 inch chord, $\gamma = 0^\circ$, large cavitator

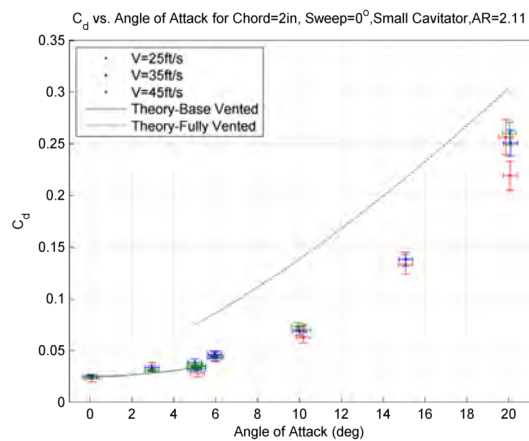


Figure D.75: Drag Coefficient C_D vs. Angle of Attack and Tunnel Velocity, 2 inch chord, $\gamma = 0^\circ$, small cavitator

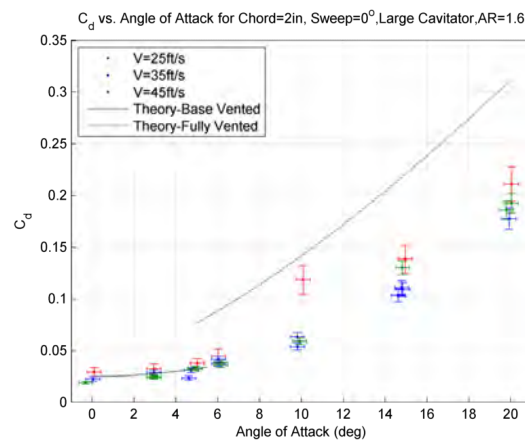


Figure D.76: Drag Coefficient C_D vs. Angle of Attack and Tunnel Velocity, 2 inch chord, $\gamma = 0^\circ$, large cavitator

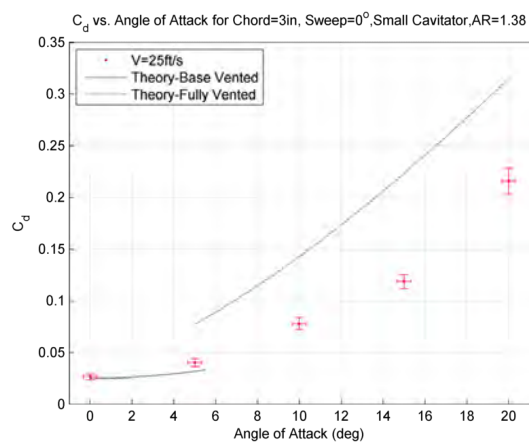


Figure D.77: Drag Coefficient C_D vs. Angle of Attack and Tunnel Velocity, 3 inch chord, $\gamma = 0^\circ$, small cavitator

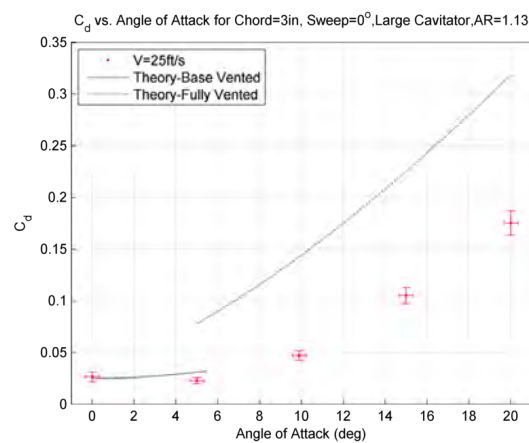


Figure D.78: Drag Coefficient C_D vs. Angle of Attack and Tunnel Velocity, 3 inch chord, $\gamma = 0^\circ$, large cavitator

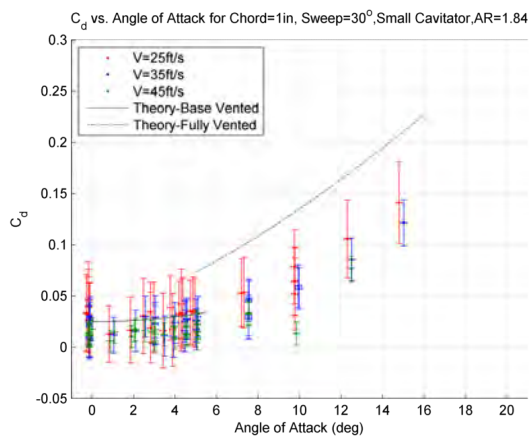


Figure D.79: Drag Coefficient C_D vs. Angle of Attack and Tunnel Velocity, 1 inch chord, $\gamma = 30^\circ$, small cavitator

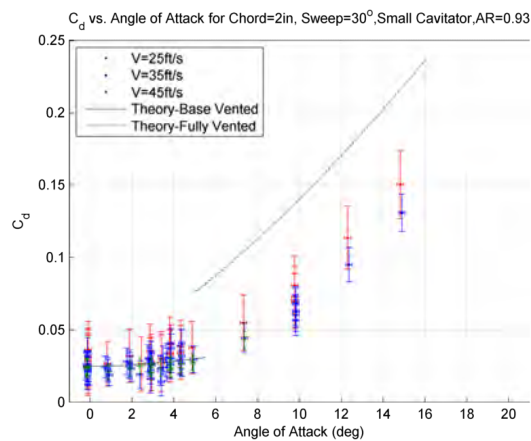


Figure D.80: Drag Coefficient C_D vs. Angle of Attack and Tunnel Velocity, 2 inch chord, $\gamma = 30^\circ$, small cavitator

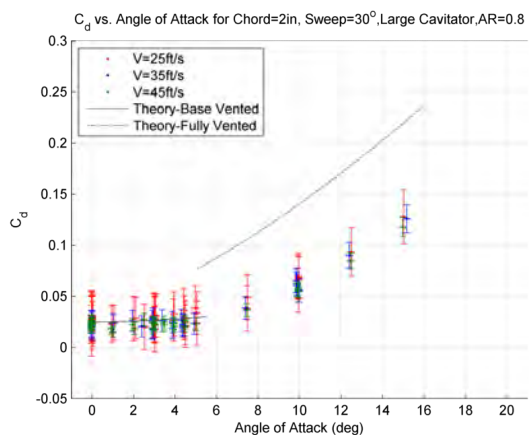


Figure D.81: Drag Coefficient C_D vs. Angle of Attack and Tunnel Velocity, 2 inch chord, $\gamma = 30^\circ$, large cavitator

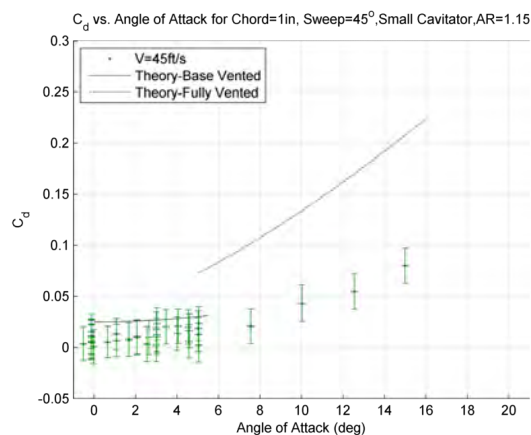


Figure D.82: Drag Coefficient C_D vs. Angle of Attack and Tunnel Velocity, 1 inch chord, $\gamma = 45^\circ$, small cavitator

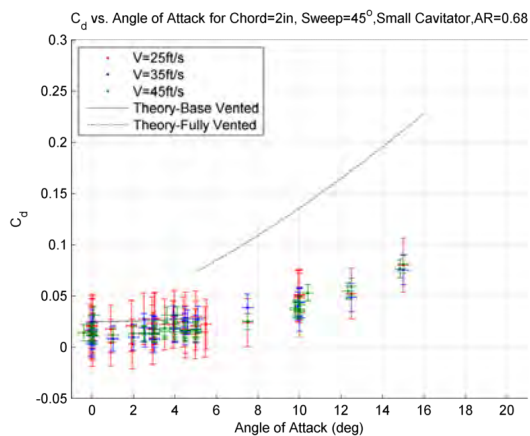


Figure D.83: Drag Coefficient C_D vs. Angle of Attack and Tunnel Velocity, 2 inch chord, $\gamma = 45^\circ$, small cavitator

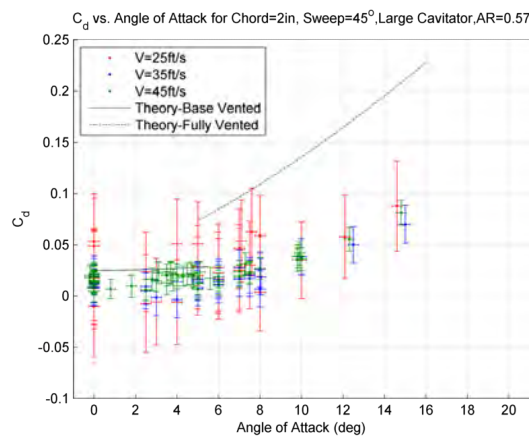


Figure D.84: Drag Coefficient C_D vs. Angle of Attack and Tunnel Velocity, 2 inch chord, $\gamma = 45^\circ$, large cavitator

D.8 Measured Moment Coefficient

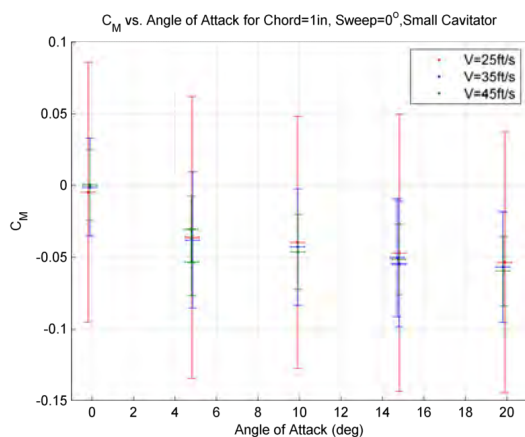


Figure D.85: Moment Coefficient C_M vs. Angle of Attack and Tunnel Velocity, 1 inch chord, $\gamma = 0^\circ$, small cavitator

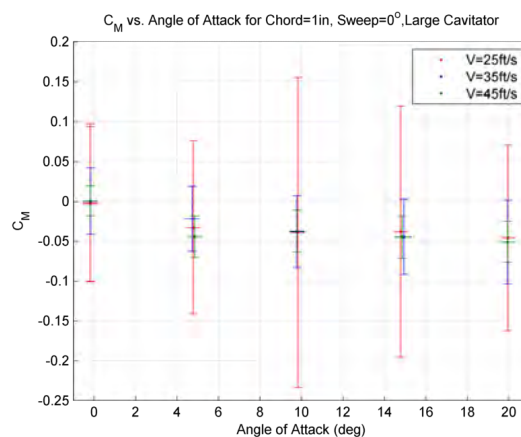


Figure D.86: Moment Coefficient C_M vs. Angle of Attack and Tunnel Velocity, 1 inch chord, $\gamma = 0^\circ$, large cavitator

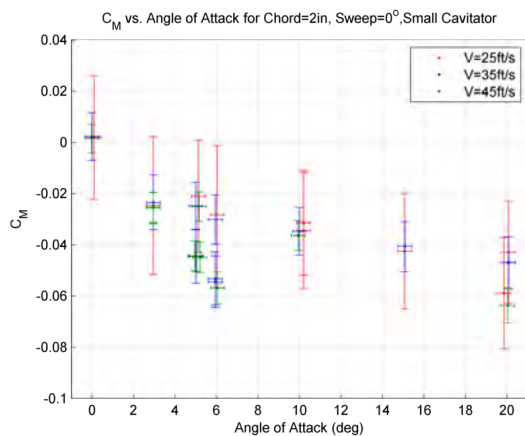


Figure D.87: Moment Coefficient C_M vs. Angle of Attack and Tunnel Velocity, 2 inch chord, $\gamma = 0^\circ$, small cavitator

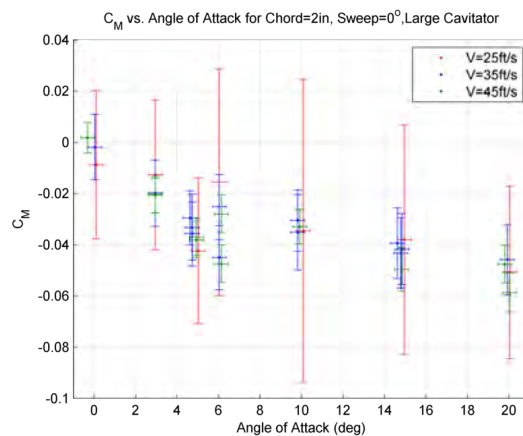


Figure D.88: Moment Coefficient C_M vs. Angle of Attack and Tunnel Velocity, 2 inch chord, $\gamma = 0^\circ$, large cavitator

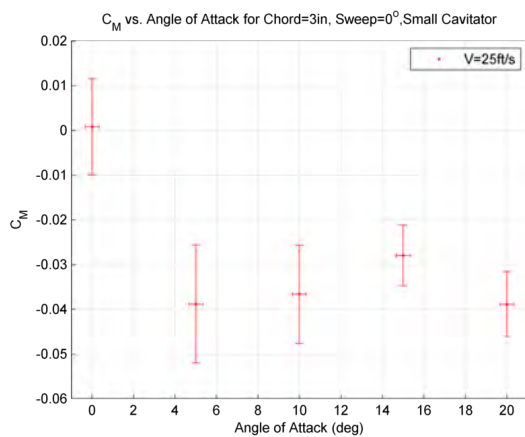


Figure D.89: Moment Coefficient C_M vs. Angle of Attack and Tunnel Velocity, 3 inch chord, $\gamma = 0^\circ$, small cavitator

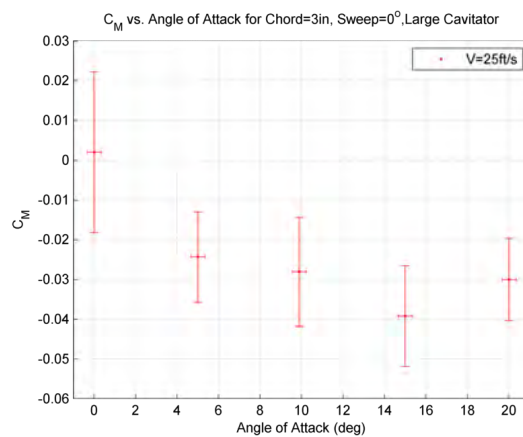


Figure D.90: Moment Coefficient C_M vs. Angle of Attack and Tunnel Velocity, 3 inch chord, $\gamma = 0^\circ$, large cavitator

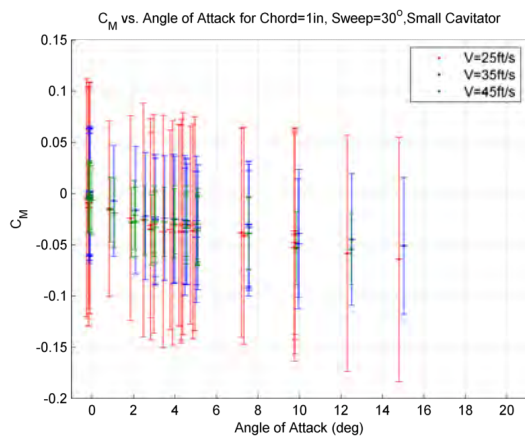


Figure D.91: Moment Coefficient C_M vs. Angle of Attack and Tunnel Velocity, 1 inch chord, $\gamma = 30^\circ$, small cavitator

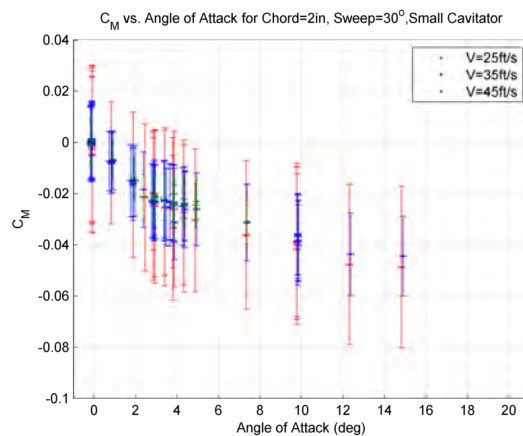


Figure D.92: Moment Coefficient C_M vs. Angle of Attack and Tunnel Velocity, 2 inch chord, $\gamma = 30^\circ$, small cavitator

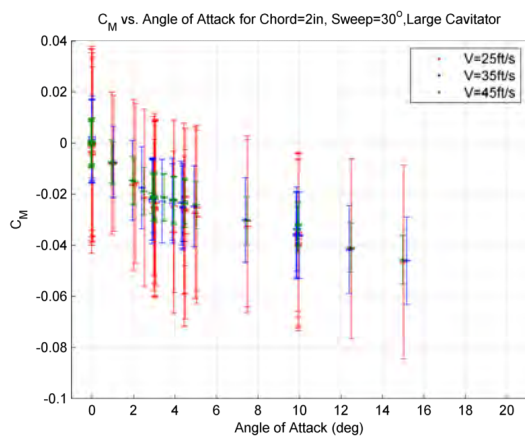


Figure D.93: Moment Coefficient C_M vs. Angle of Attack and Tunnel Velocity, 2 inch chord, $\gamma = 30^\circ$, large cavitator

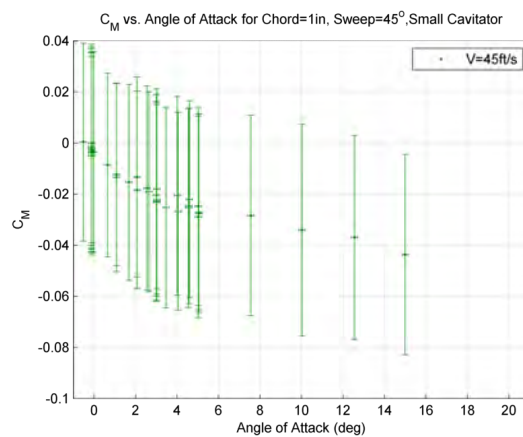


Figure D.94: Moment Coefficient C_M vs. Angle of Attack and Tunnel Velocity, 1 inch chord, $\gamma = 45^\circ$, small cavitator

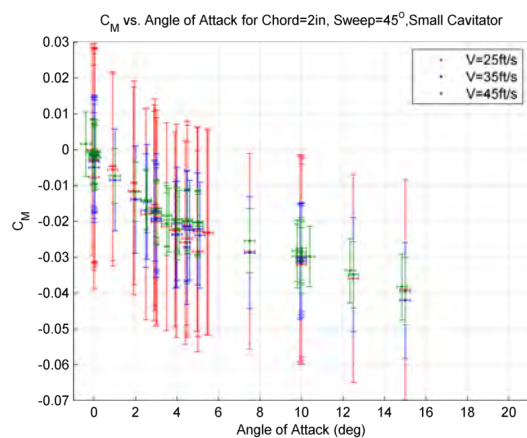


Figure D.95: Moment Coefficient C_M vs. Angle of Attack and Tunnel Velocity, 2 inch chord, $\gamma = 45^\circ$, small cavitator

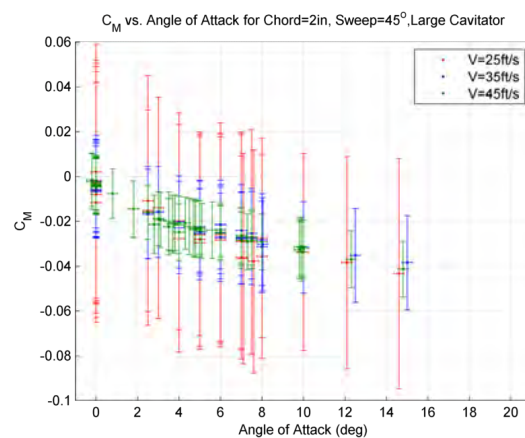


Figure D.96: Moment Coefficient C_M vs. Angle of Attack and Tunnel Velocity, 2 inch chord, $\gamma = 45^\circ$, large cavitator

Appendix **E**

Transition Angles of Attack

Plots are presented showing the angle of attack where transition between base and fully ventilated operation occurred. Each figure will show the angles of attack plotted against tunnel velocity for a particular combination of sweepback angle, chord length, and cavitator size. Data for the transition between base ventilated to fully ventilated will be presented first, followed by the data for the transition back. Red lines connect mean values for a particular tunnel velocity.

E.1 Transition to Fully Ventilated

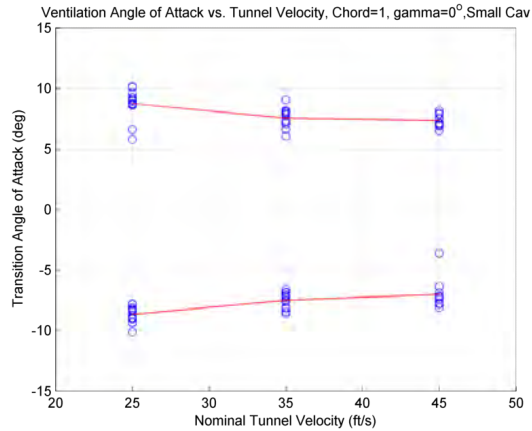


Figure E.1: Angle of attack where fin transitioned to fully ventilated, 1 inch chord, $\gamma = 0^\circ$, small cavitator

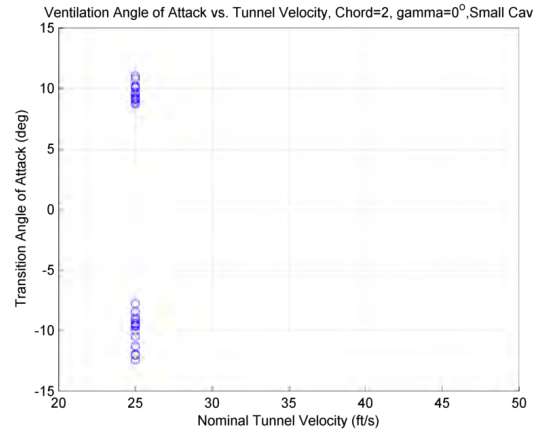


Figure E.2: Angle of attack where fin transitioned to fully ventilated, 2 inch chord, $\gamma = 0^\circ$, small cavitator

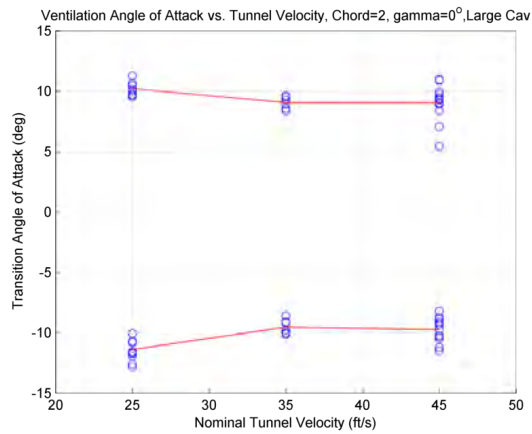


Figure E.3: Angle of attack where fin transitioned to fully ventilated, 2 inch chord, $\gamma = 0^\circ$, large cavitator

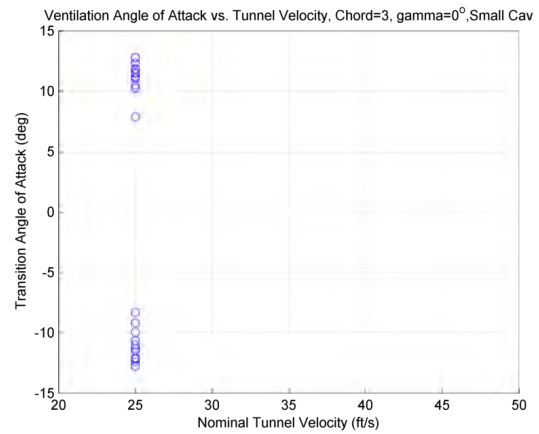


Figure E.4: Angle of attack where fin transitioned to fully ventilated, 3 inch chord, $\gamma = 0^\circ$, small cavitator

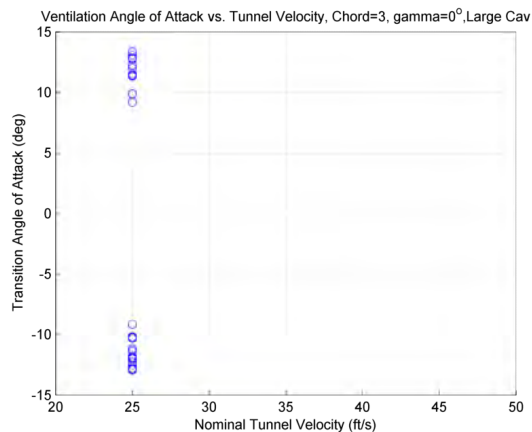


Figure E.5: Angle of attack where fin transitioned to fully ventilated, 3 inch chord, $\gamma = 0^\circ$, large cavitator

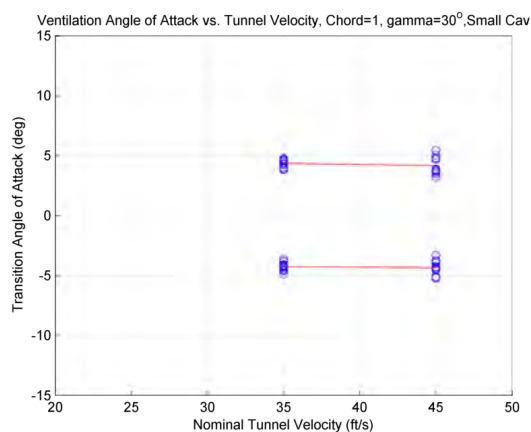


Figure E.6: Angle of attack where fin transitioned to fully ventilated, 1 inch chord, $\gamma = 30^\circ$, small cavitator

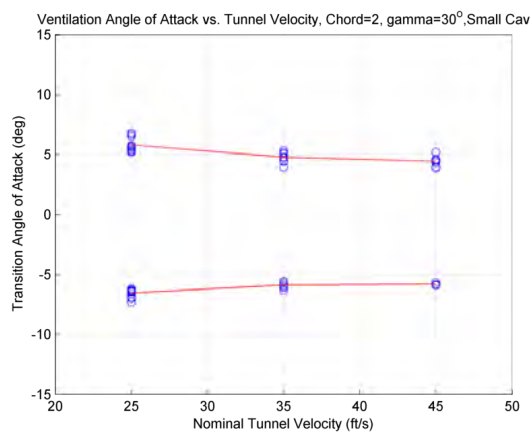


Figure E.7: Angle of attack where fin transitioned to fully ventilated, 2 inch chord, $\gamma = 30^\circ$, small cavitator

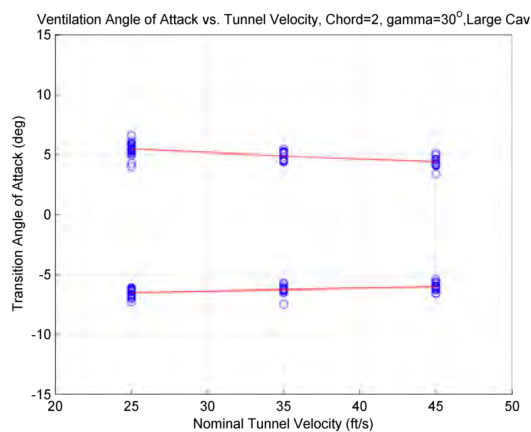


Figure E.8: Angle of attack where fin transitioned to fully ventilated, 2 inch chord, $\gamma = 30^\circ$, large cavitator

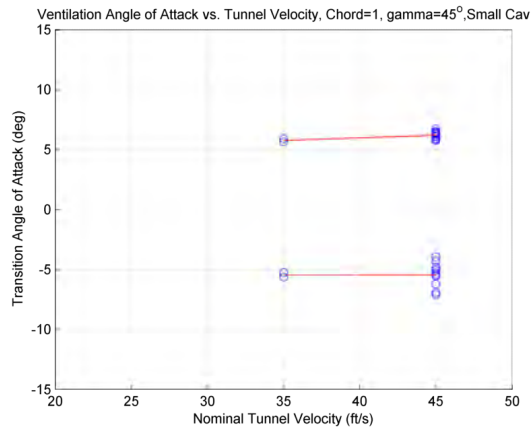


Figure E.9: Angle of attack where fin transitioned to fully ventilated, 1 inch chord, $\gamma = 45^\circ$, small cavitator

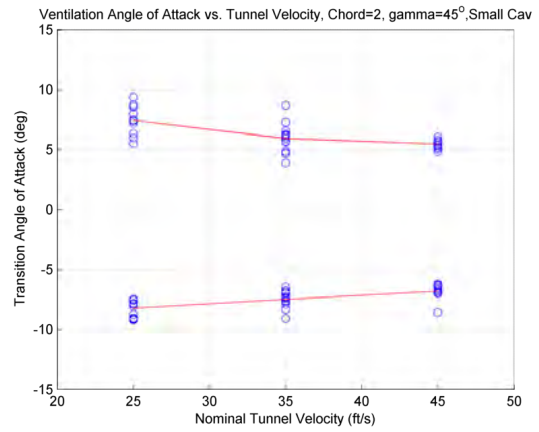


Figure E.10: Angle of attack where fin transitioned to fully ventilated, 2 inch chord, $\gamma = 45^\circ$, small cavitator

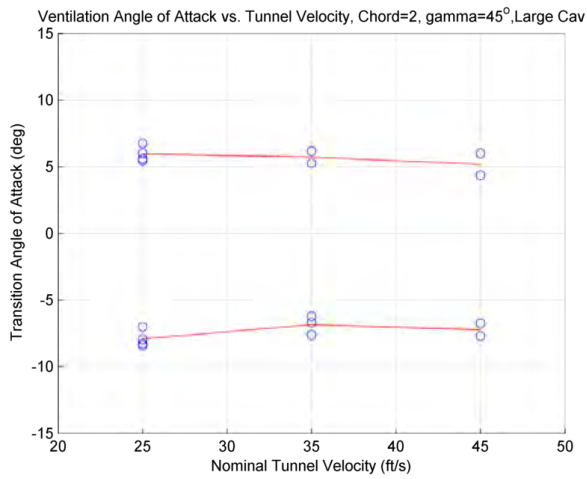


Figure E.11: Angle of attack where fin transitioned to fully ventilated, 2 inch chord, $\gamma = 45^\circ$, large cavitator

E.2 Transition to Base Ventilated

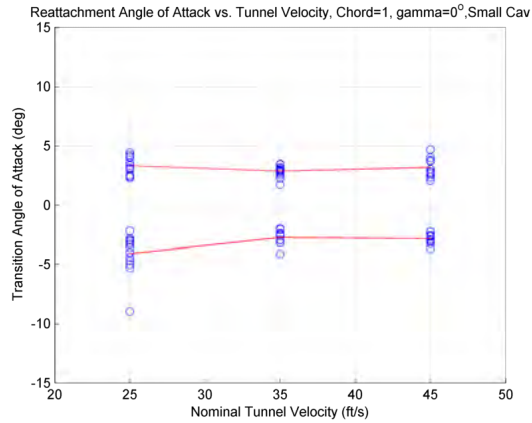


Figure E.12: Angle of attack where fin transitioned to base ventilated, 1 inch chord, $\gamma = 0^\circ$, small cavitator

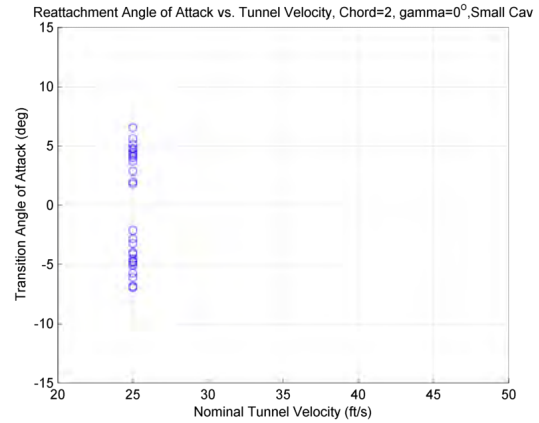


Figure E.13: Angle of attack where fin transitioned to base ventilated, 2 inch chord, $\gamma = 0^\circ$, small cavitator

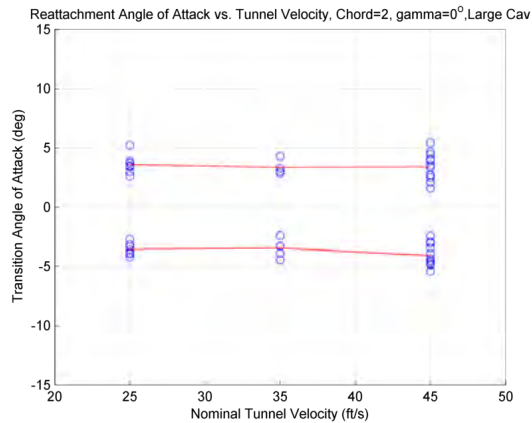


Figure E.14: Angle of attack where fin transitioned to base ventilated, 2 inch chord, $\gamma = 0^\circ$, large cavitator

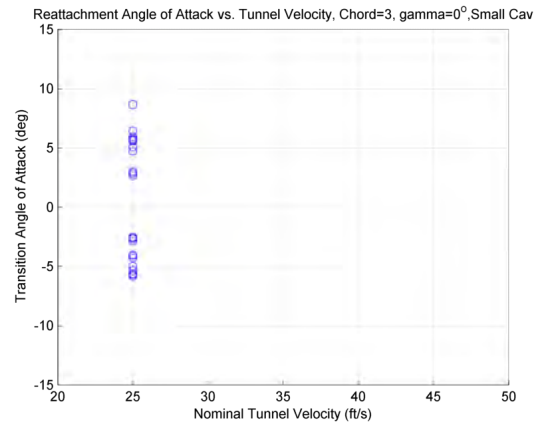


Figure E.15: Angle of attack where fin transitioned to base ventilated, 3 inch chord, $\gamma = 0^\circ$, small cavitator

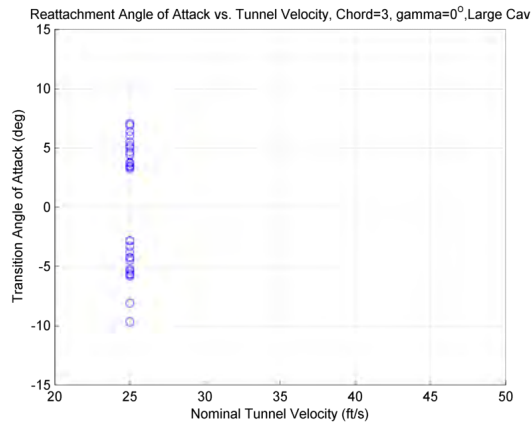


Figure E.16: Angle of attack where fin transitioned to base ventilated, 3 inch chord, $\gamma = 0^\circ$, large cavitator

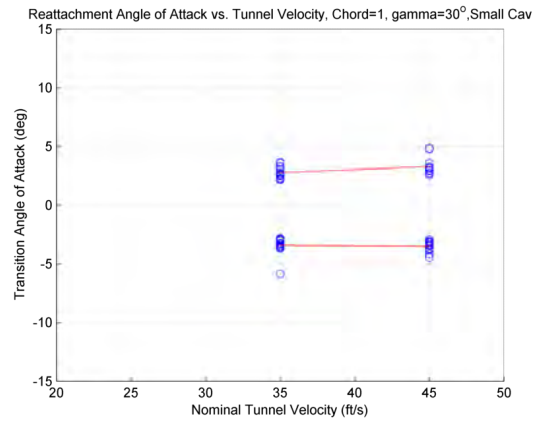


Figure E.17: Angle of attack where fin transitioned to base ventilated, 1 inch chord, $\gamma = 30^\circ$, small cavitator

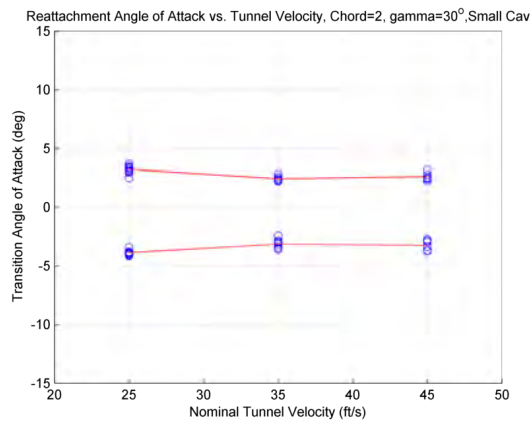


Figure E.18: Angle of attack where fin transitioned to base ventilated, 2 inch chord, $\gamma = 30^\circ$, small cavitator

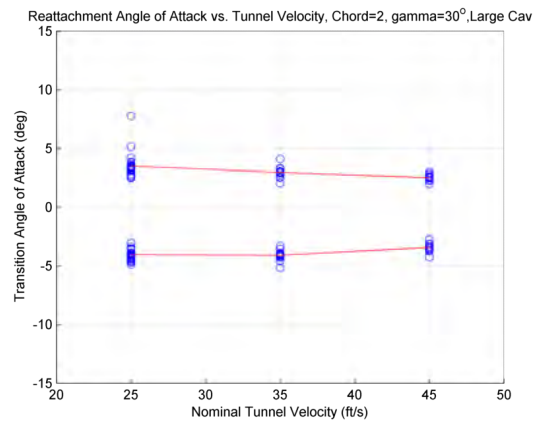


Figure E.19: Angle of attack where fin transitioned to base ventilated, 2 inch chord, $\gamma = 30^\circ$, large cavitator

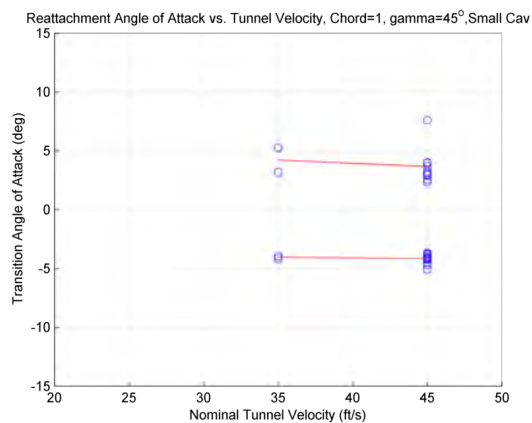


Figure E.20: Angle of attack where fin transitioned to base ventilated, 1 inch chord, $\gamma = 45^\circ$, small cavitator

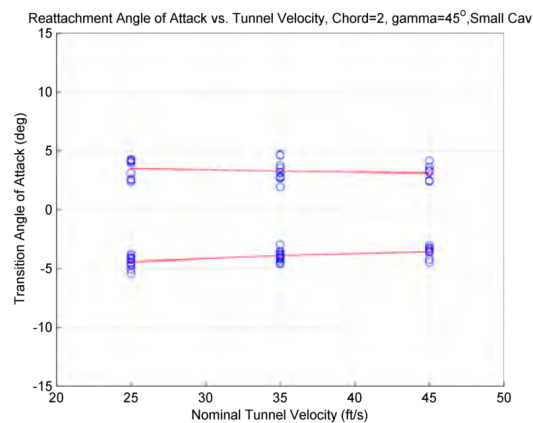


Figure E.21: Angle of attack where fin transitioned to base ventilated, 2 inch chord, $\gamma = 45^\circ$, small cavitator

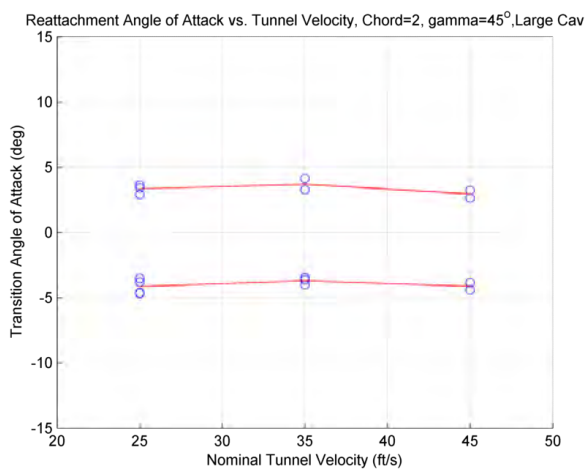


Figure E.22: Angle of attack where fin transitioned to base ventilated, 2 inch chord, $\gamma = 45^\circ$, large cavitator

Bibliography

- Anderson, J.D. *Aircraft Performance and Design*. WCB McGraw-Hill, 1999.
- Auslaender, J. Low drag supercavitating hydrofoil sections. Technical Report 001-7, Hydronautics Inc., April 1962.
- Baker, E.S. Review of supercavitating hydrofoil experiments. Technical report, David Taylor Model Basing NSRDC, 1975.
- Breslin, J.P. and Delleur, J.W. The hydrodynamic characteristics of several surface-piercing struts. Technical Report TR-596, Experimental Towing Tank, Stevens Institute of Technology, January 1956.
- Breslin, J.P. and Skalak, R. Exploratory study of ventilated flows about yawed surface piercing struts. Technical Report NASA Memo 2-23-59W, Experimental Towing Tank, Stevens Institute of Technology, April 1959.
- Campbell, J. and Hilborne, D.V. Air entrainment behind artificially inflated cavities. In Cooper, Ralph D., editor, *Second Symposium on Naval Hydrodynamics-Hydrodynamic Noise/Cavity Flow*, pages 467–483. Office of Naval Research, August 1958.
- Christopher, K.W. and Johnson, V.E. Experimental investigation of two low-drag supercavitating hydrofoils at speeds up to 200 feet per second. Technical Note D-436, National Aeronautics and Space Administration, Washington, August 1960.
- Coleman, H.W. and Steele, W.G. *Experimentation and Uncertainty Analysis for Engineers*. Wiley Interscience, 2 edition, 1999.
- Conolly, A.C. Prospects for very-high-speed hydrofoils. *Marine Technology*, 12(4):367–377, October 1975.
- Cox, A.D. and Clayden, W.A. Cavitating flow about a wedge at incidence. *Journal of Fluid Mechanics*, 3(6):615–637, 1958.

- Dzielski, J.E.; Sammut, P., and Datla, R. Planing-hull forces and moments on a cylindrical body in a cavity. In *Proceedings of the 8th International Symposium on Cavitation*, number 285, August 2012.
- Franc, J.P. and Michel, J.M. *Fundamentals of Cavitation*, volume 75 of *Fluid Mechanics and Its Applications*. Kluwer Academic Publishers, 2004.
- Helmbold, H.B. Der unverwundene ellipsenflügel als tragende fläche. German wartime report, Deutschen Luftfahrtforschung, 1942.
- Helmholtz, V. *Über Discontinuirliche Flüssigkeitsbewegungen*. Monatsberichte der königlichen Akademie der Wissenschaften zu Berlin, April 1868.
- Hjartarson, A.; Mokhtarzadeh, H.; Kawakami, E.; Balas, G., and Arndt, R. A dynamic test platform for evaluating control algorithms for a supercavitating vehicle. In *Proceedings of the 7th International Symposium on Cavitation*, 2009.
- Hoerner, S.F. *Fluid Dynamic Drag*. Self Published, 1958.
- Johnson, V.E. The influence of depth of submersion, aspect ratio, and thickness on supercavitating hydrofoils operating at zero cavitation number. In Cooper, Ralph D., editor, *Second Symposium on Naval Hydrodynamics-Hydrodynamic Noise/Cavity Flow*, pages 317–365. Office of Naval Research, August 1958.
- Kermeen, R.W. Experimental investigations of three-dimensional effects on cavitating hydrofoils. Technical report, California Institute of Technology, 1960.
- Kinnas, S.A. Supercavitating 2-d hydrofoils: Prediction of performance and design. In *Supercavitating Flows*, number 21 in RTO-EN-010, January 2002a.
- Kinnas, S.A. Supercavitating 3-d hydrofoils and propellers: Prediction of performance and design. In *Supercavitating Flows*, number 23 in RTO-EN-010. NATO, 2002b.
- Knapp, R.T.; Daily, J.W., and Hammitt, F.G. *Cavitation*. McGraw-Hill, 1970.
- Lewis, E.V. *Principles of Naval Architecture*, volume Volume II-Resistance, Propulsion, and Vibration. SNAME, 1988.
- Maixner, M.R. An experimental investigation of wall effects on supercavitating hydrofoils of finite span. Technical report, Massachusetts Institute of Technology, 1977.
- Meijer, M.C. Pressure measurements on flapped hydrofoils in cavity flows and wake flows. Technical report, Karman Laboratory of Fluid Mechanics and Jet Propulsion, California Institute of Technology, 1965.
- Milne-Thomson, L.M. *Theoretical Hydrodynamics*. Macmillan and Co, St. Martin's Street, London, 2nd edition, 1949.

- Morgan, W.B. Surface-piercing struts (strut ventilation). In *Proceedings of the 12th International Towing Tank Conference*, number Appendix IVb in Cavitation, pages 377–381. ITTC, September 1969.
- Parkin, B.R. Experiments on circular arc and flat plate hydrofoils in noncavitating and full cavity flows. Technical Report 47-6, Hydrodynamics Laboratory at California Institute of Technology, February 1956.
- Pearce, B.W. *Ventilated Supercavitating Hydrofoils for Ride Control of High-Speed Craft*. PhD thesis, University of Tasmania, 2011.
- Rae Jr., W.H. and Pope, A. *Low-Speed Wind Tunnel Testing*. Wiley, 2 edition, 1984.
- Ransleben Jr., G.E. Experimental determination of steady and unsteady loads on a surface piercing, ventilated hydrofoil. *Journal of Ship Research*, 1969.
- Roshko, A. A new hodograph technique for free-streamline theory. Technical Report TN-3168, National Advisory Committee for Aeronautics (NACA), Washington, July 1954.
- Saunders, H.E. *Hydrodynamics in Ship Design*, volume 2. SNAME, 1957.
- Savitsky, D. and Breslin, J.P. Experimental study of spray drag of some vertical surface-piercing struts. Technical Report 1198, Davidson Laboratory, Stevens Institute of Technology, December 1966.
- Schauer, T.J. An experimental study of a ventilated supercavitating vehicle. Master's thesis, University of Minnesota, March 2003.
- Semenenko, V.N. Dynamic processes of supercavitation and computer simulation. In *Supercavitating Flows*, number 12 in RTO-EN-010. NATO, January 2002a.
- Semenenko, V.N. Artificial supercavitation. physics and calculation. In *Supercavitating Flows*, RTO-EN-010. NATO, January 2002b.
- Sierra Series 830/840/860 Side-Trak and Auto-Trak mass flow meters and controllers*. Sierra instruments inc, g.1-2-06 edition, 1994.
- Song, C.C.S. Vibration of cavitating hydrofoils. Technical report, Saint Anthony Falls Hydraulic Laboratory, University of Minnesota, October 1969.
- Stinebring, D.R.; Billet, M.L.; Lindau, J.W., and Kunz, R.F. Developed cavitation-cavity dynamics. In *Supercavitating Flows*, RTO-EN-010. NATO, 2002.
- Tulin, M.P. and Burkart, M.P. Linearized theory for flows about lifting foils at zero cavitation number. Technical Report C-638, David Taylor Model Basin, February 1955.

- Tulin, M.P. and Hsu, C.C. New applications of cavity flow theory. In Inui, Takao, editor, *13th Symposium on Naval Hydrodynamics-Impact of Hydrodynamics Theory upon Design Practice, with Emphasis on High Performance and/or Energy Saving Ships*, pages 107–158, October 1980.
- Verron, J. and Michel, J.M. Base-ventilated hydrofoils of finite span under a free surface: An experimental investigation. *Journal of Ship Research*, 1984.
- Waid, R.L. and Lindberg, Z.M. Experimental and theoretical investigations of a supercavitating hydrofoil. Technical Report 47-8, California Institute of Technology, April 1957.
- Wetzel, J.M. Ventilation of bodies piercing a free surface. In Cooper, Ralph D., editor, *Second Symposium on Naval Hydrodynamics-Hydrodynamic Noise/Cavity Flow*, pages 447–467. Office of Naval Research, August 1958.
- Wosnik, M. and Arndt, R.E.A. Control experiments with a semi-axisymmetric supercavity and a supercavity-piercing fin. In *Proceedings of the 7th International Symposium on Cavitation*, number 146 in CAV2009, August 2009.
- Wu, T.Y. A free streamline theory for two-dimensional fully cavitating hydrofoils. Technical Report 21-17, Hydrodynamics Laboratory at California Institute of Technology, July 1955.